Advances in Physics, 2013
Vol. 62, No. 2, 113–224, http://dx.doi.org/10.1080/00018732.2013.808047

Taylor & Francis
Taylor & Francis Group

REVIEW ARTICLE

Plasma nanoscience: from nano-solids in plasmas to nano-plasmas in solids

K. Ostrikov[a]*, E.C. Neyts[b] and M. Meyyappan[c]

[a]*CSIRO Materials Science and Engineering, PO Box 218, Lindfield NSW 2070, Australia;* [b]*University of Antwerp, Department of Chemistry, Research Group PLASMANT, Universiteitsplein 1, B-2610 Wilrijk-Antwerp, Belgium;* [c]*NASA Ames Research Center, Moffett Field, CA 94035, USA*

(*Received 11 March 2013; final version received 21 May 2013*)

The unique plasma-specific features and physical phenomena in the organization of nanoscale solid-state systems in a broad range of elemental composition, structure, and dimensionality are critically reviewed. These effects lead to the possibility to localize and control energy and matter at nanoscales and to produce self-organized nano-solids with highly unusual and superior properties. A unifying conceptual framework based on the control of production, transport, and self-organization of precursor species is introduced and a variety of plasma-specific non-equilibrium and kinetics-driven phenomena across the many temporal and spatial scales is explained. When the plasma is localized to micrometer and nanometer dimensions, new emergent phenomena arise. The examples range from semiconducting quantum dots and nanowires, chirality control of single-walled carbon nanotubes, ultra-fine manipulation of graphenes, nanodiamond, and organic matter to nano-plasma effects and nano-plasmas of different states of matter.

PACS: 81.07.-b Nanoscale materials and structures: fabrication and characterization; 68.35.-p Solid surfaces and solid-solid interfaces: structure and energetics; 68.65.-k Low-dimensional, mesoscopic, nanoscale and other related systems: structure and nonelectronic properties; 81.16.-c Methods of micro- and nanofabrication and processing; 52.77.-j Plasma applications; 82.33.-z Reactions in various media

Keywords: nanoscale solid systems; self-organization; plasma-specific effects; structural and functional properties; nano-plasmas

Contents **PAGE**

*Corresponding author. Email: kostya.ostrikov@csiro.au

1. Introduction

Nanoscience is a commonly known research field which deals with objects of nanometer and sub-nanometer dimensions, the basic organizing principles of these objects, and the unique properties these objects possess compared with bulk objects made of the same material(s) [1]. But what is *plasma nanoscience*? From the combination of the two terms *plasma* and *nano*, it is clear that this is a field at the intersection of plasma science and nanoscience. A more in-depth understanding comes from focusing on *dimensions*, *organization*, and *properties*. One should also note that matter exists in four basic states, and the plasma state is one of them. From basic symmetry considerations, nanometer-sized objects should exist in these four basic states, namely solid, liquid, gas, or plasma.

From merely the dimensional perspective, plasma nanoscience should deal with the plasma state of matter confined to nanometer dimensions. However, from the organizational perspective, there is a variety of options of assembly of nanoscale objects using precursors in different states. Indeed, one can assemble solid nanoparticles (NPs) using (e.g. precipitating) precursors in the liquid, gaseous, or plasma states. Liquid nano-droplets can be produced by manipulating (e.g. heating or condensing) precursors in the solid, gaseous, or plasma states, etc. Depending on the specific way of organization, the arrangement of atoms in nanoscale objects may also be different. This, in turn, leads to differences in the physical and chemical *properties* of the objects produced.

Hence, there arises another possibility – to use precursors in the ionized (plasma) state and follow how they organize into solid nanoscale objects. A plasma typically produces a plethora of different precursor species (molecules, atoms, and radicals), in a large number of different energetic states (ionized, excited, metastables, and ground states) compared with solid, liquid, or gaseous precursors. These plasma precursors are thus very likely to assemble into solid objects with quite different atomic arrangements. This in turn will lead to the different properties of these nano-solids.

This possibility also exists for bulk objects. However, when dealing with small objects, greater precision is required, simply because of the basic requirement to confine matter to nanometer or even subnanometer dimensions. This is why the way of organizing matter at the nanoscale should be more precise, more 'careful'. These basic considerations also apply to modifying existing nanoscale solid objects. In this case, there are numerous options to modify such objects using species in the same or different states of matter. Therefore, using plasma-produced species should lead to quite different outcomes compared with other environments.

1.1. *Scope of plasma nanoscience research*

In basic terms, what does plasma nanoscience study? On the one hand, it studies the unique way of using ionized gases to produce or modify nanoscale solids, thereby giving them different properties compared with other ways of organization that use precursors in other states of matter. This is why the title of this review contains 'nano-solids in plasmas'. On the other hand, if it is possible to confine the plasma to nanometer dimensions, it will almost certainly have very different properties compared with bulk plasmas. This focus is denoted by the 'nano-plasmas' in the title.

As will be discussed in this review, the ability to control nanoscale localization of energy and matter delivered from the bulk plasmas to developing nano-solids is the key to achieve the desired morphological, structural, and functional properties. On the other hand, the energy and matter can also be confined to nanoscales if the plasma itself is confined to the nanoscale, in other words, when nano-plasmas are generated. These nano-plasmas can be sustained near the surface of a bulk solid, for example, under extremely non-equilibrium conditions of very dense plasmas of physical vapors of solids. The bulk plasmas can be used to produce nanoscale solids which in turn can confine nano-plasmas, or have nano-plasmas in their vicinity. In all these cases, the plasma state is in contact with a surface with nanoscale features or dimensions. The physics of these nanoscale interactions is what makes this field particularly interesting. This is the reason why the title of this review bridges nano-solids (produced) from plasmas with nano-plasmas (sustained) in or near solids.

In general, plasma nanoscience focuses on the specific roles, purposes, and benefits of the ionized gas (plasma) environments in assembling, processing, and controlling microscopic and nanoscale (including biological) objects in natural, laboratory, and technological environments and to find the most effective ways to ultimately bring these unique plasma-based processes to the deterministic level [2]. One of the primary aims of this research is to find optimum plasma process parameters to minimize the number of experimental trials one needs to undertake to achieve nanostructures (NSs) and nanomaterials with the desired properties, which in turn determine their performance in practical applications. Numerous effects of microscopic and nanoscale localizations of energy and matter in plasmas produced from gases, liquids, and solids and the associated interactions of such plasmas with matter in different phases are also of primary interest.

Plasma nanoscience is a relatively new research field which emerged in the last two decades because of the rapid advent of nanoscience and nanotechnology and continuously increasing demand for applications of low-temperature plasmas in nanoscale synthesis and processing. Such plasmas have been used in materials science and microelectronics for decades as a viable fabrication tool.

However, as the number of nanomaterials of different structures, composition, morphology, and dimensionality experienced a rapid surge, it became increasingly clear that nanoscale synthesis and processing is very different compared with bulk solids. From the fundamental perspective, this refers to the much higher required precision in the ability to control energy and matter during the production or modification of nanomaterials.

Following the pioneering discovery of fullerenes in laser-generated vapor plasmas of graphite [3] and carbon nanotubes (CNTs) produced from arc discharge plasmas [4], the number of successful applications of low-temperature plasmas in nanofabrication has skyrocketed. From merely CNT synthesis and microstructuring of semiconductors in the early 1990s, the plasma success stories have expanded into a plethora of pure and hybrid nanoscale objects of virtually any dimensionality spanning across a very large number of materials systems. More importantly, in some cases, it became possible to achieve certain objectives only using tailored plasmas while other techniques failed. This is why a clear understanding on how exactly plasma-specific effects work in such nanoscale processes was urgently required.

After years of experimental trials, theoretical studies, and numerical simulations, it became possible not only to use low-temperature plasmas for nanoscale processing with the level of confidence comparable with processing of bulk materials, but also, in many cases, achieve outcomes superior to those achieved by other common techniques, e.g. based on thermal chemical vapor deposition (CVD), wet chemistry-based synthesis and processing, laser-assisted microfabrication, etc. This review will focus on such examples and on the underlying physics of the elementary processes involved.

Plasma nanoscience is intrinsically multidisciplinary. It involves elements of basic sciences such as physics and chemistry of solids, liquids, gases, and plasmas, materials science, nanoscience, optics, astrophysics, molecular, radical, and cell biology. From the applications perspective, it also involves knowledge from related engineering and technological sciences such as nanotechnology, materials and device engineering, and design, as well as chemical, mechanical, electrical, electronic, and optoelectronic engineering.

There is a large number of relevant monographs and reviews published to date (see, e.g. [5–19] and references therein). These publications mostly focus on the types of plasmas used, materials systems, envisaged applications, etc. The *scope of this review* is unique as it aims to explain, from the unifying physical principles (e.g. involving concepts of nanoscale localization, determinism, self-organization, non-equilibrium, complexity, etc.), how plasmas can be used to produce or process matter (including hard, soft, and living matter) with spatial localization in the sub-nanometer to micrometer range, as well as to discuss the unique properties of nano-plasmas.

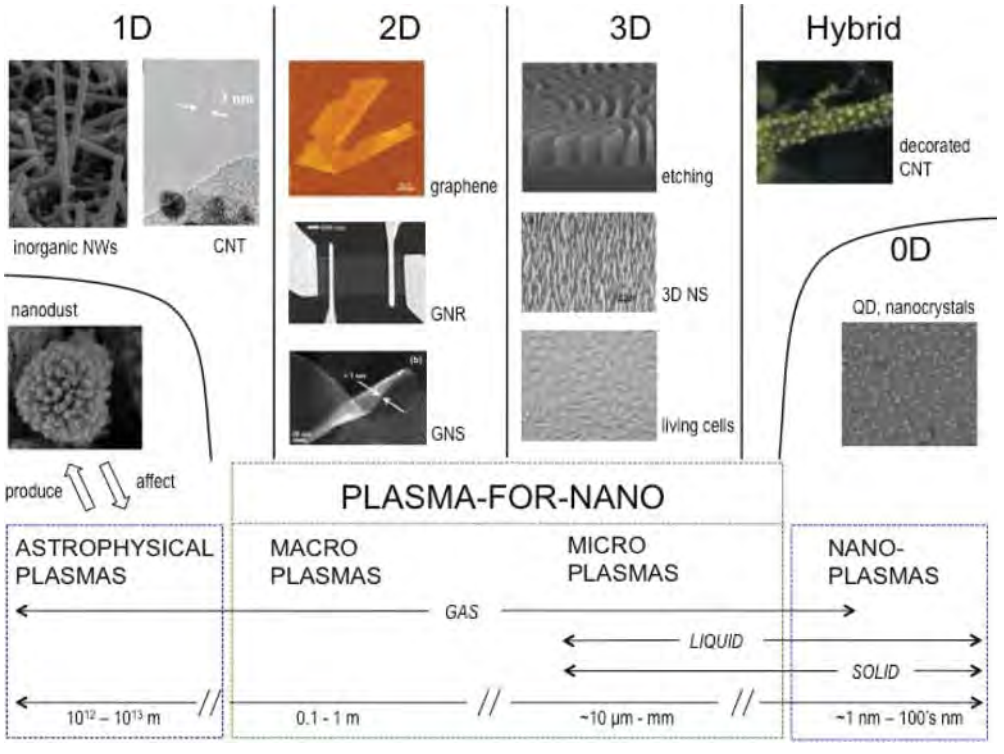

Figure 1. Scope of plasma nanoscience research. Plasmas in gases and liquids are used to produce nanoscale solid objects of various dimensionality, structure, and elemental composition (denoted 'plasma-for-nano' in the figure). Plasmas with micrometer and nanometer spatial localizations (denoted 'micro-' and 'nano-plasmas' in the figure, respectively) are possible in gases, liquids, and solids. Generation and collective behavior of dust NPs in astrophysical and space environments (denoted 'astrophysical plasmas' in the figure) are also of interest but outside the scope of this review. Fragments of images are reproduced with permissions from [20] [Copyright ©2006 Wiley-VCH Verlag GmbH & Co. KGaA, Weinheim], [21] [Copyright © 2005 National Academy of Sciences, USA], [22] [Copyright © 2009 American Institute of Physics], [23] [Copyright © 2007 with permission from Elsevier], [24,25] [Copyright ©IOP Publishing. Reproduced by permission of IOP Publishing. All rights reserved]. All other fragments are from original unpublished research in K. Ostrikov's laboratories. All relevant team members are gratefully acknowledged. Notes: 0D, zero-dimensional; 1D, one-dimensional; 2D, two-dimensional; 3D, three-dimensional; NS, nanostructure; NW, nanowire; QD, quantum dot; CNT, carbon nanotube; GNR, graphene nanoribbon; GNS, graphene nanosheet.

Figure 1 shows the scope of plasma nanoscience research. In addition to the already mentioned nano-solids from plasmas (denoted and used hereafter as *plasma-for-nano* for brevity and simplicity) and *nano-plasma* domains, it also involves *astrophysical plasmas*. These domains, although vastly different by their spatial localizations (from 10^{12}–10^{13} m for plasmas at astrophysical scales down to nanometer-sized plasmas), can have one crucial common attribute – nanoscale objects.

Indeed, nano- and micrometer-sized solid dust nucleates in the relatively cold environments of stellar envelopes and plays a critical role in the energy and mass transfer on the scale of the Universe, where plasmas constitute more than 99% of visible matter [26]. This relation between the microscopic solid objects and plasmas is reflected by the arrows on the left-hand side of

Figure 1: plasmas produce (dust) NPs which in turn affect the plasma. This interdependence persists both locally, over microscopic scales, and globally, over macroscopic scales, which can be as large as the dimensions of astrophysical objects such as galaxies.

This leads to the two essential attributes of the *plasma–solid systems* (PSSs) of our interest. The first attribute is *self-organization* which results from the interplay between the plasma and solid components involved. The other attribute is the *multi-scale nature* of this system, where very diverse physical phenomena may take place at different spatial and temporal scales.

These basic attributes are also common to other phase combinations and to the *plasma-for-nano* and *nano-plasma* domains in Figure 1. The plasma-for-nano domain involves plasmas in gases and liquids localized across the dimensions of plasma reactors commonly used for nanomaterials synthesis and processing (0.1–1 m) and more recent microplasma discharges ($\sim$10 μm–1 mm). Plasmas in both gases and liquids have been used for the synthesis and processing of nanoscale objects of different elemental composition, structure, and dimensionality, as shown in Figure 1. These objects include zero-dimensional (0D) quantum dots (QDs) and nanocrystals, one-dimensional (1D) nanowires (NWs) and CNTs, and two-dimensional (2D) flat (e.g. graphene, organic monolayers) and bent (e.g. graphene nanoribbons (GNRs), graphene nanosheets (GNSs), nanowalls, etc.) structures.

Further examples include more complex three-dimensional (3D) objects such as vertical pyramid-like pillars produced by plasma etching, other 3D NSs, and also living cells. Many of these objects have intricate internal and surface structures. For example, living cells have organelles of sub-micrometer dimensions both in the intracellular space and on the surface, CNTs have narrow channels along their length, whereas many other nanomaterials have similarly small features both in their interior (e.g. embedded QDs or pores, regular arrays of atomic vacancies, etc.) or on the surface (e.g. nanometer surface texture).

These objects may also be arranged in complex patterns and arrays. For instance, CNTs or inorganic NWs can be arrayed through self-organized growth, while nano-pillars can be carved out of a monolithic piece of crystalline Si wafer by reactive etching. These are the two *fundamental approaches to nanoscale synthesis*. The first case refers to the bottom-up, self-organized growth or nano-assembly, while the second one is an example of top-down nanofabrication. Importantly, not only can a plasma be used in both cases, but in many cases, it also shows superior performance compared with other (e.g. thermal CVD and wet chemistry-based) nanoscale synthesis and processing techniques. In some cases, plasmas can even enable nanoscale processes which are not possible otherwise under the same conditions. This review will show examples of specific benefits of using plasmas in nanoscale synthesis and processing and reveal the underlying physical processes that make these benefits possible.

Nanoscale structures can also be organized on the surface or inside other objects of different dimensionality. Figure 1 shows an example of a hybrid structure made of a 1D CNT decorated by small 0D metal NPs. Such hybrid and multi-dimensional arrangements are used to modify properties of the nanomaterials involved and produce physical effects (e.g. electron transport, energy band structure, interaction with light, etc.) which are difficult or impossible to achieve using the constituent materials separately. Plasmas have also been used to produce and modify such (and many other) hybrid multi-dimensional objects, also with several advantages compared with other approaches.

The last (but not the least) domain in Figure 1 is *nano-plasmas*. By nano-plasmas, we refer to plasmas confined to sub-micrometer dimensions.

Here, we would like to stress two important features shown in Figure 1. First, plasmas can be produced from gases, liquids, and solids. The fourth, plasma state is achieved through state transformations from gas, liquid, or solid phases. When such transformation is complete, the same bit of original matter cannot simultaneously be in the plasma and some other (e.g. solid, gas, or

liquid) state. However, incomplete phase transitions may result in mixed phases, e.g. partially ionized gases where the ionized (plasma) and charge neutral gaseous phases coexist.

Second, the plasmas feature very different sizes. The denser and cooler the matter, the smaller is the minimum size of the plasma which is determined by a few multiples of the electron Debye length

$$\lambda_{\mathrm{D}} = \frac{V_{Te}}{\omega_{pe}}, \tag{1}$$

which decreases with the plasma density and increases with the electron temperature. Here, $V_{Te} = (k_{\mathrm{B}}T_{\mathrm{e}}/m_{\mathrm{e}})^{1/2}$ is the electron thermal velocity, $\omega_{pe} = (4\pi n_{e0}e^2/m_{\mathrm{e}})^{1/2}$ is the Langmuir (plasma) frequency, e, T_{e}, m_{e}, and n_{e0} are the charge, temperature, effective mass, and equilibrium number density of electrons, respectively, and k_{B} is Boltzmann's constant. According to the classical plasma definition, charge neutrality has to be preserved well beyond the Debye sphere with λ_{D} as a radius. However, the principle of the Debye length does not apply to all plasmas. This is the case for electronegative or electropositive plasmas with unbalanced electric charges or microplasma discharges with delocalized charge distributions where charge balance is sustained dynamically.

The minimum plasma size can be in the nanometer range, e.g. under conditions of ultra-high-energy-density (HED) laser ablation of solid targets. This is why ultra-small laser plasmas may be generated in localized areas on solid surfaces thereby producing tiny features on the surface. The possibilities and specific mechanisms to enable these effects will also be considered in this review.

1.2. *Aims, focus, and unifying physics*

This review aims to critically review the physical phenomena related to

(1) *nanoscale organization* of solid-state matter using plasmas in gases and liquids, and
(2) *nano-plasmas* confined in sub-micrometer volumes and possibly surrounded by gas, liquid, or solid matter or a combination thereof,

by focusing on the plasma-specific organizing principles, nanoscale energy- and matter localization effects, as well as the arising structural, morphological, and functional properties of the nano-solids involved.

In other words, here we focus on highly unusual features of non-equilibrium plasmas and physical mechanisms of using these features to achieve the required nanoscale solid objects and their arrays and networks. The particular highlight here is on *nanoscale localization of energy and matter* and *non-equilibrium and kinetic features* that determine the physics of nanoscale interactions in the PSSs most common to nanoscience. We also critically examine the physics of nano-plasmas generated near solid surfaces.

In particular, this review aims to clarify the following questions:

What can be achieved at the nanoscale using plasmas?

What unique plasma-specific physical processes (e.g. non-equilibrium, complexity, kinetics, self-organization, etc.) are involved?

How can plasma-specific effects be used to tailor the organization and properties of the nanoscale solid objects to meet the requirements in applications?

Which plasmas to use to achieve superior outcomes?

Can the plasma be confined to nanoscales and how can it be used?

In a simple catchphrase, the aim is to show *how and why plasma-specific effects make a difference at nanoscales*.

The unifying physics-based approach to describe these phenomena is based on the concepts of *nanoscale localization*, *determinism*, *organization*, *non-equilibrium*, and *complexity*. As mentioned above, the nanoscale localization of energy and matters arises when the dimensions of either the solid objects or the plasmas are in the nanometer range, or when both are within nanoscales. By nanoscales here we broadly imply spatial scales ranging from fractions to hundreds of nanometers; outside of this range, we use terms 'atomic' and 'micrometer' to determine the relevant scales.

Determinism stems from Feynmann's vision to 'arrange atoms, the way we want them', which is one of the guiding principles of nanoscience. This usually refers to achieving the required effects by customizing the nanoscale organization of matter. The latter can be achieved using either a 'top-down' fabrication or 'bottom-up' self-organization or a combination thereof. The importance of controlled self-organization is rapidly gaining momentum as the feature sizes of nanoscale objects continuously decrease and the 'top-down' techniques are rapidly reaching their intrinsic physical limits. Non-equilibrium conditions are critical for nanoscale synthesis while complexity determines the available controls of organization.

The required effects can be achieved through nanoscale organization of matter using plasmas. Plasmas feature a higher degree of complexity and allow nanoscale synthesis under unique non-equilibrium conditions compared with neutral gases. Under such conditions, the structure and properties of the produced nanoscale solid objects are determined by the complex interplay of the process kinetics and equilibrium thermodynamics. These objects find themselves in exotic metastable states, which offer truly unique structural, electronic, optical, and other properties hardly achievable in the equivalent bulk materials. This is why one can expect many distinctive possibilities for the highly controlled synthesis of more complex and 'non-equilibrium' nanoscale objects from non-equilibrium plasmas.

We will discuss how plasma-specific, long-range electromagnetic field-related effects can be used to control the structure and hierarchical arrangements of many nanoscale solid objects and their patterns. Plasma–surface interactions also enable unique control over the surface energy, shaping, faceting, etc. of these objects by significantly affecting the multi-stage nanopattern development from nucleation of small clusters to NS self-organization in 3D mesoscopic patterns.

Therefore, one can expect that exotic non-equilibrium plasma conditions may lead to the fast, dynamic, non-equilibrium way of organization of solid matter. Moreover, the specific complexity of the plasma state should lead to many diverse options for effective control of self-organization, which may not be available for other states of matter. Ultimately, the self-organization which is controlled/guided by the plasma-specific effects should reach the deterministic level when it is possible to produce nanomaterials with the desired properties. Plasma nanoscience research helps finding and utilizing this control.

1.3. *Organization of the review*

The aims, focus, and the unifying physics defined above determine the structure of the review. The main part is composed of the four main sections. The *overarching logic* is to first identify the most relevant plasma-specific control mechanisms in the assembly of nanoscale solids, then show how they work at every stage of this assembly, and then show specific examples from a broad range of materials systems, followed by discussing the physics of localizing plasmas to nanometer dimensions.

Section 2 introduces a conceptual approach to deterministic nanoscale synthesis and processing through the effective control of self-organization pathways in PSSs. This section will first introduce the PSSs of interest, the spatial scales and basic control mechanisms involved. The key focus here is on the most relevant self-organization pathways and the plasma-specific effects to control them.

In Section 3, we follow the nanoscale assembly, step-by-step, from precursor species generation to nucleation and growth of individual solid NSs and their patterns, and show uniquely plasma-specific effects during each step. This section uses a few focused examples of the most common nano-solids.

Section 4 provides a broad coverage of nanoscale objects and features assembled or modified using plasmas. Each subsection discusses the intended applications of related solid materials, existing problems in their synthesis and processing using other approaches, plasma-specific effects that enable the desired effects (e.g. advantages in the synthesis process, superior properties, etc.), and the remaining challenges. Wherever appropriate, these effects are linked to the physical effects from Sections 2 and 3. Because of the very large number of examples that cover dielectric, semiconducting, and metallic materials in all dimensionalities (from 0D QDs from 3D nanoarrays, as well as structures of a hybrid dimensionality), it is impossible to provide the exhaustive and in-depth coverage of all structural, morphological, and functional (e.g. electronic, optical, magnetic, etc.) properties of all the materials involved. While we discuss the most essential of such properties (most prominently those that are affected by the plasma), wherever possible, we refer the reader to relevant publications which focus on some of these properties.

The scope of Section 5 is the plasmas localized to nanometer dimensions. Examples include very dense plasmas of physical vapors of solids and plasmon-assisted nano-plasma formation near the surface of the NP.

The review concludes with the summary of the most interesting and generic physical effects and a brief outlook for the future research in this field. For the convenience of readers, the acronyms used in this review are summarized in Appendix 1.

Given the breadth of the topic, it will be a futile attempt to provide the fully exhaustive coverage of the relevant existing knowledge. This is why we apologize to the authors of any relevant publications which are not mentioned due to the obvious space and time limitations. This is why we cover the *plasma-for-nano* and *nano-plasma* domains in Figure 1, primarily focusing on the plasma-specific physical effects that make a difference at nanoscales while keeping in mind the unifying physical principles discussed in Section 1.2.

The analysis and comments in this review may not always be the same with the opinions of other researchers. This is why we welcome any comments or discussions on any relevant topic and hope that our effort will stimulate further development of this very interesting field. Just like a *difference* in chemical potentials between two phases drives self-organization (as will be discussed in the following section), a difference in scientists' opinions drives progress in the field.

2. Self-organized plasma-solid systems

Having mentioned the issue of controlled self-organization, we can now clarify how to achieve this in self-organized PSSs. A PSS is a system where a plasma faces a solid and affects processes on its surface or within its bulk. Such systems are non-equilibrium in the presence of significant transfer of energy and matter. This happens, e.g. when the system (e.g. a solid NS on the surface) cannot reach its thermodynamically defined equilibrium (minimum free energy) state while new material is delivered. This happens during the growth or processing of nanoscale objects and the rates of dynamic material re-organization determine the nature and degree of non-equilibrium, which in the plasma can be very different than in the equivalent neutral gas. The system is self-organized when it has the ability to rearrange its constituents when it is left on its own, i.e. without any external action [27].

The most critical factor that enables this ability is the *driving force*, which in many cases is related to significant variations of a physical quantity (e.g. density, temperature, etc.) in space

and a mechanism capable to sustain any rearrangement within the system which can reduce these variations. For example, for multicomponent mixtures of different species on the surface, a generic expression for the driving force for nucleation [28]

$$\Delta g = \Sigma_i n_i \Delta \mu_i \tag{2}$$

relates the supersaturation Δg, the number of species n_i, and the driving forces

$$\Delta \mu_i = \mu_{\alpha i} - \mu_{\beta i} \tag{3}$$

for each individual component (species), where $\mu_{\alpha i}$ and $\mu_{\beta i}$ are the chemical potentials of the old (e.g. gas) and the new (e.g. solid) phases, respectively. These chemical potentials depend on the prevailing process conditions, such as gas pressure, surface temperature, interface energy, plasma-specific parameters (e.g. ionization degree), etc. Importantly, the overall driving force (2) must be positive for a new phase to form. The composition of the new phase is affected by the driving forces of individual components (3); not all of these species may necessarily form a new phase.

The driving force formalism may be generically used during solid NS growth on a surface from a plasma phase. In this case, building material can be delivered to the surface non-uniformly, and the difference between the local densities of adsorbed atoms (adatoms) sustains surface diffusion (SD), which aims to minimize the initial non-uniformity of the adatom density. However, the rates of this reorganization will depend on the amount of energy the adatoms have, which in most cases is determined by the surface temperature, which also depends on the plasma conditions. Hence, the rates of thermal hopping of these adatoms will determine how fast the system can equilibrate. However, it already becomes clear that plasma-specific effects (e.g. surface heating and ion impact) will definitely affect adatom migration and consequently, the equilibrium states of the PSS.

In this section, we will consider the basics of diffusion-driven self-organization and how exposure of a solid surface to a plasma can lead to faster and more exotic self-organization. While the focus here is on the cases involving mass relocation about the surface, ion-assisted surface nanostructuring (e.g. rippling) without significant mass relocation, is considered as well.

One should always keep in mind that any rearrangement of atomic matter at nanoscales should be guided to achieve some specific purpose. In other words, such organization should ultimately be deterministic no matter which specific nanoassembly approach (e.g. bottom-up or top-down or a combination of the both) is used. This is why we will first show some examples of deterministic arrangement of nanoscale objects and will then discuss how to control self-organization in the PSSs of interest.

2.1. *Deterministic requirements at nanoscales*

Without trying to give an exhaustive definition of determinism, it would suffice to say that this term refers to the ability to achieve pre-determined outcomes – for example, produce specific NSs by customizing the plasma-based process and reduce the number of trials to the absolute minimum. These outcomes are usually determined by the specific requirements of the envisaged applications.

For example, by controlling vapor transport, one can achieve size- and shape-selective growth of inorganic NWs, nanoribbons, and other-related structures for electronic and optoelectronic applications [29], produce self-assembled, deterministic networks of wired nanotubes to achieve nanoscale electrical connectivity [30], biomaterials by design with the desired biological response [31], or customize crystalline structure of materials to achieve the desired properties using first-principles calculations [32].

In many cases, structural hierarchy at different spatial scales determines physical properties of nanoscale objects. For example, precisely designed molecular building blocks can be used to create hierarchical arrays and networks through reticular synthesis where structural integrity of these blocks remains unchanged during the assembly [33]. Hierarchically structured CNT arrays can be tailored to allow a strong shear binding-on and easy normal lifting-off thereby mimicking the 'gekko feet' effect [34]. Hybrid materials usually feature a significant hierarchy in the sizes of different components which is very common to nature-designed biological objects [35].

A certain degree of ordering of nanoscale objects is required in many applications. For example, 2D or 3D order is required to improve the density of information storage [36], improve photoconversion efficiency of third-generation photovoltaic solar cells [37], or produce regular arrays of size-uniform metal NPs for deterministic nanoscale synthesis (e.g. CNT or QD arrays) [38]. This order can be periodic or custom-designed aperiodic, or even irregular, and can apply to NP sizes, shapes, and other characteristics [39].

Determinism also implies selecting the best process that suits the requirements for specific applications. Figure 2 shows two examples of deterministic arrangements of solid NSs to minimize light reflection from the surface; one process (a) relied on catalytic thermal CVD, while the other one (b) on plasma etching. The aim in both cases is to achieve a pre-determined level of light absorption. In the first case which involved multi-stage, highly precise, and sophisticated fabrication of ordered CNT arrays, a record low light reflection of a small fraction of a percent was achieved [40]. The light reflection in the second case was slightly higher, yet remained below 1% in a very broad spectral range [41].

However, the arrays of silicon nanocones that enabled this functional performance were produced in a very simple, cheap, and environment-friendly single-stage plasma process. Therefore, for anti-reflection devices with ~1% tolerance within the broad spectral range, the second, plasma-based process may be considered as a simpler and viable alternative. However, precise fabrication of CNT arrays will certainly be advantageous for anti-reflection applications with tolerance levels of just a fraction of a percent.

In the first case (Figure 2(a)), thin (few-wall) CNTs of thickness d were arranged in a regular array using pre-patterned metal catalyst [40]. The inter-nanotube spacing was adjusted to achieve

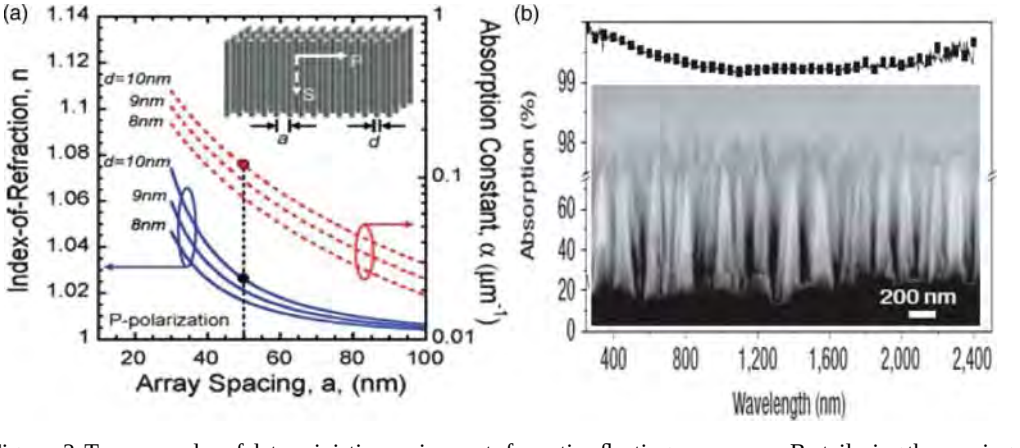

Figure 2. Two examples of deterministic requirements for anti-reflecting nanoarrays. By tailoring the spacing between a few-wall-thick CNTs, it is possible to maximize anti-reflection properties of CNT arrays (a) [Reprinted with permission from [40], Copyright © 2008 American Chemical Society]. A quite similar effect can be achieved by mask-less self-organized plasma etching of Si (b) [Reprinted/adapted by permission from [41], Copyright © 2007 Macmillan Publishers Ltd].

the extremely low coefficient of optical reflection $R^{p} = 0.02\%$ for p-polarized light. Numerical results in Figure 2(a) suggest that this can be achieved when the array spacing a between ∼10 nm thick CNTs is ∼50 nm. In this case, the effective refraction index $n^{p}_{eff} = 1.026$ and the effective absorption constant $\alpha^{p}_{eff} = 0.12$. R^{p} can be further decreased by adjusting the array spacing. However, any such adjustment requires changing the entire catalyst pattern, which in turn involves several nanofabrication steps, such as using masks, pattern delineation, and catalyst material evaporation through the mask. CNT growth is usually carried out after the catalyst pattern is prepared. Different nanotube patterns usually require new masks or templates with different pore sizes and spacings between the pores.

In the second case, excellent anti-reflection properties were achieved through a much simpler plasma-based process, which does not require any masks, pattern delineation, catalyst, or material deposition [41]. Figure 2(b) shows anti-reflection properties of a fairly regular array of high-aspect-ratio Si nanotips produced through the self-masked plasma etching of a 6-inch Si wafer. A typical length and the base width of the Si nanotips are approx. 1.4–1.6 μm and 100–200 nm, respectively. These large-area nanoarrays produced in a simple, single-step, environment-friendly process feature excellent anti-reflecting properties over a broad spectrum. Indeed, the effective light absorption appears to be higher than 99% over the ∼200–2400 nm spectrum. Surface nanostructuring allows one to dramatically improve the anti-reflection properties compared with a flat Si surface. These Si nanotip arrays can also be deterministically tailored to mimic optical response of biological objects (e.g. moth eye, butterfly wing, etc.) to develop next-generation biomimetic photonic NSs [42].

The examples in Figure 2 were also chosen to introduce two very different approaches to nanoscale fabrication to achieve the desired functional (in this case anti-reflection) properties. The first approach involves preparation of regular patterns using customized masks followed by (bottom-up) CNT growth at pre-determined positions. It involves a larger number of steps and offers a higher precision of nanotube positioning. However, care should be taken to grow the CNTs to the same length and ensure that nucleation takes place on every catalyst nanoparticle (CNP) to avoid major defects in the array. Plasma-assisted CNT growth can be used to help achieving higher growth rates and better uniformity of nucleation across the pattern as predicted by numerical simulations [43]; however, this possibility still awaits its experimental realization. The second approach uses low-temperature reactive plasmas of $CH_4 + SiH_4$ gas mixtures to generate small SiC clusters which serve as self-organized masks for the subsequent Si wafer etching in H_2+Ar plasmas. This essentially self-organized process is considered in Section 4.5.2 [44].

Both processes aimed to achieve the desired optical properties and used a combination of different approaches. Pre-patterning and guided bottom-up growth was used in the first case while self-organized, bottom-up self-masking and top-down etching were used in the second case. These synergistic combinations reflect the modern trend in nanofabrication which relies on various combinations of the bottom-up and top-down fundamental approaches rather than using them separately. Indeed, the top-down approaches based on lithography, masking, etc. are rapidly nearing their physical limits while the bottom-up nanoassembly is difficult to control.

This is why, without trying to be exhaustive, in this review, we will focus on the mechanisms that are particularly effective in a plasma and highlight the cases when the synergism between the different approaches helps achieving the desired outcomes (e.g. structure, properties, etc.). These approaches involve a large number of elementary processes that unfold at multiple spatio-temporal scales. Therefore, effective control of these elementary processes is central to the ability to achieve deterministic outcomes, no matter which approach or combination of approaches is used. For this reason, in the following section, we will discuss the different spatial scales involved and indicate some examples of the elementary processes that can be controlled in each case.

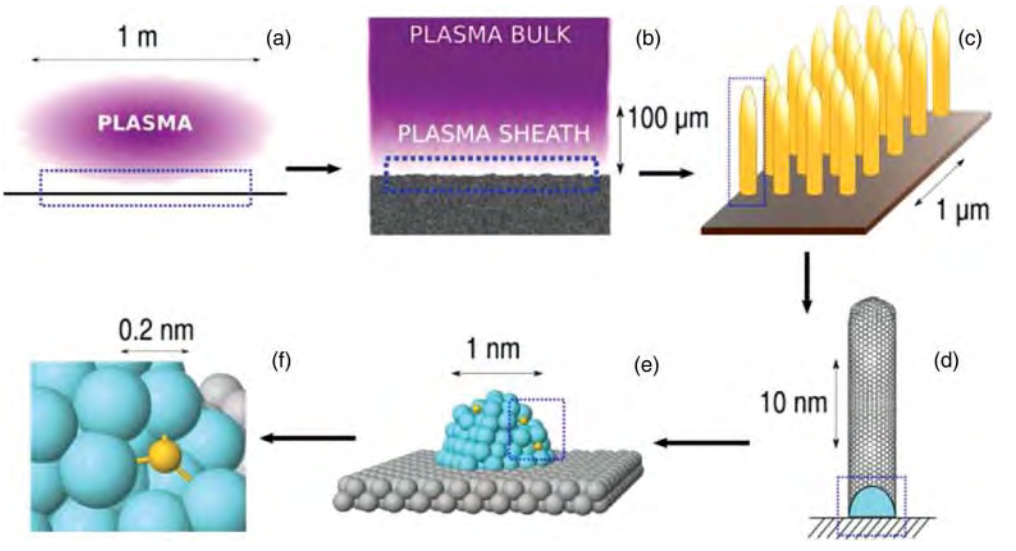

Figure 3. Spatial scales used to study self-organized nanoscale PSSs: (a) plasma in a reactor chamber; (b) plasma sheath near a solid surface; (c) pattern (array) of solid NSs; (d) individual NS; (e) CNP; and (f) atoms and interatomic bonds.

2.2. *Spatial scales and controls*

A typical PSS involves a gaseous plasma in contact with a nanostructured solid surface. These systems are highly complex because of the very strong hierarchy of the spatial scales involved and a large number of physical and chemical processes that take place at each of these scales. The spatial scales of particular interest to the formation of nanoscale objects in plasmas are shown in Figure 3, where each panel represents a higher-magnification zoom of the previous one. To achieve effective control at the atomic level in NSs, every relevant elementary process should proceed in the 'correct' way. Here, we summarize the most typical effects at each spatial scale, with more specific details following in Section 3.

At the scales of typical plasma reactors (up to ∼1 m, panel (a)), one has to produce species (building units, BUs) to use in the NS production and also to sustain appropriate channels of heat exchange between the solid surface and the plasma bulk. Ignition and stability of the plasma discharge are determined by the power deposition and the balance of species and energy.

The surface of a solid substrate that is used for the NS production (CNTs in this example) is in direct contact with the plasma as shown in Figure 3(b). Upon this contact, a self-organized plasma sheath is formed. Typical dimensions of the sheath range from tens of microns in dense (typically $n_e \sim 10^{11}$–10^{12} cm^{-3}) plasmas to ∼1–2 cm (typically $n_e \sim 10^8$–10^9 cm^{-3}) in low-density plasmas used in materials synthesis and processing. The sheath width

$$\lambda_S \sim \lambda_D \left(\frac{2eU_0}{k_B T_e}\right)^{3/4} \tag{4}$$

can also be controlled by applying a voltage U_0 to the surface and by modifying the discharge conditions (e.g. input power, gas pressure, and composition) which affect the electron temperature T_e. The higher the plasma density, the smaller is λ_D (see Equation (1)), and the thinner is the plasma sheath. Conversely, a larger surface bias and higher electron temperatures result in thicker plasma sheaths. Equation (4) is valid for a collision-less sheath (e.g. of low-pressure plasma discharges)

when the pulse duration of the applied bias τ_0 is much longer than the ion traverse time τ_i through the sheath [6].

The sheath formation is a self-organized process which shields the plasma from the electric field on the solid surface. This field arises when more mobile electrons deposit on the surface much faster than the ions. Therefore, to maintain charge neutrality in the plasma bulk and shield it from the electric field on the surface, an ion 'coat' is formed and the ion density within the sheath is higher than the electron density. The electric field peaks at the surface and vanishes in the plasma bulk, where the plasma is charge neutral. The ions are thus driven toward the surface and transfer energy upon impact.

Low-temperature plasmas are usually weakly ionized, $n_n \gg n_e$, where n_n is the density of neutral species such as molecules, radicals, and atoms. In thermally non-equilibrium plasmas

$$T_e \gg T_i \sim T_n, \tag{5}$$

where T_e, T_i, and T_n are the temperatures of electrons, ions, and neutrals. This is why electron-impact reactions play a major role in the species (e.g. radical) production, which takes place in the plasma bulk, within the sheath, and also on the nanostructured surface. The plasma-produced species (ions, radicals, atoms, etc.) in turn interact with the surface and lead to numerous processes of exchange of energy and matter such as heating, deposition, etching, recombination, and several others.

Of particular importance are the processes of the energy and matter exchange over the dimensions of the patterns and surfaces of NSs. These two spatial scales are shown in Figure 3(c) and 3(d). At the nanopattern scale ($\sim$1 μm in this example), control should be exercised over the amount of BUs and heat delivered to the pattern, either directly from the plasma or from the surface. Indeed, BUs can be created from the gas-phase precursors or via extraction from the surface (e.g. by sputtering or etching), whereas the surface can be heated both externally (e.g. substrate heating from underneath or focused laser from above) and through the plasma–surface interactions (e.g. upon ion recombination on the surface). It is also critical to determine the NS positions within the pattern as well as the amounts of BUs and energy per NS. The delivery of energy and matter in turn strongly depends on the NS sizes and their positioning within the array.

The next hierarchical level is represented by individual NSs (Figure 3(d)), which also have their own hierarchical structure. For example, single-walled carbon nanotubes (SWCNTs) of a millimeter length develop from tiny nanometer-sized metal CNPs, which sustain the nanotube nucleation and growth processes. This is why processes at the scales of the SWCNT length are different compared with the processes on the surfaces and within the small CNPs. Although the BU (carbon atom) incorporation takes place through the catalyst, the CNT lateral surfaces play the key role in the BU collection, transformation, and redistribution.

These surfaces significantly contribute to the production of carbon atoms (e.g. by ion impact reactions) and their transport to the CNP for the subsequent incorporation into the nanotube wall. The shorter and the hotter the SWCNT, the easier it is for the adsorbed carbon atoms or radicals to migrate to the catalyst and then incorporate into the wall after overcoming a certain energy barrier. This is why it is very important where and how carbon precursor species are delivered on the nanotube surface. The plasma effects can be used to control the species delivery and heat transfer to the developing nanotubes, see Sections 3.3–3.5.

Similar processes take place during the nucleation of the CNT cap on the CNP surface. These processes are confined to the CNP dimensions, e.g. $\sim$1.0 nm (or even smaller) for SWCNTs. The cap nucleation kinetics is determined by the surface and bulk diffusion (BD) of carbon atoms and the formation of a graphene monolayer (GML) which bends to detach from the surface and form a stable SWCNT cap [45,46]. Numerous plasma-assisted processes (e.g. species production,

hopping, detachment, etc.) on the CNP surface have a major effect on the nanotube nucleation and growth [17]. For very thin nanotubes, the quasi-classical diffusion treatment based on the densities of carbon atoms may fail. In this case, movements of each individual atom become decisive and could be predicted using sophisticated atomistic simulations [47,48]. In Figure 3(e), gray spheres represent substrate material, blue spheres represent atoms of metal catalyst (e.g. Ni), while C atoms are shown by yellow spheres.

The last (Figure 3(f)) spatial scale corresponds to the sizes of atoms and atomic bonds, which are typically in the ∼0.1–0.2 nm range. These atomic scales are characterized by ultra-fast dynamics, e.g. atomic vibrations in the lattice, bond formation, etc. The effectiveness of atomic bond formation is determined by the ability of interacting atoms to share electrons and establish stable orbitals. This is why small relative motions of atoms with respect to each other as well as their bonding are perhaps the most important processes that determine self-organization of matter at these scales.

The plasma may affect the processes even at the atomic-level scales. Indeed, the energy states of the atoms involved may be modified through the interaction with the plasma ions and electrons; this will affect the minimum energy configurations within the CNP or in the nanotube cap. Moreover, microscopic electric fields in the plasma may induce polarization (charge redistribution) along the dangling bonds of the carbon and metal atoms, which in turn affect their ability to form stable bonds [48].

Self-organized processes and their driving forces in PSSs are thus numerous and vary from one spatial scale to another. Hence, the growth of SWCNTs (e.g. thickness, chirality, length, etc.) in the plasma will be different compared with other processes. This conclusion is supported by numerous results of theoretical, computational, and experimental studies discussed in this review and elsewhere in the literature.

For example, a self-organized electric field near the surface is one of the major driving forces for the redistribution of ion fluxes over the micrometer nanopattern scales. This driving force is stronger at higher ion energies and fluxes. The non-uniformity of density of adsorbed carbon atoms along the lateral surface of the nanotube is a driving force for adatom redistribution over the surface. One can control this driving force by tailored, non-uniform deposition of carbon species from the plasma and adjusting the rates of C atom production in different areas on the CNT surface; both these factors are related to the non-uniformity of microscopic electric fields near the nanotube surface, which can also be controlled [49].

Similarly, the driving force for the SWCNT cap nucleation on the catalyst surface is the difference in chemical potentials within and on the surface of the supersaturated NP. In this case, plasmas can also control the driving force, e.g. by localized exchange of energy and matter on the CNP surface, see Section 3.3. The next step is to review the most relevant self-organization pathways and how plasma-specific effects can be used to control them.

2.3. *Self-organization pathways and plasma effects*

2.3.1. *General formalism*

Solid NS formation usually proceeds through a sequence of events which starts from deposition of BUs, their redistribution, clustering, formation of stable nuclei, followed by the growth, shape and structure formation, and relaxation. Although these events also take place in the formation of NSs in the plasma bulk (see, e.g. Section 4.1.2), here we focus on surface-supported growth. Low-temperature growth is particularly important from the energy efficiency perspective and also allows NS formation on temperature-sensitive substrates such as polymers and plastics. Under such conditions, the rates of redistribution of the deposited material due to random

thermal motion are quite low and non-uniform distributions of atoms on the surface usually form.

In the presence of these deposits, the surface energy is higher compared with a clean surface, which indicates that the system is *non-equilibrium*. Therefore, the system will attempt to invoke some mechanism to reduce its surface energy. This mechanism is due to the non-uniformity of adatom density on the surface and creates a *kinetic* force that drives these atoms to self-organize into more compact clusters thereby minimizing the surface energy. Hence, nucleation is an energetically favorable process and is determined by an interplay of thermodynamic and kinetic factors. As the NSs inevitably shrink, they may form in a single nucleation event [50] and the ability to control the nucleation becomes critical.

Surface diffusion is an effective kinetic pathway of self-organization of solid NSs, especially at low temperatures [51]. Here, we will consider two cases of diffusion, with and without significant mass relocation about the surface. The first case (the main focus of this section) originates when species of a solid material are deposited onto the surface (e.g. from a vapor phase), while the second one is typical for ion-assisted nanoscale surface structuring (e.g. surface sputtering and rippling). Both cases bring about a plethora of interesting physical effects at low temperatures. Since low-temperature operation is one of the key advantages of plasma-based nanoscale synthesis, one can thus expect a particular importance of kinetic, e.g. diffusion-related self-organization pathways. This in turn allows the formation of metastable NSs or nanometer surface textures, which feature highly unusual morphological, structural, electronic, and other properties.

Temporal dynamics of deposition, redistribution, and relaxation, therefore, becomes critical for the NS formation. After the nucleation process is complete, the as-formed cluster increases in size and an island forms as the new atoms attach to it during the deposition process. Meanwhile, the atoms in the island tend to rearrange to reshape the cluster and form a more regular, minimum-energy structure. One example of such rearrangement is shown in Figure 4. Bond-counting kinetic Monte Carlo simulations were used to study the equilibration processes of an initially elongated nanoisland of 8232 atoms under different surface conditions [52]. At room-temperature conditions, a clear faceting (nanocrystal attribute) of the island was observed within $\sim$100 s, as can be seen from Figure 4(a). At higher temperatures ($T = 700$ K), the reshaping takes place much faster, within only $\sim$1 μs (Figure 4(b)). However, the island structure is amorphous and crystalline facets do not form. The observed reshaping of the island proceeded by diffusion of atoms over the surface, e.g. from a facet to an edge or another facet, etc.

This process is characterized by the kinetic barrier $E_{\rm dif}(n_{\rm na}, E_{\rm ad})$ which is determined by the number of neighboring atoms $n_{\rm na}$ and the adhesion energy $E_{\rm ad}$, which vary between different crystal facets. This kinetic barrier and the surface temperature are the decisive factors that determine the hopping frequency

$$\omega(n_{\rm na}, E_{\rm ad}, T) = \nu_D \exp\left[-\frac{E_{\rm dif}(n_{\rm na}, E_{\rm ad})}{k_{\rm B}T}\right], \tag{6}$$

where ν_D is the attempt frequency, and $k_{\rm B}$ is the Boltzmann constant. If the temperature is lower, the kinetic barrier should also be reduced to maintain the same hopping frequency as at higher T. Importantly, lower kinetic barriers have resulted in faster NS relaxation, especially at lower temperatures. This result is consistent with experimental observations that metastable self-organized NSs can form within unexpectedly short times, thus indicative of some unique and effective kinetic self-organization pathways and a possible unusually high degree of self-organization at low temperatures [51], which is due to strong diffusion currents

$$J_D = -\aleph \nabla \mu(r), \tag{7}$$

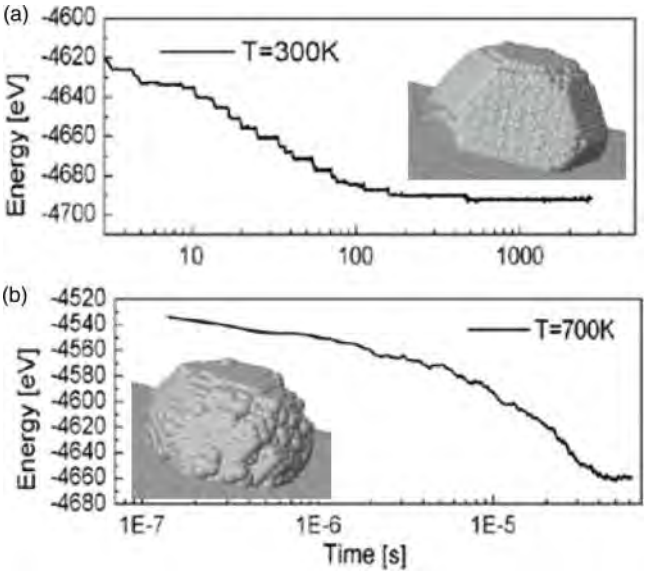

Figure 4. Dynamics of nanocrystal faceting at different temperatures. Lower-temperature process (a), although produces better faceting, is several orders of magnitude longer than at the higher temperature (b) [Reprinted with permission from [52], Copyright © 2007 Elsevier].

where $\mu(r)$ is the chemical potential, and $\aleph$ is a phenomenological transport coefficient. The gradient of the chemical potential $\nabla\mu(r)$ is therefore a driving force for the diffusion-driven self-organization. The stronger the non-equilibrium (gradient), the stronger is the driving force, and the more effective is the self-organization.

Diffusion currents given by Equation (7) and the continuity equation are commonly used to introduce the phenomenological diffusion coefficient

$$D = D_0 \exp\left(-\frac{\mathcal{E}_\mathrm{d}}{k_\mathrm{B}T}\right), \tag{8}$$

where $\mathcal{E}_\mathrm{d}$ is the diffusion barrier energy which is determined by the difference between the minimum and the maximum of the periodic surface potential energy. Equation (8) is more accurate at lower temperatures when the residence time of adatoms in the potential well is much longer than the characteristic times of surface phonon vibrations [51]. In this case, the solid surface may be treated as rigid.

2.3.2. *Plasma effects*

Therefore, when trying to engage the plasma to custom-made self-organized solid NSs at low temperatures, one has to understand how it may affect the SD processes. First, larger gradients of the chemical potential $\nabla\mu(r)$ can be produced through a more localized, non-uniform deposition of BUs from the plasma, for example, using ion-focusing effects and a very fast material delivery [49]. Second, the temperature of the top layer on the surface can be increased by the plasma exposure, which will increase the hopping frequency given by Equation (6). Third, the diffusion barriers $\mathcal{E}_\mathrm{d}$ may also be reduced through the unique, electric-field mediated polarization effects [48] which may modify (e.g. reduce) the adhesion/bonding energy of an atom (e.g. a yellow atom in Figure 3(f))

on a plasma-exposed surface [53]. This energy may be quite different in the crystal facet, edge, or corner locations [54].

Using a macroscopic treatment, it was shown that the presence of a non-uniform electric field $E(r)$ in the vicinity of a nanostructured plasma-exposed surface leads to the effective increase of the diffusion coefficient

$$D = D_0 \exp\left(-\frac{\mathcal{E}_\mathrm{d} - \mathcal{E}_\mathrm{pl}}{k_\mathrm{B}T}\right), \tag{9}$$

through the reduction of the potential barrier by

$$\mathcal{E}_\mathrm{pl} = \lambda_\mathrm{lat}[\tilde{p} + \tilde{\alpha}E(r)]\frac{\partial E(r)}{\partial r}, \tag{10}$$

where $\tilde{p}$ and $\tilde{\alpha}$ is the dipole moment and polarizability of an adsorbed species on the surface, and λ_lat is the lattice constant [53].

Fourth, the plasma sheath electric field (which is normal to the surface away from it and has a horizontal component upon approaching the NSs/nanofeatures) can be used to tune the NS morphology and arraying. Indeed, the interplay between the surface energy, energy of the substrate–NS interface, and the electrostatic energy determine a driving force for mass relocation through SD [55].

In this case, the variation of the free energy of the system G with mass relocation $\delta c(\mathbf{r}, t)$ determines the chemical potential

$$\mu = \frac{\delta G}{\delta c} \tag{11}$$

in Equation (7). The free energy of a charged NP developing on a dielectric surface

$$G = G_\mathrm{phs} + G_\mathrm{el} + G_\mathrm{int}^\mathrm{g} + G_\mathrm{int}^\mathrm{s} \tag{12}$$

in turn includes contributions from the chemical energy of phase separation G_phs, electrostatic energy G_el, energy of the NP-gas interface $G_\mathrm{int}^\mathrm{g}$, and the energy of the NP-substrate interface $G_\mathrm{int}^\mathrm{s}$ [55]. The latter may include surface stress-related contributions, which can also be modified by the plasma-specific effects (e.g. ion impact). It was also shown that electric field effects significantly contribute to morphological stabilization of stressed surfaces [56]. Therefore, electric fields may control diffusion-based self-organization, which may in turn lead to effective control of shapes, sizes, and positioning of solid NSs on plasma-exposed surfaces (Section 3).

Surface diffusion involving mass relocation is one of the main contributors to the growth and reshaping of surface-supported solid NSs. For example, the amount of BUs that can be collected from the surface and then used in NW growth has a Gaussian distribution with the characteristic length, the migration length λ_mig [57]. Each circular surface area $\mathrm{d}A = 2\pi r\,\mathrm{d}r$ contributes material to the growth, and the NW radius increase is

$$\mathrm{d}R_\mathrm{growth} \sim (\sqrt{2\pi})^{-1}\lambda_\mathrm{mig}\exp\left[\frac{-r^2}{2\lambda_\mathrm{mig}^2}\right]\mathrm{d}A, \tag{13}$$

whereas the total growth rate can be obtained by integrating Equation (13) over the entire material collection (e.g. adatom capture) area A. Plasma exposure strongly affects material collection from the surface. For example, long-range interactions in PSSs modify adatom densities around the NSs thereby enhancing their growth.

2.3.3. *Ion-related effects*

Since plasma-exposed surfaces are intrinsically subjected to ion fluxes, the effects of the ion bombardment on the surface processes are of particular interest. The key effects of the ion–surface interactions are the modified SD and morphology. These effects are primarily determined by the ion energy and fluxes.

When an ion impinges on a solid surface, it transfers energy to the surface atom. This leads to several interesting effects. If the ion hits an adatom, the hopping frequency (also frequently termed migration probability) of the adatom

$$\omega(n_{\rm na}^i, E_{\rm ad}^i, T^i) = \nu_D^i \exp\left[-\frac{E_{\rm dif}(n_{\rm na}^i, E_{\rm ad}^i) - \delta E_{\rm i}}{k_{\rm B} T^i}\right], \tag{14}$$

is significantly modified compared with Equation (6). First of all, as the adatom receives a fraction of the ion energy $\delta E_{\rm i}$, the effective kinetic barrier $E_{\rm dif}(n_{\rm na}^i, E_{\rm ad}^i) - \delta E_{\rm i}$ becomes lower than $E_{\rm dif}(n_{\rm na}^i, E_{\rm ad}^i)$, leading to the higher hopping frequency. The reduction of the effective kinetic barriers is perhaps one of the most common effects of the ion–adatom interactions.

However, because the atoms firmly bonded in the top surface layer are also exposed to ion impacts, this also changes the background conditions for the adatom diffusion. This is why all the key parameters in Equation (14) have been labeled with superscript *i*. Indeed, sufficiently intense ion fluxes lead to higher surface temperatures $T^i > T$, which enhances the adatom SD through stronger phonon vibrations associated with the atoms in the near-surface layer. Since the energies of the ions generated by the plasma always feature relatively broad energy distributions, some ions from the high-energy tail of the distribution may sputter some surface atoms [58]. This sputtering may reduce the number of neighboring atoms $n_{\rm na}^i < n_{\rm na}$, which will also lead (after a relaxation) to a distortion of the lattice constant $\lambda_{\rm lat}$, which affects both ν_D^i and $E_{\rm ad}^i$.

Therefore, sputtering, which occurs when the ion energy exceeds the surface atom displacement threshold (which depends on the bond strength of the surface atoms and the relative masses of the impinging ions and the surface atoms), may significantly affect the SD. Importantly, the sputtering may lead to the two major effects [59,60]: (i) effective SD without mass relocation; (ii) the possibility to both enhance and suppress the diffusion.

The first effect stems from surface erosion in selected areas, which does not lead to mass transfer about the surface and is nearly temperature-independent. The second effect is determined by the ion energy and flux, angle of incidence, as well as the surface material and temperature. Under certain conditions [59], the ion-induced effective diffusion may dominate over thermally activated diffusion. This effect is quantified by comparing the coefficients of the thermally activated $D_{\rm T}$ and ion-induced $D_{\rm I}$ diffusion, a combination of which determines the total diffusion constant

$$D_{\rm tot} = D_{\rm T} + D_{\rm I}. \tag{15}$$

Typically, ion sputtering leads to the pronounced morphological rearrangement of the surface layer due to preferential surface erosion in specific areas. This surface structuring is quantified by rather complex morphological phase diagrams which incorporate the effects of several factors such as effective SD (including both ion- and thermally activated) rates, surface tensions, effects of anisotropy, and surface temperature.

For example, morphological instabilities may lead to the surface ripples [61], when valleys are eroded faster than crests. These ripples may be oriented in different directions, for example, either along the *x* or *y* direction in the surface plane. The wavelength of these ripples [59]

$$\lambda_{\rm ripple} = 2\pi\sqrt{\left|\frac{D_{\rm tot}}{\varpi}\right|} \tag{16}$$

is determined by the total diffusion constant (15) and the absolute value of the largest of the surface tension coefficients ϖ. Interestingly, the periodicity of the ripples (16) often appears at the nanometer scales. As such, this effect is useful for solid surface nanostructuring with periodic linear structures.

However, ion-induced diffusion without mass relocation dominates at high ion energies, typically in the kilovolt range. This energy range is commonly used for plasma immersion ion implantation (PIII) which is presently a common tool in plasma processing of a broad range of solid materials [62]. Because of the high ion energies and the associated surface erosion, significant caution should be exercised to avoid damage to the developing delicate NSs, such as graphenes, single-walled nanotubes, or polymers.

Nevertheless, controlled ion damage may, in some cases, be used intentionally to enable a certain functionality. For example, the top sections of multi-walled carbon nanotubes (MWCNTs) were intentionally converted into amorphous phase by impact of $\sim$10 kV energetic Ar^+ ions to enable interesting superhydrophobic properties in CNTs [63].

Unless specified otherwise, most of the examples in this review focus on cases when ion-sputtering effects are not dominant. In most cases, this is achieved by the appropriate selection of the most suitable plasmas and the associated ion energy distributions.

2.3.4. *Temporal dynamics*

The temporal dynamics of the nano-solid nucleation and growth processes is characterized by several time scales. These time scales correlate the deposition of building material and the processes of redistribution of this material over the surface. For example, when solid NSs are created by cluster deposition, the clusters may diffuse, coalesce, and even evaporate from the surface before they dissociate [64,65]. What is important is how fast these clusters are delivered to the surface. For example, if the deposition time t_{depos} is larger than the time needed for SD t_{dif} but is still shorter than the cluster coalescence time t_{coalesc}, i.e.

$$t_{\mathrm{dif}} < t_{\mathrm{depos}} < t_{\mathrm{coalesc}}, \tag{17}$$

the NS formation will be dominated by the cluster diffusion rather than the cluster coalescence. In this example, a fairly slow evaporation will also likely lead to the piling up of material on the surface, unless the diffusion-driven material redistribution processes are effective.

In other words, the NS formation strongly depends on the *demand, supply, and redistribution of BUs* on the surface. The demand is determined by the NS arrays to be produced, the supply – by the rates of BU creation and delivery, and the redistribution – by the strength of the driving force for self-organization on the surface. These criteria will be used to discuss the role of the plasma effects in the production of metastable NSs where the *rates* of supply and redistribution of material and energy are critical.

Importantly, many exotic metastable NSs and self-organized arrays can be produced in PSSs under far-from-equilibrium conditions. These conditions are very different compared with common physical vapor deposition (PVD)/CVD systems and are related, e.g. to thermal non-equilibrium between the plasma species, anisotropicity, and non-uniformity of the distribution of electric field, pressure, surface stress (e.g. due to the ion bombardment), and local heating.

Some other factors such as strong imbalance between the rates of heating and cooling and non-uniformity of long-range electromagnetic forces also contribute to the departure of the system from equilibrium. In turn, these factors lead to a variety of unique, plasma-specific driving forces for self-organization over different spatial scales.

For example, strong thermal non-equilibrium (5) of low-temperature plasmas leads to the enhanced production of BUs via electron-impact reactions; these reactions are not common to

neutral gases. As a result, higher rates of material supply, and hence, more non-equilibrium conditions can be produced on the surface. In turn, these conditions may lead to stronger driving forces for diffusion-based self-organization at shorter time scales, characterized by non-uniformities of adatom density on the surface (e.g. within the adatom capture zones around the NSs).

On the other hand, longer-range non-uniform electric fields make it possible to control SD over the scales that are much larger than the adatom capture zones around the NSs. In this way, self-organization of large mesoscopic patterns can also be affected by the plasma-produced electric fields. Long-range ordering is also possible due to the magnetic field effects, e.g. in 3D arrays of Co magnetic nanodots in diamond-like matrices produced by plasma processing [66,67].

The time scales for different metastable states to reach their equilibrium states and the associated energy barriers determine the outcome of the NS formation through the competition of thermodynamic and kinetic effects. If a metastable NS with exotic properties is targeted, this structure has to be formed well before it can rearrange into thermodynamically prescribed basic shape or another, more stable (in the thermodynamic sense) shape, over the characteristic time τ_{trans}.

Therefore, if the least stable structure is the target, the building material should be delivered and arranged and then kinetically stabilized in the desired shape, fast, well before the processes of atom relocations become significant. Indeed, atomic transport from one facet to another determines shape evolution and may lead to metastable nanocrystals with a very strong presence of reactive (typically higher-index, less equilibrium) facets [68–71]. To minimize the possibility of relaxation of the desired structure to any other (more stable) structure, τ_{trans} should satisfy [72]:

$$\tau_{\text{trans}} > \tau_{\text{gen}} + \tau_{\text{deliv}} + \tau_{\text{diff}} + \tau_{\text{incorp}} + \tau_{\text{recryst}} + \tau_{\text{coat}}, \tag{18}$$

where τ_{gen} and τ_{deliv} are the times required to produce and deliver the BUs, τ_{diff} is the characteristic time of their diffusion/hopping over the surface (e.g. from one facet to another), τ_{incorp} is the time of BU incorporation into the facet, and τ_{recryst} is the recrystallization time. Additional processing (e.g. surface passivation) is often required to retain the structure in the desired metastable state. This process effectively increases the transition barrier ΔU and is characterized by the time scale τ_{coat}.

Transition from an ordered to a less-ordered structure may happen as a result of thermal fluctuations that are present in virtually any device. This issue is particularly significant for small NSs because of the small energy barriers to be overcome upon transition to another state. This is the reason why such small structures are eager to reshape even upon the addition of small amounts of heat, while larger nano-objects usually 'freeze' in whatever shape they were created [69]. Indeed, it was estimated that the activation energy for the shape transitions may exceed $\sim 40\, k_{\text{B}}T$ for nanocrystals with a radius exceeding ~ 100 nm [71]. Such high barriers are very difficult to overcome via thermal activation.

Therefore, in order to be able to control the shape of small QDs, it is critical to produce them at low temperatures and increase ΔU by stabilizing their surfaces. Non-equilibrium plasmas show particular advantages to implement both the nanoassembly at low temperatures and the effective surface passivation (e.g. hydrogenation) [73]. More importantly, the plasma-based processes offer advantages at every formation stage of metastable NSs in Equation (18) and form the basis of the non-equilibrium nanoarchitectronics approach [72]. Some of these time scales are shown in Figure 5 which summarizes the time scales involved in the transfer of energy and matter [74].

Indeed, electron-impact reactions in the plasma and ion-assisted reactions on the surface are very effective and fast channels for the BU generation (τ_{gen}, bars 11 and 13 in Figure 5 for the electron- and ion-assisted reactions, respectively). The ion fluxes also significantly shorten the material delivery time τ_{deliv}, compared with the typical times of neutral transport (bar 14). Due to

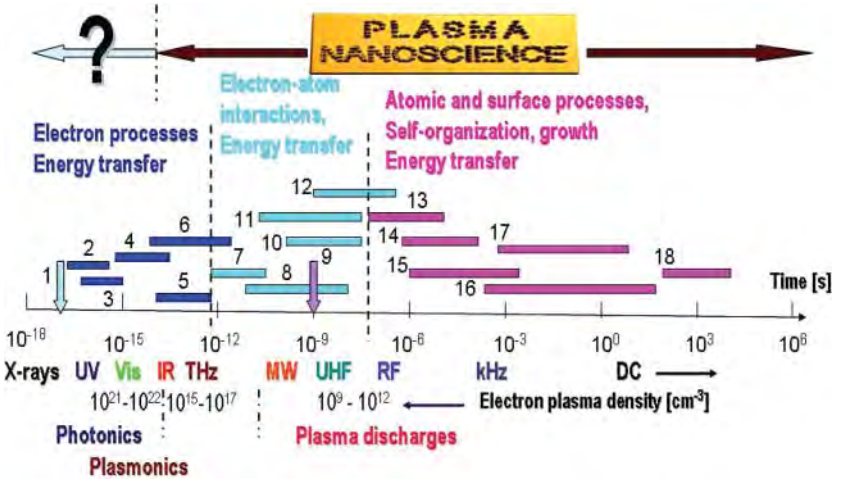

Figure 5. Temporal scales of transfer of energy and matter at nano- and subnanometre scales [74]. (1) Shortest controllable time scale. (2) Electron dynamics in atoms. (3) Attosecond laser pulses. (4) Electron correlation, hole dynamics. (5) Femtosecond (fs) laser pulses. (6) Phonon processes, bond formation/breaking, atomic reorganization in phase transitions, electron-phonon scattering. (7) Electron-surface atom energy transfer in fs laser plasmas. (8) Energy transfer via lattice vibrations. (9) Atomic clock precision. (10) Atomic motion, residence, and clustering on solid surfaces. (11) Electron collisions in low-temperature plasmas. (12) Electron transport, NP/nanofeature charging, breakdown dynamics in low-temperature plasmas. (13) Ion collisions, transport, and residence in plasma reactors. (14) Neutral (e.g. radical) collisions, transport and residence in plasmas. (15,16) Formation of nanocrystals and self-organized patterns at high (∼1000°C) and low (∼10 s–100°C) temperatures (17) CNT and metal oxide NW growth in a plasma. (18) Metal oxide NW growth in thermal CVD [Copyright ©IOP Publishing. Reproduced from [74] by permission of IOP Publishing. All rights reserved].

the plasma heating and polarization effects, the time scales of SD $\tau_{\rm diff}$ and other atomic processes on the surface (bar 10) can also be reduced.

The time scales of BU incorporation, recrystallization, and lattice relaxation are also affected by the energetic states of the impinging plasma species and the localized surface heating through the surface recombination and ion bombardment. Thus, the NS and self-organized nanopattern formation can be faster in the plasma than in equivalent thermal processes (shift to the left in bars 15–17). Non-equilibrium low-temperature plasmas also show a remarkable dissociation ability and are used to produce reactive species (e.g. atomic hydrogen) to passivate or stabilize surfaces. This in turn may shorten $\tau_{\rm coat}$ and increase ΔU.

Figure 5 also shows the time scales of other processes involved in the BU production and NS formation ('plasma-for-nano' in Figure 1) such as electron transport and nanostructured surface charging (bar 12), and reactive radical production and transport (bar 14). It also shows characteristic time scales of collective oscillations in plasmas of different densities and sizes. Typical low-pressure plasmas used in nanoscale synthesis and processing produce plasma oscillations in the radiofrequency (RF) to microwave (MW) ranges. On the other hand, dense micro/nano-plasmas of hot laser plasmas are expected to produce infrared (IR) radiation. Similarly, oscillations of cold electrons in metal NPs may sustain localized surface plasmons (LSPs) in the ultra-violet (UV), visible (Vis), and IR ranges. For a more extensive discussion of the time scales of interest and challenges in nanoscale transfer of energy and matter, we refer to the original publication [74].

Therefore, low-temperature plasmas is a *reactive and fast-responding non-equilibrium environment* which offers a range of unique controls of self-organization in PSSs. In particular, a

range of driving forces for self-organization at different time scales and constructive interplay between thermodynamic and kinetic factors can be used to produce metastable NSs with exotic properties. The following section uses focused examples to show how to achieve these effects using low-temperature plasmas.

3. Plasma controls in nano-solid formation: fundamentals

The ability to control the formation of regular patterns and arrays of NSs (referred to as nanoarrays for simplicity) critically depends on the understanding of the plasma-specific mechanisms at the many spatial and temporal scales involved (Figures 3 and 5). The 'BU' approach describes the sequence of events that take place during the formation of self-organized patterns in non-equilibrium PSSs [6]. This sequence includes the stages of BU generation and delivery, surface preparation, NS nucleation and growth, and pattern self-organization. While the BUs are generated and delivered, the growth surface should be suitably prepared for the nucleation. While the NS grows, the self-organized pattern of a large number of these structures also develops. This approach can be used for the quasi-deterministic synthesis of self-organized arrays which involves the sequence of steps and feedbacks that span spatial scales from atomic sizes ($\sim 10^{-10}$ m) to the sizes of large plasma reactors ($\sim$1 m) [75]. In this section, we will focus on *nanoscale* plasma–surface interactions, nucleation and growth of solid NSs, as well as the formation of self-organized patterns and arrays.

3.1. *Generation of building units*

The BUs that are required for nanoscale synthesis can be produced in the plasma bulk and within the sheath in addition to the nanostructured surface where they are typically produced in thermal CVD. The plasma can generate BUs in very different forms which include atoms, ions, radicals, molecules, and nanoclusters. These species can also be produced in a variety of energetic states depending on their electric charge and the degree of excitation.

The generation mechanisms of these species are very diverse and can be split into two main groups. The first group of processes is based on electron-impact reactions, which stem from the strong thermal non-equilibrium of the plasma and a significantly higher energy of electrons compared with the energies of other plasma species such as ions and neutrals. Typical examples of electron-impact reactions that are particularly relevant to synthesis and processing of carbon-based NSs are

$$e^- + CH_4 \rightarrow CH_4^* + e^- \tag{19}$$

for excitation,

$$e^- + CH_4 \rightarrow CH_4^+ + 2e^- \tag{20}$$

for ionization, and

$$e^- + CH_4 \rightarrow CH_3 + H + e^- \tag{21}$$

for dissociation of the CH_4 precursor molecule.

Electron-impact reactions (Equations (19)–(21) and many others) make the plasma environment unique compared with the neutral gas-based processes as they produce ions and lead to high rates of the dissociation and formation of a very large number of radical species. Moreover, many of these species find themselves in a variety of excited states [76] which makes them more reactive during the interaction with the nanostructured surfaces and other plasma species [77].

The latter interactions form the second group of reactions that are based on collisions of heavier species such as ions, radicals, and molecules. These reactions usually proceed through the exchange

of atoms or electrons and also lead to the generation of a variety of reactive species in excited and ionized states, which in turn affect the discharge kinetics and plasma–surface interactions [78]. The numerous pathways of the formation of the BUs have been discussed previously [6]. For example, if a CH_3 radical (which is believed to play a role in the growth of single-crystalline carbon nanotips, CNTPs) is targeted, in addition to the electron-impact reaction (21), it also can be generated through representative neutral–neutral

$$H + C_2H_5 \rightarrow 2CH_3 \tag{22}$$

and ion-neutral

$$Ar^+ + CH_4 \rightarrow CH_3{}^+ + H + Ar \tag{23}$$

reactions. Note that Ar^+ ion-assisted reactions similar to Equation (23) can be used to dissociate hydrocarbon precursors both in the gas phase and on the surface, which is a unique feature of plasma environments compared with equivalent neutral gases.

Here we only stress that plasma discharges offer a unique environment not only for the production of a variety of reactive radical species, but also for the clustering and polymerization, which takes place in the gas phase and leads to the formation of nanoclusters and NPs, which in turn also significantly affects the discharge kinetics and species production [79,80].

Figure 6 shows three more salient features of particular interest for nanoscale synthesis and processing. The first feature is the ability to dissociate molecules and produce reactive radicals (Figure 6(a)). This graph shows the computed densities of the neutral and ionized plasma species produced in inductively coupled plasmas in $Ar+Cl_2$ gas mixtures used for reactive chemical etching and microstructuring of Si wafers in microelectronics [81]. Large amounts of reactive Cl atoms enable the effective, high-rate etching through the formation of silicon chloride-based volatile products.

The plasma is weakly ionized, which is reflected by a low ionization degree

$$\varsigma_{\text{ion}} = \frac{\Sigma_j n_j^i}{\Sigma_k N_k} \ll 1, \tag{24}$$

where n_j^i is the number density of ionic species j and N_k is the number density of neutral species k. In the example in Figure 6(a), even though the density of Ar^+ ions is three–four orders of magnitude lower than the density of Ar atoms, the plasma dissociates chlorine molecules very effectively. Indeed, the number density of Cl atoms appears to be higher than the density of Cl_2 molecules, even at very low input powers.

This outstanding dissociation ability of the plasma has been commonly attributed to the non-equilibrium (e.g. non-Maxwellian) electron energy distribution functions (EEDFs) [82]

$$f(\epsilon_e) = \xi_1 \sqrt{\epsilon_e} \exp(-\xi_2 \epsilon_e^x), \tag{25}$$

where ϵ_e is the electron energy, while ξ_1 and ξ_2 are energy-dependent coefficients ($x = 1$ corresponds to the Maxwellian EEDF). The EEDFs can be effectively controlled by the plasma parameters to customize electron populations in specific energy ranges for the production of the desired species.

For example, the dissociation energy of oxygen molecule O_2 is lower compared with N_2 and if the EEDF peak $\text{Max}[f(\epsilon_e)]$ is adjusted above the O_2 dissociation threshold $\Xi_{\text{diss}}^{O_2}$ yet below the N_2 dissociation threshold $\Xi_{\text{diss}}^{N_2}$,

$$\Xi_{\text{diss}}^{O_2} < \text{Max}[f(\epsilon_e)] < \Xi_{\text{diss}}^{N_2}, \tag{26}$$

then the preferential generation of oxygen atoms and other reactive oxygen species (ROS) can be achieved. This selectivity is important for the synthesis of metal oxide NWs (Section 4.2.3) and

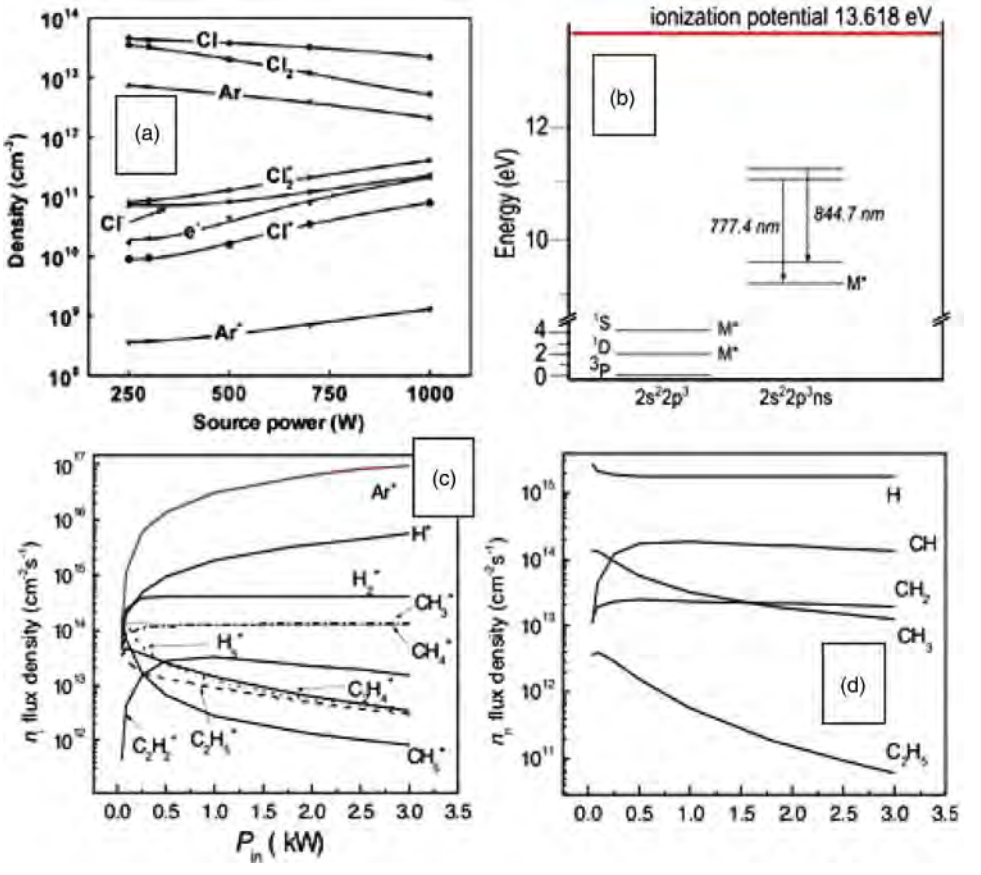

Figure 6. Low-temperature, thermally non-equilibrium plasmas sustain very high rates of dissociation and production of reactive radicals, such as Cl atoms for Si etching (a) [Copyright ©IOP Publishing. Reproduced from [81] by permission of IOP Publishing. All rights reserved]. Long-living excited states of plasma-produced reactive species are of interest to numerous applications (b) [Copyright ©IOP Publishing. Reproduced from [86] by permission of IOP Publishing. All rights reserved]. Ion fluxes may deliver more material to the surface compared with neutral fluxes (c) and (d) [Reprinted with permission from [88], Copyright © 2004 American Institute of Physics].

plasma interactions with biological objects (Section 4.5.6). Another commonly used options to enhance selective radical production are to generate electron distributions with two characteristic average electron energies (bi-Maxwellian EEDFs) or boost electron populations in the higher-energy tail of the distribution (Druyvesteyn EEDFs).

Plasma-produced ROSs are of particular interest because of their long-living excited states. Figure 6(b) shows the first three excited states of oxygen atoms which are metastable with radiative decay lifetimes of ∼1 s, ∼100 s, and 185 μs [83–86]. These states are fairly stable and can be further excited to the next levels shown in Figure 6(b). Radiative decay of these levels produces very strong IR emission with the wavelengths ∼777 and 845 nm, which are commonly used as fingerprints of ROSs produced in extremely non-equilibrium oxygen plasmas [86].

Comparing the above lifetimes with the time scales in Figure 5, one can conclude that these metastable ROSs can very realistically take part in the nucleation and growth of metal oxide nanocrystals (e.g. NWs) while retaining their long-living excited states. This is why plasma oxidation of nanoscale features and oxide NS production are very effective and unique compared

with thermal processes or plasma oxidation of bulk materials. This highly unusual reactivity lasts over the entire growth process and helps explaining the metal oxide NW growth in just a couple of minutes [87] compared with days in some thermal processes (bars 16 and 18 in Figure 5).

3.2. *Plasma sheath and surface conditions*

Fluxes of the neutral and charged species determine the surface conditions which are very different compared with other (e.g. neutral gas) environments. The number of neutral species deposited per unit time per unit surface can be approximated as [88]

$$\Phi_j^n = \tfrac{1}{4} N_j \upsilon_j V_{Tj}^n, \tag{27}$$

where N_j, υ_j, and V_{Tj}^n are the number density, sticking probability, and thermal velocity of neutral species j. Because of the absence of reactive dangling bonds, the sticking probability of non-radical species is negligibly small. For radical species, they are typically of the order of a few percent or lower. For example, $\upsilon_{\mathrm{CH}} \sim \upsilon_{\mathrm{CH_2}} \sim 0.025$, $\upsilon_{\mathrm{CH_3}} \sim \upsilon_{\mathrm{C_2H_5}} \sim 0.01$, while $\upsilon_{\mathrm{H}} \sim 0.001$ [89–93].

Within the global discharge model [88], the ion flux is

$$\Phi_j^k = \beta_S n_k^i V_{\mathrm{B}k}^i, \tag{28}$$

where n_k^i and $V_{\mathrm{B}k}^i$ are the density and Bohm velocity of ion species k, and β_S is a geometric factor which accounts for the discharge dimensions, ion mean free path, etc.

The contributions from the charged species materialize through the process of formation of the plasma sheath, which starts from the establishment of a negative surface charge due to the rapid (bar 12 in Figure 5) deposition of the highly mobile plasma electrons. This is followed by the formation of a very unique self-organized structure with uncompensated bulk charge and continuous flows of ions toward the surface; this occurs over ionic time scales (bar 13).

The energy the plasma ions acquire upon impact on the floating (i.e. electrically disconnected from ground) solid surface is approximately equal to the electric potential drop across the sheath

$$\mathcal{E}_{\mathrm{i}}^k = e(\varphi_{\mathrm{pl}} - \varphi_{\mathrm{float}}) = \frac{k_{\mathrm{B}} T_{\mathrm{e}}}{2} \ln\left(\frac{m_{\mathrm{i}}^k}{2m_{\mathrm{e}}}\right), \tag{29}$$

where φ_{pl} and φ_{float} are the plasma and floating potentials, respectively, and m_{i}^k is the mass of ionic species k, whereas e and m_{e} are the electron charge and mass, respectively. Importantly, potential drop (29) is always positive; in other words, the plasma potential is always higher than the surface potential. This leads to continuous ion flows onto the surface and effective repulsion of negative charges (e.g. anions or negatively charged NPs or nanoclusters) away from the surface.

Panels (c) and (d) in Figure 6 show the fluxes of ions and neutrals in the $\mathrm{Ar}+\mathrm{H_2}+\mathrm{CH_4}$ plasma-based synthesis of single-crystalline CNTPs [88]. Even though the ionization degree of the plasma (24) is very low, the fluxes of the ions are in many cases comparable, or even exceed the fluxes of neutral radicals [88,94]. In other words, ions play a prominent role in the delivery of building material to the surface in addition to surface heating. The energetics and kinetics of the plasma discharge can be tailored to produce species selectively to achieve the favorable surface conditions. Figure 7(a) and 7(b) show a typical situation when ion fluxes are deposited on the pattern of Ni CNPs on a Si substrate and the CNTs that nucleate and grow from these NPs.

The negative charge is a common feature of plasma-exposed surfaces which neutralize positive ions. It has several important implications for nanoscale processes. First, the negative electric charge covers even the smallest features on nanostructured surfaces and determines the microscopic electric fields in the vicinity of NSs (Figure 7(c)). These electric fields may have both the normal and parallel (with respect to the surface) components of the electric field. As a result, the electric

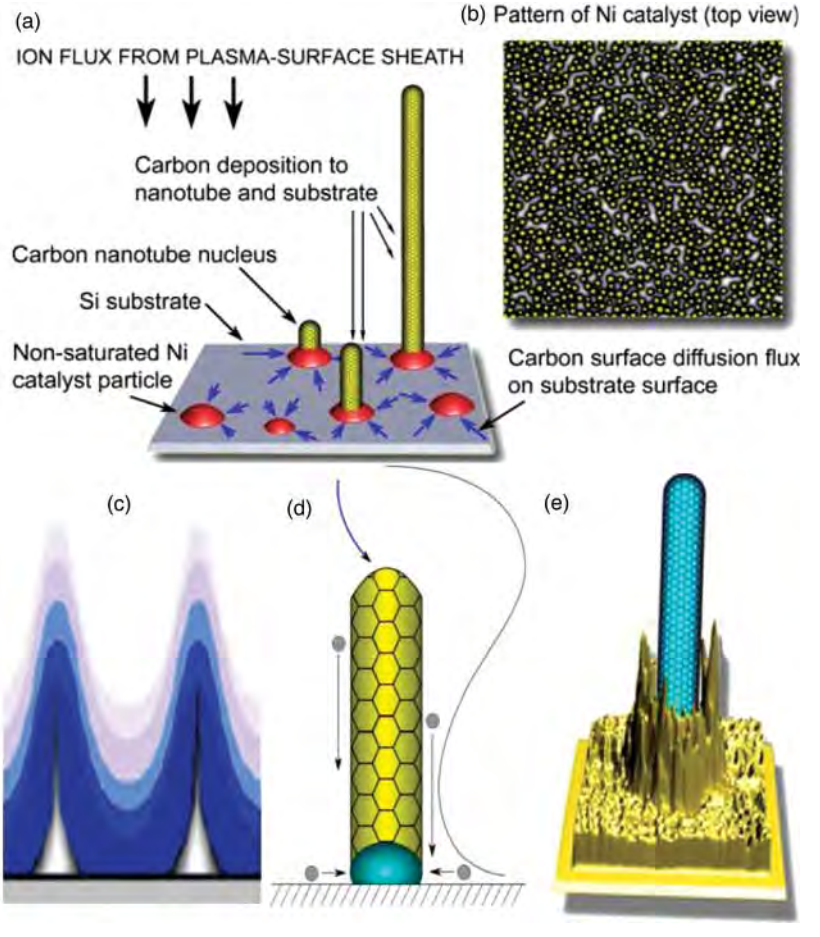

Figure 7. Ion fluxes (a) and density of carbon atoms (b) in the nucleation and growth of CNTs on a self-organized pattern of Ni CNPs [Reprinted with permission from [95], Copyright © 2008 American Institute of Physics]. Topography of microscopic electric field near high-aspect-ratio NSs (c) [Copyright ©IOP Publishing. Reproduced from [49] by permission of IOP Publishing. All rights reserved]. Axial (d) and azimuthal (e) profiles of ion deposition in CNT growth. Panel (e) reproduced from [96] with permission. [Copyright © 2008 IEEE].

field lines and hence, the ion fluxes converge near the sharp tips of the NSs as shown in Figure 7(d) and a significant amount of ions is deposited and then neutralized in the top section of the nanotube. In regular patterns, the distribution of ion fluxes around the NSs is typically axially symmetric as shown in Figure 7(e). This in turn leads to fairly uniform BU incorporation into the CNP.

After the ions are neutralized on the surface and other neutral species are deposited, the material redistribution over the surface is determined by the surface conditions on and between the CNPs. The directions of carbon SD fluxes toward the catalysts are shown in Figure 7(a). These fluxes are determined by 2D gradients of chemical potential over the surface, which act as a driving force for the self-organized nanotube growth from CNPs. A very non-uniform distribution of carbon adatom densities within the catalyst pattern is shown in Figure 7(b).

The rates of the surface processes (e.g. SD) are determined not only by the amount of material deposited, but also by the surface temperature, as well as by the distributions of surface stresses

and charges, which appear to be strongly interdependent. In plasmas, intrinsic surface heating mechanisms are possible due to the ion bombardment or recombination. These effects can be controlled to adjust the surface temperature, e.g. to make it higher than the temperature achieved through external heating, or, alternatively, to completely replace the external heating by the intrinsic plasma heating.

In particular, the surface recombination of long-living, metastable plasma-produced radicals releases significant energy. In some cases, this energy is sufficient to produce solid NSs even without any external heating, e.g. metal oxide NWs of Section 4.2.3. The surface stress is controlled by the ion impact. Since the distribution of ion impact points is very non-uniform (e.g. can peak in selected areas on the NS surface) due to the non-uniformity of microscopic electric fields and surface electric charges, the stress distribution can also feature non-uniformities over comparable spatial scales.

The surface conditions critically depend on the energy and fluxes of the ions upon impact on the surface, which can be controlled by the sheath thickness, which in turn depends on the plasma density, electron temperature, and surface bias. It is more difficult to control the impact points of neutral species. However, their densities, fluxes, energetic states, and lifetimes can be controlled by the power, pressure, and gas flows in the discharge.

As mentioned in Section 3.1, plasmas very effectively produce highly reactive atomic and radical species that can be used to control the surface energy. For example, surface termination by reactive hydrogen atoms reduces the surface energy. If the surface is fully passivated, the ion bombardment may be used to activate suitable dangling bonds to be used as anchoring points for the nucleation and growth of new NSs [97].

This discussion only covers the basic conditions on plasma-exposed surfaces. Some of these conditions are unique even in the synthesis and processing of thin films and bulk materials. Importantly, nanoscale localization of energy and matter on the surfaces and in the vicinity of nanoscale objects leads to the very interesting physics of *nanoscale* plasma–surface interactions.

3.3. *Nanoscale plasma–surface interactions*

Nanoscale localization of plasma–surface interactions arises in two typical types of situations. In the first case, it is due to the nanometer sizes of the structures or features being grown or processed, even in bulk plasmas. This is a very common situation because of the very large number of nanoscale solids synthesized or processed using plasmas. For example, when a small feature is produced on a Si surface using reactive ion etching (RIE), knowledge on the exact points of impact of the reactive ions is needed to study the evolution of the nanoscale etching profiles.

The other types of situation happen when a nano-plasma is in contact with the surface. For example, this occurs during surface electrification using nanoscale corona discharge generated around a conducting nanometer-sized tip of a scanning tunneling microscope [98]. However, the second situation is very rare because of intrinsic difficulties to generate nano-plasmas in air, primarily because of insufficient electron densities to reduce the Debye length (1) to the nanoscales. More discussions about nano-plasma generation from different states of matter are given in Section 5.

In another example considered in more detail below, CNTs nucleate and grow on metal CNPs following the sequence of events sketched in Figure 8(a) [95,99]. The first two steps are needed to produce a pattern of CNPs; steps three and four denote a partial and full CNP saturation with carbon, respectively. After the NPs are saturated with carbon, the nanotubes nucleate (step 5) and then grow (step 6) provided that more carbon atoms are supplied through the CNP. An example of a base-led growth of a SWCNT is shown. Panel (b) shows more details of the elementary processes that take place on the surface and within a nanometer-sized CNP during its saturation with carbon (stages 3 and 4) [100]. Panel (c) shows the details of nucleation of a nanotube cap on the CNP

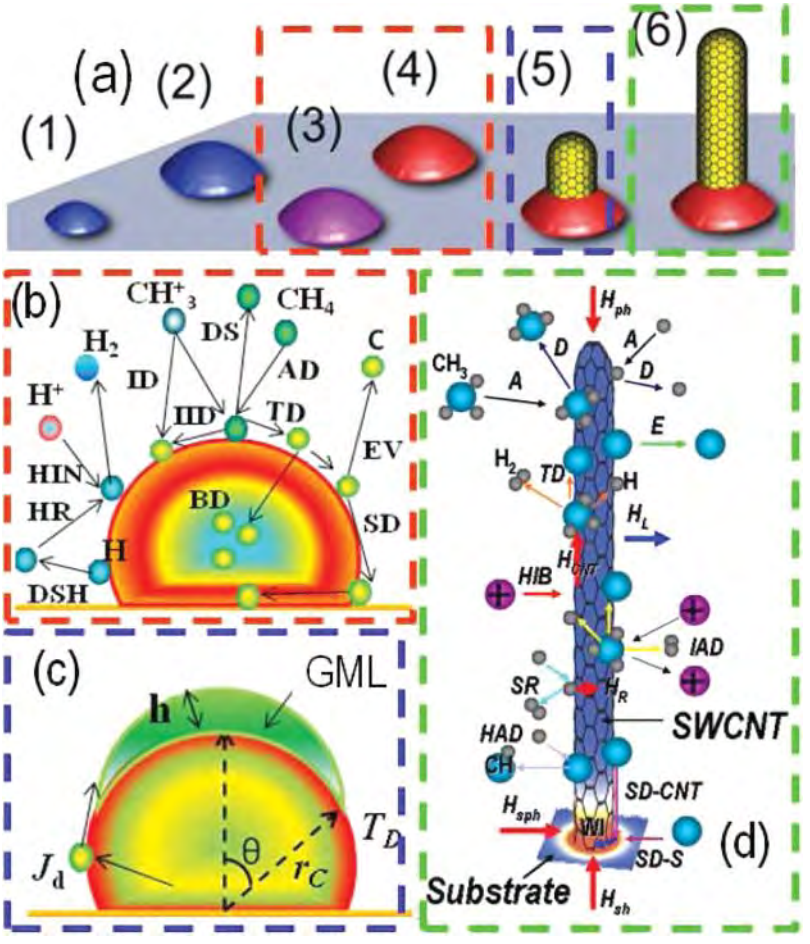

Figure 8. Stages of CNT nucleation and growth from metal CNPs (a) [Reprinted with permission from [95], Copyright © 2008 American Institute of Physics]. Nanoscale plasma–surface interactions across a metal CNP and main elementary processes (b); CNP saturation, carbon extrusion, and monolayer nucleation (c) [Reprinted with permission from [100], Copyright © 2011 American Chemical Society]. Elementary processes of energy and matter transfer in SWCNT growth (d) [101]. The most important surface processes involved in carbon atom production and CNP heating in panel (b) are ion-induced dissociation (IID), ion decomposition (ID), hydrogen recombination (HR), hydrogen-induced neutralization (HIN), adsorption of hydrogen atoms (ADH), desorption of hydrogen atoms (DSH), adsorption (AD) and desorption (DS) of hydrocarbon radicals, evaporation (EV), bulk diffusion (BD) and surface diffusion (SD) of carbon atoms, and thermal dissociation (TD) of hydrocarbon radicals. Panel (d) [Reproduced from [101], Copyright © 2011 IEEE].

surface (stage 5), while panel (d) shows a multitude of elementary processes on the surface of a developed SWCNT [101].

Importantly, all six stages involve interactions of the plasma-generated species with liquid (e.g. CNP, if the melting temperature is reached) and solid (CNT walls) surfaces with at least one dimension in the nanometer range. Even if a SWCNT grows to a several microns length, its thickness typically remains of the order of ∼1 nm (Figure 8(d)), and nanoscale plasma–surface interactions still prevail even at advanced growth stages.

Another important feature sketched in Figure 8(a) is that the nanotubes are thinner than the CNPs. This common experimental observation suggests that the nanotube thickness is not merely determined by the catalyst material and sizes but also by the synthesis process. Thus, *kinetic* phemonena are crucial (Section 2.3). On the other hand, thickness of nanotubes and NWs grown in the plasma and neutral gas-based processes using CNPs of the same size, is also quite different [10].

Therefore, *kinetics of nanoscale plasma–surface interactions* plays a major role in the nucleation and growth of surface-supported NSs. Why are these interactions different from the interactions of plasmas with bulk or thin-film materials? Basically, because of the nanoscale localization of the energy and matter transfer processes, such as the volume and surface of the CNP in Figure 8(b)–(c). Since the surface area-to-volume ratio in NPs are much higher than in bulk materials, elementary processes on plasma-exposed nanoscale surfaces are decisive.

The first striking observation from Figure 8(b)–(d) is the overwhelming complexity and multitude of the processes involved, with only a few most significant ones shown. We discuss only the most essential physics and refer the interested reader to the original publications for many other (e.g. chemical) aspects [100,101]. After carbon precursors deposit (as ions or neutrals) on the CNP surface, they undergo thermal and ion-assisted dissociation. Since thermal dissociation of a CH_4 precursor requires temperatures above 800–900°C, this is an important factor in the high temperatures required for the purely thermal SWCNT growth. In a plasma, in addition to effective production of CH_x radicals via the gas-phase (e.g. electron-impact) dissociation, precursor dissociation also takes place directly on the CNP surface via a number of ion-assisted processes, similar to Equation (23).

These processes are incorporated into the mass balance equation for carbon atoms on the semi-spherical surface of a CNP [100]

$$\Im_{\mathrm{C}}^{+} + D_{\mathrm{S}} \frac{1}{r_{\mathrm{C}}^2 \sin\theta} \frac{\mathrm{d}n_{\mathrm{C}}^{\mathrm{S}}}{\mathrm{d}\theta} (\sin\theta) \frac{\mathrm{d}n_{\mathrm{C}}^{\mathrm{S}}}{\mathrm{d}\theta} - \Im_{\mathrm{C}}^{-} = 0, \tag{30}$$

where $n_{\mathrm{C}}^{\mathrm{S}}$ is the surface density of carbon species on the surface, D_{S} is the SD coefficient, r_{C} is the CNP radius, and θ is the azimuthal angle, see Figure 8(c). The first term $\Im_{\mathrm{C}}^{+}$ in Equation (30) describes the creation of carbon atoms on the surface of a CNP due to thermal and ion-induced dissociation of hydrocarbon radicals and ions. The second term accounts for redistribution of the carbon atoms due to the SD, and the third term $\Im_{C}^{-}$ quantifies carbon losses due to desorption, interactions with atomic hydrogen, and diffusion into the NP bulk.

Recombination of ionic and radical species on the surface also leads to localized CNP heating, which in turn increases the NP temperature T_{CNP} by ΔT without the need to increase the temperature of the whole substrate T_H by ΔT via external heating. The NP surface temperature T_{CNP} is obtained from the energy balance equation which takes into account the heats associated with *localized* NP heating

$$\mathcal{H}_{\mathrm{heat}}^{\mathrm{CNP}} = \mathcal{H}_{\mathrm{ad}} + \mathcal{H}_{\mathrm{ibomb}} + \mathcal{H}_{\mathrm{irec}} + \mathcal{H}_{\mathrm{ineutr}} + \mathcal{H}_{\mathrm{nrec}}, \tag{31}$$

and cooling

$$\mathcal{C}_{\mathrm{cool}}^{\mathrm{CNP}} = \mathcal{C}_{\mathrm{dis}} + \mathcal{C}_{\mathrm{des}} + \mathcal{C}_{\mathrm{evap}} + \mathcal{C}_{\mathrm{intH}} + \mathcal{C}_{\mathrm{other}}, \tag{32}$$

which both involve numerous channels. In Equation (31) $\mathcal{H}_{\mathrm{ad}}$ is due to adsorption (AD) of hydrocarbon and hydrogen species, $\mathcal{H}_{\mathrm{ibomb}}$ is due to kinetic energy transfer through the ion bombardment, $\mathcal{H}_{\mathrm{irec}}$ and $\mathcal{H}_{\mathrm{ineutr}}$ are related to ion recombination and neutralization, while $\mathcal{H}_{\mathrm{nrec}}$ is due to the surface recombination of neutrals. The heat loss channels in Equation (32) are due to species dissociation $\mathcal{C}_{\mathrm{dis}}$, desorption $\mathcal{C}_{\mathrm{des}}$, evaporation $\mathcal{C}_{\mathrm{evap}}$, interaction with hydrogen atoms $\mathcal{C}_{\mathrm{intH}}$, and some other mechanisms $\mathcal{C}_{\mathrm{other}}$.

Importantly, Equations (30)–(32) are subject to appropriate boundary conditions in limited nanometer space. The rates and energy barriers of several reactions also include corrections due to nanoscale size effects. These and several other specific factors make nanoscale plasma–surface interactions markedly different compared with the interactions with bulk solid materials.

One of the consequences of localized plasma heating is that in many nanoscale synthesis processes *temperatures of external heating T_H are markedly lower* compared with similar thermal processes. Moreover, for the effective nanoscale process to proceed, the CNP should be predominantly and selectively heated locally (rather than the entire substrate). The improvement of this effect manifests good *energy-efficiency* of the plasma-based processes. Moreover, lower process temperatures lead to much lower rates of BU evaporation/desorption from the surface (denoted EV in Figure 8(b)) thereby also leading to the superior *matter-efficiency*. These features represent a major opportunity for energy- and matter-efficient plasma-based nanoscale synthesis and processing of the future.

The as-produced carbon atoms then migrate about the CNP surface (denoted SD in Figure 8(b); the associated SD flux is J_s) and also diffuse into the catalyst bulk (denoted BD, the associated flux is J_v). Jointly with other carbon atoms that arrive from the substrate surface or directly from the plasma, these atoms saturate the CNP as shown in Figure 8(c). After the density of dissolved carbon in the CNP reaches the supersaturation threshold, carbon material is extruded toward the surface, as denoted by J_d in the same panel. This extruded material joins carbon atoms redistributed on the surface-by-SD, to form a GML, which bends to form a SWCNT cap (Section 3.4).

Plasma-specific processes of the species production and localized heating lead to faster GML nucleation by relying on the SD-driven self-organization, rather than 'waiting' till the processes of BD, supersaturation, and extrusion are complete. These conclusions are supported by the experimental measurements of activation energies of surface and BD in plasma-assisted growth of various carbon NSs where the SD is the main growth rate-controlling mechanism, especially at low temperatures [102,103]. The BD pathway is the main option in many purely thermal processes [104].

However, during the nanotube nucleation (e.g. cap formation), care should be taken so as not to destroy the monolayer of carbon atoms by the ion bombardment. Indeed, destruction of the ordered carbon network was observed at ion energies exceeding ~30 eV, which is of the order of the energy of carbon bonding in a stable sp^2 hexagonal configuration [105]. This is why the energy distributions of the ions generated in the plasma should be adjusted to effectively dissociate hydrocarbon precursors on the CNP surface yet without causing any damage to the as-nucleated GML.

There are several other important mechanisms of nanoscale plasma–surface interactions which also significantly affect the metal catalyst and the CNT nucleation on them. For example, plasma-produced reactive hydrogen atoms not only etch amorphous material, but also prevent metal catalyst from unwanted oxidation; both these factors help maintaining the CNPs catalytically active throughout the nanotube nucleation and growth process. Other known effects of the nanoscale plasma–surface interactions include but are not limited to ion-enhanced diffusion (mobility) of carbon atoms on the CNP surface, preventing CNPs from agglomeration, and enhancing solubility of carbon atoms in CNPs [17].

The unique nanoscale plasma–surface interactions considered in this section lead to the very interesting outcomes of SWCNT nucleation as discussed in Section 3.4. These interactions also continue playing a major role during the nanotube growth stage, see Section 3.5 for more details.

3.4. *Nanostructure nucleation*

Nucleation of NSs in a plasma involves several competing mechanisms. On the one hand, the network-forming processes contribute to the stable nuclei formation, while several other processes

such as etching or sputtering may destroy these nuclei. For example, impact of ions with the energies higher than the energy of C–C bonds in a hexagonal sp^2 network, may break these bonds and produce defects in the GML on a CNP. Therefore, care should be taken to customize the ion fluxes and energies to avoid unnecessary damage to the semi-spherical cap that is formed during the nucleation stage, which will be considered below.

The effect of the plasma exposure on the nucleation of SWCNTs on Au CNPs is shown in Figure 9(a)–(c) [100]. The as-formed GML features a critical diameter $d_{\rm cr}$ (Figure 9(a) and 9(b)), beyond which it is stable. The minimum energy (nucleation barrier) ΔG_N should be overcome to enable the GML nucleation. The critical GML diameter

$$d_{\rm cr} = \frac{2Br_C}{(A^2 + B^2)^{1/2}} \tag{33}$$

is determined by the CNP radius r_C (Figure 8(c)), energies of the GML-vapor $\gamma_{\rm GV}$, GML–CNP $\gamma_{\rm GS}$, and CNP-vapor $\gamma_{\rm SV}$ interfaces (entering A), energy of the strained CNP edge (entering B), and the difference in the chemical potentials in the solid and liquid phases

$$\Delta\mu_{\rm sl}^{\rm GT} = \mu_{\rm s} - \mu_{\rm l} - \frac{2\Delta\Omega_{\rm ls}\gamma_{\rm SV}}{r_C} \tag{34}$$

modified by the size-dependent Gibbs–Thomson (GT) effect. This effect is described by the third term on the right-hand side of Equation (34) and is particularly important for small NPs because of the $\propto r_C^{-1}$ dependence. Here, $\mu_{\rm s}$ and $\mu_{\rm l}$ are the chemical potentials of the solid and liquid phases without the GT effect, and $\Omega_{\rm ls}$ is the difference in elementary volumes per atom in the liquid and solid phases.

Importantly, $\Delta\mu_{\rm sl}^{\rm GT}$ enters A and is the *driving force* for GML nucleation. As can be seen from Equation (34), this driving force becomes weaker for smaller CNPs due to the GT effect [106], which reduces the NP supersaturation. This effect increases the nucleation barrier ΔG_N in thermal processes, and very high temperatures and pressures are usually required to nucleate SWCNTs on small CNPs.

The plasma and the GT effects interplay constructively to nucleate and then bend the GML to form a nanotube cap. The work of GML bending

$$\Delta E = E_{\rm K} - W_{\rm ad} \tag{35}$$

is the difference between the kinetic energy $E_{\rm K}$ of coordinated detachment of carbon atoms from the catalyst surface and the work of adhesion $W_{\rm ad}$ of the as-nucleated layer [107].

This interplay leads to several effects suggesting significant advantages of the plasma-based processes in the nucleation and growth of size- and even possibly chirality-selective growth of thin SWCNTs, on small CNPs, at low process temperatures. First, the same critical diameter $d_{\rm cr}$ can be achieved at temperatures significantly lower than in thermal CVD (Figure 9(b)); this is the consequence of a dramatically reduced nucleation barrier ΔG_N. Second, at the same temperatures, $d_{\rm cr}$ is also smaller, which means that thinner SWCNTs can nucleate in a plasma, on catalysts of the same size. Third, it is much easier to bend the GML in a plasma as the energy of bending ΔE is typically several times higher, see Figure 9(c).

A combination of these effects allows one to compute the 3D process parameter maps to determine the optimum plasma process parameters when selective nucleation of SWCNTs of a certain thickness (and hence, chirality) is possible; one such map is shown in Figure 9(a). These calculations help explaining the results of recent experiments which suggest the possibility of effective control of SWCNT thickness and chirality distributions using plasmas and tailored catalysts [107–110].

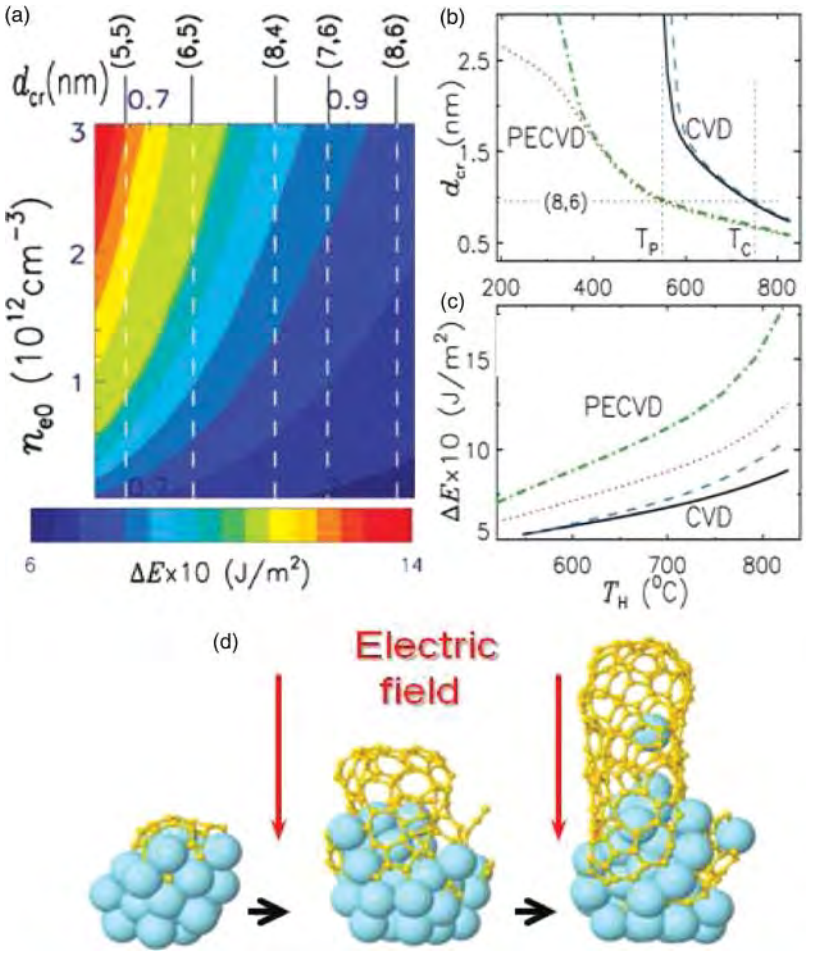

Figure 9. Effects of the nanoscale plasma–surface interactions on the nucleation of SWCNTs (a–c) [Reprinted with permission from [100], Copyright © 2011 American Chemical Society]. Numerical simulations confirm experimentally observed SWCNT nucleation at the Ni CNP summit, followed by the vertical alignment (d) [48].

The fast plasma kinetics also leads to the possibility to clearly separate the onset of nucleation of SWCNTs of different thickness/chirality, which is characterized by the thickness-dependent incubation times [111]

$$\tau_{\text{inc}} = \tau_{\text{d}} + \tau_{\text{p}} = \frac{2n_{\text{C}}^{\text{S}}}{J_{\text{v}} + J_{\text{s}}}, \tag{36}$$

which combine the times needed for carbon atoms to dissolve into the CNP (τ_{d}) and then precipitate (τ_{p}) at the CNP's surface, where n_{C}^{S} is determined from Equation (30) and J_{v} and J_{s} are the fluxes of bulk and SDs, respectively. This selectivity offers an interesting opportunity to enable the as yet elusive time-programed synthesis of SWCNTs with controlled thickness and possibly chirality [107].

There are a few more manifestations of the benefits of CNT nucleation in low-temperature plasmas. First, the electric field in the plasma sheath promotes nucleation of SWCNTs at the top of the metal CNP as shown by the results of hybrid molecular dynamics (MD)/force-biased Monte

Carlo simulations in Figure 9(d) [48]. The SWCNT cap not only nucleates and bends at the CNP summit, but also prominently elongates along the direction of the electric field, giving rise to the commonly observed vertical growth of CNTs in the plasma [5,112]. Interestingly, in thermal CVD, the nucleation points of many 1D NW-like structures are more often observed closer to the NP edge with the interface [50].

The physics behind this preferential nucleation is in the electric-field enhanced mobility of carbon atoms on the CNP surface. Under conditions of typical electric fields generated in the plasma sheath at low pressures used for SWCNT growth [109], the contribution of the electric field-induced mobility turns out to be stronger compared with thermal hopping, which in turn leads to the upward surface fluxes that tend to converge at the CNP summit [48].

Since the electric field can control the mobility of carbon atoms during the nucleation process, lower temperatures of external heating may be required for nanotube nucleation. This is consistent with the plasma-enabled reduction of the nucleation temperature presented in Figure 9. The most obvious benefit arises when the temperature is reduced below the CNP melting temperature. In this case, the catalyst can be maintained in the solid (crystalline) state, enabling its facets to act as a template for the nanotube nucleation. Unfortunately, a very large number of defects inevitably appear during the nucleation and growth at low temperatures.

Interestingly, the ion bombardment in a narrow energy window effectively enhances the nanotube cap nucleation and reduces the defect concentration, without increasing the growth temperature. This healing effect of the ion bombardment is rather counterintuitive, because defect creation and other damaging effects are commonly expected.

This possibility was very recently confirmed by a complementary study involving state-of-the-art reactive MD simulations and experiments on the ion bombardment of as-nucleated SWCNTs [113]. These simulations involved a model of the repulsive Ni/C – Ar^+ interaction described by a repulsive Molière potential employing Firsov constants:

$$V_{\mathrm{M}} = \frac{Z_1 Z_2 e^2}{4\pi\varepsilon_0 r} \sum_{i=1}^{3} \eta_i \exp\left(-\frac{\delta_i}{l_{\mathrm{scr}}} r\right), \tag{37}$$

where r is the scalar distance between the impinging Ar^+ ion and the targeted C or Ni atom, Z_i is the nuclear charge of atom i, e is the elementary charge, ε_0 is the permittivity of space, and l_{scr} is the screening length, determining the effective interaction range of potential (37). The values for η_i are $\{0.35; 0.55; 0.1\}$, and the values of δ_i are $\{0.3; 1.2; 6.0\}$ for $i = \{1; 2; 3\}$, respectively.

The processes observed in the numerical experiments are clearly different in three energy ranges, and are found to be directly related to the maximum transferable kinetic energy

$$\mathcal{T}_{\max} = \mathcal{E}_{\mathrm{ion}} \frac{4m_1 m_2}{(m_1 + m_2)^2}, \tag{38}$$

where m_1 and m_2 are the masses of the impinging ion (with energy $\mathcal{E}_{\mathrm{ion}}$) and the C-atom hit. At low-ion impact energies, when $\mathcal{T}_{\max}$ is below the energy required to displace C-atoms from their positions at the surface [114], the effect of the ion bombardment is negligible. In the range 10–25 eV, however, the ions can displace the surface C-atoms, allowing more extensive and stable ring structures to form (Figure 10(a) and 10(b)). At still higher energies, when $\mathcal{T}_{\max}$ is near or above the C-displacement energy, carbon atoms can be displaced from their stable lattice positions in existing ring structures, thus damaging the nucleating cap [113].

Experimentally, ultra-short SWCNTs were grown to validate the simulations. When a bias of -20 V was applied, a significant increase in the (sp^2 order-related) G-peak in the Raman spectrum was found, whereas a strong decrease in the G-peak is observed when applying a bias of -50 V (Figure 10(c)) [113].

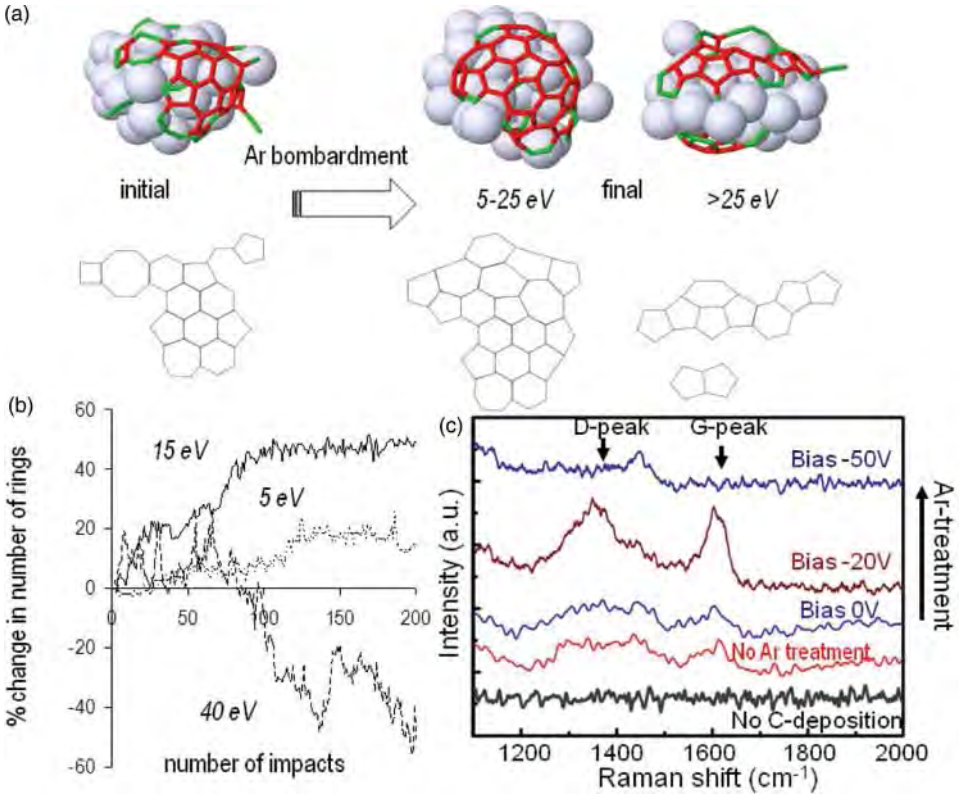

Figure 10. Enhanced nucleation of a SWCNT by low-energy ion bombardment [Reproduced with permission from [113], Copyright © 2013 by the American Physical Society]: (a) Representative snapshots of the effect of Ar^+ bombardment with medium (15–25 eV) and high (30 eV) energy on the SWCNT cap; (b) average percent change in the number of rings in the cap over 10 simulations, each consisting of 200 consecutive ion impacts, for 5, 15, and 40 eV; (c) experimental Raman spectra for as-nucleated SWCNTs subjected to Ar^+ ion bombardment under various biases.

It should be noted that the ion bombardment differs in two main aspects with thermal annealing. First, the ions act as an external agent, interacting directly with the carbon network, rather than acting through the metal NP. Second, ion bombardment is a local influence, affecting only (or mostly) the C-atom(s) directly hit, whereas thermal annealing affects the system as a whole.

Therefore, the ion bombardment, often regarded as an 'evil', can be gainfully used in even so delicate processes as nucleation of SWCNTs. In the following subsection, we will consider the plasma-specific effects during the next, growth stage of the nanotubes.

3.5. *Nanostructure growth*

The pronounced vertical alignment is perhaps one of the most frequently cited benefits of using plasmas in the growth of CNTs and many other 1D NSs [2,5]. This effect was observed by a very large number of researchers, with the first reports on the observation and interpretation of this phenomenon (Figure 11(a)) dating back to 1998–2001 [112,115,116].

This alignment is indeed very strong and the electric field control of the nanotube growth direction is very effective. In the example shown in Figure 11(b), the direction of the applied electric field was changed, and the CNTs with a well-defined zigzag structure were produced

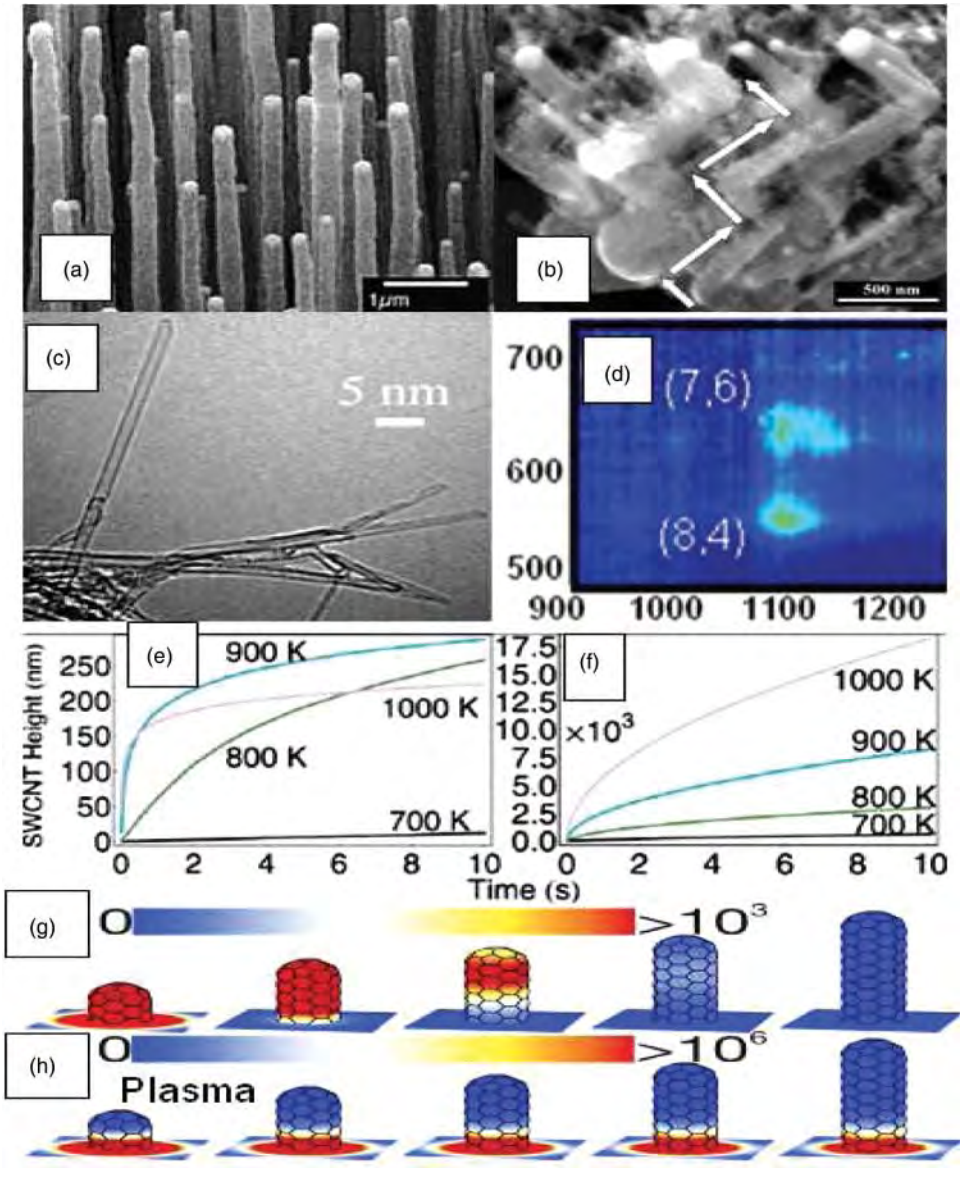

Figure 11. Vertical alignment of MWCNTs in a plasma (a) [Reprinted with permission from [112], Copyright © AAAS]. Zig-zag nanotube structures produced by varying the direction of DC electric field during the plasma growth (b) [Reprinted with permission from [117], Copyright © 2004 American Chemical Society]. Plasma-produced SWCNTs show superior structural quality (c) [Reprinted with permission from [108], Copyright © 2008 American Chemical Society] and chirality distributions (d) [Reprinted with permission from [107], Copyright © 2010 American Chemical Society] evidenced by transmission electron microscopy (TEM) and photoluminescence emission (PLE) imaging, respectively. SWCNTs grow faster in a plasma than in thermal CVD (e) and (f), in part because of BU delivery to the CNP at the nanotube base (g) and (h), as confirmed by numerical simulations [Reprinted with permission from [120], Copyright © 2008 American Institute of Physics].

during direct current (DC) plasma-enhanced chemical vapor deposition (PECVD). Moreover, the nanotubes maintained the same diameter before and after each bend while preserving the catalyst particle at the tip [117].

This alignment is a result of a complex interplay of several mechanisms. One of the earlier mechanisms [116] explains the vertical alignment by the balance of stresses in the developing 1D NSs. Recently, it was revealed that this vertical alignment may not necessarily emerge during the nucleation stage and proceeds through the three stages from randomly entangled, to partially aligned and fully aligned nanotubes. More importantly, the plasma etching (again, process kinetics) is an important factor that determines the CNT growth mode and vertical alignment [118].

Temperatures for solid NS growth using plasmas are usually markedly lower compared with equivalent thermal processes; in some cases, this temperature difference can reach a few hundred degrees. For example, SWCNTs grow in a plasma at temperatures as low as ∼450°C, while heating to ∼800–900°C is used in thermal CVD [119]. As discussed in Sections 3.3 and 3.4, these lower growth temperatures are due to the lower energy barriers for the NS nucleation.

Despite much lower growth temperatures, the plasma-produced CNTs and their arrays often feature superior quality, as evidenced in Figure 11(c) and 11(d). The nanotubes in panel (c) have a clear, defect-free single-walled structure, which is also evidenced by the strong radial breathing modes and a typically very high ratio of the intensities of the G and D bands in the Raman spectra [108].

The SWCNT patterns synthesized in a plasma can feature narrow size and chirality distributions as shown in a PLE map in panel (d) [107]. As a result, very large fractions (e.g. as high as 96%) of semiconducting SWCNTs can be produced [108]. The mechanisms of reducing the size and chirality distributions have been discussed in Section 3.4. However, the physics of the observed SWCNT chirality selectivity is still unclear, in part because of the recently revealed changes of the nanotube chirality during the nucleation stage [47].

During the advanced growth stages, the CNT growth rates can be estimated by

$$\mathcal{R}_{\rm gr}^{\rm CNT} = \frac{m_{\rm C}}{\rho_{\rm CNT} S_{\rm CNP}} (J_{\rm s} + J_{\rm v}), \tag{39}$$

where $m_{\rm C}$ is the mass of a carbon atom, $\rho_{\rm CNT}$ is the nanotube mass density, and $S_{\rm CNP}$ is the surface area of the CNP which supports the growth (e.g. through which carbon atoms incorporate into the developing NS).

As discussed above, several plasma-related mechanisms may increase the fluxes $J_{\rm s}$ and $J_{\rm v}$ and decrease $S_{\rm CNP}$ (e.g. reduce the nanotube thickness). This is why it is not surprising that plasma-based processes also very often feature higher growth rates compared with similar thermal processes in the same gases and under the same conditions, see Figure 11(e) and 11(f). In particular, these results suggest that in the base-led SWCNT growth mode, plasma-produced carbon atoms reach the catalyst and incorporate into the nanotube walls much faster than without the plasma.

In addition, effective etching of amorphous carbon by the plasma-produced reactive hydrogen atoms maintains the CNP catalytically active longer, which results in taller nanotubes. Panels (g) and (h) show the possibility to control the plasma parameters to deliver the ions as close as possible to the CNP where carbon BUs are needed for the growth (red spots denote higher density of ion impacts) [120].

This is possible to implement by controlling the topography of the microscopic electric fields near the nanostructured surface

$$\mathbf{E}(\mathbf{r}) = \sum_i \int_{S_i} \frac{\rho_i \, {\rm d}S_i}{4\pi\varepsilon_0 r^3} \mathbf{r} + \mathbf{E}_{\rm sheath}, \tag{40}$$

and the energy of ions that follow the electric field lines [49]. The first term in Equation (40) represents the microscopic field produced by the nanotube arrays, while the second term $\mathbf{E}_{\text{sheath}}$ is the field within the plasma sheath. Here, ρ_i is the charge density on the CNT surfaces. The curvature of the resulting electric field near the nanotubes strongly depends on both the plasma and the nanoarray parameters and can be optimized to enable selective delivery of the ions to the specific areas on the NS surface.

This targeted BU delivery is complemented by the fast downward travel of carbon species along the nanotube length and also by the reduced desorption rates of these species from the surface. A combination of these factors leads to very high CNT growth rates in plasma-based processes.

3.6. *Self-organized pattern formation*

The previous sections dealt with the nucleation and growth of individual solid NSs. Let us now consider plasma-specific effects in the development of self-organized patterns and arrays of two types.

The first type of patterns uses pre-formed features such as arrays of CNPs as in Figure 2(a). In this type of patterns, the positions of individual NSs are predetermined, e.g. by the CNP positions.

In a plasma, 1D NSs grow in the direction of the electric field, see Section 3.5. Some nanotubes may grow with different rates and vary in length. Since all the NSs in the pattern share the incoming flux of precursor species, the nucleation and growth exhibits collective behavior. The underlying mechanism is based on the dynamic flux redistribution between the substrate and surfaces of the NSs. For example, simultaneous saturation of CNPs is desirable for the formation of length-uniform arrays of CNTs and other 1D NSs (e.g. inorganic NWs).

It was reported that the degree of simultaneity of CNP saturation with carbon in plasma-based processes is higher than in the equivalent thermal CVD. This effect owes to the more regular redistribution of carbon flux caused by the microscopic electric field effects [43]. Surprisingly, plasma-guided self-organization thus also plays a role even in the arrays with pre-determined positions of individual NSs.

Figure 12 shows examples of self-organization in the second type of patterns where solid NSs nucleate randomly. This randomness leads to additional complexity. However, reasonable ordering persists even in self-organized 2D and 3D arrays [66,67]. In addition to the balance of material supply and consumption which controls the first type of patterns, the stress and surface energy landscapes, along with non-uniform temperature distributions play a vital role in the second case.

An interplay of these factors leads to very different self-organized patterns of SiO_2 NSs (Figure 12(a) and 12(b)) on stainless steel substrates exposed to remote MW microplasmas of $Ar+O_2$ gas mixtures [121]. These patterns require different plasma conditions, temperature gradients, and stress levels. Weak thermal gradients under higher temperatures lead to the low stress levels and hence, the nanodot morphology (a). On the other hand, stronger thermal gradients at lower temperatures generate much higher stress levels (arrows in (b)) leading to the self-organized hexagonal cells. Relative contents of working (Ar^+ ions) and building (O atoms) units are also different in both cases. A higher density of Ar and a lower density of oxygen lead to highly stressed (e.g. due to a stronger ion bombardment) and less dense (due to reduced BU delivery) patterns in Figure 12(b). Customized oxygen-based plasmas can produce self-organized patterns of randomly nucleated nanodots, NWs, nanowalls, and other oxide NSs (Section 4.2.3).

Figure 12(c) shows the temporal dynamics of the formation of a dense and uniform 3D array or carbon nanocones (bottom right) on very non-uniform patterns of Ni CNPs (top left). A combined experimental and numerical study [122] has revealed that this self-organization proceeds through several stages. First, a primary rarefied array of nanocones is formed (top right), followed by nucleation and faster growth of smaller nanocones between them (bottom left). Importantly, this

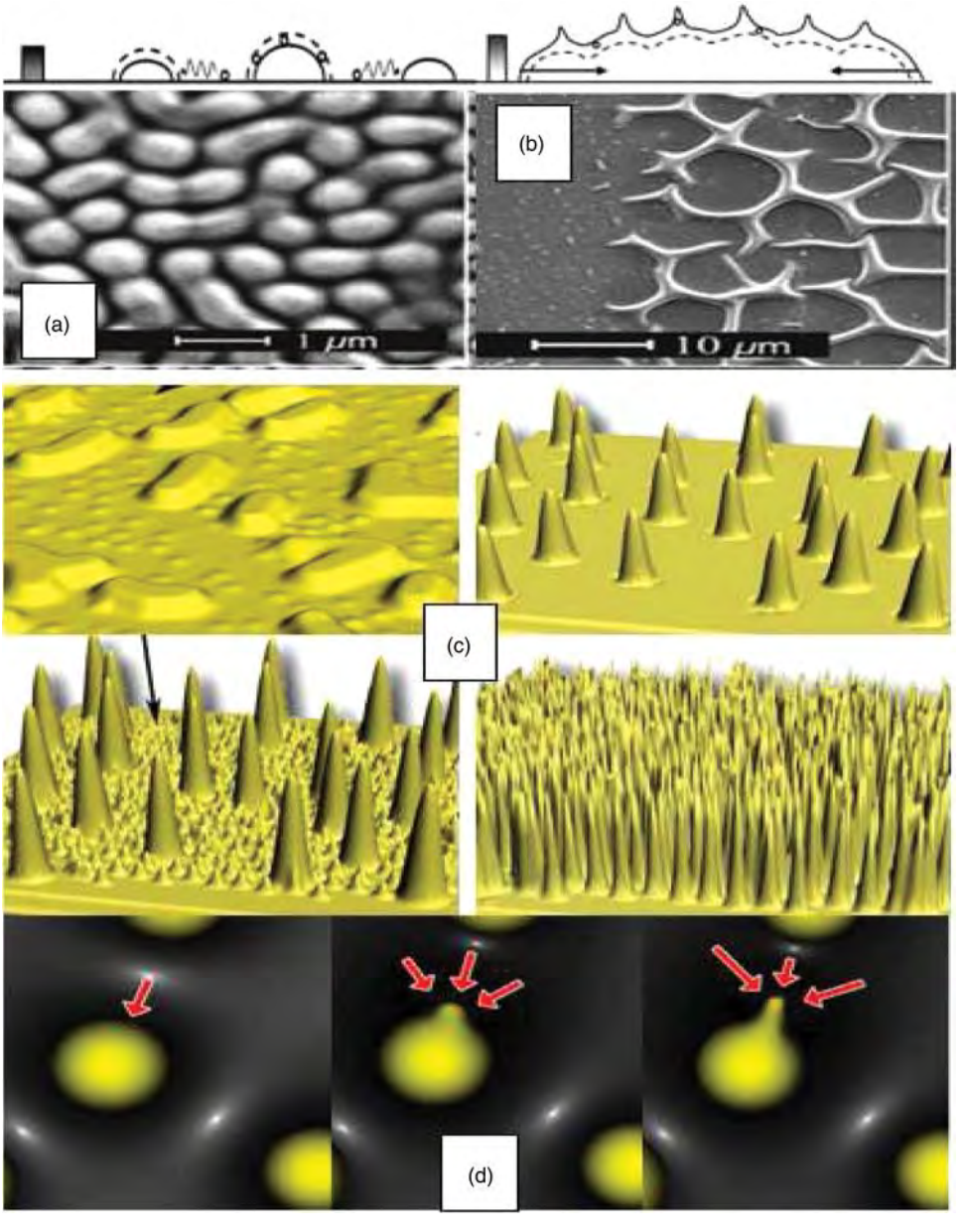

Figure 12. Self-organized SiO_2 nanoarrays from $Ar+O_2$ microplasmas (a) and (b) and sketches of surface temperature gradients (bars), stress levels (arrows), and profiles formed [Reprinted with permission from [121], Copyright © 2010 American Institute of Physics]. 3D self-organized growth of uniform arrays of carbon nanocones from non-uniform catalyst patterns (c) [Reprinted with permission from [122], Copyright © 2007 Elsevier]. Self-alignment of carbon NW connections between Ag particles on Si (d); carbon fluxes are shown by arrows [Reprinted with permission from [123], Copyright © 2009 Elsevier].

process is due to the plasma-specific redistribution of carbon BUs across the 2D substrate and the surfaces of developing NSs and is not possible in the equivalent thermal process.

An example of one such 2D rearrangement of carbon BUs on a plasma-exposed Si surface between Ag particles is shown in Figure 12(d). As mentioned in Section 3.5, this leads to

Table 1. Activation energies for surface processes and densities of features [124–129].

Energy/density	Feature	Numerical value
ε_{d}	Surface diffusion activation energy for Si surface	∼1.1 eV
ε_{V}	Adatom activation energy on surface vacancy	∼1.43 eV
ε_{i}	Adatom activation energy on interstitial atom	∼1.25 eV
ε_{F}	Adatom activation energy on Frenkel defect	∼1.5 eV
η_V	Surface density of vacancies	$\sim 5.0 \times 10^{15}\,\mathrm{m}^{-2}$
η_{i}	Surface density of interstitial atoms	$\sim 5.0 \times 10^{15}\,\mathrm{m}^{-2}$
η_{F}	Surface density of Frenkel defects	$\sim 1.0 \times 10^{15}\,\mathrm{m}^{-2}$
ε_{D}	Adatom activation energy on dislocation	∼1.2 eV
η_{D}	Surface density of dislocations	$\sim 1.0 \times 10^{15}\,\mathrm{m}^{-2}$
ε_{S}	Adatom activation energy at step terrace (Ehrlich–Schwoebel barrier)	∼2.2 eV
η_{S}	Surface density of step terrace sites	$\sim 8.5 \times 10^{15}\,\mathrm{m}^{-2}$
ε_{P}	Adatom activation energy on nano-grain boundaries of Si surface	∼2.2 eV
η_{P}	Surface density of nano-grains on Si surface	$\sim 1.0 \times 10^{15}\,\mathrm{m}^{-2}$
R_{C}	Correction coefficient for SD on a real-roughness surface	∼0.97
$\varepsilon_{m\mathrm{S}}$	Adatom activation energy on substitutional atom	∼1.3 eV
$\eta_{m\mathrm{S}}$	Surface density of substitutional atoms	$\sim 8.5 \times 10^{15}\,\mathrm{m}^{-2}$

microscopic electric fields with a component parallel to the surface. Adatoms respond to this long-range non-uniform electric field. Both the electric field and its non-uniformity are the strongest along the line connecting two adjacent CNPs. As a result, carbon wires nucleate and then grow along this direction [123]. Physically, this effect is quite similar to the SWCNT nucleation in a vertical electric field (Figure 9(d)). This horizontal growth evidences that the growth direction of 1D carbon wires can also be controlled using *self-organized* microscopic electric fields, in addition to external fields (Figure 11(b)).

The development of self-organized nanopatterns in Figure 12(c) and 12(d) can be described using the following 2D diffusion equation of carbon atoms [124]

$$\frac{\partial \xi}{\partial t} = D_S \left(\frac{\partial^2 \xi}{\partial x^2} + \frac{\partial^2 \xi}{\partial y^2} \right) + \Psi^+ + \Psi^-, \tag{41}$$

where ξ is the surface density of carbon atoms, whereas Ψ^+ and Ψ^- are the source and sink terms of carbon atoms that add to the surface and leave it, respectively. The diffusion coefficient D_{S} is given in Equation (8), with the effective energy barrier

$$\mathcal{E}_{\mathrm{d}}^{\mathrm{eff}} = \frac{\Sigma_k \varepsilon_k \eta_k}{\Sigma_k \eta_k} \tag{42}$$

and pre-factor D_0 modified to incorporate several features (e.g. imperfections) of surfaces of real solid materials summarized in Table 1. In Equation (42), η_k is the surface density of kth feature expressed in m^{-1}, and ε_k is the energy barrier associated with kth feature.

Although the focus of the original report [124] was on the effect of the electric field on the formation of self-organized connections between the microparticles, several other effects can drive this process. Similar to Figure 12(a) and 12(b), surface stress between the particles plays an important role. Indeed, the stress magnitude is higher in the area between the two adjacent particles. Hence, the surface stress should enhance carbon adatom incorporation into the micrograins. Consequently, the levels of the particle supersaturation with carbon should be higher at the surfaces facing the nearest neighbor. This also helps the nucleation of the 1D carbon structures connecting the closest micrograins.

Here, we stress that during this self-organized growth process, the electric, adatom density, stress, and chemical potential fields self-organize in a complex and possibly, coordinated way

to sustain the connection growth between the two nearest micrograins [124]. This interesting possibility still awaits its conclusive experimental verification.

Plasma-specific phenomena also affect the development of many other self-organized nanopatterns and arrays, with further examples related to diamond-like [130], Ni [131], Ge [132], and SiO_2 [133] nano-islands. Although every process is different, the physics of these self-organization phenomena is quite similar and based on the effects discussed in this section. With this knowledge, we can now review several classes of nanoscale solids and plasma processes.

4. Nano-solids from plasmas: plasma-specific effects and physical, chemical, and functional properties

The previous section focused on a sequence of events and elementary processes during the formation of solid NSs and nanoarrays on plasma-exposed surfaces. Here, we use a different approach to cover a broad range of materials systems and NSs. These objects are split according to their dimensionality, similar to Figure 1.

This choice is dictated by the ability of nano-solids to confine electrons in a different number of dimensions, which in turn determines their properties and applications. Each of these 'dimensional' categories features typical materials systems, e.g. carbon- and silicon-based, inorganic, organic, living, etc. materials. Where appropriate, we also discuss the plasma-specific physical effects and the associated materials structure and performance in applications.

This is why, as mentioned in Section 1.3, each section first introduces the envisaged applications of the solid materials, then any existing problems in their synthesis and processing, followed by a critical discussion of the plasma-specific effects that lead to any process improvements or enable some new features. The focus of these discussions is on the final outcomes rather than the dynamics of nucleation and development of the structures, which were discussed in a greater detail in Sections 2 and 3. Nonetheless, wherever possible, we comment on these features and refer the reader to the appropriate sections in this review.

The number of nano-solid systems referred to in this section is very large. This is why we discuss only the most essential of those properties of these solids that were affected by any relevant plasma-specific effects. The focus is mainly on the morphological, structural, and selected functional properties. We also provide links to relevant solid-state physics and chemistry, materials science and nanoscience literature which provide exhaustive coverage of the properties and applications for the main materials types considered in this section.

4.1. *Quantum dots nanocrystals, and nanoparticles*

Here, we consider three basic options of the production and organization of 0D solid NPs using plasmas: QDs embedded in bulk solid materials, unsupported nanocrystals and NPs, and surface-supported nanoarrays.

4.1.1. *Quantum dots*

4.1.1.1. *Semiconducting QDs.* Semiconducting QDs, which feature strong electron quantum confinement in all three dimensions, are usually unsupported, surface-supported, or embedded in a matrix of a bulk material. A large variety of unsupported QDs have been produced using colloidal chemistry approaches; this is a very active and well-developed research field. Here, we discuss the latter two options which have been demonstrated using low-temperature non-equilibrium plasmas. Figure 13(a) shows a cross-sectional high-resolution transmission electron microscopy (HRTEM) image of *a*-Si QDs embedded in a silicon nitride film [134]. These 3D QD patterns are produced

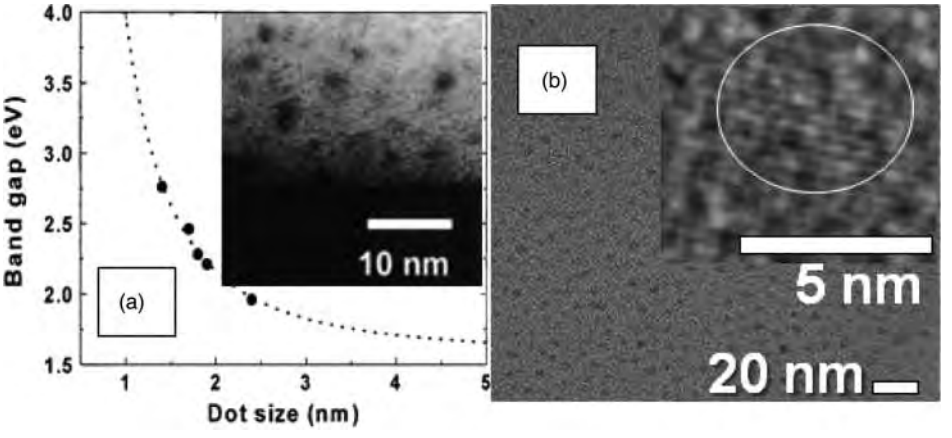

Figure 13. *a*-Si QDs in a SiN film grown by PECVD and their bandgap versus QD size [Reprinted/adapted with permission from [134], Copyright © 2001 American Physical Society]. Crystalline Si QDs in an *a*-Si matrix produced using SiH_4 plasmas with very low or no dilution in H_2 (b) [Reprinted/adapted with permission from [136], Copyright © 2009 American Chemical Society].

at very high growth rates from 1.4 to 3.2 nm/min using reactive mixtures of SiH_4 and N_2 gases. The dark spots in Figure 13(a) represent QDs with an average size ∼1.9 nm and a dot density of $\sim 1.0 \times 10^{19}\,\mathrm{cm}^{-3}$.

The quantum confinement effects are manifested by the wider bandgap energies for smaller QD sizes. The experimental points fit the dashed line plotted using the effective mass theory for three-dimensionally confined Si QDs [134]

$$E(a) = E_{\mathrm{bulk}} + \frac{\sigma_{\mathrm{qconf}}}{a^2}, \tag{43}$$

where E_{bulk} is the bandgap of bulk Si, a is the QD size (diameter), and σ_{qconf} is the electron confinement parameter. These results thus evidence the effective electron confinement in the *a*-Si QDs, which leads to the observed strong photoluminescence (PL). The value of the achieved electron confinement parameter $\sigma_{\mathrm{qconf}} = 2.4\,\mathrm{eV}\cdot\mathrm{nm}^2$ is more than three times larger compared with 2D *a*-Si quantum wells [135]. This can be explained by noting that

$$\sigma_{\mathrm{qconf}} \propto \frac{1}{m^*} = \frac{1}{m_{\mathrm{e}}^*} + \frac{1}{m_{\mathrm{h}}^*}, \tag{44}$$

where m_{e}^* and m_{h}^* are the effective masses of electrons and holes, m^* is the reduced mass, and the effective masses in amorphous materials are commonly assumed to be isotropic in all three directions [134].

Importantly, the degree of passivation of QD surfaces which determines the PL efficiency can be effectively controlled through altering the rates of reactive species production (e.g. nitrogen or hydrogen dissociation) in the plasma discharge by the operating parameters. The degree of passivation of *a*-Si by SiN in Figure 13(a) is very high [134]. This very effective plasma-assisted surface passivation by SiN is commonly used in the fabrication of photovoltaic solar cells [24]. The degree of passivation of Si QDs determines the difference between the luminescence energy E_{lum} and the absorption energy E_{abs}, which is in turn determined by the density of deep luminescence centers such as the surface states.

The density of such states is usually higher in nanocrystalline Si (nc-Si) made of single-crystalline Si QDs embedded in an *a*-Si matrix (Figure 13(b)). To improve the surface passivation,

heavy dilution of SiH_4 in H_2 is commonly used [136,137]. However, this very significantly affects the growth rates, and hence, the material cost in the solar cell production. The outstanding ability of thermally non-equilibrium plasmas to dissociate precursor species has led to the unique possibility to avoid hydrogen dilution and produce high-quality *nc*-Si films at low-process temperatures ($\sim$150°C) where the QD formation was observed.

Si QDs in Figure 13(b) feature the preferential (111) growth orientation and the crystalline fraction can be controlled from 0% to 86%. The QDs can be grown at very competitive growth rates of up to $\sim$2.5 nm/s using fairly low power densities of $\sim$40 mW/cm^3, and very low or no hydrogen dilution of silane precursors. These features are very difficult to achieve otherwise. This is why low-temperature plasmas are commonly used in flat display and solar cell technologies.

4.1.1.2. *QD formation and properties: numerical simulations.* The mechanism of the Si QDs formation from the plasma is not fully understood. Nonetheless, it is clear that the nanocrystals may form either through localized crystallization on the surface as the *a*-Si film grows or may form and be delivered from the gas phase. The energy of the plasma-grown Si nanocrystals upon deposition appears to be a critical factor which determines the structure selectivity between the amorphous and nc-Si films [137]. This energy is determined by the interplay of charging mechanisms and the (electrostatic, ion and neutral drag, etc.) forces acting on the NPs in the plasma [9,79,80].

Using a multilevel simulation strategy, Vach *et al.* [138,139] simulated the controlled growth of silicon nanoclusters in a plasma. Most importantly, it was found that when there was no atomic hydrogen present in the plasma, small Si:H nanocrystals could not be formed. In contrast, under plasma conditions leading to very low H-impact rates, the formation of hydrogen-rich, small nanocrystals was found. When higher H-impact rates were allowed, hydrogen-poor crystallites appeared.

Representative examples of Si_nH_m clusters studied by these numerical simulations under typical plasma conditions are shown in Figure 14(a). Interestingly, the hydrogen atoms always remain on the outside of the Si_nH_m clusters. The variety of such structures indicates that the plasma conditions can be adjusted such that the resulting NP properties can be tuned. This ability is of crucial importance in the plasma-assisted fabrication of polymorphous solar cells [137].

For example, using an intermediate flux of hydrogen atoms (which is possible to implement in real plasma experiments by controlling the degree of hydrogen dissociation), one can produce a unique structure with a Si atom shifted off the center shown in Figure 14(b). This asymmetry leads to the very large permanent dipole moment $\sim$1.9 D (Debye units), which is comparable to a water molecule [138]. This dipole moment is visualized by the 3D and 2D profiles of the electron density calculated from the total self-consistent field density mapped with the corresponding electrostatic potential in Figure 14(b). Importantly, the presence of this dipole moment enables the unique possibility to align these Si:H nanoclusters in the plasma electric field. This alignment in turn may lead to the electrostatic attraction of the oppositely charged poles of different nanoclusters thereby forming chain- or wire-like nanoassemblies. This is an interesting example of the use of tailored BUs to assemble more complex structures. We emphasize that both stages of this process benefit from the plasma-specific effects [138].

In a subsequent computational study [140], it was shown that the reaction mechanisms of the Si:H nanoclusters on Si-surfaces depend mostly on the impact energy, but are not very sensitive to the cluster size. Moreover, a good agreement with experimental results was obtained. To allow a comparison between impacts of various cluster sizes, the effect of the impact energy was quantified through the impact energy coefficient

$$\alpha_{\text{imp}} = \frac{E_{\text{imp}}/N_{\text{cl}}}{E_{\text{sub}}}, \tag{45}$$

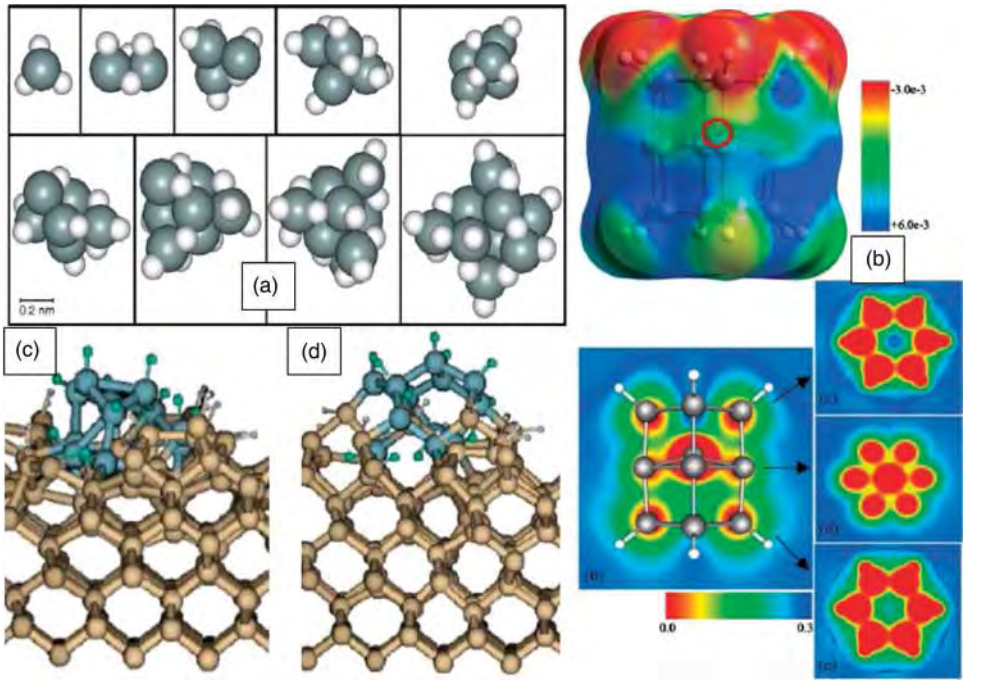

Figure 14. Plasma-grown silicon hydride nanoclusters, their electronic properties and role as BUs in crystalline Si growth studied by *ab initio* numerical simulations [138–140]. Si_nH_m clusters grown under typical plasma conditions (a) [Reprinted with permission from [139], Copyright © 2006 Elsevier]. 3D profiles of electron density of a hydrogenated Si NP with the 'off center' Si atom (encircled); this non-symmetric atomic arrangement leads to a very strong permanent dipole moment visualized by graded colors (b) [Reprinted with permission from [138], Copyright © 2005 American Physical Society]. Plane cuts of the $Si_{19}H_{12}$ NP in different directions produce 2D contour plots of the electron density also shown in the lower section of panel (b) [138]. Panels (c) and (d) show a temporal dynamics of epitaxial recrystallization of a $Si_{12}H_{12}$ nanocluster after 0.42 and 6.0 ps after the impact on the Si surface; surface temperature is $T = 300$ K and the cluster impact energy $E_{imp} = 60$ eV [Reprinted with permission from [140], Copyright © 2010 American Chemical Society].

where E_{imp} is the cluster impact energy, N_{cl} is the number of silicon atoms in the cluster, and E_{sub} is the cohesive energy of the substrate.

Using the definition (45), one can discern three distinctive regimes [140]. Low impact energies lead to reflection of the cluster, medium impact energy lead to soft landing, while higher energies lead to the fragmentation of the clusters. Impact-induced dissociation followed by fragment migration, penetration, and partial surface damage, on the other hand, is observed at higher cluster energies. The reported difference in reactivity of smaller and larger clusters stems from the different and size-dependent structural stability of the clusters. These findings are consistent with the experimental results [141].

Of particular interest is the possibility to epitaxially grow nc-Si films by such cluster impacts. The results of simulations in Figures 14(c) and 14(d) show that such epitaxial growth is possible, as evidenced by the epitaxial-like recrystallization of clusters (d) after the loss of the initial cluster structure following surface impact (c) [140].

The ability to tailor the structure and electronic properties of nanocluster BUs and their integration into nanostructured Si films is indispensable for the development of the third-generation

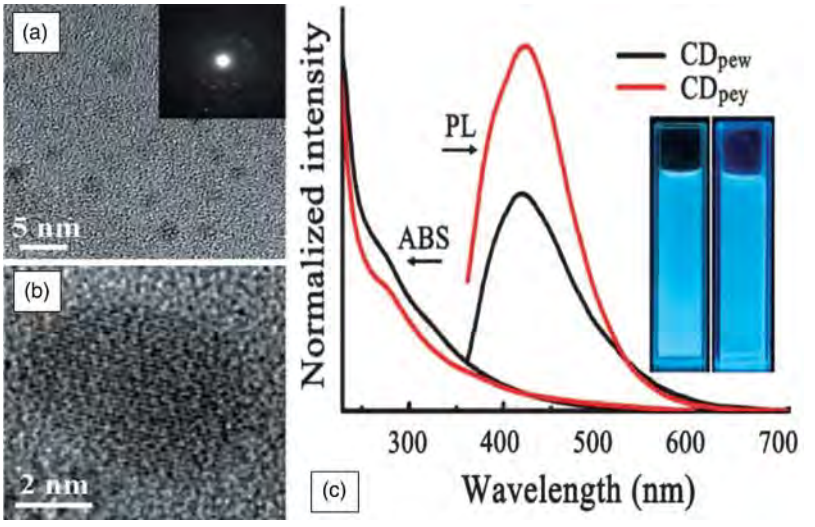

Figure 15. High-resolution TEM micrographs (a) and (b) and optical emission/absorption spectra (c) [144] of atmospheric-pressure plasma-synthesized C-dots using natural egg yolk precursor in aqueous solution. Panel (b) shows a selected C-dot at higher magnification. Inset in panel (a) shows a typical electron diffraction pattern. Spectra of PLE and UV/Vis absorption of C-dots in aqueous solution (c); excitation wavelength is 360 nm. CDpey and CDpew denote egg yolk and white produced C-dots. Inset in panel (c) shows optical images of CDpew (left) and CDpey (right) solutions under UV light exposure [Reproduced with permission from [144], Copyright ©2012 Wiley-VCH Verlag GmbH & Co. KGaA, Weinheim].

photovoltaic solar cells, thermoelectric, energy storage, optoelectronic, and several other advanced applications [24,37]. A clear opportunity for future research exists in the understanding of the possible contribution of the plasma-specific effects to improve the formation and ordering of self-organized 3D structures in nc-Si which may form during heteroepitaxial growth and chemical synthesis [142].

4.1.1.3. *C-dots.* The discussions above are related to more traditional examples of plasma-assisted synthesis of Si-based QDs. In these examples, which have dominated the literature for about a decade, low-pressure (e.g. in the 10 s–100 s mTorr range) plasma discharges in highly toxic and flammable gaseous precursors of relevant materials (e.g. silane, germane, etc.) have been commonly used.

Recently, several new possibilities to synthesize QDs of other materials systems using different plasmas and precursors have been demonstrated. For instance, atmospheric-pressure dielectric barrier discharge (DBD) plasmas were used to produce luminescent carbon QDs (commonly termed C-dots [143]) from natural egg yolk and white precursors [144]. As can be seen from Figure 15(a) and 15(b), plasma-produced C-dots have quite similar sizes and morphological appearance compared with Si QDs in Figure 13(b).

The C-dots represent a new class of recently discovered carbon nanomaterials which typically feature spherical morphology and tunable surface functionalities. They are mostly composed of sp^2 hybridized carbon and as such may be termed nanocrystalline graphitic nanodots, in particular because of the above-mentioned similarity to nc-Si. This makes them very different compared with diamond NPs which will be considered in Section 4.5.4.

The size and surface termination of the C-dots can be effectively tuned by the synthesis process parameters. This leads to the size- and excitation energy-dependent PLE. Importantly, because

of their biocompatibility, the C-dots are considered as viable alternatives to commonly used metal and semiconducting QDs, which are often not only toxic, but are also produced using hazardous precursors such as the SiH_4 used to synthesize *nc*-Si discussed above. Despite many recent achievements, the degree of control of size, elemental composition (e.g. oxygen content), defects, and surface functional groups still remains quite limited. Consequently, tunability of the optical luminescence while minimizing absorbance, quantum yield of photon emission, and the fluorescence lifetime still remain significant issues.

Unlike many conventional methods of synthesizing C-dots, the atmospheric plasma-based process [144] relied on natural and renewable carbon precursors, namely egg yolk and white. The C-dots showed good crystalline quality as can be seen in HRTEM micrograph from Figure 15(b); the typical size of the C-dots produced was under ∼5 nm. X-ray photoelectron spectroscopy and Fourier transform infrared spectroscopy analyses also confirmed the presence of C=C, C–OH, C–O–C, and C=O functional groups.

The yolk-produced C-dots showed somewhat better crystalline structure, which was explained by the higher presence of lipids in egg yolk (∼33%) compared with egg white (∼0.01%). It was suggested that the higher density and viscosity of the yolk was favorable to enhance electron-ion recombination processes on the surface, which in turn promotes NP crystallization. However, the mechanism of the plasma-enabled nanodot formation is presently unclear and requires a dedicated study of the different mechanisms of interaction of atmospheric-pressure plasmas with liquid media of different densities and lipid contents. Despite significant recent progress [145], studies of plasma–liquid interactions are presently at the early stage.

The significant difference in the structural properties has led to the stronger PLE from the egg yolk-derived C-dots, as can be seen from Figure 15(c). The maxima of the absorbance and PL emission show a very clear spectral separation allowing for the blue emission to be detected easily, as can be seen from the inset. Moreover, the time-dependent fluorescence

$$\Upsilon(t) = \alpha_1 \exp\left(\frac{-t}{\tau_1}\right) + \alpha_2 \exp\left(\frac{-t}{\tau_2}\right) \tag{46}$$

showed contributions from two time-resolved decay lifetimes τ_1 and τ_2 with fractional contributions α_1 and α_2, respectively. By fitting the experimental spectra with Equation (46) provided the estimate of the average lifetime [144]

$$\bar{\tau} = \frac{[\alpha_1\tau_1^2 + \alpha_2\tau_2^2]}{[\alpha_1\tau_1 + \alpha_2\tau_2]} = 6.37 \pm 0.05\,\text{ns}, \tag{47}$$

which is comparable with the lifetimes of C-dots produced by other (e.g. wet chemistry, laser ablation, thermal, etc.) routes [143,146]. The competitive quantum yield (∼8% and ∼6% for the egg yolk and white-produced C-dots, respectively) and the improved (by ∼10%) photostability suggests that the atmospheric-pressure plasma-based processes are indeed viable alternatives to the many existing wet chemistry-based approached to the synthesis of luminescent C-dots.

This very interesting development opens an opportunity to develop cheap (e.g. vacuum-free, atmospheric-pressure) and environment-friendly plasma processes based on natural and renewable precursors. In this example, the egg yolk and white served mainly as carbon precursor, while the non-equilibrium plasmas (Equation (5) also holds for atmospheric-pressure DBDs) were used to effectively reform the precursor material into relevant hydrocarbon species. One can thus expect that a wider range of atmospheric plasma- and natural precursor-based processes will emerge for the synthesis and processing of a range of nanoscale solid materials using precursors with high natural abundance. This area is very new and offers numerous opportunities for the studies of the plasma-specific mechanisms that lead to precursor conversion into solid NSs.

4.1.2. *Nanocrystals and nanoparticles*

Nanoparticle production has been demonstrated from the plasmas in both gases and liquids. The plasmas used also range from thermally non-equilibrium plasmas of low-pressure discharges to thermal plasmas at atmospheric pressure and more recently, to non-equilibrium atmospheric-pressure microplasmas in gases and liquids [9–12,15,16,147]. The materials composition is also very diverse ranging from more traditional carbon- and silicon-based NPs, to oxides, nitrides, metal NPs of binary, ternary, and quaternary elemental compositions. These NPs also range in size thereby exhibiting very different electron confinement properties.

In this section, we only focus on the selected types of crystalline NPs produced using three distinctively different types of plasmas, namely non-equilibrium low-pressure plasmas, gaseous microplasmas, and microplasma-assisted NP synthesis in liquid media. There is some ambiguity regarding the allocation of any particular NPs to the specific dimensionality because only very small NPs qualify as 0D NSs. Therefore, any larger NPs in this subsection are mentioned either from the earlier development perspective or have a significant potential for further size reduction.

4.1.2.1. *Nanocrystals from low-pressure plasmas.* Formation of semiconducting NPs in the plasma bulk has been a subject of intense studies for more than two decades. Recently, the paradigm has shifted from the management of (shapeless, amorphous, agglomerate, etc.) particulate contamination [79] to intentional, quasi-deterministic synthesis of high-quality semiconducting nanocrystals with specific shapes [9]. The mechanisms of the formation of amorphous Si clusters in reactive SiH_4-based plasmas are relatively well understood [148–150].

However, it only recently became possible to use plasma-grown Si nanocrystals in photovoltaic and nanoelectronic devices [151–153]. In addition to the effective and high-rate production of *nc*-Si films (Section 4.1.1), well-shaped and passivated Si and Ge nanocrystals can be produced in the plasma bulk and then deposited on the surface without any significant damage. A Si nanocrystal with a clear-cut cubic shape is shown in Figure 16(a).

This is why the synthesis of faceted nanocrystals in a plasma has attracted strong interest. This process shows several interesting features discussed in Section 2.3 because it is conducted under

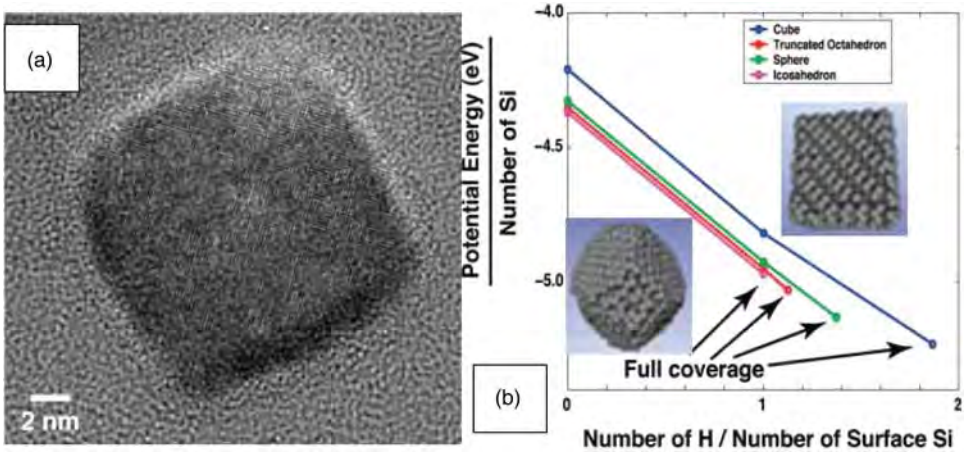

Figure 16. HRTEM image of a plasma-produced Si nanocrystal of a cubic shape (a) [Copyright ©IOP Publishing. Reproduced from [152] by permission of IOP Publishing. All rights reserved]; surface coverage by hydrogen is a key factor in thermokinetic shape selection (b) [Reprinted/adapted with permission from [155], Copyright © 2008 American Chemical Society].

far-from-equilibrium conditions when the developing nano-solid phase effectively exchanges energy with the plasma environment. At equilibrium, the fluxes of the energy received $J_{\mathcal{E}}^{+}$ and lost $J_{\mathcal{E}}^{-}$ by the developing NP are balanced and determine its surface temperature [154]. The integrated incoming energy flux

$$J_{\mathcal{E}}^{+} = J_{\mathcal{E}}^{\mathrm{e}} + J_{\mathcal{E}}^{\mathrm{i}} + J_{\mathcal{E}}^{\mathrm{rec}} + J_{\mathcal{E}}^{\mathrm{ass}} \tag{48}$$

includes contributions from electron $J_{\mathcal{E}}^{\mathrm{e}}$ and ion $J_{\mathcal{E}}^{\mathrm{i}}$ fluxes, as well as the energy influx densities due to recombination of charged species $J_{\mathcal{E}}^{\mathrm{rec}}$ and dissociated molecules $J_{\mathcal{E}}^{\mathrm{ass}}$. The energy flux released by the particle is

$$J_{\mathcal{E}}^{-} = J_{\mathcal{E}}^{\mathrm{rad}} + J_{\mathcal{E}}^{\mathrm{cond}}, \tag{49}$$

where $J_{\mathcal{E}}^{\mathrm{rad}}$ is the energy loss due to radiation and $J_{\mathcal{E}}^{\mathrm{cond}}$ is due to heat conduction through the interactions with neutral gas species. The electron and ion fluxes in Equation (48) are determined by the floating potential on the NP surface V_{float} which is retarding to the electrons and accelerating to the ions. The ion- and neutral recombination terms entering Equation (48) will be used in Section 4.2.3 in the discussion of plasma-enabled inorganic NW synthesis, while all other terms can be found in the original publication [154].

As a result, nanoscale plasma–surface interactions (which are similar to Section 3.3) lead to highly-non-equilibrium NP heating, with their surface temperatures being up to several hundred degrees higher than the neutral gas temperature [152]. These particles can also reside in the plasma long enough (in part due to electric charging and levitation) to change their shape. This shape change happens faster when the surface temperature is higher, similar to Figure 4. The shape formation is controlled by the dynamic changes in the surface energy through the effective surface hydrogenation in a plasma [155].

The shape of the NPs is determined by minimization of the temperature-dependent Gibbs free energy [156]

$$G_{\mathrm{NP}}(T) = G_{\mathrm{NP}}^{\mathrm{bulk}}(T) + G_{\mathrm{NP}}^{\mathrm{surf}}(T) + G_{\mathrm{NP}}^{\mathrm{edge}}(T) + G_{\mathrm{NP}}^{\mathrm{corner}}(T) + G_{\mathrm{NP}}^{\mathrm{def}}(T), \tag{50}$$

which is a sum of contributions from the NP bulk $G_{\mathrm{NP}}^{\mathrm{bulk}}(T)$, surface $G_{\mathrm{NP}}^{\mathrm{surf}}(T)$, edges $G_{\mathrm{NP}}^{\mathrm{edge}}(T)$, corners $G_{\mathrm{NP}}^{\mathrm{corner}}(T)$, as well as planar or point defects $G_{\mathrm{NP}}^{\mathrm{def}}(T)$. As shown in Figure 16(b), the final shape of a Si nanocrystal is determined by the extent of surface hydrogenation, which strongly affects $G_{\mathrm{NP}}^{\mathrm{surf}}(T)$. The cubic shape requires the largest surface passivation of almost two hydrogen atoms per Si atom on the surface. These results obtained through the study of the process kinetics by MD simulations are also consistent with thermodynamic arguments suggesting that the equilibrium shape of a surface-hydrogenated Si nanocrystal is cubic while spherical shapes are ubiquitous if the Si surface is bare [54].

This surface passivation is easier to implement in a plasma where the rates of production of H atoms are typically much higher than in neutral gases, because of very high dissociation rates (e.g. Figure 6(a)), which can be achieved by adjusting the EEDF given by Equation (25) to maximize the number of electrons with the energy above the dissociation threshold of a hydrogen molecule of $\sim$4.53 eV.

Structural stabilization is the next step in the process kinetics described by Equation (18), where the plasma non-equilibrium also plays a critical role. Effective heat exchange between the NPs and background gas lead to the heat extraction and the NPs 'freeze' in the as-formed shape, see Section 2.3. Moreover, fairly large amounts of plasma-dissociated atomic hydrogen help producing another plasma-specific effect of fast recrystallization of the developing crystalline Si network assisted by the rapid and effective incorporation of reactive hydrogen atoms [157].

This is a clear example of the very unique non-equilibrium process conditions enabled by the plasma environment, which in turn lead to the formation of exotic yet very useful (see the discussion about PL emission and surface passivation in Section 4.1.1) nanocrystals that do not normally form in neutral gases under thermal equilibrium conditions. It is possible that QDs (Section 4.1.1) also follow a similar scenario. However, because of the very small size, it is presently very difficult to control their shapes and size distributions.

These advances made it possible to fabricate light-emitting devices using small Si nanocrystals, which are produced, passivated, and then deposited onto glass substrates pre-coated with a transparent conducting oxide layer [153]. Importantly, all the stages of this process are conducted in the plasma gas phase, while the parameters of the resulting nanocrystal film can be effectively tuned to control the emission characteristics. For example, films containing Si nanocrystals with the average diameters of 5.1, 4.1, and 3.1 nm produce PL peak wavelengths of 900, 817, and 707 nm, respectively [153]. Importantly, bulk Si which features an indirect energy bandgap, is not a luminescent material. Intense research efforts by several research groups are underway to explain the mechanisms of PL from plasma-produced Si QDs and one should expect many interesting results in the near future.

4.1.2.2. *Nanocrystals from microplasmas.* Microplasma environments offer a very unique environment for the effective synthesis and functionalization of a large number of NPs and NSs [11]. As mentioned in Section 3.3, microscopic plasma localization is beneficial for the selective treatment (e.g. patterning or functionalization) or NS growth within microscopic spots on the surface. The plasma size can be reduced by producing a discharge within thin channels or reducing the inter-electrode gap. This leads to many interesting physical phenomena which make microplasmas very different from their bulk counterparts.

Most prominently, size reduction to micrometer dimensions makes it possible to maintain thermal non-equilibrium for continuously operated (i.e. not pulsed or transient) plasmas even at atmospheric pressure. When the discharge size decreases, the relative size of the charge-non-neutral areas (e.g. sheaths) increases, which leads to stronger electric fields between the electrodes. Consequently, the EEDF departs from Maxwellian, with the maximum shifting toward higher energies. The electron density also increases, most likely because of the higher rates ν_{en} of the electron–neutral collisions. Moreover, more frequent collisions of neutrals with the electrodes or reactor walls lead to dissipation of a substantial fraction of the energy they receive through collisions with other species. As a result, gas temperature T_g may become much lower than T_e and the plasma is thus thermally non-equilibrium.

Conditions of the energy and species balance lead to the following basic scaling law:

$$T_g \propto (p_0 D^2 \varepsilon n_e \nu_{nheat})^{2/3} \tag{51}$$

which relates the gas pressure p_0, plasma size D, electron density n_e, average energy ε, and the effective rate of collisions leading to the heating of neutrals ν_{nheat}. Equation (51) shows that the gas temperature can be decreased quite effectively ($T_g \propto D^{4/3}$) by reducing the plasma size. This effect is quantified in Figure 17(a) which shows the thermal equilibrium ($T_g = T_e$) and non-equilibrium ($T_g = 0.1T_e$) isotherms [11]. The gray area represents the thermal non-equilibrium regime ($T_e \gg T_g$). More importantly, this regime can be achieved at atmospheric pressure (a horizontal short dashed line) when the plasma size is reduced below a certain threshold. The area of non-equilibrium microplasmas is also indicated by an arrow pointing to the left.

Under such conditions, the plasma is very reactive while remaining cold. This is favorable for the effective generation of reactive species at low temperatures, which is required in most nanoscale processes.

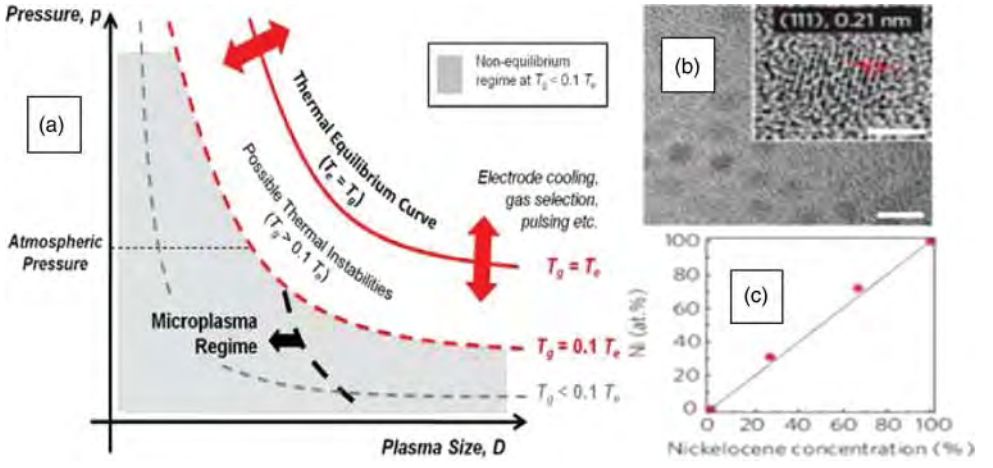

Figure 17. Isotherm boundaries of plasma non-equilibrium and conditions for microplasma regime (a) [Copyright ©IOP Publishing. Reproduced from [11] by permission of IOP Publishing. All rights reserved]. TEM of $Ni_{0.27}Fe_{0.73}$ (b) CNPs for SWCNT growth. Linear dependence of Ni content in CNPs and concentration of nickelocene precursor (c). Panels (b) and (c) are reprinted with permission from [158] [Copyright © 2009 Macmillan Publishers Ltd].

A striking example of this effect is shown in Figure 17(b) and 17(c) where microplasmas of gas mixtures of argon with metalorganic precursors nickelocene and ferrocene were used to synthesize small Ni_xFe_{1-x} CNPs for the growth of SWCNTs [158]. The particle diameter and the lattice spacing were fine-tuned by varying the relative concentrations of Ni and Fe in the alloy. This in turn leads to the ability to control and in particular, significantly narrow down the distributions of chiralities of the SWCNTs grown on these catalysts.

More importantly, the content of Ni in the CNPs increases linearly with the nickelocene flow, see Figure 17(c). This is a clear indication of the very effective precursor dissociation in non-equilibrium microplasmas. Moreover, this linear relationship makes it possible to predict the relative contents of Ni and Fe in the catalyst alloy even before the measurements of the elemental composition.

These non-equilibrium features of gaseous microplasmas have led to a variety of self-organized nanopatterns, with representative examples shown in Figure 12(a), 12(b), and 12(d). Strongly non-uniform electric fields, densities of BUs, surface stresses, and temperature distributions on microplasma-exposed surfaces lead to a variety of interesting self-organization phenomena under far-from-equilibrium conditions. These phenomena in turn not only lead to exotic nanopatterns [159], but also to the many high-quality hierarchical nanoarchitectures of particular interest to several applications including energy storage, optoelectronics, and sensing [160–162].

4.1.2.3. *Nanocrystals from plasmas in liquids.* A variety of nanocrystals have also been synthesized and functionalized using non-equilibrium plasmas in liquids. Strong thermal and chemical non-equilibrium together with the very high densities makes such plasmas suitable for the liquid-phase production of a variety of NPs and hybrid NSs [163,164].

One can thus boost electrochemical reactions in the liquid precursor phase, e.g. in $AgNO_3$ and $HAuCl_4$ solutions to produce high-quality crystalline Ag and Au NPs, respectively [165]. The liquid precursor solution can be used as an electrode of the discharge, while a gas-phase plasma jet as another electrode [166]. In this case, the NPs are produced by the direct reduction

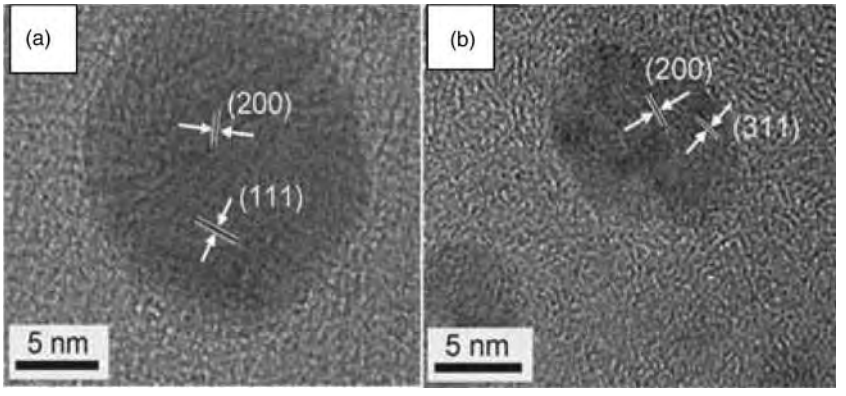

Figure 18. TEM of Ag (a) and Au (b) NPs produced by microplasma reduction of $AgNO_3$ and $HAuCl_4$ precursors, respectively, in thin PVA films [Reproduced with permission from [165], Copyright © 2011 Wiley-VCH Verlag GmbH & Co. KGaA, Weinheim].

of the precursor in the plasma. The NP sizes can also be monitored *in situ* by analyzing their size-dependent plasmonic responses [167]. However, after synthesis, the NPs need to be collected and then transferred to be used in device fabrication.

Using DC microplasmas in contact with water or ethanol, it is possible to tailor the sizes, structure, and surface properties of Si nanocrystals [168]. In this way, the Si nanocrystal surfaces can be passivated with oxygen- or organic-based functional groups. The microplasma treatment in ethanol drastically enhances the PL intensity and also leads to the very strong shift of the PL maximum toward lower photon energies. Importantly, the reported changes are microplasma-enabled and are not possible to reproduce using conventional electrochemistry. Moreover, as the crystal sizes are typically below 5 nm, and the PL exhibits a clear size-dependence, these nanocrystals may also be reasonably considered as 0D Si QDs. This simple microplasma-based process may, therefore, be considered as a potential viable alternative to the high-precision Si QD synthesis in low-pressure plasmas discussed above.

Surface-supported nanocrystals can also be produced by direct plasma exposure of aqueous solutions of metal salts and polymers spin coated onto a substrate [165]. An atmospheric-pressure, room-temperature microplasma jet in an Ar flow was used for electrochemical reduction of metal cations to crystalline Ag and Au NPs shown in Figure 18. The achievable spatial localization of the microplasma was $\sim$30 μm, which is particularly interesting for the development of new micropatterned devices.

This interesting result owes to the strong non-equilibrium, high reactivity, and micrometer spatial localization of microplasmas. The plasma is cold and is suitable for polymer processing without causing any significant damage. The produced Au and Ag NP arrays in turn enable a variety of size-dependent plasmonic effects upon excitation with a suitable light source.

4.1.3. *Nanoarrays*

Regular arrays of small nanodots are of a significant interest for many applications ranging from bio-sensing to optoelectronics and photonics. A certain degree of uniformity of the feature sizes and shapes as well as the pattern regularity over reasonably large surface areas are required in most cases. This can be achieved using either the bottom-up or top-down approaches.

In the top-down approach, pattern transfer using pre-formed masks is usually required. These masks may be prepared by direct feature writing, e.g. using focused ion beams or lasers. However,

it is very difficult to achieve very small feature sizes to meet the demands of the present-day nanofabrication.

Recently, various nanoporous structures proved very effective as etching masks. These structures are typically formed through the customized growth leading to the nanopore or nanochannel formation. In some cases, such as in self-organized porous alumina templates, the dimensions and mutual position of the pores can be tailored. This in turn leads to the possibility of customized transfer of regular patterns to the surface using plasma-assisted RIE.

The pores may also be used for the formation of regular arrays of NPs or nanorods on the surface by evaporating or sputtering solid material through the porous template. This approach is a combination of top-down pattern transfer and bottom-up growth and is very effective to produce regular arrays of CNPs for CNT growth similar to Figure 2(a).

The delivery of building material for the nanoarray formation commonly benefits from plasma-assisted techniques, such as ionized physical vapor deposition (i-PVD) [62], pulsed laser deposition (PLD) [169], and several others. The obvious benefit of using plasmas is in the generation of ion species whose energies and fluxes can be optimized to pass through the nano-channels and reach the substrate. Reactive ions, e.g. CF_x^+ can be used to etch the pattern through the mask opening. On the other hand, metal ions may condense at the substrate surface to produce regular arrays of metal nanodots or nanorods. In this way, using plasmas may extend the lifetime of such templates and also substantially improve the resulting pattern quality because of the very high rates of nanopore clogging when evaporation or thermal CVD are used. Plasma discharges are also effective for the conditioning of the nanoporous templates after the deposition; this can be easily arranged in the same reactor without disrupting the vacuum cycle.

Another option for nanoscale pattern transfer is based on plasma-assisted RIE through an etching mask made by a self-assembled monolayer of nanospheres (Figure 19(a)–(d)). The plasma ions and other reactive species (in this example, mostly CF_x^+ and CF_x) pass through the pores between the closely packed nanospheres in a monolayer and interact with the underlying Si surfaces to form regular hexagonal patterns of small nanopores shown in Figure 19(a) and 19(b) [170]. Numerical simulations of ion deposition [171] show a clear correlation between the positions of the peaks of the ion flux densities upon impact on the surface (Figure 19(c) and 19(d)) and the triangular dips and linear trenches etched on the Si surface (panels (a) and (b)).

Hence, the plasma-produced ion species play a major role in the nanoscale etching. This process can be conducted at room temperature and is suited for nanostructuring of delicate- and temperature-sensitive materials. The ion fluxes and energies can be controlled (e.g. to control the energy released through the ion collisions with the surface) using substrate bias. To mitigate any adverse effects of surface charging, the bias can be tailored as a sequence of pulses; the pulse duration can be adjusted to drive the ions through the pore channels before any significant charge build-up and let the charge dissipate between the ion pulses. In this way, the process throughput and precision can be improved [172].

The second, bottom-up approach leads to the formation of reasonably ordered nanodot arrays through self-organization in randomly nucleated nanopatterns. Indeed, self-organization in non-equilibrium plasmas produced better size and positional uniformity of Ni nanodot arrays on a Si(100) surface compared with the similar neutral gas-based process [173]. The results of numerical simulations of the nanopattern development under conditions of neutral and ionized metal vapor deposition are shown in Figure 19(e) and 19(f), respectively. In case (f), the Si surface is in direct contact with the plasma, while the surface in panel (e) is uncharged. The Ni nanodot arrays on the plasma-exposed surface are more uniform in size and in terms of the local-order measure (LOM)

$$\mathcal{M} = \frac{\sigma_{\mathrm{NND}}}{\bar{\chi}_{\mathrm{NND}}}, \tag{52}$$

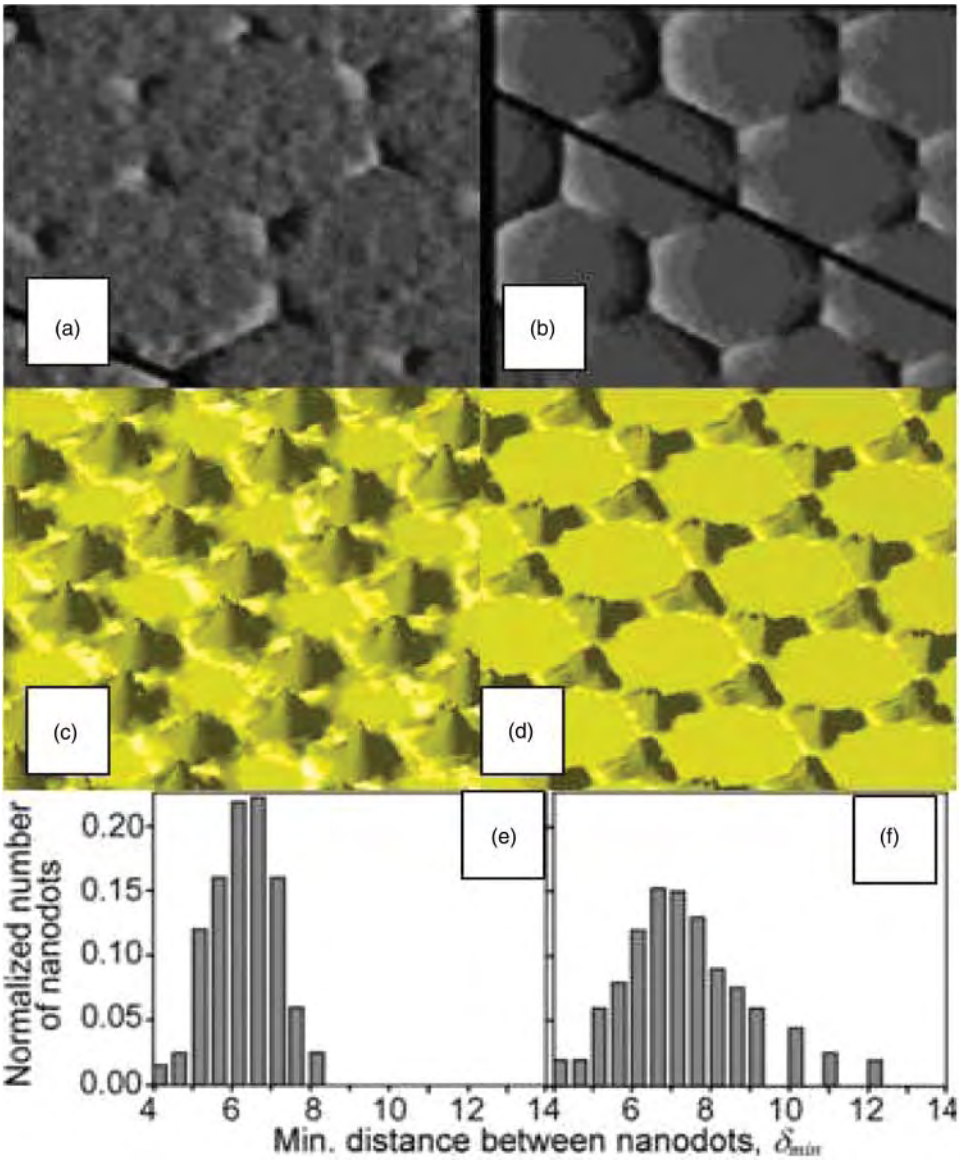

Figure 19. Regular nanopore patterns on Si(111) using self-assembled nanosphere monolayer as a mask for plasma etching (a) and (b) [Reprinted with permission from [170], Copyright © 2004 American Chemical Society]; larger nanospheres produce pattern (a). Numerical simulations reveal correlation between the nanopatterns and micro-topography of ion fluxes (c) and (d) [Copyright ©IOP Publishing. Reproduced from [171] by permission of IOP Publishing. All rights reserved]. Direct plasma exposure improves ordering in self-organized Ni nanodot arrays on Si(100) (e) and (f) [Reprinted with permission from [173], Copyright © 2008 American Institute of Physics].

where $\bar{\chi}_{\mathrm{NND}}$ and σ_{NND} are the mean nearest neighbor distance (NND), and the standard deviation of the NND. The LOM in Equation (52) can be used as a measure of positional uniformity of self-organized nanoarrays.

The observation in Figures 19(e) and 19(f) was explained by introducing 2D patterns of Ni adatom capture zones (Section 2.3). These areas become larger relative to the small nanodot sizes

when the surface is charged. In this case, smaller dots grow faster than the larger ones, eventually leading to the fairly size- and position-uniform arrays. These results suggest that plasma non-equilibrium and complexity lead to better ordering and size uniformity in self-organized arrays of randomly nucleated metallic nanodots. This phenomenon is generic and applies to other materials systems.

Controlled ordering and inter-particle spacing is crucial for the envisaged functional properties of the self-organized nanoarrays. For example, it is imperative to estimate length scales over which a QD interacts with its neighbors. An order of magnitude estimate can be obtained by analyzing the Hamiltonian [174]

$$\mathcal{H} = \frac{\mathbf{p}^2}{2m_e^*} - V_0[e^{-(r_1^2/2R^2)} + e^{-(r_2^2/2R^2)}] \tag{53}$$

of a model system of an electron in two Gaussian potential wells, which approximates a system of two neighboring QDs. Here, m_e^* and $\mathbf{p}$ are the effective mass and momentum of the electron, V_0 is the depth of the potential well, and R is the radius of the both QDs. Furthermore, $r_1 = \sqrt{x^2 + y^2}$ and $r_2 = \sqrt{(x - x_0)^2 + y^2}$, where x_0 is the spacing between the two Gaussian wells (QDs).

The ground states of the model Hamiltonian in Equation (53) show several important features that are applicable to most 2D arrays of QDs [174]. When the distance between the QDs is small, electrons can tunnel between the two dots, resulting in a lower ground state energy. While the distance between the two QDs increases, the system's ground state energy asymptotically approaches the energy of a the ground state of a single QD. The energy also increases when the QD's radius becomes smaller, which is the consequence of a stronger electron confinement.

Therefore, the electronic and optical responses in nanoarrays with the mean inter-dot distances much larger than the estimated electron tunneling length, will be mostly determined by the combined properties of non-interacting individual QDs, their sizes and positioning within the array. In the opposite case, the electron tunneling should be carefully taken into account.

Relating the plasma-process-specific morphological parameters of nanopatterns and arrays to their electronic, phononic etc. properties and consequently, functional performance, is one of the key goals of the plasma nanoscience research. Due to the overwhelming complexity, only phenomenological or process-specific links presently exist. An interesting methodological approach to link the process parameters, morphological, and electronic properties of silicon-germanium ($Si_{1-x}Ge_x$, $0 \leq x \leq 1.0$) NSs produced using plasmas has recently been proposed [175]. In particular, the effect of the QD-morphology-controlled density of the electron trap states on the PL intensity can be approximated as [175]

$$I_{PL} = I_0 \exp(-V_c N_{nr}), \tag{54}$$

where I_{PL} is the actual intensity of the PL emission line affected by quantum confinement and non-radiative recombination via trap states in the QD volume, I_0 is due to the radiative recombination of the electron–hole pairs, and N_{nr} is the volume density of non-radiative recombination centers (traps).

The effect of the surface morphology comes along through the contribution of V_c, which is the volume of confinement of the excited carriers. In other words, V_c is the QD volume, which can be roughly estimated as $\sim h_{rms}^3$, where $\sim h_{rms}$ is the root-mean-square roughness of the surface, which can be obtained, e.g. through the Atomic Force Microscopy (AFM) measurements. Therefore, the plasma control of surface morphology may be used to tailor the electronic and optoelectronic (e.g. luminescent) responses of self-organized nanoarrays.

Dense 3D arrays of Si QDs may enable the as yet elusive multiple exciton generation in the photovoltaic photon energy conversion [176,177]. However, the degree of spatial uniformity of

such arrays still requires improvement. The QD arrays can also form on plasma-exposed surfaces, e.g. Ge QDs produced using germane-based precursors [178]. An interesting hybrid structure made of SiC nanoislands with dense nanocrystalline inclusions was also reported [179].

4.2. *1D nanostructures*

Plasmas are particularly suitable for the synthesis of many 1D NSs, which commonly leads to the pronounced vertical alignment, substantially reduced growth temperatures, higher growth rates, and in many cases also superior structural properties and performance in applications compared with the equivalent thermal processes. Given the very large number of relevant reports, we will only use a few representative examples to show a few salient features and comment on the most important physics involved. This subsection considers 1D carbon NSs (Section 4.2.1), silicon (Section 4.2.2), and other inorganic (Section 4.2.3) NWs.

4.2.1. *1D carbon nanostructures*

Figure 20 shows typical examples of 1D carbon NSs produced using low-temperature plasmas, namely carbon nanofibers (CNFs) (a–c), MWCNTs (d) and (e), and a thin (∼0.75 nm) SWCNT (f). Many plasma-specific effects related to SWCNT nucleation and growth have been discussed in previous sections. This is why the main focus here is on CNFs and MWCNTs.

In a plasma, the CNFs and MWCNTs more commonly grow in a tip-led mode [182]. In the early growth stage, the initially semi-spherical metal CNPs reshape and detach from the surface as the nanotube/nanofiber walls nucleate; this is evidenced by *in situ*, real-time transmission electron microscopy (TEM) [183]. The formation of MWCNTs proceeds through the formation of step terraces on the catalyst surface. This surface structure is metastable and has a relatively high surface energy. Nucleation of carbon chains on these terraces minimizes the surface energy and eventually leads to the formation of straight nanotube walls, which support and lift the CNP as the growth proceeds. The number of the terraces presumably determines the number of the walls. The CNP elongation and detachment from the substrate is facilitated by surface charges and is one of the reasons for the preferential growth of MWCNTs and CNFs in the tip-led mode in PECVD [5].

Therefore, the process kinetics and non-equilibrium, as well as the metastable states play the key role in the selectivity of the nanotube growth mode. Moreover, fast carbon material extrusion through the catalyst (Section 3.4) give a stronger upward push to the CNP to detach from the surface and determines its reshaping.

The location of the CNP on top of the nanotubes or nanofibers largely determines the nature of the nanoscale plasma–surface interactions. Although these interactions mostly follow the basic trends discussed in Section 3.3, there are a few distinctive features of these interactions.

The most notable feature is the effect of direct heating or even possible cooling of the CNP through its energy exchange with the ions and neutral species in the plasma. The ion focusing by the sharp tips of the CNTs/CNFs and recombination of the plasma species lead to the heating of the CNPs on their top, quite similar to the heating effects of Si nanocrystals considered in Section 4.1.2. Since the length of the plasma-grown nanotubes or nanofibers may be a few tens or even hundreds of micrometers, the difference between the temperatures of the CNP T_{CNP}, the top surface of the supporting substrate T_{sub}, and the substrate holding platform T_{sh} can be quite significant. These temperatures are related through [184]

$$T_{\mathrm{sh}} = -T_{\mathrm{sub}}^{0} \ln\left[\exp\left(-\frac{T_{\mathrm{sub}}(T_{\mathrm{CNP}})}{T_{\mathrm{sub}}^{0}}\right) - f(d, T_{\mathrm{CNP}}, \xi_{\mathrm{Si}}, \xi_{\mathrm{C}})\right], \tag{55}$$

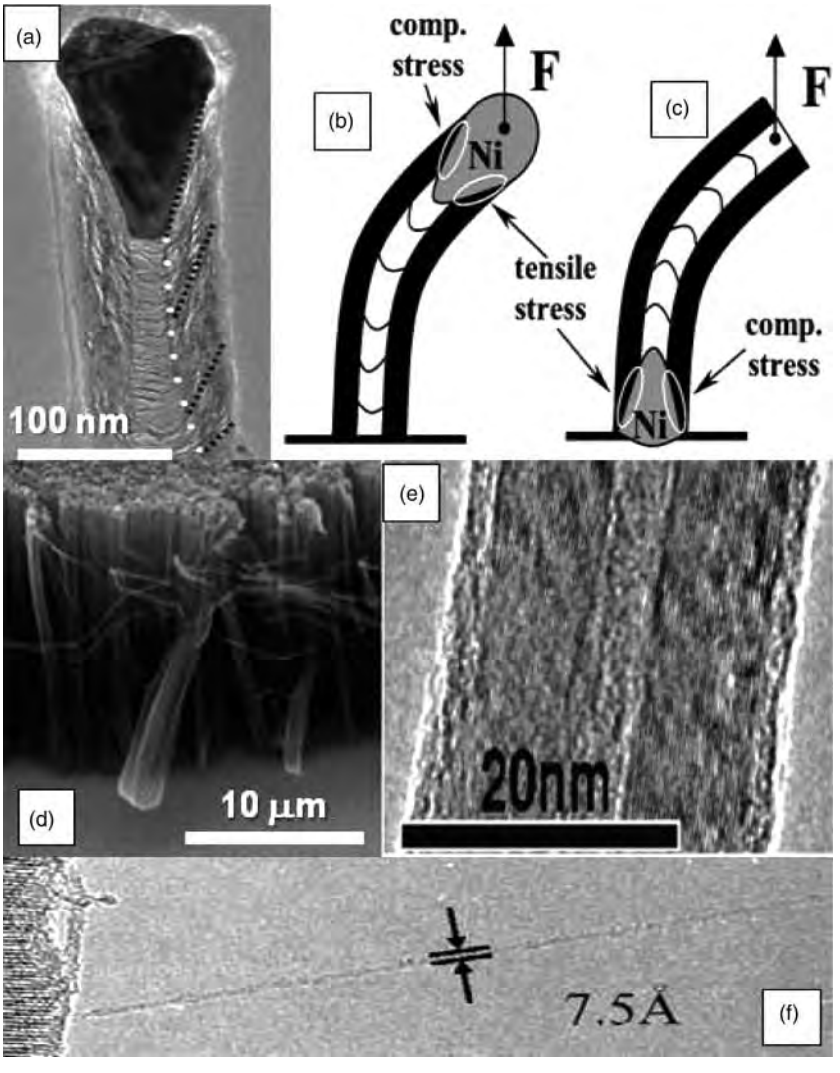

Figure 20. HRTEM image of a CNF produced in a fast (5 min) plasma process shows cone-like catalyst and bamboo-like walls (a) [Reprinted with permission from [180], Copyright © 2004 American Institute of Physics]. Mechanism of vertical alignment of CNFs in a plasma (b) and (c) [Reprinted with permission from [116], Copyright © 2001 American Institute of Physics]. Scanning electron microscopy (SEM) and HRTEM images of MWCNTs grown by catalyzed PECVD (d) and (e) [Copyright ©IOP Publishing. Reproduced from [10] by permission of IOP Publishing. All rights reserved]. A TEM image of a SWCNT grown by PECVD on zeolite support (f) [Reprinted with permission from [181], Copyright © 2003 Elsevier].

where $T^0_{\rm sub}$ is the temperature of the external substrate heating in the absence of the plasma, while $\xi_{\rm Si}$ and $\xi_{\rm C}$ are the heat conductance of the Si substrate and the carbon NS, respectively.

One important conclusion from Equation (55) is that the difference

$$\Delta T = T_{\rm CNP} - T_{\rm sh} \tag{56}$$

between the temperatures of the catalyst and the substrate holder can in some cases be as high as ∼100°C. This result is consistent with numerous experimental observations [5,10] and is valid

under conditions when the effect of the ion bombardment is particularly important while the temperature of the operating gas T_g is higher than T_{CNP}. In this case, the CNP receives heat through the impacts of both ions and the hot neutral species.

However, in the opposite case when $T_{CNP} > T_g$ and the effect of ion collisions with the CNP is weak, the temperature of the substrate holder may be even higher than T_{CNP}. Consequently, some energy supplied to the substrate heater would unnecessarily be wasted to heat the cold background gas while the CNP heating may be ineffective. This in turn may lead to the much reduced NS growth rates and even possibly to the growth termination, e.g. due to the catalyst poisoning because of the insufficient carbon diffusion at reduced temperatures.

This conclusion points at the crucial importance of controlling energy consumption in nanoscale synthesis and in particular, reducing the unnecessary energy waste. Ultimately, only the CNP on top of the CNF should be heated to sustain the NS growth, and not the entire substrate, the substrate holder, or the reactive gas in the entire growth chamber. Implementation of this effect may be a very significant advance toward energy- and atom-efficient nanotechnology of the future.

Although it is presently not clear how to implement this idea in practice (e.g. in large-area nanotube growth), there are some indications on the principal possibility of this effect. For example, by heating the nanotubes developing in the tip-led growth mode externally by a laser beam, it is possible to drastically reduce the temperature of the external substrate heating to $\sim$350°C [185] to make the growth process compatible with the present-day integrated circuit technologies. Further efforts in this direction are therefore warranted in the near future.

CNFs commonly feature a bamboo-like structure shown in Figure 20(a). In this typical example, the CNP has an elongated near-conical shape. The NS walls nucleate as stacked conical layers on the catalyst as can be seen from panels (a)–(c). Kinetics-wise, it means that the rates of carbon atoms delivery, hopping, and rearrangement on the CNP surface favor the formation of fairly large GMLs that encage the lower, elongated section of the CNP. Several plasma-specific effects, such as ion-assisted production of carbon atoms, localized catalyst heating through ion impact, energy exchange between the CNF and the environment, the presence of hydrogen in the precursor gas mixture, and several others, play a critical role [184,186].

The mechanisms of vertical alignment during the nucleation stage of SWCNTs in a plasma were discussed in Section 3.4. For larger NSs such as CNFs or MWCNTs, additional factors such as stress generation and relaxation also play a major role as sketched in Figure 20(b) and 20(c). When a 1D NS grows along the direction of the electric field in the plasma, the electric field creates a uniform tensile stress across the interface between the catalyst and the nanofiber; this stress distribution becomes non-uniform if the nanofiber bends [116]. Interestingly, in panels (b) and (c), the stresses are distributed in the opposite way which leads to the restored CNF alignment only in the case of the tip-led growth, which is most common for plasma-based processes.

The pronounced vertical alignment of the plasma-produced CNTs, nanofibers and some other 1D NSs is important for many applications [187]. One of the most common examples is a strong enhancement of the electron field emission (EFE) from the CNT/CNF arrays which is commonly described by the Fowler–Nordheim equation [188]

$$J_{em} = \frac{\gamma_1(\beta E)^2}{\Phi} \exp\left(-\frac{\gamma_2 \Phi^{3/2}}{\beta E}\right), \tag{57}$$

where J_{em} is the emission current density, Φ is the work function, and $\gamma_{1,2}$ are geometry-related constants. Here, β is the field enhancement factor which can be very high (e.g, $\sim 10^3$ or even higher) for the CNTs and nanofibers. Moreover, additional ordering of the CNT/CNF arrays also prevents undesired destructive EFE interference due to the NS crowding [189].

Approximately a decade ago, the EFE was considered as one of the key applications of these high-aspect-ratio NSs. However, the present-day range of applications of these NSs is much broader and involves areas as diverse as energy, health, environment, and security [14,187,190].

For many years, it was believed that metal NPs are absolutely essential to catalyze the growth of 1D carbon NSs. However, the first reports on the synthesis of SWCNTs used non-metallic catalysts, such as zeolite microporous materials (Figure 20(f)) [181]. Oxides and carbides (e.g. SiO_2, SiC, etc.) also showed the catalytic activity to produce CNTs.

However, any catalyst ultimately needs to be avoided to enable integration of carbon NSs into the presently Si-dominant nanodevice platform and also to minimize the unnecessary yet inevitable Ohmic losses during the electron current conduction in nanoelectronic circuitry. Hence, dielectric catalysts such as oxides or nitrides are even more detrimental than conventional metallic CNPs. Similarly, the CNT growth rates are usually lower when non-metallic catalysts are used. Moreover, the use of toxic and expensive metals raises continuously escalating environmental, cost-, and energy-efficiency concerns.

Recently, it was shown that a direct exposure of features of arbitrary shape (e.g. lines and dots) written on a Si surface to high-density plasmas of CH_4-based gas mixtures leads to the high-rate, catalyst-free growth of vertically aligned MWCNTs [191,192]. This is only possible when the plasma is in a direct contact with the substrate; no nanotubes are produced when thermal CVD or remote plasmas are used. This is an interesting manifestation of a plasma-enabled phenomenon. The mechanism of this effect involves nucleation of carbon walls on semi-molten small Si features accompanied with the formation of the segregated SiC nanophase, which in turn catalyzes the CNT nucleation.

Moreover, it was possible to resolve the nanotube nucleation events on the small Si nanofeatures [192]. This is an important advance because of the intrinsic common difficulty of the plasma-based NS growth experiments which require pressures that are orders of magnitude higher than during the real-time HRTEM or low-energy electron microscopy observations of nucleation processes under ultra-high-vacuum conditions.

Nevertheless, it is clear that both oxide and metal catalysts can be eliminated and the plasma exposure enables a catalyst-free integration of carbon NSs into Si-based nanodevices. However, a significant reduction of the process temperature is still required to meet the nanodevice temperature tolerance requirements. This is why such plasma-enabled, catalyst-free growth processes offer very interesting prospects for future studies.

4.2.2. *Silicon nanowires*

Inorganic NWs are among the most advanced building blocks of nanoelectronic, optoelectronic, energy conversion and sensing devices [193]. Silicon NWs are of particular interest to Si-based device platforms, not only because of the obvious compatibility and epitaxy considerations, but also because they offer several highly unusual properties which are difficult to achieve using bulk Si or Si NPs. To materialize these benefits, it is crucial to maximize the quantum confinement effects in the NWs.

Reducing the NW thickness to the low-nm range is an obvious way to achieve this. However, a typical thickness of the majority of the reported Si NWs is a couple of tens of nanometers. 1D electron transfer is extremely appealing for electronics. However, the NWs should not only be single-crystalline, but also have a regular crystallographic structure with the pre-determined orientation. This structure and orientation should be selected to enable the fastest possible electron and hole transport. This is critical for the next-generation ultra-fast switches and computer logic devices. Unfortunately, it is very challenging to achieve all these properties in the same NW array to materialize their promises.

Indeed, common thermal catalytic growth based on a Vapor–Liquid–Solid (VLS) mechanism and a tip-led mode usually results in fairly thick (several tens of nm) Si NWs. These NWs often show a cubic structure and grow in (111) direction. A major challenge is to grow Si NWs with the more non-equilibrium wurtzite structure and also to achieve the preferential (110) growth at low, nanodevice-benign temperatures.

Moreover, (110) NWs are much thinner than (111) NWs and their VLS nucleation barriers increase due to the GT effect. As we have discussed in Section 3.4, the GT effect leads to higher solubility of BUs as the catalyst size decreases. Smaller CNPs also produce higher stress levels, which leads to strong outward BU fluxes. Hence, it becomes more difficult to nucleate the Si layers at the interface between the CNP and the substrate. Higher process temperatures and pressures are thus needed, which is not only unwelcome from the nanodevice integration perspective, but also because of the unnecessary waste of energy and matter.

A similar waste happens when Si NWs are thinned using surface oxidation followed by the removal of SiO_2 from the surface. This process is also very difficult to control and there is a real danger to oxidize and hence, completely destroy the whole NW [194].

Figure 21 shows examples of the plasma processes which help solving these problems. Panel (a) shows a crystalline ∼10 nm-thin Si NW grown by Au catalyst-assisted PECVD [195]. In purely thermal CVD, the NWs are much thicker under similar process conditions [196–198]. These observations are explained by multiscale, multi-phase numerical modeling which demonstrates that the nucleation threshold and the minimum thickness of the Si NWs can be substantially reduced (at the same external heating temperature of the substrate) when a plasma is used [199]. Nanoscale plasma–surface interactions and localized heating also mitigate the adverse GT effect and result in much thinner Si NWs at much lower temperatures and pressures than in similar thermal CVD processes.

Si NWs with wurtzite structure can also be synthesized by PECVD, as confirmed by the selected area electron diffraction pattern in Figure 21(b). These NWs were produced through the *in situ* generation of indium catalyst droplets and subsequent growth on an indium tin oxide substrate [196].

Panels (c)–(h) in Figure 21 show that even a short (∼ 2.5 min) exposure to the plasma is very effective to simultaneously improve the selectivity of the NW growth direction and reduce their thickness. Indeed, starting from the same Au CNP pattern with the size distributions shown in (c), purely thermal CVD predominantly produces Si(111) NWs with the average thickness of ∼60 nm (d), whereas thin (∼20 nm) and more size-uniform Si(110) NWs grow in the plasma-enhanced process (e). Moreover, the frequency of Si(110) NWs (see the SEM image in the inset of panel (h)) is almost two orders of magnitude higher compared with the much thicker (∼50–60 nm) Si(111) NWs imaged in the inset of panel (g).

This striking experimental observation can be explained by considering the thermokinetic effects of nanoscale plasma–surface interactions sketched in Figure 21(f)–(h) [200]. These effects lead to the much larger difference in the Gibbs free energies between the (111) and (110) growth directions

$$\Delta G = \Delta G^{(111)} - \Delta G^{(110)} \tag{58}$$

in PECVD compared with purely thermal CVD. In other words, the (110) becomes a clearly preferential growth direction in the plasma, which explains the experimental observations [197].

The difference in the Gibbs free energies (58) can be used to estimate the diameter of the Si NW

$$d_{\mathrm{NW}} = 2\frac{\Delta G - [\gamma_{\mathrm{SV}}^{(111)} - \gamma_{\mathrm{SV}}^{(110)}]\Delta S}{(\gamma_{\mathrm{LS}}\delta)^{(111)} - (\gamma_{\mathrm{LS}}\delta)^{(110)}} \tag{59}$$

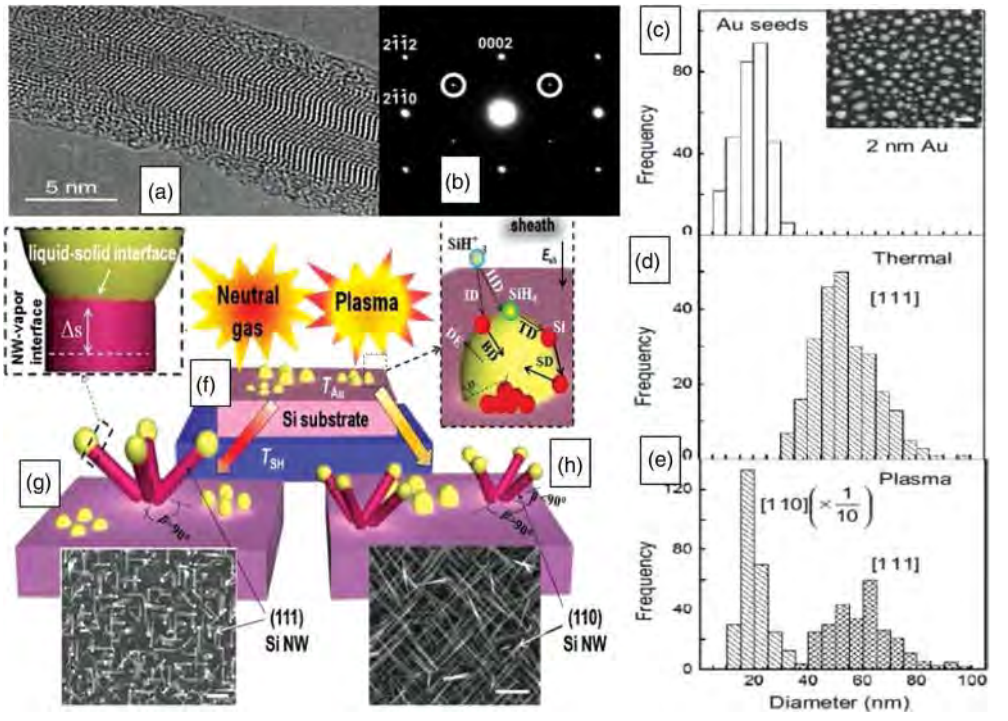

Figure 21. HRTEM of a thin crystalline Si NW grown by PECVD (a) [Reprinted with permission from [195], Copyright © 2003 American Institute of Physics]. Diffraction pattern of a wurtzite Si NW (b) [Reproduced from [196] by permission of the Royal Society of Chemistry]. Size distributions and SEM of Au CNPs shown in the inset, scale bar is 50 nm (c); size distributions of Si NWs grown in thermal (d) and plasma-assisted processes (e); insets in panels (g) and (h) show SEM of Si(111) and Si(110) NWs grown in thermal- and plasma-assisted processes, respectively (scale bars are 500 nm); the frequency of much more abundant Si(110) NWs in (e) is multiplied by 0.1 [197]. Elementary processes on Au CNP (top right), liquid–solid interface area (top left), growth experiment (f) and the outcomes in thermal (g) and plasma (h) processes [200]. Panels (c)–(e) and insets in panels (g) and (h) are reproduced with permission from [197] [Copyright ©2007 Wiley-VCH Verlag GmbH & Co. KGaA, Weinheim]. Panels (g)–(h) are reproduced with permission from [200] [Copyright © 2013 American Chemical Society].

which is assumed to be equal to the critical diameter of the Si monolayer formed at the interface between the catalyst and the substrate. Here, γ_{LS} and γ_{VS} are the surface energies for the liquid–solid and NW–vapor interfaces, respectively, with the superscripts denoting the NW crystallographic orientation. Parameters $\delta^{(111)}$ and $\delta^{(110)}$ quantify the cross-section geometries of the (111) and (110) growth directions observed in the experiments [201,202], and ΔS is the thickness of the NW surface just beneath the interface denoted in Figure 21. As mentioned above, the NW thickness given by Equation (59) is typically clearly smaller in PECVD compared with the equivalent neutral gas-based processes.

These plasma-specific effects require a more thorough study, e.g. a combination with the thermodynamic stability arguments and extension to a larger number of crystallographic orientations. For more details about the various growth approaches, thermodynamics, and electronic properties of Si NWs, please refer to the recent review [203]. In the following subsection, more plasma-specific effects in the synthesis of inorganic NWs of binary solids will be considered.

4.2.3. *Other inorganic nanowires*

The outstanding ability of low-temperature plasmas to dissociate and excite numerous molecular and radical species under conditions of strong thermal non-equilibrium has enabled many unique opportunities in nanoscale synthesis and processing. In particular, it became possible to dissociate reactive oxygen and nitrogen gases in the ionized gas phase while keeping the temperature of working gas low. In this subsection, we will mostly focus on the processes where interaction of oxygen plasmas with solid surfaces leads to the fast production of large amounts of high-quality oxide NSs with representative examples shown in Figure 22(a)–(e).

One of the most promising approaches toward large-scale plasma-assisted synthesis of oxide NWs is based on a direct exposure of solid (e.g. metal) surfaces (e.g. thin foils) to reactive oxygen plasmas [205,206]. This process has been demonstrated for a large number of materials systems (e.g. Fe_2O_3, Nb_2O_5, V_2O_5, CdO, CuO_2, SiO_2, WO_2, WO_3, etc.) and is enabled by the interactions of ionic and (excited) neutral oxygen species with the solid surface and does not rely on any external heating [207]. The top layer of the surface where the NSs nucleate is heated through the recombination of the plasma species.

Oxygen atoms also play a role of BUs and combine with metal atoms to form metal oxides. Therefore, the rates of production of oxygen atoms determine both the surface heating and the oxide phase formation. However, well-defined NSs only appear when a delicate balance between these two factors is reached. Indeed, too strong heating may easily lead to the evaporation of the entire thin metal foil. On the other hand, excessive (e.g. too fast) delivery of oxygen may lead to the uniform oxidation of the entire surface (or even the entire film) rather than to the NS formation.

Therefore, the clue to explain the nucleation of thin NWs on metal surfaces exposed to reactive oxygen plasmas is again in *nanoscale* plasma–surface interactions. The nanometer surface morphology appears to be critical for the NW nucleation. The most delicate moment in this process is a very gentle heating of the surface layer to the temperature which is slightly below the melting point of bulk metal, yet sufficient to at least partially melt small nanoscale surface features. This is indeed possible since the melting temperatures decrease as the NPs get smaller. For example, while the melting point of bulk Si is ∼1412°C, 2 nm-sized NPs can melt at only ∼300°C [208].

The surface heating is entirely due to the plasma and it is believed that the heat transfer is dominated by the surface recombination of ion and neutral species. The associated energy influx densities are [154]

$$J_{\mathcal{E}}^{\mathrm{rec}} = \Sigma_k j_k^i (E_k^{\mathrm{ion}} - E_k^{\mathrm{diss}}) \tag{60}$$

for the surface recombination of ionic species k and

$$J_{\mathcal{E}}^{\mathrm{ass}} = \gamma_k N_k \sqrt{\frac{8 k_{\mathrm{B}} T_{\mathrm{gas}}}{\pi m_k}} E_k^{\mathrm{diss}} \tag{61}$$

for the associative recombination of neutral radicals on the surface. In Equations (60)–(61), j_k^i is the ion flux, E_k^{ion} and E_k^{diss} are the ionization and recombination energies, respectively. Here, N_k is the density of recombining species (mostly oxygen radicals in the examples considered in this section), m_k is their mass, and T_{gas} is the gas temperature. The coefficient γ_k accounts for the recombination probabilities of different plasma-generated species on the surface.

This localized surface heating produces small nanoscale surface features where metal atoms are not so rigidly stuck in their lattices, while oxygen atoms can penetrate easier compared with the surrounding solid material. Consequently, these features may be saturated with oxygen and small oxide nuclei may form.

It is important that the amount of oxygen atoms matches the amount of metal atoms available for bonding. Otherwise, uncontrollable recombination of loose O-atoms may lead to the undesirable

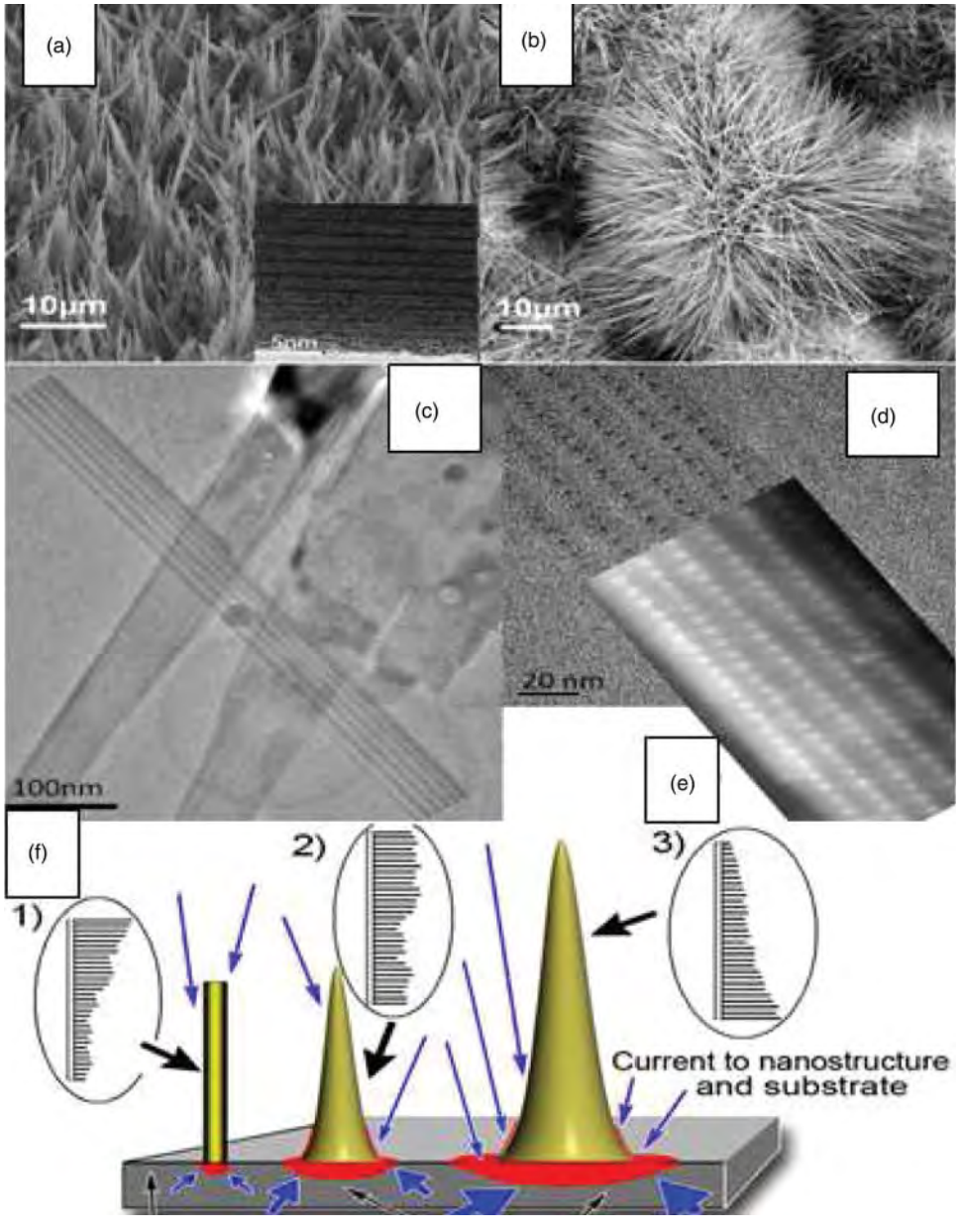

Figure 22. 1D metal oxide NWs grown using *plasmoxy nanotech* approach [15]: (a) Nb_2O_2; (b) β-Ga_2O_3; and (c–e) MoO_x imaged by SEM and HRTEM. Shape of Fe_2O_3 NWs is controlled by ion flux distributions (f) [Reprinted with permission from [204], Copyright © 2009 American Institute of Physics]. Panels (a)–(e) reproduced from [15] by permission of IOP Publishing. Copyright ©IOP Publishing. All rights reserved.

surface overheating as well as possible uniform and deep oxidation. This condition is a reflection of one of the basic conditions for the successful formation of NSs on plasma-exposed surfaces, namely, a delicate balance between the demand and supply of BUs and energy discussed in Section 3.

After the nuclei are formed, the 1D NSs are shaped under strongly non-equilibrium conditions as shown in Figure 22(f). At this stage, plasma-specific effects continue playing a prominent role. Many of the NWs that form through the direct surface exposure to oxygen plasmas grow by basal attachment of newly nucleated layers [87]. If the base does not widen, the NWs grow straight upwards (sketch 1 in panel (f)) and sharp nanoneedle-like 1D structures form. If this widening takes place, the NW base becomes larger during the growth process and high-aspect-ratio conical structures form (sketches 2 and 3 in panel (f)). Interestingly, this effective control of the NW shape can be implemented by controlling the microscopic ion flux distributions along the surfaces of the substrate and the growing NSs.

As was explained in Section 3.2, the sheath width can be controlled by the plasma density and external bias; the ratio of the sheath width to the NW length determines the microscopic profile and non-uniformity of ion deposition. In the example shown in Figure 22(f) the process parameters (e.g. surface bias) were varied to increase the ion flux and also to vary its distribution over different areas on the NS and substrate surfaces [204]. In the first case, the ion flux was predominantly deposited to the top section of the NW; the hot base did not widen and straight nanoneedle-like structures formed. When a significant fraction of the ion flux was deposited close to the NS base, the hot basal area widened and nanoconical structures developed.

Importantly, this shape selectivity is enabled by non-equilibrium process kinetics and nanoscale plasma–surface interactions, quite similar to the examples considered in Sections 4.1.2, 4.2.1, and 4.2.2. These strong non-equilibrium conditions lead to very high growth rates of the NWs. It typically takes only up to a few minutes to grow a fully developed NW with the length of several tens of micrometers while fairly similar thermal- or catalyst-assisted processes usually last several hours and even longer [209]. This plasma-enabled process is single-step, fast, energy-efficient, environment-friendly, and does not need any catalyst or pre-formed patterns. Combined with the good NW quality, it offers exciting prospects in various applications such as gas sensing, energy conversion, etc. [210,211].

Other plasma-based processes, such as PECVD, catalyst-assisted growth, plasma flight-through synthesis, as well as hybrid approaches have also been successfully used for high-rate, large-quantity production of high-quality inorganic NWs, not merely limited to metal oxides [193,211,212]. For example, ultra-fast kinetics and non-equilibrium conditions in the gas phase of dense MW plasmas enable bulk production of SnO_2, ZnO, TiO_2, and Al_2O_3 NWs [213]. The NWs nucleate on metal NPs while they move through the high (from a few Torr to atmospheric)-pressure $Ar+O_2$ plasma jet. The growth process is very fast (fractions of a second) and can lead to NW production with rates $\sim$5 kg/day. This unique high-throughput process is not possible without the plasma. To enable partial NP melting needed for the NW nucleation, the heating should be very effective during the NP flight through the plasma.

A comparative analysis of the effects of heat transfer to the NPs by conduction, convection, radiation, collisional heating, and surface reactions suggests that the latter mechanism is dominant. The most important reactions involve recombination of the plasma-produced oxygen and hydrogen radicals, as well as metal oxidation on the surface, similar to the growth of surface-supported NWs discussed above. This similarity of the plasma-specific effects is further evidenced by the recent synthesis of TiO_2 NWs by the direct exposure of Ti foils or powders to atmospheric-pressure microplasmas under fairly similar conditions as in the previous example [214].

The NP size is also critical because the NW nucleation ceases above certain threshold when the plasma heating becomes less effective. The nucleation of NWs can be explained using thermodynamic stability analysis which relates the supersaturation levels and the sizes of critical nuclei to the NP temperature determined by the MW input power and other discharge conditions [215].

There are several opportunities in this area, in particular, in deeper understanding of the underlying mechanisms of the energy and matter exchange in localized plasma–surface interactions,

nucleation, and thermokinetic selection of the growth direction, shape selectivity, and control during the growth (e.g. maintaining 1D growth avoiding the formation of 2D nanowall-like structure) [216], tailoring the internal structure (e.g. vacancies and porosity), customizing the electronic and chemical properties for targeted applications, and several others.

Importantly, this class of nanoscale objects is a clear manifestation of a uniquely plasma-enabled phenomenon which certainly deserves further in-depth studies. For more information about the physical properties, characterization, and applications of inorganic NWs, please refer to the recent monograph [193].

4.3. *2D nanomaterials*

As the dimensionality of nanoscale objects increases, the nanoscale plasma–surface interactions also change and are determined by the 2D structure and morphology of these objects. In this section, we consider graphene, graphene oxide (GO), and GNRs (Section 4.3.1), vertically aligned 2D carbon structures such as carbon nanowalls (CNWs) and GNSs (Section 4.3.2), and also some 2D NSs of other solid systems (Section 4.3.3). Generally, numerous plasma-based processes have been used not only to grow these 2D structures, but also to modify, shape, functionalize, activate, decorate, and condition them.

4.3.1. *Graphene, graphene nanoribbons, and graphene oxide*

4.3.1.1. *Graphene.* 2D graphenes are made of a single or just a few layers of sp^2-networked carbon atoms [217]. Graphenes feature many truly unique properties such as exceptional electron and heat conductivity, toughness, optical transparency, chemical reactivity, etc., which makes them ideal for a broad range of applications in nanoelectronics, photonics, sensing, and several other areas. However, single-layer graphene shows semi-metallic properties and bandgap opening is one of the major present-day challenges on the way of its widespread applications.

The ultra-fine, atomic-thin structure of graphene makes its synthesis and processing very delicate. To synthesize such a material on the (e.g. catalyst) surface, one needs to assemble a monolayer (or a just a few layers) of carbon atoms. Moreover, the monolayer should be stable and defect-free. Hence, the amount of material that needs to be delivered to the surface to produce graphenes should be small and the monolayer nucleation should be fast and take place over the entire surface area.

The first requirement is similar to the SWCNT nucleation (Section 3.4), whereas the second one is different and applies to flat catalyst surfaces. This is why very high temperatures (typically well above 800–900°C) and metal catalysts such as Pt, Co, Ni, Cu, Ru, Ir, and some others are usually required. Graphene growth using a suitable crystalline face has been demonstrated. However, significant difficulties (e.g. uniformity of the number of layers in different areas) still remain while using polycrystalline catalysts, which are very attractive because of the obvious lower material cost.

Mechanism-wise, there are two common types of graphene growth on catalysts with high (e.g. Ni) and low (e.g. Cu) carbon solubility. In the first case, carbon atoms first saturate within the catalyst layer and then segregate toward the top surface to nucleate a GML. When the solubility is low, the graphene nucleation takes place entirely on the surface. In thermal CVD, both processes require very high heating temperatures. The nucleated graphene then needs to be separated from the supporting catalyst, which is often commonly achieved by completely etching the catalyst, or alternatively, using specific chemicals that unbind the graphene from the growth substrate. Achieving large-area, single-layer graphene with a small number of large 2D crystalline grains, and ultimately, the single-crystalline structure is a significant challenge [218,219].

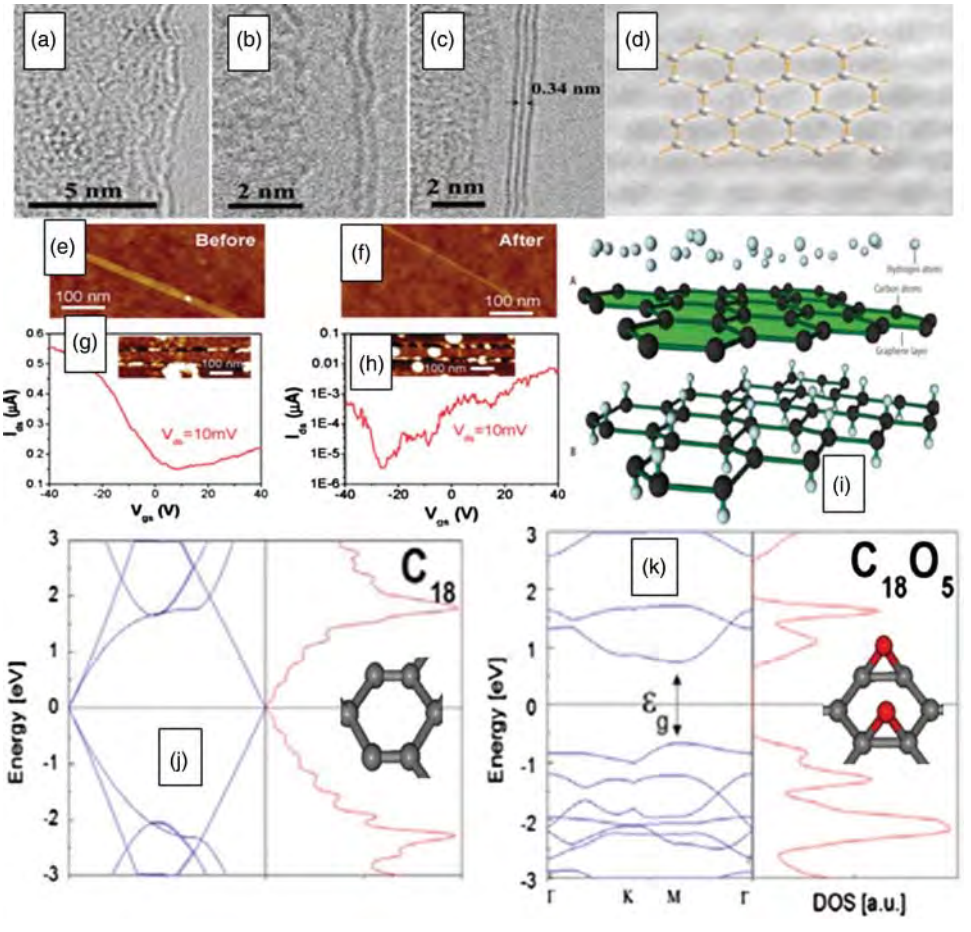

Figure 23. Single-layer (a), bi-layer (b), and tri-layer (c) graphenes on polycrystalline Co film grown by PECVD [Copyright ©IOP Publishing. Reproduced from [220] by permission of IOP Publishing. All rights reserved]. HRTEM image of graphene (d) synthesized by remote PECVD on Ni catalyst [Reprinted with permission from [221], Copyright © 2010 American Institute of Physics] AFM images of GNRs before (e) and after (f) etching in H_2 plasmas; nanodevice performance of these GNRs (g) and (h) [Reprinted with permission from [222], Copyright © 2010 American Chemical Society]. Reversible hydrogenation of graphene surfaces leads to non-conducting, bent graphane [223] (i) (sketch reprinted from [224] with permission from AAAS). O_2 plasma exposure leads to attachment of O-atoms to carbon network and bandgap opening of graphene (j) and (k) [Copyright ©IOP Publishing. Reproduced from [225] by permission of IOP Publishing. All rights reserved].

Plasma-assisted growth and processing of graphenes is a relatively new area with a relatively small number of relevant publications. The reason is that it is usually quite challenging to simultaneously deliver small amounts of material and enable fast and uniform nucleation, while avoiding any damage due to the ion bombardment. Nevertheless, there are several examples of successful plasma-based growth of graphenes, see Figure 23(a)–(d). TEM images in panels (a)–(c) show one to three layers of graphene synthesized on a polycrystalline Co film by a RF PECVD in a mixture of CH_4, H_2, and Ar gases. This process is extremely fast and requires only 40 s to produce the graphenes at a relatively low temperature of 800°C [220].

In another example in panel (d), the amount of carbon material involved in the synthesis was reduced using a remote plasma configuration [221]. This approach is quite similar to the synthesis of SWCNTs (Section 3.5). In this example, single- and few-layer graphenes grow on Ni(111) single crystals and also polycrystalline nickel films. A special advantage of using remote plasmas in the growth of graphenes is to eliminate the effect of the plasma electric field, which on the one hand facilitates the formation of a nanotube cap (Figure 9(d)) and accelerates the plasma ions on the other. Even though the plasma was remote to the growth substrate, a major reduction (from ∼1000°C in thermal CVD to only ∼650°C in PECVD) of the process temperature was reported [221]. Moreover, the growth process was very fast lasting only ∼1 min. These and several other results suggest that the plasma-based graphene growth is both versatile and scalable.

Significant caution toward using plasmas in the synthesis and processing of a so delicate 2D nanomaterial as graphene naturally stemmed from the possible adverse effects of the ion bombardment. However, it was recently demonstrated that minute traces of polymer impurities can be removed from graphene surface by exposing it to low-density ($\sim 8.5 \times 10^8$ cm^{-3}) remote Ar plasmas [226]. Importantly, this room-temperature treatment does not damage the graphene structure and, moreover, is capable to restore its pristine defect-free state. This process is compatible with Si-based nanoelectronics and can be regarded as a viable alternative to thermal vacuum or electric current annealing or wet-chemical processing.

On the other hand, graphene doping or defect incorporation may be intentional to enable certain functionality, such as controlling electrical conductivity type (e.g, n- or p-type) or chemical reactivity. Examples in Figure 23 show the plasma effects on the bandgap of graphene. Surface hydrogenation was used to bend a free-standing graphene layer to form non-conducting graphane (i) [223]. By oxidizing the graphene surface in a plasma, it became possible to enable a quite significant bandgap opening (j), (k) [225,227]. Importantly, these processes are reversible, which may lead to high-throughput, low-temperature interconvertible graphane-to-graphene growth and processing [228]. Successful doping of graphene with nitrogen from reactive plasmas in ammonia has also been demonstrated [229]. Opening and etching of carbon dangling bonds and creation of multiple vacancies is also possible using plasmas. Some examples related to GNRs will be discussed below.

Other possibilities in the rapidly developing area of surface and defect engineering of graphene are discussed elsewhere [230]. Raman spectroscopy can be used to identify the nature of defects in graphene, for example, sp^3-type or vacancy-type defects created [231]. Recently, the extreme selectivity of the outcomes of the remote hydrogen plasma reactions with graphene of different number of layers was demonstrated [232]. Indeed, fairly uniformly distributed holes are formed on basal planes of monolayers, while the edges are etched. On the other hand, size-uniform hexagonal features are etched on bi-layer and thicker graphene sheets. These features develop from the existing defects through highly anisotropic etching. The etch rates are also very sensitive to temperature and the best results are achieved at 400°C, although room-temperature etching is also quite effective [232].

The mechanisms of these highly promising plasma effects are presently unclear. Importantly, these mechanisms are more likely to be due to the properties of graphene layers and their interactions with the plasma species rather than the substrate effects because very similar observations were made on both relatively rough SiO_2 and nearly atomically smooth mica. These results complement several relevant observations by other authors which include faster hydrogenation of bi-layer and thicker sheets compared with monolayer graphene, highly anisotropic etching along specific crystallographic directions, and some others [233–235]. Identifying and better understanding of the specific roles of relevant plasma species and the mechanisms of their interactions with different atomic arrangements in graphenes of different number of atomic layers may shed some light on these highly promising recently discovered control possibilities. Initial studies [232] draw

parallels with erosion of graphitic materials by low-energy hydrogen ions [236–238] and suggest the important role of hydrogen radicals and H^+, H^{2+}, and H^{3+} ions. However, finding the specific contributions of these reactive species requires precise measurements and modeling of their relative abundance in the plasma discharge and offers an interesting opportunity for future studies.

Reduction of graphene growth temperature still remains a significant issue where plasma-based approaches are expected to produce a significant contribution in the near future. A promising result on the synthesis of a few-layer graphenes on Cu catalyst in $Ar+C_2H_2$ microwave plasmas at temperatures as low as 240°C has recently been reported [239]. However, limited details of the temperature measurements (which as discussed in Section 4.2.1 can be ∼100°C or even higher than supplied through external heating) prevent us from commenting on this issue.

4.3.1.2. *Graphene nanoribbons.* Low-temperature plasmas were also used for high-precision, ultra-fine selective etching of edges of GNRs (thin strips of graphene) shown in Figure 23(e)–(h). The initially 14 nm-thick GNRs (e) were thinned to only 5 nm (f) after a short exposure to hydrogen plasmas [222]. This delicate etching did not produce any structural damage to the main body of the nanoribbon. More importantly, this precise thinning of the GNR in one dimension has led to the bandgap opening of the originally metallic GNR. This in turn resulted in a dramatic increase of the source–drain current versus gate voltage ($I_{ds}(V_{gs})$ in panels (c) and (d)) nanodevice characteristics.

Several other examples confirm the utility of low-temperature plasmas to fine-tune the properties of graphenes and GNRs. A combination of nano-masks (e.g. nanospheres or NWs) and nanoscale reactive etching in low-density, low-temperature O_2 plasmas was used to fine-tune the bandgap of ultra-narrow GNRs [240] and enable their applications in field effect transistor devices [241].

Precise interactions of low-density plasmas with partially masked MWCNTs also enabled a new class of graphene-based materials, namely surface-supported bent GNRs. In particular, by adjusting the plasma etch time, it became possible to produce single-layer, bilayer, and trilayer GNRs, the bent analogs of flat graphenes [242–244].

In a recent example, narrow GNRs (∼23 nm) were grown directly between the source and drain electrodes of a field-effect transistor using plasmas of CH_4+H_2 gas mixtures and narrow (less than 30 nm) Ni nanobars with a typical thickness below 50 nm, and a rapid heating [245]. Under certain conditions, Ni catalyst evaporates from underneath the nanoribbon thus creating a graphene nano-bridge between the electrodes.

The GNRs exhibit a very clear bandgap of ∼58.5 meV and a very high (∼10^4) on/off ratio without hysteresis during the transistor operation. At high temperatures, the electron transport in these nanoribbons followed

$$\mathcal{G}_e \sim \exp\left(\frac{-\epsilon_a}{2k_B T}\right), \tag{62}$$

where the transport activation energy $\epsilon_a \sim 16.2$ meV was obtained from a linear fit to the Arrhenius plot. At lower temperatures, the electron behavior in the nanoribbons followed the variable-range hoppinig approximation

$$\mathcal{G}_e \sim \exp\left[-\left(\frac{T_0}{T}\right)^{\ell}\right], \tag{63}$$

where $\ell \sim 0.5$. Importantly, these electron transport features are competitive with GNRs synthesized using sophisticated lithographic procedures [246].

A combination of a quite similar nickel nanobars, plasmas, and rapid heating/cooling opened a highly unusual possibility to nucleate single- and few-layer GNRs at the interface between the

nanobar and the SiO_2 substrate [247]. This advance contributes to the solution of a significant problem of direct, transfer-free synthesis of graphene on insulators such as silica. Because of very high optical transmittance of both silica and graphene, this combination also offers several interesting opportunities for applications in nano-optics.

However, the Ni catalyst still needs to be removed after graphene growth, e.g. by chemical etching. This is why direct, etch-free growth of graphene directly on SiO_2, BN or similar dielectric substrates is highly warranted in the near future and plasma-based approaches are expected to contribute to the solution of this problem.

Moreover, the mechanism of selectivity of nucleation of graphene layers either on top or at the bottom of Ni nanobars still remains unclear. These phenomena may be explained by comparing the rates of carbon atom delivery $\Upsilon_{\rm del}$, diffusion to the bottom interface $\Upsilon_{\rm difb}$, their segregation toward the upper surface $\Upsilon_{\rm seg}$, graphene nucleation at the top $\aleph_{\rm t}$ and bottom $\aleph_{\rm b}$ interfaces, and Ni evaporation $\Re^{\rm Ni}_{\rm evap}$. For example, for the formation of graphene nanobridges, it is important that

$$\Upsilon_{\rm del} \sim \Upsilon_{\rm seg} \sim \aleph_{\rm t} > \Re^{\rm Ni}_{\rm evap} \gg \aleph_{\rm b}, \tag{64}$$

which means that graphene nucleation on the plasma-exposed Ni surface should be faster than the nanobar evaporation and much faster than the nucleation of graphene at the bottom interface. Alternatively, nucleation conditions at the bottom interface may not be met during the process [245]. However, only detailed numerical modeling studies may validate this phenomenological argument.

The above non-exhaustive examples suggest that despite significant caution, plasma-specific effects can and should be used for the growth and ultra-fine processing of even so delicate nanoscale objects as graphenes. Moreover, these effects should be explored to solve the persistent problem of GNR chirality control, similar to the SWCNT case of Section 3.4. This may lead to better selectivity between the antiferromagnetic and non-magnetic responses of zig-zag and armchair GNRs actively pursued in nanomagnetism research [248].

4.3.1.3. *Graphene oxide.* As we have seen from Figure 23(j) and 23(k), plasmas are effective at oxidizing graphene, thus forming GO. The opposite, reduction of GO is also possible, especially because of the plasma reactivity, for instance, in producing reactive hydrogen atoms and ions. These species effectively reduce oxygen content in GO, ultimately leading to pure graphene. The presence of oxygen determines the GO bandgap, being wider in stoichiometric GO and much smaller when oxygen content is low.

The reduction process of GO in a low-temperature remote CH_4-based plasmas is also accompanied by a very clear defect healing as can be seen in the Raman spectra from Figure 24(a) [249]. Indeed, as the plasma exposure duration increases, the graphene signature 2D peak increases, while the ratio of the defect-related D and graphitic structure quality-related G-peaks decreases in nearly two times, from 1.03 to 0.53. Therefore, relaxation of C–C bonds can be considered as a driving force for the GO reduction. The plasma-based method is very fast ($\sim$10 min) and requires lower temperatures ($\sim$600°C) compared with other methods labeled in Figure 24(b) [249].

More importantly, the recovered low sheet resistance of the GO ($\sim$9 kΩ/square) appears to be reasonably close to that of pristine graphene [249]. The larger sheet resistance of the reduced graphene oxide (r-GO) compared with pristine graphene is mostly due to its rougher surface and defect presence. In this case, the carrier transport is described by the 2D variable hopping model with the conductance

$$\mathcal{G}_{\rm e}^{\rm rGO} \sim \exp\left(-\frac{\rho_{\rm hop}}{T^{1/3}}\right), \tag{65}$$

where

$$\rho_{\rm hop} = \left[\frac{3}{k_{\rm B}N(E_{\rm F})\lambda_{\rm L}}\right]^{1/3}$$

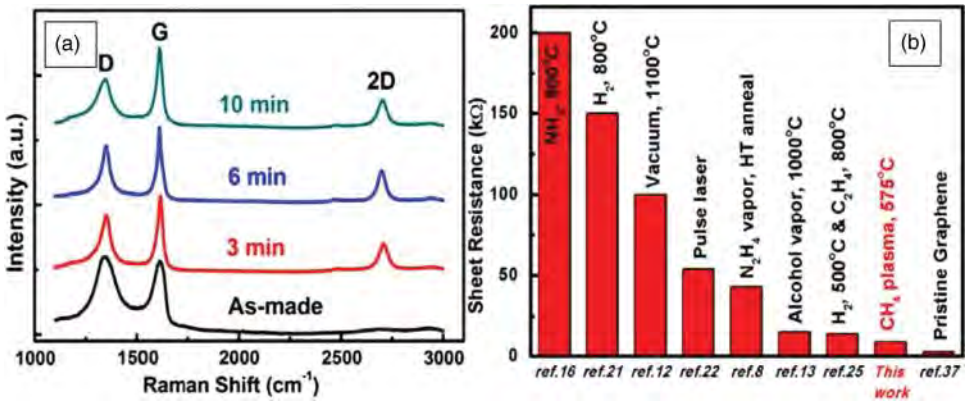

Figure 24. Raman spectra of as-made and plasma-reduced (after 3, 6, and 10 min plasma treatment) GO (a). Comparison of sheet resistances of pristine graphene, CH_4 plasma-reduced GO ('This work' means Ref. [249]), and other reports on GO reduction (reference numbering as in the original publication). Both figures are reprinted with permission from [249] [Copyright © 2012 Elsevier].

is the hopping parameter, $N(E_F)$ is the density of mobile carriers, E_F is the Fermi energy, and λ_L is the localization length [249]. Larger conductance implies larger $N(E_F)$ and λ_L which is attributed to larger graphene crystalline domains. This is another manifestation of the importance of the ultimate achievement of large-area single-crystalline graphene mentioned at the beginning of Section 4.3.1.1.

Effective reduction of GO was also demonstrated using atmospheric-pressure plasmas in $Ar+H_2$ gas mixtures, at significantly lower temepratures (down to ~70°C [250]). The achieved sheet resistances of r-GO were also competitive, for example, $4.77 \times 10^4\ \Omega$/square at 70°C. Therefore, plasma-based reduction of GO can be regarded as a viable alternative to solution-based chemical methods which use strong and hazardous reactants such as hydrazine (N_2H_4) or sodium borohydride ($NaBH_4$) and often introduce significant impurities and defects [250]. Selectivity of the plasma-assisted GO reduction in the presence of reactive chemicals is an interesting area to explore.

To end this section, we stress that graphene-related research is a very rapidly expanding field with a huge number of publications. This is why we refer the reader to the selected reviews which cover the interesting physics and applications of graphene and related structures and materials [230, 251–253].

4.3.2. *Graphene nanosheets*

Let us consider vertically standing and unsupported graphenes (VSGs and USGs, respectively) as alternatives to horizontal graphenes supported by solid substrates. In both cases, the growth is essentially catalyst-free and is enabled by the plasma. Such graphenes have an obvious advantage over the flat surface-bound counterparts. Indeed, both surfaces and at least three open reactive edges of the VSGs or USGs can be utilized in applications (e.g. biosensing), while surface-bound counterparts effectively use only one surface.

However, producing the VSG and USG structures is quite challenging. Indeed, the stability of straight few-atomic-layer-thin VSGs is an issue. On the other hand, synthesis of USGs requires effective control of nucleation in the gas phase, which is very difficult because of the very fast process kinetics. Figure 25 evidences solutions to these problems using low-temperature plasmas.

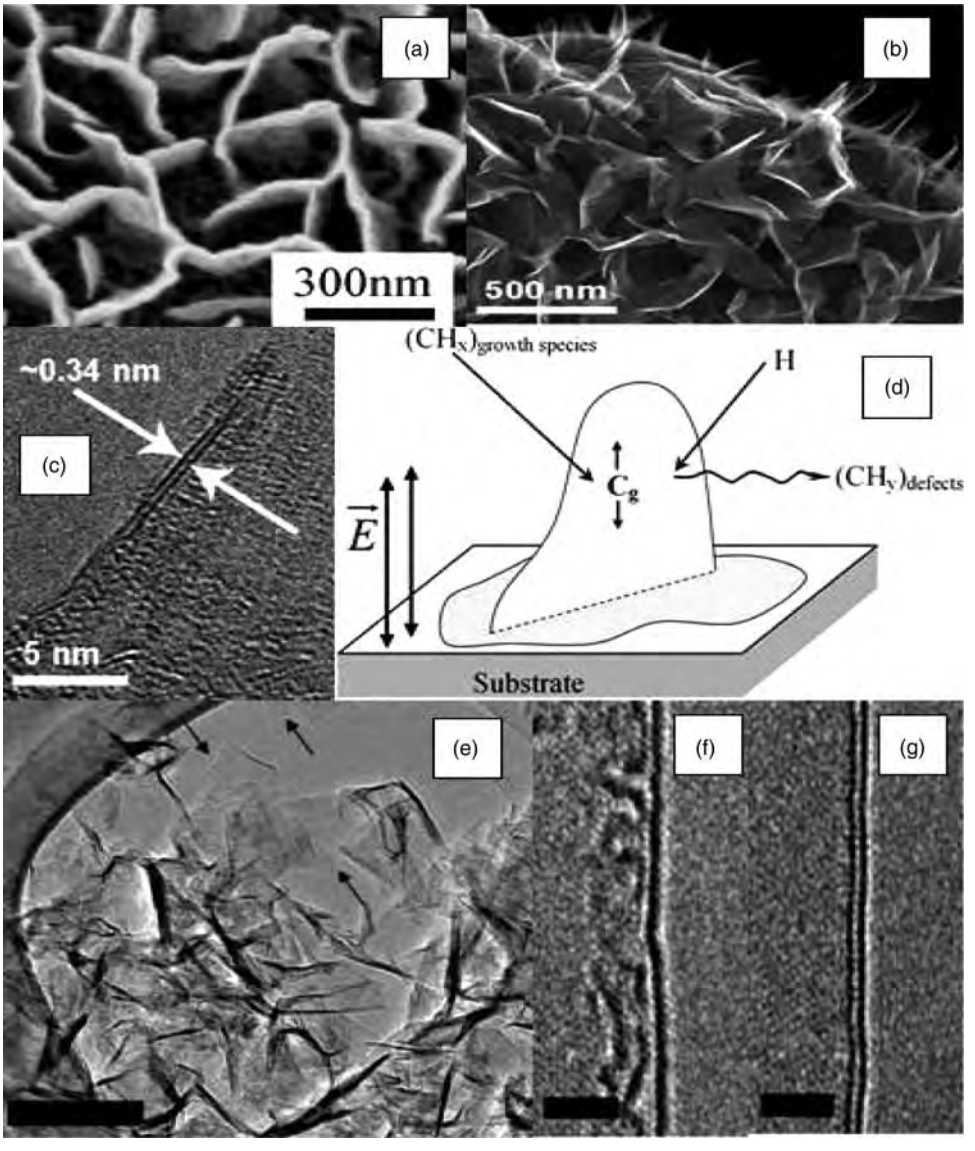

Figure 25. CNWs from plasmas with H radical injection (a) [Reprinted with permission from [254], Copyright © 2004 American Institute of Physics]. Vertical GNSs grown by RF PECVD on a Ni wire (b); HRTEM of bi-layer graphene (c); and GNS growth model (d) [Reprinted with permission from [23], Copyright © 2007 Elsevier]. TEM of GNSs grown by passing ethanol droplets through Ar plasma, arrows point at monolayer graphene (e); TEM images of (f) single-layer and (g) bi-layer graphene [255]. Scale bar is 100 nm in (e) and 2 nm in (f) and (g). Panels (e)–(g) reprinted with permission from [255], [Copyright © 2008 American Chemical Society].

4.3.2.1. *Surface-supported vertical graphenes.* Figure 25(a) shows vertically standing carbon nanowalls (CNWs) grown by hydrogen radical-assisted PECVD on a Si surface without any catalyst, using fluorocarbon precursor [254]. Similar CNWs were produced by other groups [256,257]. Interestingly, such catalyst-free CNW growth is only possible in a plasma. This plasma-enabled

phenomenon was explained through the study of kinetics of the plasma-assisted reorganization of underlying thin oxide layers followed by the formation of self-organized chains of small carbon clusters on which the nanowall nucleation takes place [258].

As the plasma-based growth techniques matured, it became possible to produce very thin carbon nanosheets of only a few atomic layers thickness [259]. One example of such vertical graphene structures supported by the curved surface of a Ni wire is shown in Figure 25(b) [23]. Some of these structures can be as thin as only two atomic layers, see TEM image in panel (c).

The growth model of these vertical 2D NSs in panel (d) includes AD of hydrocarbon BUs (CH_x), diffusion of carbon species (C_g), etching of defects and amorphous carbon by reactive H atoms (CH_y), as well as the vertical NS orientation due to the anisotropic polarizability effects in the vertically oriented electric field $\vec{E}$ in the plasma sheath [23]. However, this model cannot quantify the number of vertical graphene walls that can nucleate and detailed numerical modeling or *ab initio* simulations are needed. It is also unclear how the NSs nucleate to simultaneously extend in the horizontal and vertical directions. Physically, the reason for the vertical alignment may be very similar to the SWCNTs in Figure 9(d).

This result was achieved using Ni catalytic support and the issue of direct growth of atomically thin VGS structures directly on Si still remains open. Recently, it became possible to produce two to six atomic layers-thick vertical graphenes using CNWs [260] or silicon nanograss [261] as supporting and growth guiding structures. Combined with the unique plasma-enabled activation of the thin top reactive edges of the VSGs and their decoration with even thinner CNPs opens an opportunity to achieve vertically standing single-layer graphenes.

These and some other modifications of vertical few-layer graphenes have several interesting properties, such as a variety of morphologies, a very high length of open reactive edges (e.g. up to $\sim 10^3$–10^4 m per gram of material), as well as good electric conductivity and structural stability. Moreover, they may form 3D networks with a high-density of Y- and T-shaped junctions between vertically standing nanosheets. This combination of properties makes such structures suitable for a number of applications such as electric double-layer capacitors (supercapacitors) [259], gas and bio-sensors [262], and several others.

Recently, uniquely plasma-enabled, catalyst-free synthesis of a few-layer vertical graphenes directly on Si/SiO_2 substrates using natural precursors has been demonstrated [263]. For example, rapid reforming of natural honey exposed to reactive low-temperature $Ar+H_2$ plasmas produced high-quality, ultra-thin vertical graphenes, typically three to eight atomic layers thin. Importantly, this transformation is only possible in the plasma and fails in similar thermal processes.

The plasma-enabled process is energy-efficient, environmentally benign, and is much cheaper than common synthesis methods based on purified hydrocarbon precursors. The graphenes produced also retain the essential minerals of natural honey, feature ultra-long, open reactive edges. Enhanced with suitable metal NPs these vertical graphene structures show reliable gas- and bio-sensing performance. Interestingly, very similar structures can be produced in a plasma from very different precursors in all three states of matter, such as methane (gas), milk and honey (liquid), butter (soft solid) and crystalline sugar (hard solid). These interesting experimental results will soon be reported and will require appropriate theoretical interpretation.

4.3.2.2. *Unsupported graphenes from gas phase.* Using plasmas, it is also possible to produce very thin flakes of USGs directly in the gas phase, without using any catalysts. The results in Figure 25(e)–(g) show very thin graphene flakes synthesized in the gas phase of atmospheric-pressure MW plasmas [255]. Some of these flakes are only one to two atomic layers thick as seen from panels (f) and (g), respectively. The graphene sheets were synthesized by passing liquid ethanol droplets into an argon plasma; these droplets have a residence time of the order

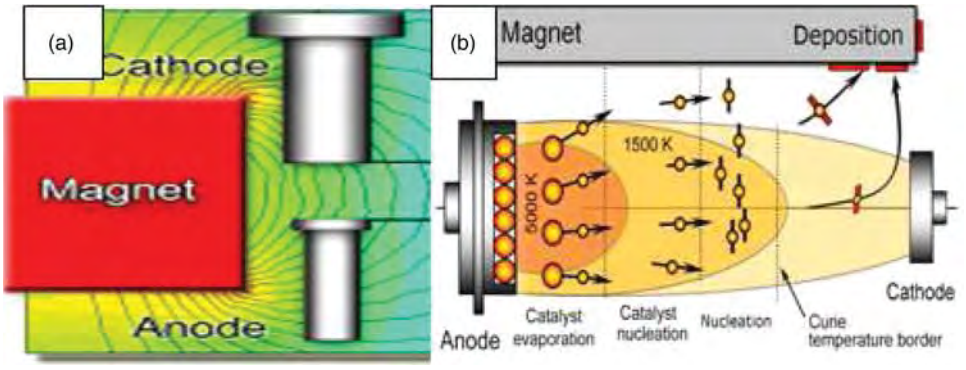

Figure 26. Magnetically enhanced arc discharge for production and separation of graphene flakes and SWCNTs (a) [Reproduced from [265] by permission of the Royal Society of Chemistry]. Non-uniformity of magnetic fields and temperature create non-equilibrium environment for fast moving CNPs on which graphenes and nanotubes nucleate (b) [Reprinted with permission from [266], Copyright © 2010 Elsevier].

of 0.1 s inside the discharge. During this time, ethanol rapidly evaporates, dissociates, and then condenses under strongly non-equilibrium conditions, which also include rapid cooling. This simple approach features high rates of nanoflake collection (∼2 mg/min) and is promising for large-scale graphene production, which can also be achieved in high-pressure (e.g. thermal) plasma discharges.

Arcs and other high-pressure discharges feature high plasma densities (e.g. up to 10^{17} cm^{-3} in arcs) and very high rates of collisions. Similarly, the minimum spatial localization of the plasma (the Debye sphere) becomes much smaller compared with the low-pressure case. This is why high-pressure plasmas show very different effects at nanoscales. Indeed, high plasma and radical densities lead to very strong fluxes of energy and matter onto the growth surface, which leads to very high NS nucleation and growth rates. This is why high-pressure plasmas are deemed viable for industrial-scale NP production [147,264].

On the other hand, very high rates of collisions lead to the effective and rapid nucleation in the gas phase. The sheaths in high-pressure plasmas are typically strongly collisional and the ions lose most of their energy ($\nu_{in} \sim \nu_{nn}$) while traversing the sheath. In this case, the ion damage to delicate NSs such as SWCNTs is minimized. This is why the quality of CNTs, fullerenes (e.g. C_{60}), and graphenes produced in high-pressure plasmas is usually very high, which is evidenced by a very small number of ion-bombardment-induced structural defects [162].

These salient features lead to the nucleation of small (e.g. graphitic) nanofragments without any catalyst or nucleate on fast-moving CNPs and produce large NSs even during the very short times needed for these particles to cross the gap between the points of injection and collection. In many cases, the CNPs are produced by metal evaporation from the anode (Figure 26). The gas temperature near the anode can be very high; for example, at least several thousand Kelvin in thermal plasmas of atmospheric-pressure arcs [267]. The NSs grown on these NPs are usually collected at the opposite electrode (cathode) or at special collecting surfaces such as the surfaces of a cubic magnet in panel (a). The precursor material is also commonly evaporated from one or both electrodes.

For example, conducting graphite electrodes are used to evaporate carbon BUs for the growth of graphene flakes or CNTs. The customized Ni-Y catalyst is embedded into the anode. The distributions of the density of the ionized BU vapor and the gas temperature are very non-uniform as can be seen from Figure 26. Both these features enable a deterministic, single-step production

and magnetic separation of graphene flakes and CNTs in an arc discharge [265]. To achieve this, the high-temperature growth and low-temperature separation zones are separated and the CNTs and graphenes are captured in different areas on the magnet.

The nanotubes and graphenes are simultaneously produced on the CNPs when they enter the high-temperature, high-plasma-density growth zone (Figure 26(b)) [266]. Despite a very short residence time, the CNTs grow to a significant length (e.g. tens of μm); this process is enhanced by adding Y to the catalyst which easily forms carbides. When the catalyst-supported NSs enter the area with much lower temperature, the growth process is inhibited. Moreover, Ni transits to the ferromagnetic state near the Curie point ($\sim$350°C). This lower-temperature zone thus separates lighter CNTs and heavier graphene flakes. Because of this mass difference, the magnetic force is also different, and the nanotubes and graphenes deposit in different areas of the magnet.

Despite thermal equilibrium of thermal plasmas, the NS growth process is strongly non-equilibrium, very fast, and is kinetically driven. The balance between the delivery of BUs to the catalyst surfaces (mostly determined by the density of ionized carbon vapor) and their gainful use in the growth (controlled by the gas temperature) changes dramatically while the CNP crosses several different zones in the discharge. This rapidly changing kinetic process is enabled both by the non-uniformities of the magnetic field, plasma density, and gas temperature as well as by the rapid CNP transport across these non-uniform areas. More examples of the NP production in high-pressure plasmas, their properties, and applications can be found elsewhere [15,147].

4.3.3. *Other 2D nanomaterials*

Although a large number of other 2D nanomaterials is known, the question remains if they can be made atomically thin and also put in a heterolayered 'sandwiched' stack [268]. Of special interest is whether plasma effects can be gainfully used similar to Sections 4.3.1 and 4.3.2.

One typical example is heterolayered structures and superlattices, e.g. alternating thin layers of GaN and InGaN semiconductors used in optoelectronic devices. If the thickness of these layers is in the nanometer range, quantum wells are formed near the hetero-interfaces, which in turn offers unique quantum confinement effects. Plasmas have been successfully used to grow or facilitate the growth of GaN nano-layers with much low growth temperatures and high growth rates [269].

In particular, plasmas are commonly used in the growth of ultra-thin epitaxial semiconducting layers for the generation of atomic nitrogen through the effective dissociation of nitrogen molecules. One example is the plasma-assisted molecular-beam epitaxy of complex InGaGdN/GaN magnetic semiconductor superlattice structures [270].

Low-temperature plasma treatment can also be used to improve the properties of heterostructured 2D nanomaterials. For example, delicate treatment of InGaZnO periodic superlattice structures with Ar plasmas dramatically reduces the electrical resistivity without affecting the microstructure or decreasing the thermal conductivity. As a result, the thermoelectric properties of these 2D nanomaterials are much improved [271].

This interesting result may be related to the improvement of crystalline structure (e.g. compactifaction) and defect removal upon impact of low-energy Ar^+ ions. This is a typical of the many manifestations that the ion bombardment can be beneficial rather than commonly asserted detrimental, see other examples in Sections 2.3.3 and 3.4.

Another example is the PECVD of 2D diamond superlattices made of heterolayers of pure ^{12}C and ^{13}C carbon isotopes [272]. In this case, the plasma-specific effects are similar to the nano-diamond synthesis of Section 4.5.4.

Another example is the formation of ultra-thin nanolayers of magnetic alloys for spintronics and data storage produced using various modifications of the i-PVD. Functional 2D layers (e.g. transparent nanometric organic luminescent films) for organic photovoltaic and light-emitting devices produced by plasma polymerization [273] are discussed in Section 4.5.5.

Vertically oriented 2D nanomaterials synthesized or processed using plasmas are also numerous [274,275]. However, their thickness is usually much larger compared with the thinnest vertical graphenes of Section 4.3.2 and a substantial effort is required to ultimately achieve atomically thin, vertically standing 2D NSs.

2D nanomaterials produce unique quantum states of matter such as topological insulators (TIs) which simultaneously show insulating and conducting properties [276]. Typical TIs arise in 2D quantum wells (e.g. HgTe/CdTe) or in 3D materials with 2D topological conducting surface states (e.g. HgTe, BiSb, Bi_2Te_3, and Bi_2Se_3) which may be similar to the bandgap-less states of graphene [277]. These materials enable effective electron spin control (e.g. spin-polarized currents along different interfaces in quantum-well TIs) actively pursued in spintronics. Exploration of plasma-based synthesis of these and many other 2D and topological materials is therefore warranted.

4.4. *Hybrid nanomaterials*

Nanomaterials with hybrid dimensionality feature many unique properties that are not common to their constituent elements of different dimensionalities taken separately. The constituents usually have different elemental composition and structure, which leads to even more exotic physical properties when combined in a hybrid structure. For example, combining 1D CNTs with small 0D metal or semiconducting NPs leads to highly unusual electron transport through the CNT–NP interface [278,279]. This in turn enables new functionalities in the molecular-level sensing and energy storage [280].

Moreover, the electron transport strongly depends on the precise NP placement. The adhesion, bonding, interface stability, and electron transport are very different for NPs at the base, tip, or lateral surface of a SWCNT. Indeed, when the NP is at the SWCNT base, the electrons mostly pass through the reactive edges of the rolled graphene sheet. When the NP is placed at the tip of the nanotube, the electron transport is determined by the interface with the carbon atomic network which includes pentagonal carbon cells. The surface of the SWCNT cap is less reactive compared with the open edges but more reactive compared with the lateral surface made of a rolled sp^2 hexagonal sheet of carbon atoms.

Therefore, nanometer-scale selectivity of the placement and firm, defect-free attachment of small metal NPs to the nanotube surface, has recently become highly topical. This problem also applies to a large number of 1D/0D hybrid nanoarchitectures as well to other possible combinations of NSs with different dimensionalities, e.g. 2D nanowalls decorated with 0D NPs, 3D nanocones decorated with 0D NPs which in turn catalyze and support 1D NWs, etc.

Let us now discuss how plasma-specific effects enable high-quality hybrid structures with the unique properties desired for the envisaged applications [12,14]. First, plasma-enhanced methods enable controllable synthesis and post-processing of the broad range of nanomaterials of different dimensionalities.

Second, many examples evidence that the decoration of one NS with another can be implemented in the same reactor in a continuous, uninterrupted process flow, e.g. in the same vacuum cycle.

Third, plasmas are very effective for the highly controlled surface conditioning and functionalization. If special care is taken to avoid undesirable surface damage (e.g. the ion energy adjusted to be below the threshold for the destruction of a hexagonal carbon network, see Section 3.4),

this can be used to suitably prepare the surface of the supporting (e.g. 1D) NS for decoration by other (e.g. 0D) NSs. Importantly, surface dangling bonds may be activated without any significant structural damage.

Fourth, quite differently from neutral gas- and wet-chemistry approaches, plasmas offer selectivity and effective control over the placement of BUs in specific areas with nanometer and even better precision. For example, the ion focusing effect (Section 3.5) allows one to deposit metal atoms directly at the tip of a SWCNT, with the size as small as $\sim$0.5 nm.

Fifth, the plasma-specific selective heating around the point of nucleation of the decorating NPs on the surface of the supporting NS is expected to lead to fewer defects and hence, a better-quality interface between the NSs of different dimensionalities.

For example, using the same plasma reactor and vacuum cycle, two-layer vertical graphene structures with highly unusual electrical properties were produced [260]. Initially, well-graphitized self-organized CNWs were grown in a plasma-enabled, catalyst-free process, without any pre-patterning. The top edges of the nanowalls were then activated by the ion bombardment, to open dangling bonds. Subsequently, Cu NPs were deposited on the edges, in a highly selective fashion. Finally, few-carbon-layer-thin vertical graphenes were grown on the Cu NP-decorated edges to produce a two-layer self-organized nanoarchitecture with unique properties; it was not possible to synthesize them without plasmas. This architecture showed an exotic temperature dependence of the electrical conductivity partially recovering the semi-metallic property of a single-layer horizontal graphene [260].

Potential damage to the supporting NSs due to the ion bombardment may be quite significant. This is why it is critical to select suitable plasmas and process parameter range. For example, atmospheric-pressure plasma jet with a sub-mm spot size was used to treat MWCNTs before depositing Au NPs on them (Figure 27(a)) [281]. This choice was dictated not only by the need of the selected-area decoration, but also by the fact that ion energies in a collisional sheath of atmospheric-pressure plasmas are much lower than under low-pressure conditions.

Importantly, the atmospheric microplasma jet produces a 3D microfluidic channel on dense arrays of vertically aligned CNTs, which confines Au nanodot aqueous solution. As can be seen from panel (a), the Au NPs only attached to the surfaces of MWCNTs that were exposed to the plasma jet [281]. A white dashed line shows the rough boundary of the plasma-exposed area. The resulting hybrid 3D NS is then used as an effective microscopic area-selective sensing platform based on the surface-enhanced Raman scattering.

Using hot-filament plasma CVD, it also recently became possible to decorate vertically aligned MWCNTs with dense patterns of small Si nanodots. These hybrid structures are very stable in reactive chemical environments and significantly improve performance of Li-ion batteries by combining excellent electrochemical response of Si NPs and electronic conduction of MWCNTs [279].

Figure 27(b)–(e) shows exotic hybrid structures where 0D fullerenes C_{60} (b) and azafullerenes $C_{59}N$ (d) are encapsulated by 1D SWCNTs [282]. Substitution of a N atom in C_{60} was achieved by a mild exposure of the fullerenes to low-density nitrogen plasmas. The plasmas have been chosen deliberately to have a relatively wide sheath to generate a small number of N^+ ions with the energies above the threshold of substitutional incorporation into the C_{60} network. The SWCNTs were also synthesized using plasmas (Section 3.5).

Remarkably, the plasma ion-irradiation method was also used to encapsulate the C_{60} and $C_{59}N$ structures into the SWCNTs. As a result, while the C_{60} – SWCNT structure showed the typical p-type characteristics (panel (c)), the $C_{59}N$ – SWCNT hybrid clearly revealed the n-type properties as shown in panel (e). Both the classical and density functional theory MD simulations elucidated the mechanism for this process, albeit for Ni incorporation to produce metallofullerenes [283,284].

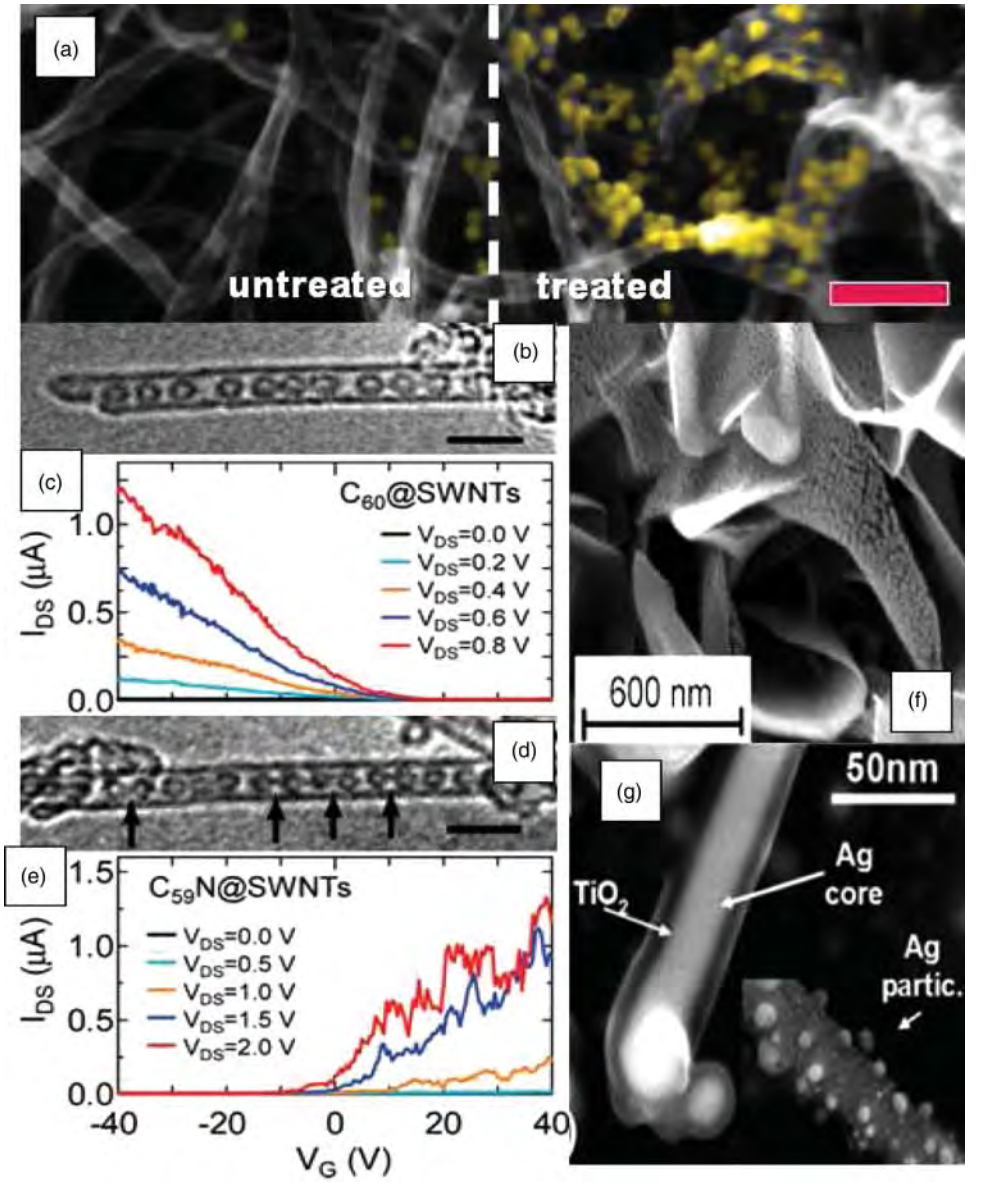

Figure 27. Atmospheric plasma jet treatment improves decoration of MWCNTs with Au NPs (a); scale bar is 200 nm [Reproduced from [281] by permission of the Royal Society of Chemistry]. C_{60} encapsulated SWCNTs (b) show enhanced p-type characteristics (c) compared with pristine SWNTs, whereas N-doped $C_{59}N$ encapsulated SWCNTs (d) show n-type behavior (e) [Reprinted with permission from [282], Copyright © 2008 American Chemical Society]. Vertical graphenes decorated with ordered self-organized arrays of Au NPs (f) [Reproduced from [262] by permission of the Royal Society of Chemistry]. Ag-TiO_2 core-shell nanofibers by PECVD (g) [Reproduced with permission from [285], Copyright ©2007 Wiley-VCH Verlag GmbH & Co. KGaA, Weinheim].

Figure 27(f) shows the possibility to decorate the basal surfaces of vertical graphenes by Au NPs very uniformly, from the bottom to the top [262]. The plasma exposure also resulted in the formation of regular, self-aligned linear arrays of Au NPs within a certain distance from the edges.

No masking or pre-patterning were required. The mechanism of this self-alignment is presently unclear. It may be enabled by the interplay of the nanoscale plasma interactions (Section 3.3), non-uniform distributions of surface temperature and stress (similar to Figure 12(a) and 12(b)), and plasma-modified adatom capture zones near the nanosheet edges.

Figure 27(g) shows two different arrangements of hybrid Ag-TiO_2 core-shell inorganic nanoarchitectures produced by the plasma oxidation of Ag and the plasma deposition of TiO_2. The growth mechanism of these hybrid fiber-like architectures [285] suggests the importance of several plasma-specific effects discussed above. There are many other examples of the plasma-assisted production and processing of multi-dimensional nanoarchitectures, e.g. using various combinations of top-down and bottom-up approaches.

Physical properties (e.g. electron transport and interface phenomena) and applications (e.g. in electronic, energy storage, and sensing devices) of hybrid nanoarchitectures are discussed elsewhere (see, e.g. [278,280] and references therein).

4.5. *3D nanomaterials*

Let us now consider nano- and micrometer objects with 3D features and the relevant plasma-based approaches to produce and process them. The first two groups of examples in Sections 4.5.1 and 4.5.2 are related to nanoscale plasma etching, one of the most traditional plasma applications scaled down to the nanoscale. This will be followed by two more common groups of nano-carbons, namely 3D cone-like structures and nano-diamond in Sections 4.5.3 and 4.5.4. This subsection will conclude with the discussion of soft organic matter in Section 4.5.5 and biological objects in Section 4.5.6.

4.5.1. *Nanoscale plasma etching*

Plasma etching is one of the most established plasma technologies and the basic etching mechanisms of macroscopic (e.g. large-area surfaces) and microscopic (e.g. semiconductor microfabrication) features are well understood [286]. Research in this area has resulted in an enormous number of research publications, reviews, patents, etc. which are outside the scope of this review.

Continuous miniaturization of integrated circuitry lead to inevitable shrinking of the feature sizes. As the features entered the nanometer domain, new challenges emerged. In particular, it became critical to produce suitable masks with nanometer dimensions and to *precisely* transfer these nanoscale patterns to the underlying substrate. Since the feature sizes are already nearing the 10-nm domain, the precision of the pattern production and transfer needs to be in the sub-nm, and ultimately, atomic range. This is why we focus on the mechanisms of the *nanoscale* and *atomic-level* plasma etching.

To better understand the fundamental differences between the conventional and the nanoscale plasma etching, let us review Figure 28(a)–(d). The conventional mechanism of the plasma etching (c) involves a combination of interaction of ionic, etching, and depositing reactive species (e.g. F, Cl, H, CF_x, ions, etc.) with the surface. The rate of surface etching $\mathcal{R}_{\rm etch}$ is determined by a complex interplay of several factors such as fluxes of multiple species, reaction probabilities, and energy thresholds. Under conditions when the effect of depositing species is insignificant, the etching rate is [288]

$$\mathcal{R}_{\rm etch} = \frac{J_{\rm i}[A_{\rm s}(\sqrt{E_{\rm ion}} - \sqrt{E_{\rm th,s}}) + B_{\rm s}(\sqrt{E_{\rm ion}} - \sqrt{E_{\rm tr,s}})]}{1 + J_{\rm i}[A_{\rm s}(\sqrt{E_{\rm ion}} - \sqrt{E_{\rm th,s}}) + B_{\rm s}(\sqrt{E_{\rm ion}} - \sqrt{E_{\rm tr,s}})]/J_{\rm e}\nu_{\rm es}S_{\rm es}}, \tag{66}$$

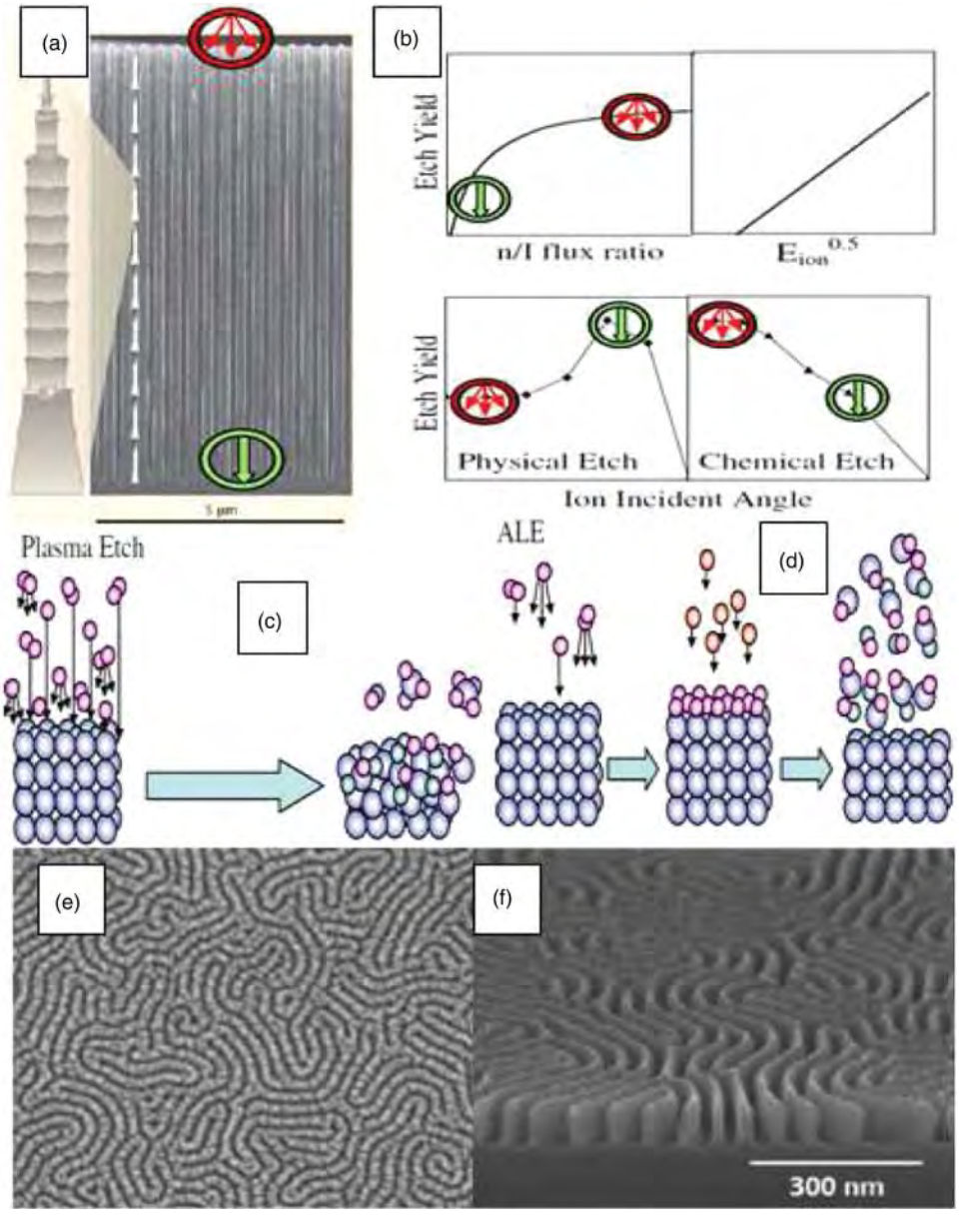

Figure 28. High-aspect-ratio trenches etched in Si (a) [287,288]; Taipei 101 building is shown for comparison of the aspect ratio. Effect of the flux ratio of neutral and ion species and ion energy on the etch yield (top row) and competition of the physical and chemical etch mechanisms (bottom row) (b); mechanisms of traditional (c), and atomic-layer (d) plasma etching [288]. Self-assembled polymer nanopatterns (e) transferred to Si (f) by nanoscale plasma etching [25].

where J_i and J_e are the fluxes of ionic and etching species, $E_{th,s}$ and $E_{tr,s}$ are transition and threshold energies, while A_s/B_s and ν_{es} refer to volume of substrate/polymer removed as a function of ion energy and etching species flux, respectively. In Equation (66), S_{es} denotes the sticking probability of the etching species to the surface.

The reactive etching species bond with the substrate atoms and form volatile compounds thereby removing matter from the surface. It is presently possible to produce very deep trenches in Si wafers, with the aspect ratios compared with some of the tallest buildings in the world (Figure 28(a)). The thickness of these channels is expected to reduce into the low-10 nm domain, which is much less than the mean free path of the reactive species used for the etching. This creates a major problem of *nanoscale localization* of the plasma etching, which is quite similar to the effects of localization of the plasma–surface interactions involved in the nucleation of SWCNTs in Section 3.4.

With regard to the high-aspect-ratio features, several important questions arise: how to ensure that the trenches are straight (i.e. highly anisotropic etching), how to deliver the etching species deeper and deeper as the features become longer and longer, how to ensure that these species will only react with the bottom surface of the trench and will not cause any damage to its side-walls, and how to extract the etching products out of the trench without them being redeposited on the channel walls? More importantly, how to control the interactions of the plasma species with the surface in the nanometer *confined* space?

The effect of the spatial confinement in this case may appear even more critical compared with Figure 8 because of the rigid vertical walls of the trench which strongly impede the mobility of the species in the gas phase. However, the walls of the trench may provide the effective species delivery and escape 'slides', in a sense similar to the evacuation of passengers from an aircraft after emergency landing. This in turn creates a very interesting physical similarity to the growth of SWCNTs in Figure 8(d) where the growth rates are largely determined by rates of surface diffusion of carbon atoms. A quite similar diffusion of metal atoms effects metallization of micrometer-sized features [62].

The mechanisms of the nanoscale plasma etching, especially in long trenches with the thickness of $\sim$10 nm, are not fully understood. However, there is a consensus on the crucial role of the reactive plasma ions which is explained in Figure 28(a) and 28(b). First, the ions can penetrate much deeper into the trenches because of the higher energies, better transport directionality and longer free paths compared with the neutral radical species. The ion incidence angles are crucial and they are determined (similar to the ion interactions with CNT arrays in Figure 7(e)) by the plasma sheath width (hence, the ion energy), the microscopic topology of the electric field near the channel mouth (similar to Figure 7(c)), and the gas pressure.

For virtually any pattern of the etching features, the plasma parameters can be adjusted to maximize the ion incidence along the channel axis thereby enabling deep penetration into the features. Near the feature mouth, the impact of neutral species usually leads to the more isotropic etching, while the ion impact leads to the highly anisotropic etching at the bottom. This is also consistent with the dependence of the etch yield on the ion energy in panel (b). However, since the density of neutrals in weakly ionized plasmas is much higher than the ion density, the increase of the ion-to-neutral density ratio leads to the better etch anisotropy, yet at the expense of the etching rates.

Therefore, the ions should be delivered straight to the bottom of the channel, without impacting on the side-walls. This leads to the yet unsolved problem of long-range 'ion shooting' with nanometer precision including the long flight through the nanometer-thick channel. One of the obvious complications is that the features get charged during the plasma exposure and the dynamically varying charge distribution is very difficult to measure or compute. These charges distort the ion trajectories from straight downward paths thus compromising the etch anisotropy.

This is why one of the most popular modern approaches to simultaneously improve the etch anisotropy and quality is to use a pulsed DC bias customized to let the surface charge dissipate between the ion flux pulses [289]. This strategy was used to fine-tune the ion flux distribution along the walls and bottom of long dielectric nanopores to enhance the process precision and throughput in nanopore processing and nano-template-assisted nanoarray production [172].

If necessary, the ions can be removed from the etching process by placing a porous carbon plate (aperture) between the plasma and process chambers, where both positive and negative ions can effectively neutralize. This process is known as neutral-beam etching and in many cases shows very high etching precision, such as nearly defect-free atomic-precision sidewall etching [290]. The neutral beam etching was recently used to fabricate 2D arrays of silicon nanodisks for QD solar cells mentioned in Section 4.1.1 [291].

An important feature of the plasma etching is the synergism between the effects of neutral, ions, and photons, which leads to the much higher etching rates compared with the cases when these species are used separately. For example, Si etching by fluorine-based compounds may be dramatically enhanced by ion-assisted effects [288], which are quite similar to those in CNT nucleation and growth (Sections 3.4 and 3.5). A similar synergism is expected to play the key role in the plasma-enhanced atomic layer etching (ALE) sketched in Figure 28(d).

The ALE is based on highly reproducible removal of atomic monolayers using a sequence of self-limiting etching steps [288]. Initially, species B are deposited to fully terminate the surface to form a self-limiting monolayer on the surface made of etching material A. Species B merely form bonds with species A without binding to each other. The strength of the B–A bonds [292] should ideally be higher compared with the loosened bonds between the first and the second layers of atoms A.

The plasma ions may be used to energize the B–A bonded species and possibly combine with them to form volatile products and gently etch only one atomic layer of atoms A. The ion energy should be adjusted to be less than the sputtering energy, yet should be enough to facilitate the formation of the volatile compounds and then detach them from the surface after breaking the already loosened bonds between the first and the second layers of the etched material.

This process should also be self-limiting. The energy of the plasma ions and their affinity to atoms A should also be insufficient to cause any damage to the second layer. The plasma-assisted ALE was studied both experimentally and theoretically for a relatively small number of materials [293,294].

A new trend is using self-organized masks, e.g. made of a self-assembled monolayer of polymer nanospheres, followed by the precise pattern transfer using highly selective, highly anisotropic plasma etching (Figure 19(a) and 19(b)). Another example in Figure 28(e) and 28(f) evidences precise transfer of self-assembled patterns of block polystyrene–polymethylmetacrylate copolymers onto a Si substrate [25]. The plasma etching takes place in nanoscale gaps between the polymer nanoribbons and deepens into the Si wafer by $\sim$100 nm.

Despite excellent precision in pattern transfer, this process requires mask preparation before the plasma etching. This raises the obvious question if the first step can be avoided and the self-organized masks could be formed during the plasma process. The following subsection gives a positive answer to this question.

4.5.2. *Self-organized arrays of inorganic nanotips*

Fabrication of self-organized arrays of Si nanotips (Figure 2(b)) by self-masked plasma etching has been mentioned in Section 2.1. This effect is fairly generic and was also demonstrated for a large number of materials systems including Si, GaN, Sapphire, and Al (Figure 29(a)–(d)). This self-masked dry etching technique can be implemented over large surface areas and at low process temperatures. The etching leads to good uniformity of 3D solid NSs, in terms of their sizes, shapes, and positioning on the substrate [44].

The growth mechanism of these nanoarrays is explained in Figure 29(e) and 29(f). To produce self-organized SiC nanomasks, plasmas in a mixture of silane and methane gases are used as sketched in panel (e). As a result, a pattern of small SiC NPs forms on the Si surface. This process

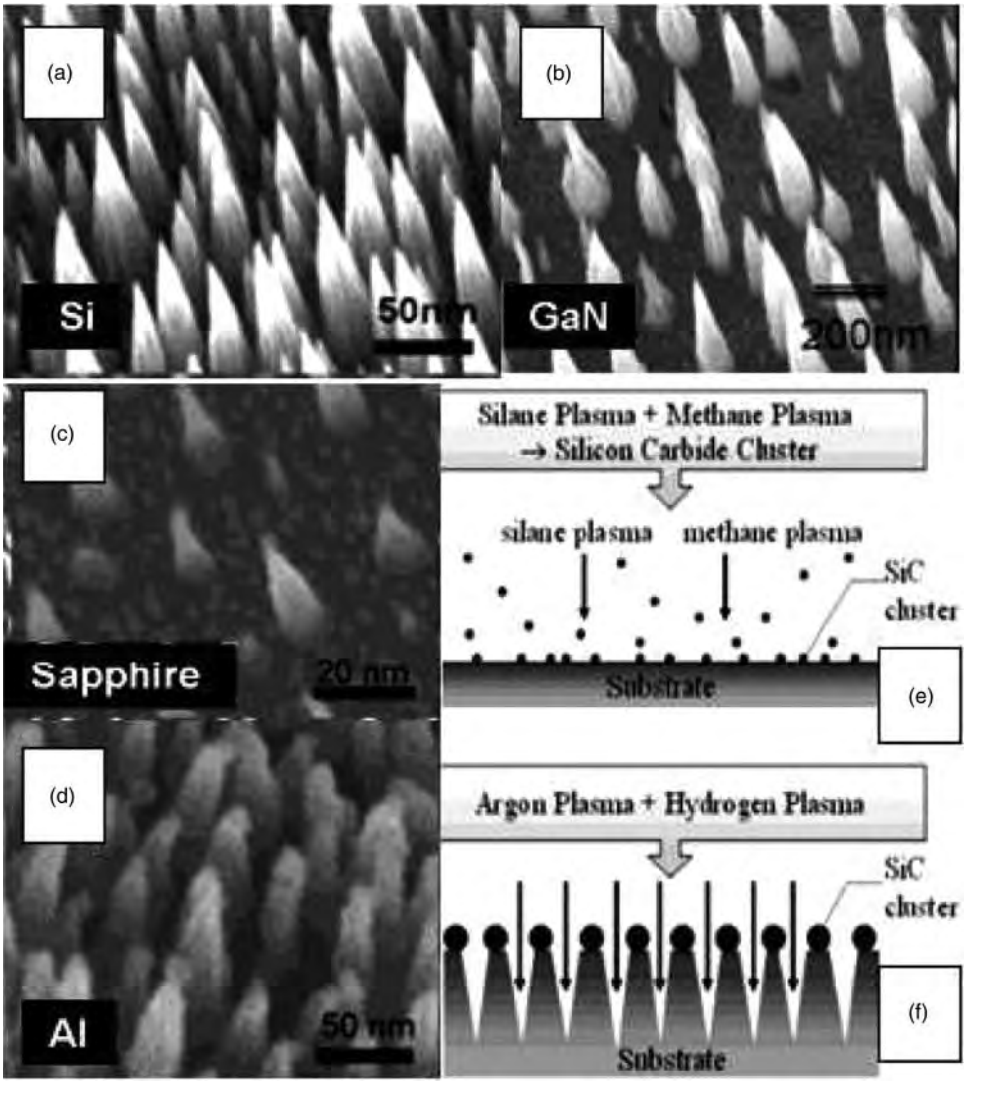

Figure 29. Self-organized arrays of inorganic nanotips fabricated by self-masked plasma etching on: single-crystalline Si (a); epitaxial GaN on sapphire (b); sapphire (c); and Al (d). Two main process steps (e,f) [Reprinted with permission from [44], Copyright © 2004 American Chemical Society].

is quite similar to the growth of self-organized arrays of SiC QDs mentioned in Section 4.1.3. The size of these NPs determine the size of the apex of the conical structures that form during the second stage as shown in Figure 29(f). During this stage, plasmas of $Ar+H_2$ mixtures are used. The degree of size and positional uniformity of the SiC NPs over the surface determine the quality of the resulting Si nanoarrays.

According to the results of several groups, the quality and effectiveness of the plasma etching is the best when both Ar and H_2 gases are used [41,44,295]. This further evidences the synergistic effects of the ionic (Ar^+ in this case) and reactive radical (H in this case) plasma species during the etching process (Section 4.5.1).

This also implies the competition between the physical sputtering, chemical etching, and material redeposition on the surface during the nanoarray formation. For example, in panels (b), (c), one can spot small cones between the large ones. They may be formed through the ion shadowing effects [295]. Another possibility is redeposition of material followed by the nucleation of the secondary nanoarray between the large cones similar to Figure 12(c). Formation of fairly rare arrays with clear-cut faceted structures suggests that nucleation followed by the crystal reshaping under non-equilibrium conditions (similar to Figure 4) may dominate over the etching effects [296,297]. Conversely, very dense arrays of Si nanograss or nanotips with very high aspect ratios are believed to form predominantly through the Ar^+ ion-assisted reactive etching of Si surface by reactive H radicals which form volatile SiH_x products upon interaction with the surface.

Compared with the approach of Section 4.5.1, the self-masking etching relies on self-organized patterns of small clusters that serve as masks. The smallest tips of the sharp conical Si structures could be ∼1 nm [44]. This means that the SiC clusters of a comparable size can be very effective as etching masks. On the other hand, a dynamic interplay of physical sputtering and chemical etching effects may also lead to the nanotip sharpening and the formation of the structures with different apex angles. This ability is of particular interest for customized, bio-inspired biophotonic arrays [42].

These arrays represent regular conical structures where the refractive index ($n(z)$) effectively varies from the substrate toward the tip of the nanocones. This makes it possible to create sub-wavelength anti-reflection surfaces where non-uniformity of $n(z)$ can be approximated by several layers with slightly different refractive indexes n_i [42]. The effective refractive index of such anti-reflection arrays n_{eff} can be fairly accurately calculated from

$$\sum_{i=1}^{k} f_i \frac{n_i^2 - n_{\text{eff}}^2}{n_i^2 + 2n_{\text{eff}}^2} = 0 \tag{67}$$

using Bruggeman's effective medium approximation [298]. In Equation (67), f_i denotes the corresponding volume fraction of ith layer, which decreases toward the summit of the nanotips.

However, the features produced through the self-masked etching are usually not as straight as in Figure 28(a), which suggests that the anisotropy of this etching process requires improvement. Nevertheless, this etching can also be considered as an example of nanoscale plasma etching because of the localization of the plasma–surface interactions within the open spaces between the small clusters that form a self-organized mask. This undoubtedly one of the most interesting plasma-enabled nanofabrication processes still warrants a significant theoretical and numerical modeling effort.

It was recently demonstrated that a p-type Si wafer attains a high-quality *p–n* junction and a very strong photovoltaic response only when nanoconical structures are formed on its surface [299]. The available interpretations involve several effects that may lead to the *p*-to-*n* type conductivity conversion [24]. However, the question why this effective conversion only takes place when a self-organized nano-texture on the Si surface is formed, remains open. Nevertheless, this result is a clear demonstration that surface-supported self-organized Si nanoarrays produced through the effects of nanoscale plasma–surface interactions, may also lead to the unusual and promising ways of achieving specific materials properties for the pursued applications.

Indeed, the formation of *p–n* junctions for crystalline Si-based solar cells is usually implemented as a separate thermal diffusion process which raises significant environmental concerns [24]. In this example, the high-quality *p–n* junction was formed, and subsequently, the effective photovoltaic response of ∼12% was achieved without the seemingly unavoidable diffusion process. The photoconversion efficiency of this type of solar cells was subsequently

improved to above ∼18.5% by precise (and also plasma-based) surface passivation by SiN layers [24] (please also see discussion on the role of surface passivation of nanocrystals in Section 4.1.1).

4.5.3. *Carbon nanotips*

CNTPs is a typical example of 3D NSs. Several plasma-based approaches have produced CNTPs in various shapes (e.g. cone-like, needle-like, pyramid-like, etc.), aspect ratios, and bonding states. Typical examples of CNTPs are shown in Figure 30. These structures differ by the structural stacking of carbon atoms and show examples of sp^3 diamond (a) and (b) and sp^2 single-crystalline (c)–(f) nanotips. Morphologically, these NSs are quite similar to the Si nanotips of Section 4.5.2 and in some cases feature comparable aspect ratios and array densities (see, e.g. Figure 12(c)).

However, owing to the much higher bonding strength, chemical stability, and melting temperatures compared with Si, it is very difficult to produce such NSs by the direct plasma etching. This is why common plasma-based approaches to synthesize CNTPs involve various combinations of catalytic growth, CVD and PVD, physical sputtering, and chemical etching effects. In most cases, the growth temperatures are significantly lower compared with similar thermal processes. Plasma-assisted techniques have also been used to customize the nanotip properties for specific applications.

For example, a combination of hot-filament and plasma CVD, complemented with ion flux control using DC bias was used to produce arrays of amorphous CNTPs [302]. Graphitic carbon films are commonly used to facilitate the nanotip formation and also serve as conducting support in EFE devices. Historically, the field emission display technology has been perhaps the most common targeted application of the CNTPs. This application demands high-aspect ratio and sharp tips for better electron emission, conducting channels in the NSs to sustain electric current, and also excellent structural stability to prolong the device lifetime.

From the structural stability perspective, diamond nanotips are very attractive. However, it is challenging to synthesize diamond NSs with high aspect ratios and acceptable conductivity. Both these problems were solved using plasmas [300]. First, high-quality ∼1 μm-tall diamond nanotips with the base width of ∼150–200 nm, firmly standing on the diamond/Si substrate were produced (Figure 30(a) and 30(b)). This carbon nano-phase is thermodynamically less stable than graphitic carbons and usually requires very high temperatures and pressures.

These conditions were partially avoided using relatively high-power MW plasmas of $Ar+CH_4+H_2$ gas mixtures which created a strongly non-equilibrium environment even at pressures ∼0.14 Torr, which are much lower than typically used in PECVD of diamond films (∼1–10 Torr or even higher). The diamond nanotips showed a good sp^3 structural quality and phase purity. It is thus not surprising to see a nearly zero electron emission current in Figure 30(a).

This problem was also solved by implanting nitrogen ions produced in N_2 plasmas. This relatively low-dose ion implantation has led to the effective substitutional doping by N atoms, rearrangements of sp^3 atomic bonds into sp^2 in localized areas, and presumably, the formation of conductive paths along the nanotips. As a result, the electron emission was not only enabled (5 min treatment in panel (a)), but also dramatically improved by precisely dosing the exposure to nitrogen ions (10 min). Very competitive EFE characteristics were achieved without any significant structural damage to the nanotip exterior structure.

The CNTP growth and shaping is a kinetics-driven process under non-equilibrium conditions where several plasma-specific effects play a key role. Figure 30(c)–(f) shows single-crystalline CNTPs made of horizontally stacked graphene sheets (panel (d)) which were synthesized in low-pressure $Ar+CH_4+H_2$ plasmas. High rates of dissociation of H_2 in the plasma enable effective

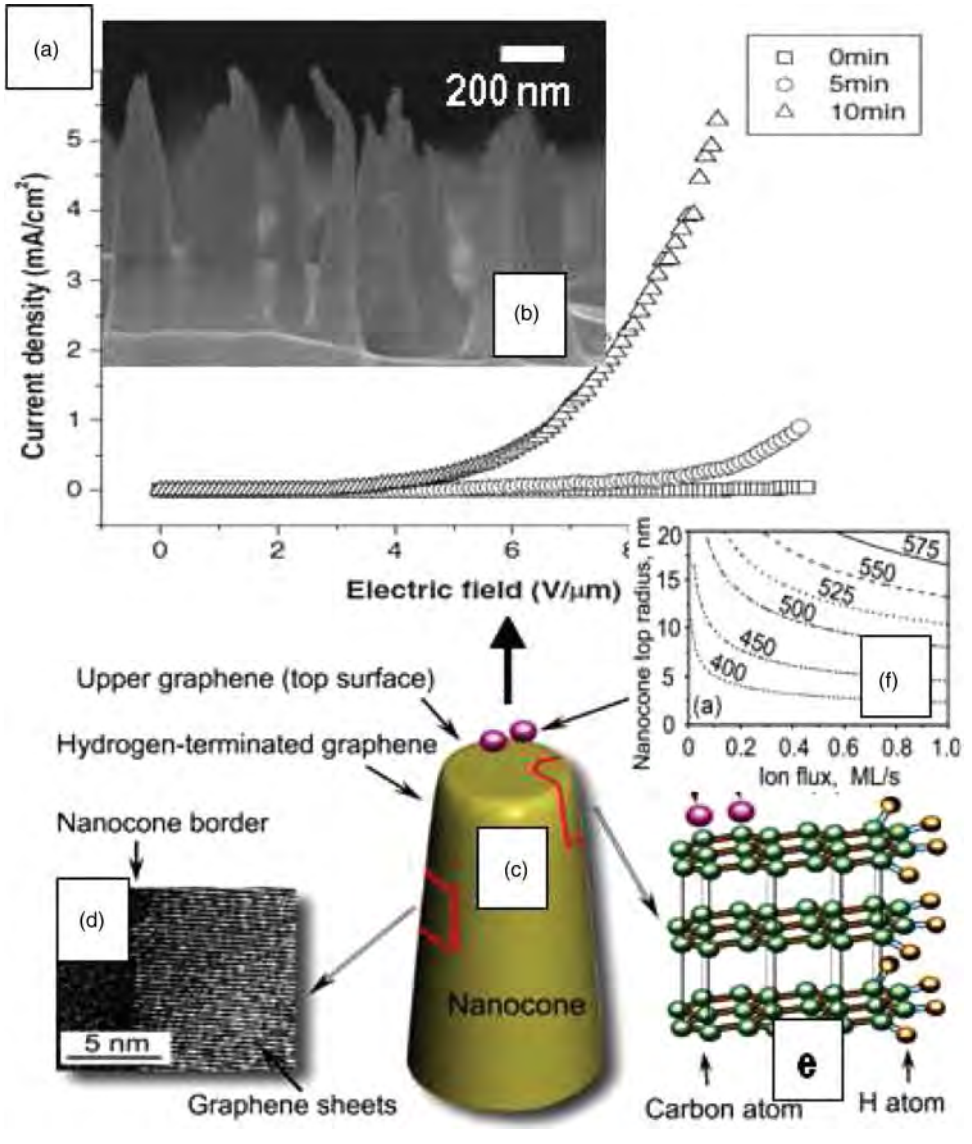

Figure 30. Field emission (a) from diamond nanotips produced by PECVD (b) improved by N_2 plasma immersion ion implantation [Copyright ©IOP Publishing. Reproduced from [300] by permission of IOP Publishing. All rights reserved]. Structure and mechanism of self-sharpening of single-crystalline carbon nanocones (c) made of a vertical stack of graphene layers terminated by hydrogen at the edges (HRTEM image (d) and atomic sketch (e)); nanocone top radius versus ion flux at different surface temperatures (f) [Reprinted with permission from [301], Copyright © 2007 American Institute of Physics].

termination of the open egdes of the graphene layers (panel (e)), which is an important pre-requisite of structural stability of this type of single-crystalline NSs.

These structures also self-sharpen during the growth to form high-aspect-ratio tapered needle-like structures [301]. This self-sharpening is related to the plasma-specific effects, most prominently, the ion fluxes to the flat top of the nanocone (panels (c) and (f)). This is yet another manifestation of the major role of the *nanoscale* plasma–surface interactions.

The variation of the carbon atom density on the flat top (a few nm across) of the nanotip in Figure 30(c)

$$\frac{\mathrm{d}n}{\mathrm{d}t} = \Psi_{\mathrm{i}} - \Psi_{\mathrm{d}} - \Psi_{\mathrm{e}} - \Psi_{\mathrm{c}} \tag{68}$$

is determined by the dynamic balance of the incoming Ψ_{i} and outgoing diffusion Ψ_{d}, thermal Ψ_{e}, and ion-induced Ψ_{c} detachment fluxes of carbon material. The critical radius for graphene nucleus formation is derived using Equation (68) under the steady-state, quasi-equilibrium conditions, and is shown in Figure 30(f). The top radius of the nanotips is in a very good agreement with the experimental results and can also be controlled by the microscopic ion flux and the surface temperature [301].

Importantly, the ion bombardment plays a critical role. Indeed, ion sputtering determines the *a*-CNTP shapes [302] consistently with Sigmund's incidence-angle-dependent sputtering theory [58]. In Figure 30, a moderate negative bias improves the structural quality of diamond and single-crystalline sp^2 nanotips, possibly due to the ion-assisted crystal densification [303]. Additionally, a high-voltage bias leads to effective nitrogen ion implantation which enables the field emission from the diamond nanotips (b) without any significant structural damage.

In addition to the strong EFE, amorphous CNTPs have also recently proved effective as sources of spectrally tunable PLE [304]. Importantly, plasma-specific effects may help adjusting the prevailing factors that determine the PL wavelength and intensity.

For instance, one common possibility to generate PL emission is through the radiative recombination of the electrons and holes in the band tail of sp^2 carbon clusters, which are created by photo-excitation of π and π^* states [305]. However, the size of spatial confinement of luminescence centers in sp^2 carbon clusters should be in the 0.94–1.15 nm range to enable direct $\pi - \pi^*$ band transitions [306]. The size $L_{\mathrm{cl}}^{sp^2}$ of these clusters can be estimated using

$$L_{\mathrm{cl}}^{sp^2} = (\alpha_1 + \alpha_2\lambda)\frac{I_{\mathrm{G}}}{I_{\mathrm{D}}}, \tag{69}$$

where λ is the excitation wavelength, and $\alpha_{1,2}$ are constants. Here, I_{G} and I_{D} are the intensities of the G- and D-peaks in Raman spectra, respectively. Here, we recall that the G-peak determines the degree of graphitic order, while the D-peak quantifies the degree of disorder and owes to the presence of defects, clusters, etc. in the structure.

From Equation (69), one can see that a larger number of smaller structural defects (which corresponds to the higher intensity of the D-peak) may be advantageous to generate PL due to the direct $\pi - \pi^*$ band transitions. The smaller sp^2 cluster sizes also lead to shorter bonds between carbon atoms and consequently, a wider bandgap. The increased separation between the π and π^* states leads to stronger PL emission at higher photon energies (e.g. shorter wavelengths, typically in the UV range). The reduced spatial localization of emission centers also leads to broader band tail distribution, which increases the PL quenching temperature T_q thereby increasing the PL intensity according to

$$\eta_{\mathrm{PL}} \propto \exp\left(-\frac{T}{T_q}\right), \tag{70}$$

where T is the measurement temperature. In this way it is possible to tune the emission wavelength and intensity to achieve stable room-temperature luminescence, which is particularly important for optoelectronic applications.

There are other mechanisms to tune the PL from CNTPs, e.g. by controlling the hydrogen and nitrogen contents. Some of these mechanisms are similar to the mechanisms of PL from C-dots

briefly discussed in Section 4.1.1.3. Addition of small amounts of nitrogen, for example, lead to sp^3 C–N bonds which enable transitions between the π^* and lone pair valance bands. These transitions produce optical emission with a longer wavelength compared with the direct $\pi - \pi^*$ band transitions, typically in the green range of the optical spectrum.

As discussed earlier in this review, plasma effects are particularly suited to generate a significant number of tolerable defects and also in specific locations. Moreover, high rates of dissociation of nitrogen can be used to control the degree of CNTP doping, and hence, the presence of nitrogen-related radiative sites. This is why it is not surprising that plasma-produced and/or processed CNTPs are quite promising for the development of next-generation optoelectronic devices with tunable spectral responses [304].

4.5.4. *Nano-diamond*

Let us consider three common types of nano-diamond materials, namely nanocrystalline diamond (NCD), ultra-nanocrystalline diamond (UNCD), and diamond NPs. NCD films contain clearly faceted diamond nanocrystals, typically of a columnar shape and a size of several hundred nanometers. Morphologically, NCD is quite similar to columnar microcrystalline Si films with a large percentage of the crystalline phase. UNCD is a morphological analog of *nc*-Si of Section 4.1.1 and features small diamond nanocrystals (typically 3–5 nm) randomly dispersed in an amorphous carbon matrix. The grain boundaries are typically less than 0.5 nm. Diamond NPs can in turn be surface-supported or freestanding. Plasma processes were used in all three cases and in many cases led to superior outcomes.

UNCD is optically transparent and is pursued for highly conformal coatings of micro- and nanometer features. Excellent biocompatibility also makes UNCD ideal for microelectrode arrays in 'bionic eye' retinal implants. Relatively high-power-density MW plasmas in hydrocarbon gas mixtures are typically used to synthesize UNCD. Relatively high (e.g. ∼700–800°C) temperatures and pressures (e.g. ∼1–10 Torr) are typical; yet they are typically much lower compared with thermal CVD. Detailed studies of optical emission during the growth process have identified carbon dimers C_2 as possible BUs of ultrananocrystalline diamond [307]. This emission is dominated by the $d^3\Pi$–$a^3\Pi(0,0)$ Swan band of C_2 species and is characteristic to UNCD of both laboratory and astrophysical origins [308]. Recent numerical studies reveal a range and specific roles of the plasma species involved in UNCD growth [309,310].

The film thickness is typically in the micrometer range, and while the density of sp^3 nanocrystallites in an *a*-C matrix can be quite high, the material quality has often been an issue. Among them, achieving void-free, dense nucleation of small diamond nanocrystallites of fairly uniform size has been challenging. This issue has escalated with the continuously increasing demand for nm-thick UNCD films.

To increase the density of nucleation, small nano-diamond seeds are used. These seeds help achieving continuous films and void-free interfaces. Figure 31(a) and 31(b) shows an example of an ultra-thin, mirror-smooth, and void-free (∼30 nm) UNCD film [311] grown in CH_4+H_2 DC plasmas. The density of ultrasonically dispersed small (intentionally chosen in the typical UNCD size range of 3–5 nm) nano-diamond powder was in the 10^9–10^{11} cm^{-2} range, which is a typical surface density of QDs of Section 4.1.1. The plasma exposure has also led to markedly increased density of the diamond nanocrystals, presumably due to the secondary nucleation.

This observation is supported by the reports on the effective control of the nucleation density and the nanocrystal sizes by the surface bias. In particular, it is commonly observed that the grain size decreases when a larger negative bias is used. This effect is believed to be due to the continuous secondary nucleation within the developing film [313], which is quite similar to the previous example.

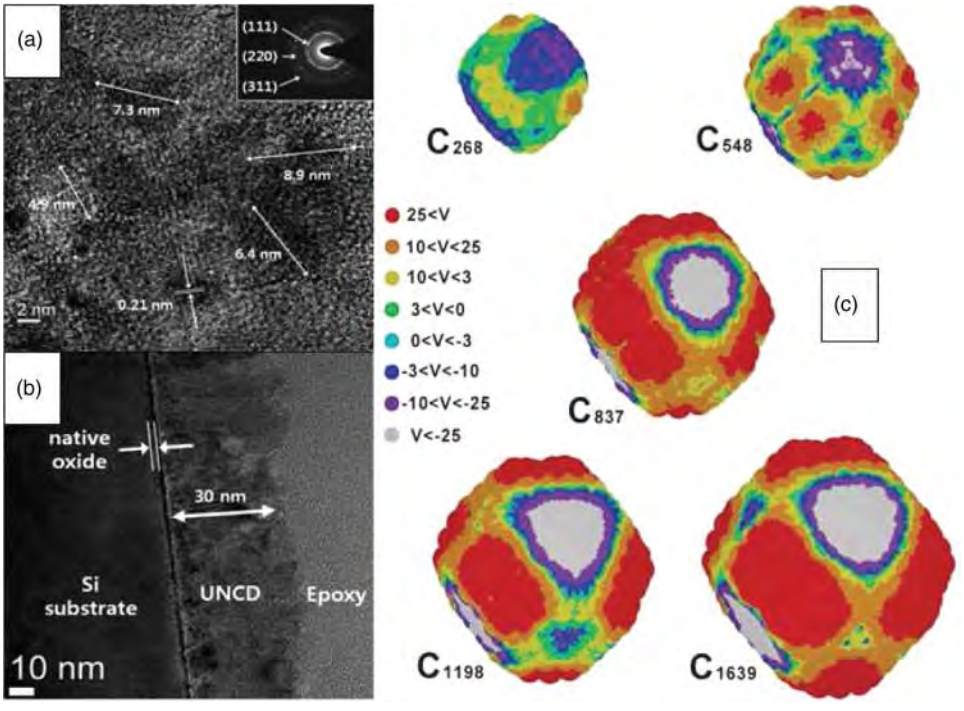

Figure 31. Plan-view HRTEM (a) with diffraction pattern (inset) and (b) cross-sectional HRTEM of ultra-thin UNCD film grown by PECVD [Reprinted with permission from [311], Copyright © 2011 American Institute of Physics]. 3D distributions of the normalized surface electrostatic potential over the facets of small nano-diamond crystals of different sizes and shapes computed using the density functional based tight binding method with self-consistent charges (c) [Reproduced from [312] by permission of the Royal Society of Chemistry].

As mentioned above, small diamond nanocrystals nucleate and grow within an amorphous carbon matrix; this process was studied using MD simulations [309,314]. These simulations explained the experimental observations and, in particular, showed that the plasma-produced $C_xH_y^+$ and H_x^+ ions penetrate into the carbon matrix and cause complementary effects. $C_xH_y^+$ ions induce nucleation of sp^3 clusters, which leads to the higher density of diamond nanocrystals. When the electric field is strong enough (e.g. bias exceeds -100 V), fairly deep incorporation of H^+ ions leads to the smaller crystal sizes. Moreover, stronger electric fields lead to the formation of sp^2 bonds in the nanocrystalline phase and a larger number of three-coordinated C atoms in the amorphous phase.

Concurrent plasma-assisted nitrogen doping has dramatically (nearly five-order-of-magnitude) improved the UNCD *n*-type electrical conductivity [307]. This phenomenon was explained by the increased grain sizes (up to $\sim$12 nm) and grain boundaries (up to $\sim$1.5 nm), where the content of sp^2 bonds also increased. The conduction path most likely formed along the sp^2-rich grain boundaries and involved π states of carbon [307].

Free-standing nano-diamond crystals also benefit from plasma effects. Indeed, applications of nano-diamonds in quantum computing, medical diagnostics, drug delivery, and luminescent imaging require uniform surface functionalization. For example, surface termination of diamond nanocrystals with hydrogen eliminates dangling sp^2 bonds from the surface [315] and stabilizes the nanocrystal, similar to Figure 16(a). Thermal hydrogenation usually requires temperatures $\sim$900°C and even higher. These very high temperatures are typically well above the melting temperatures of small NPs, which may be detrimental to the crystalline order in nano-diamond.

Plasma hydrogenation has recently been shown as an effective remedy to this problem. This treatment leads to the formation of C–H bonds on the surface of diamond nanocrystals, which also showed the unusual hydrophobic properties [316]. Plasma exposure also induces hydrophilic response from diamond surfaces functionalized with ketone-related groups or carboxylic acids [315].

An interesting point to stress is the synergistic effects of the small nano-diamond seeds and the plasma-specific effects in the UNCD nucleation and growth. In a sense, these seeds serve as catalytic supports for the void-free nucleation of the new diamond nanocrystals. As we have seen in Section 4.2.1, it is possible to avoid using catalyst in the plasma-based nanotube growth. This sparks a similar question if it is possible to completely avoid seeding in the plasma-assisted UNCD growth.

The most important consideration is how to produce or deliver similar seeds otherwise. One option would be to very carefully balance the supply of carbon atoms and the process parameters to ensure a sufficient density of 'natural' sp^3 cluster nucleation sites on the surface. As we have seen from the above examples, the best results in terms of UNCD film quality (Figure 31(a) and 31(b)) are achieved when the nano-diamond seed density is in the 10^9–10^{11} cm^{-2} range.

Interestingly, plasmas in methane–hydrogen mixtures were shown to reproducibly generate very dense arrays ($\sim 10^{12}$ cm^{-2}), of size-uniform ($\sim$10 nm) orientationally ordered (001) diamond nanocrystallites on Ir substrates [130]. These arrays emerge under far-from-equilibrium conditions when the surface bias is abruptly terminated followed by the rapid thermal quenching. It is thus worth exploring these ultra-dense arrays for UNCD seeding. However, it appears challenging to stabilize these metastable arrays and prevent a rapid island coalescence when more material is added during the growth. This work is also very relevant to the earlier discussion of self-organized kinetic processes and emergent metastable patterns on plasma-exposed surfaces in Sections 2.3 and 3.6.

Another possibility is to assemble small amorphous NPs in the ionized gas phase and then transform them into crystalline UNCD seeds upon impact onto the growth surface. The possibility of transformation of carbon nano-onions (which can realistically form in the gas phase of both space and laboratory plasmas) into nano-diamonds upon surface impact has recently been demonstrated by *ab initio* numerical simulations [317]. The transformation is kinetically driven over picosecond time scales. This strongly-non-equilibrium process is potentially a new approach for the UNCD growth.

Plasma methods of nano-diamond synthesis are also energy efficient. For example, high-quality NCD films were produced at a low temperature of $\sim$450°C while the MW plasma power was reduced in 50 times [318]. This process is converse to the UNCD case and requires suppression of the secondary nucleation, which promotes columnar growth.

An interesting opportunity exists in the highly controlled synthesis of size- and facet-specific nano-diamond crystals. *Ab initio* numerical simulations [312] show that by tuning the nanocrystal size and facet expression, it is possible to very significantly redistribute electric charge over different facets as shown in Figure 31(c). Consequently, facets with the higher electrostatic potential (e.g. red) will attract to the facets with the lower potential (e.g. gray). This effect creates an opportunity to use these nanocrystals as building blocks and the arising polarization effects in the controlled assembly of wire-like, patterned, or compact nano-diamond assemblies. A quite similar effect was discussed for the plasma-generated silicon nanoclusters in Section 4.1.1.2. A plasma-based approach toward the synthesis of made-to-order diamond-like nano-carbons is discussed elsewhere [319].

4.5.5. *Soft organic matter*

Plasma-specific effects also enable many interesting features in the synthesis, surface structuring, and processing of soft organic nanomaterials such as polymers. This class of materials is

highly promising in many fields such as health care (e.g. biomedical implants or drug/gene delivery systems), organic optoelectronics (organic light-emitting diodes), photovoltaics, and nanoelectronics.

The common issues in the synthesis, processing, and device integration of such materials are high temperature sensitivity (due to low melting temperatures), structural and morphological controls at micro- and nanoscales, modification of surface energy to enable a certain functionality, gas-phase control of cross-linking and macromolecular BUs, conformity of ultra-thin polymer layers to nanometer-sized surface features, and several others. Importantly, unique physical and chemical effects due to low-temperature plasmas in many cases help resolving these issues.

The two most common examples include plasma-produced polymers (commonly referred to as *plasma polymers*) for surface coatings with nanometer dimensions as well as precise control of surface energy by nanoscale surface texturing and/or functionalization. Owing to the very high reactivity of the plasma, these effects can be achieved even at room temperature. Figure 32 shows typical examples of low-temperature nano-structuring of polymer surfaces (panels (a)–(g)) and conformal deposition of ultra-thin plasma polymers on nanometer-sized features (panels (h)–(i)).

The plasma polymerization is unique because of the large variety of reactive species produced through the plasma-assisted fragmentation and remodeling of monomer precursors. As a result, a cocktail of original precursors, reactive radicals, non-radical neutrals, macromolecules, ions, electrons, and photons are generated. The large species produced have different structures (e.g. linear or aromatic) and charging states (cations, anions, or neutral). For many years, it was commonly assumed that merely neutral radical and molecular species play a role in the plasma polymerization [320].

However, recent advances have revealed a crucial role of the plasma ions which was commonly overlooked. Specifically, this role is evidenced by the recent demonstration of very large ions whose masses are several times larger than the masses of original precursors. Moreover, the plasma ions can supply as much as 50% of the mass of the deposited polymeric films [325]. This is supported by calculations and direct measurements showing that the ion fluxes during the synthesis of plasma polymers can be comparable to or even larger than the fluxes of neutrals. This conclusion is very similar to the results of other authors [88,94] discussed in Section 3.1.

The numerical modeling results also confirm that ion-neutral reactions trigger plasma polymerization and lead to the production of macromolecules and nanoclusters of various structures including chains and aromatic rings [326]. For example, generation of higher hydrocarbon species in acetylene plasmas proceeds via different pathways, triggered by the positive $C_2H_2^+$

$$C_2H_2^+ \rightarrow C_4H_2^+ \rightarrow C_6H_4^+ \rightarrow C_8H_6^+ \rightarrow C_{10}H_6^+ \rightarrow \cdots, \tag{71}$$

and negative C_2H^-

$$C_2H^- \rightarrow C_4H^- \rightarrow C_6H^- \rightarrow C_8H^- \rightarrow \cdots, \tag{72}$$

molecular ions. Both channels (71) and (72) produce comparable contributions [326].

This is another manifestation of the complexity of plasma polymerization in organic precursors compared with silane plasmas where negative ion (anion) – triggered nanocluster formation pathway is dominant [149] (see also Section 4.1.2). These uniquely plasma-specific ionic polymerization pathways have been largely overlooked in the earlier classical models [320].

These effects lead to high-quality, conformal, and defect (e.g. pinhole, pore, etc.)-free nanometer-thick polymer films. One such example is shown in Figure 32(h) and 32(i), where highly conformal coating with ultra-thin films of allylamine plasma polymer was used to reduce the thickness of nano-channel openings in an alumina nanoporous template. This thickness gradually reduced as the time of the plasma treatment increased. As a result, it was possible to control the rates of release of a vancomycin drug from the plasma polymer-coated channels [324].

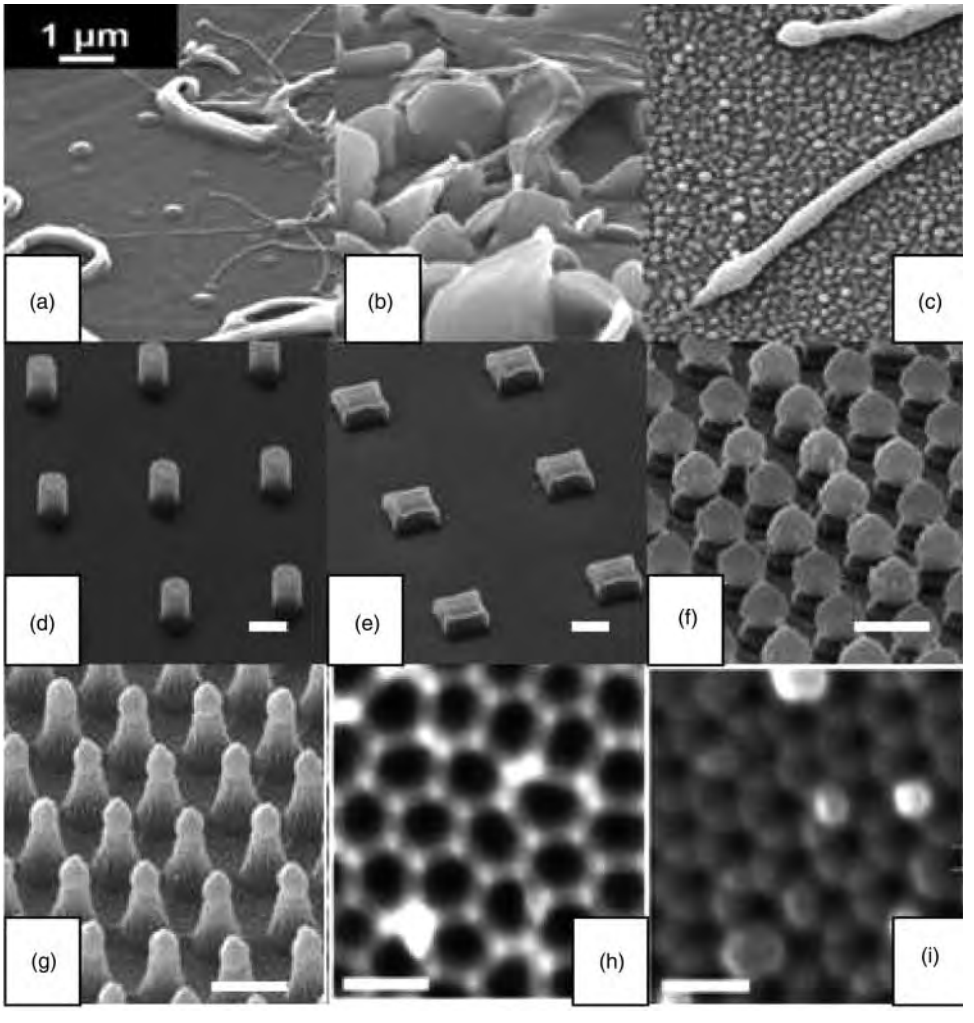

Figure 32. Plasma nano-polymers. Osteoblast cells on ribbon-like (a), petal-like (b), and nanodotted (c) polymers nanostructured in CF_x plasmas [Reproduced with permission from [321], Copyright © 2010 Wiley-VCH Verlag GmbH & Co. KGaA, Weinheim]. Ordered nanoarrays [panels (d) and (e) reproduced with permission from [322] Copyright ©2007 Wiley-VCH Verlag GmbH & Co. KGaA, Weinheim; panels (f) and (g) reproduced from [323] by permission of IOP Publishing. Copyright ©IOP Publishing. All rights reserved] produced by plasma etching. Conformal coating with nanometer precision allows tuning nanopore openings in nanoporous templates (h) and (i) [Reproduced from [324] with permission of the Royal Society of Chemistry]. Scale bar of 1 μm in panel (a) applies to all panels (a)–(c). Other scale bars: 200 nm (d) and (e); 1 μm (f) and (g); and 200 nm (h) and (i).

A very important feature of the plasma polymer nanofilms is their outstanding compatibility and adhesion with most of the commonly used inorganic substrates (e.g. silicon, gold, etc.). A likely reason is the ability of the plasma to suitably prepare the deposition surface (including surface areas with nanometer dimensions) as discussed in Section 3.3. This feature makes plasma polymers suitable for biomedical implants, *in vivo* sensing, and drug delivery systems in nanomedicine.

Low-temperature reactive plasmas are also very effective for the precise control of the surface energy through the nanoscale surface texturing and/or functionalization. The surface texturing can

be implemented in two ways, namely using the bottom-up and top-down approaches. The top-down approach is most commonly implemented using the plasma etching (e.g. in oxygen plasmas) and nanopattern transfer using pre-fabricated or self-organized masks to produce a variety of ordered nanopatterns and arrays, see examples in Figure 32(d)–(g) [322,323]. This approach is very similar to Figures 28(e) and 28(f) and 19(a)–(d).

Nanoscale etching in oxygen plasmas was also effective in processing and branching of single-crystalline organic (e.g. metalloporphyrin, metallophtalocyanine, and perylene) NWs [327]. This nanoscale plasma effect still requires adequate theoretical interpretation.

Recently, it also became possible to produce self-organized polymer nanopatterns without using any etching masks (Figure 32(a)–(c)) [321]. Mechanisms of the plasma-specific controls of the surface roughness in the bottom-up self-organization-led processes have been proposed [328]. Some of the relevant effects such as the surface stresses, heating, ion bombardment, and charging are quite similar to Figure 12(a) and 12(b). However, the major difference between the hard and soft matter cases is in the overwhelming importance of the structural and compositional polymer surface transformations even under relatively mild plasma exposures.

This is why it is very difficult to identify the prevailing driving forces that lead to the formation of the large variety of the observed self-organized patterns on plasma-exposed polymer surfaces. The ease of localized surface melting accompanied with possible structural transformations of polymeric chains is one of the critical factors which makes the self-organization processes even more non-equilibrium, kinetics-controlled compared with the cases involving hard matter. Nevertheless, the clue to identify the prevailing driving forces should still be in localized *differences* in surface conditions, including the variation in the surface reaction probabilities across the nanostructured surface induced by non-uniform exposure to virtually any constituent of the 'plasma cocktail' (electrons, ions, UV, radicals, etc.).

The plasma non-equilibrium plays a major role in the generation of a large variety of BUs in the gas phase through the electron- and ion-assisted dissociation and remodeling of the original precursor species. This approach is pursued for the development of organic nanomaterials for the next-generation organic nanoelectronic, photovoltaic, and optoelectronic devices [273]. However, the issue how exactly does the plasma non-equilibrium translates into the overwhelming variety of self-organized patterns on reactive plasma-exposed polymer surfaces, remains essentially open. Although some ideas can be drawn from the available knowledge on atomic-precision surface reconstructions using ion beams [61,329], the unique features of soft matter discussed above need to be rigorously taken into account to obtain a consistent description.

Moreover, care should be taken because the plasma treatment very often introduces defects to organic frameworks and additional effort may be required to heal these defects. Self-healing polymers have some advantage in this regard [330]. Thus, there is a clear opportunity to understand the mechanisms of these structural defects and their reconstructions. This knowledge may lead to the optimized plasma exposure, e.g. through the control of fluxes and reactivity of the main species, using remote plasmas, relative contribution of direct ion bombardment, etc. on the one hand and using appropriate polymers with the stronger self-healing ability.

Surface functionalization of soft organic matter also benefits from plasma effects. A combination of the effective production of the relevant functional groups (e.g. OH–, COOH–, NH_x, CF_x, etc.) and activation of the dangling bonds on the surface makes the plasma-assisted polymer surface functionalization particularly versatile. Since these surfaces are usually tailored to enable specific functionalities, the plasma–surface processing should have deterministic features. For example, in bio-recognition of target antigens, it is important to tether relevant antibodies to the surface areas specifically prepared (e.g. patterned) for cell attachment. In the following subsection, we will consider the plasma interactions with biological objects of different sizes and structures.

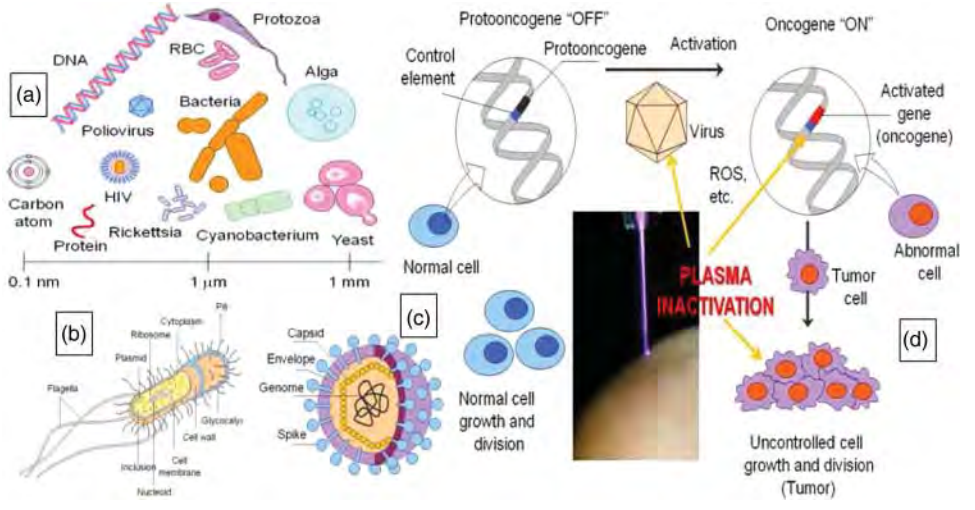

Figure 33. Sizes of biological objects (a). Structure of a bacterial cell (b) and a virus (c). Mechanisms of interactions of plasmas and viruses in cancer activation and treatment (d). Inset shows a tiny (∼10–100 μm) spot of an atmospheric plasma jet in direct contact with human skin. Parts of graphs are re-used and modified with permission from Motfolio, Copyright ©Motfolio.

4.5.6. *Biological objects*

Interactions of gaseous low-temperature plasmas with biological objects has recently become a highly topical multidisciplinary area because of the rapid advances in the plasma biology, health care, and medicine [331–333]. The key focus of these studies are the effects of low-temperature, mostly atmospheric-pressure plasmas on various biological objects of different sizes and structures sketched in Figure 33(a). These effects are relevant to pathogen inactivation in food sterilization, oral hygiene, and treatment of infections, as well as controlling cellular responses in wound healing (e.g. blood coagulation), and more recently, aggressive cancer therapies.

The biological objects range from peptides and proteins with low-nm dimensions and chain-like structure to macroscopic hierarchically structured and responsive tissues and organs. The sizes of cells are in the micrometer range and vary between prokaryotic (Figure 33(b)) and eukaryotic cells which also show very different internal and surface structures. These objects can be treated as microscopic substrates made of soft matter. These 'substrates' feature a large number of organelles (both on the surface and in the intracellular space) with sub-μm dimensions. Viruses are much smaller (typically ∼1–10 s nm) and feature genetic material encased by a layer of capsid proteins and an outer shell (Figure 33(c)).

A nucleus of a typical low-μm size contains long double-helical deoxyribonucleic acid (DNA) structures as sketched in Figure 33(d). Genes responsible for specific cellular responses are located in very small (typically nanometer) localized areas. For example, when an oncogene is activated (e.g. by oxidation involving ROS or by a virus-induced genetic mutation), intracellular signaling pathways (e.g. mediated by specific proteins) trigger faster and often uncontrollable cell growth and division which leads to the development of cancerous tumors. When this happens, the cell first tries to repair any damage caused to its genetic material, and if this is not possible, activates apoptotic (programed death) pathways mediated, e.g. by a 'guardian' protein *p53* [334]. This programed cell death follows a sequence of cellular and then nuclear disintegration steps. The products of apoptosis can be easily removed without any significant damage to the surrounding healthy cells. This approach is highly promising to enable a highly selective reducing of tumors on an otherwise healthy tissue [335]. On the other hand, very different levels of cellular organizations

make it possible to selectively inactivate bacterial pathogens without causing any damage to a healthy skin tissue.

What can the plasma do to help controlling so complex biological responses, both at the cellular and intracellular levels and how can microscopic plasma-specific effects be used? A surprisingly simple yet reasonable answer follows from the approach discussed in Section 3.1. Indeed, to induce the desired (deterministic) biological response (e.g. apoptosis), one should produce suitable biologically relevant reactive species (e.g. reactive oxygen species (ROS) or reactive nitrogen species (RNS), lipid peroxide, etc.) and then deliver them to the specified locations on the surface or in the interior of the cell, where relevant receptors that can trigger the desired signaling pathway are located. Given the microscopic sizes of the relevant surface areas, organelles, and proteins involved, nanoscale interactions of these objects with low-temperature plasmas may be particularly important.

These interactions are fundamentally similar to the microscopic plasma effects in CNT nucleation and growth (Figure 8). However, the specifics of the plasma interactions with biological objects are very different and the relevant studies of these effects are limited [336,337]. Nevertheless, the plasma interactions have been studied for biological objects of different levels of organization, sizes, and dimensionality. While *in vitro* studies at the protein, virus, cell, and tissue levels are quite common, similar studies at the sub-cellular (e.g. organelle, receptor, selected cell surface area, etc.) level are in their infancy.

Strong non-equilibrium of atmospheric plasmas very effectively produces ROS and RNS, such as O, O^*, O_3^*, OH, and NO^*. Similar to oxygen BUs in Figure 6(b), these species are long-living and induce biological responses which are difficult to achieve using other species. For example, ROSs can oxidize the DNA after permeating through the cell membrane and penetrating into the nucleus. Although measurements of the penetration depth of the plasma species into the cells are challenging, biological tests confirm the intracellular effects of the plasma-produced ROS and RNS [338].

These species can penetrate as deep as $\sim 25\,\mu m$ into a multilayer biofilm made of heat- and antibiotic-resistant *Enterococcus faecalis* bacteria and effectively inactivate them in a few tens of seconds [339]. Localized delivery of these species is also significantly affected by microscopic electric fields induced by the cell surface charging in a plasma [336], which is conceptually very similar to the BU delivery and redistribution in the growth of surface-supported NSs in Figure 7.

The energy dose delivered to the cells has to be controlled, as excessive overheating may lead to undesirable cell necrosis, loss of selectivity and even major damage of healthy cell tissues. For example, doses of the plasma exposure below $\sim 1\,J/cm^2$ are appropriate for sterilization and blood coagulation, while larger doses of ~ 2–$6\,J/cm^2$ are suitable to induce cellular apoptosis or cell proliferation effects [340]. Excessive doses of $\sim 10\,J/cm^2$ normally cause necrosis. These effects are quite similar to the control of energy delivery in the nucleation of metal oxide NWs and processing of soft organic matter (Sections 4.2.3 and 4.5.5).

Interesting synergistic effects may arise when reactive radicals and plasma-produced, coated, or functionalized NPs are used simultaneously. For example, the rates of melanoma cancer cell death increased five times after antibody-conjugated Au NPs were added to open air plasmas [341]. The use of specific antibodies improves the selectivity of cancer cell treatment as well as the penetration of the plasma-produced reactive species into the intracellular space which is normally restricted by the cell membrane [342].

Below are a few examples of *in vitro* interactions of atmospheric plasmas with proteins, viruses, and cells. Amyloid fibrils, formed by the protein α-synuclein, which underlies Parkinson disease and the amyloid-β peptide which is associated with Alzheimer disease have been successfully destroyed *in vitro* using atmospheric plasmas [343]. A very effective inactivation of adenovirus cultures was also demonstrated and imaged using green fluorescence measurements upon infecting human embryonic kidney (cell line) 293A host cells with the plasma-exposed viruses [344].

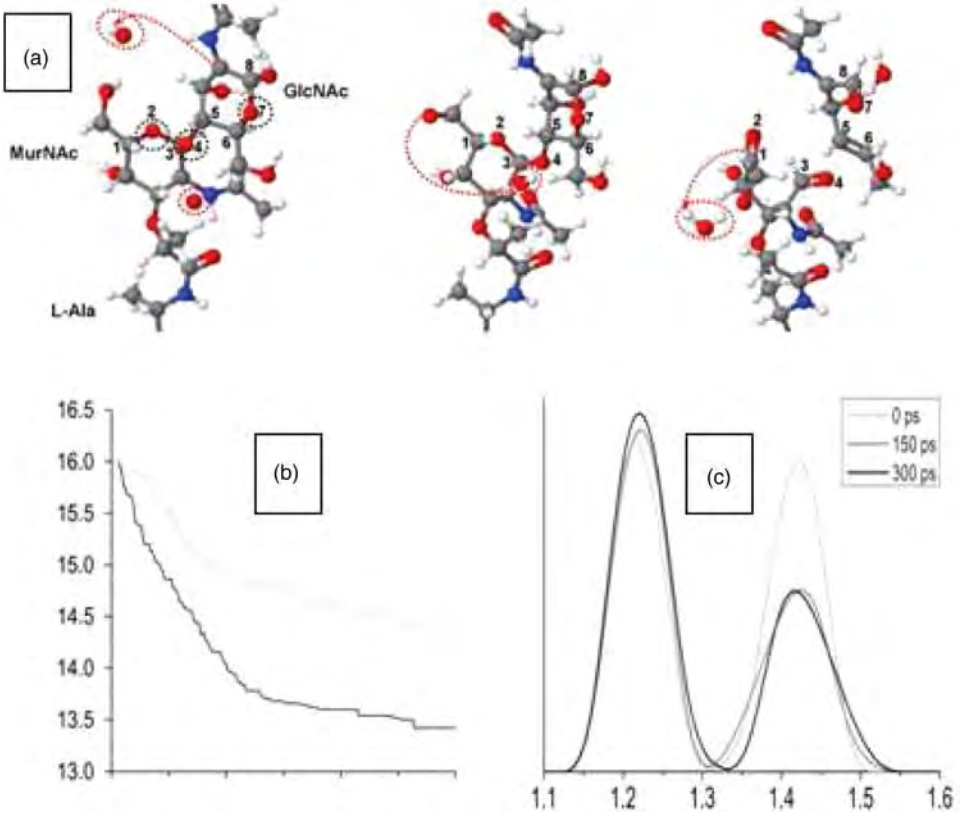

Figure 34. Interaction of reactive plasma species with the PG structure studied by atomistic simulations [346]: (a) breaking mechanism of ether bonds in PG structure by O-radical; (b) evolution of the number of ether bonds due to the interaction of O and O_3 species with PG; (c) radial distribution function of ether bonds in PG. [Reproduced from [346], Copyright © IOP Publishing Ltd and Deutsche Physikalische Gesellschaft. Published under a CC BY-NC-SA licence].

Recently, an effective approach toward the single-cell-level microplasma cancer therapy was demonstrated by confining the plasma plume to the hollow central core of an optical fiber with the inner diameter of approximately 15 μm [345]. As discussed above, this area of the plasma localization is comparable with typical sizes of most of mammalian cells.

Therefore, understanding of atomic-level interactions of the plasma-generated species with peptides and proteins is highly warranted. Recent numerical simulation study [346] reports on the mechanisms of interaction of oxygen-containing radicals with peptidoglycan (PG). PG was used as a model system, as it forms the outer cell barrier of gram-positive bacteria such as *Staphylococcus Aureus*.

It was found that both O-radicals and O_3 molecules effectively break structurally important C–O ether bonds in the murein part of PG, leading to structural damage of the bacterial cell wall (Figure 34). This underlying mechanism is based on multiple H-abstraction, leading to double-bond formation and dissociation of ether bonds. Breaking of C–C and C–N bonds was observed as well.

The subsequent study [347] revealed the mechanisms of interactions of H_2O_2 molecules with PG. In this case, the formation of HO_2 hydroperoxyl radicals is observed. These radicals

are experimentally known to be strong bactericidal oxidants, leading to bacterial inactivation in aqueous environment.

This area presently remains largely unexplored and represents an opportunity for future studies. This can in part be attributed to the fact that numerical simulations of the interaction of the plasma with living cells are far more difficult compared with modeling a similar interaction with solid materials, due to the complexity of their structure and functions in an organism.

We note that in the case in Figure 33(d), viruses may also need to be treated in the intracellular space to avoid their undesirable replication and release of the viral genetic material which may be a strong factor in enhancing the oncogene activation. Also, plasma exposure should not negatively affect the existing genomic, proteomic, and transcriptomic landscapes of the cells which in turn determine the cellular self-regulation pathways that may prevent the uncontrolled cell growth and division [334]. Solution of this problem may help tackling cancer, an issue with a century-long history.

5. Nano-plasmas: interplay of the size and the fourth state of matter

This section focuses on the second aim of the review (Section 1.2), namely nano-plasmas near or from solid matter. We will also consider a typical example when nanoscale plasmas near a solid NP may be excited. The effects of the nanoscale spatial localization of the energy and ionized matter are of primary interest. In Section 5.1, we discuss the possibility to generate very dense and strongly-non-equilibrium plasmas in physical vapors of solids produced through the interaction of intense lasers with solid (e.g. metal) surfaces. In Section 5.2, we present an example when plasmons within a gold nanosphere help generating gaseous nano-plasmas confined within a liquid nano-bubble developing around the NP.

5.1. *Non-equilibrium nano-plasmas of solids*

Let us now consider strongly-non-equilibrium plasmas in physical vapors of solid materials. These vapors are produced by exposing solid target surfaces to laser beams (laser ablation) or plasmas. The evaporated species (BUs) are ionized and then undergo energetic condensation onto a solid substrate. In PLD used for the synthesis of a large number of nanofilms and NSs, the target is exposed to a pulsed laser beam. HED plasmas of dense plasma focus or Z-pinch devices also rapidly evaporate material of solid targets to produce a variety of BUs.

The degree of ionization of the BU vapor in both cases is very high, and is often close to unity. While HED plasmas require source gases, PLD may be conducted under high-vacuum conditions. In another example of the i-PVD, atoms of a solid material are sputtered from a target by the plasma ion bombardment [62]. In this case, the vapor of the sputtered species is weakly ionized and less energetic and dense compared with the PLD and HED plasmas.

Here, we focus on non-equilibrium phenomena and plasma dimensions using PLD as an example. This choice is motivated by the discovery of fullerenes C_{60} in hot carbon vapor plasmas produced by pulsed laser ablation of graphite and nucleation of carbon clusters in a thermalizing He flow [3]. Interestingly, this discovery, which has made an enormous impact on the present-day nanoscience and nanotechnology, was made in a 'plasma nanoscience-type' experiment which aimed at revealing the effects of plasmas and ion-molecule reactions on the formation of long-chain carbon molecules in circumstellar shells and interstellar space [348].

Laser ablation plumes contain stable neutrals (atoms, molecules, and clusters) as well as metastable species, ions, and electrons. An inherent pulsed nature of PLD opens new avenues for far-from-equilibrium surface processes which lead to many diverse metastable nanomaterials [349]. When a solid target is exposed to a laser beam, energetic ($\sim$1–100 eV) species are produced in a dense plasma plume. The plasma is highly ionized, in some cases reaching $\sim$100%

ionization degree. The flux of the charged species has a fountain-like shape and rapidly cools upon deposition onto a substrate. These two features are similar to the HED plasma case [350,351]. The temperature in the localized plasma plume can be as high as ∼20,000 K. Noting that the plasma size is typically just a fraction of a millimeter, and using a typical ablation yield (for metals) of $\sim 10^{15}$ atoms per pulse, one can estimate the ionized gas pressures of the order of 10^9 Pa [352].

Under such conditions, the Debye length (1) of the plume plasma is a few orders of magnitude smaller than the axial plasma dimension, and can be in the range of *a few hundred nanometers*. Importantly, the ratio of the Debye length to the plume size increases only slightly during the plasma expansion [353]. Surface processes (e.g. migration, nucleation, etc.) can be enabled using the energy of the impinging species and in many cases no external substrate heating is necessary. The degree of ionization of the ablated plasma as it expands and then impinges on the substrate is much lower (∼1% or even less) than in the ablated plume near the target [352], yet remains much higher compared with low-pressure discharge plasmas.

PLD allows BUs ablated from metal to combine with the species generated in the plasmas of feed gases to produce, e.g. metal oxide or nitride compounds. Gases are also used to thermalize the plasma species through multiple collisions. For example, in the pioneering synthesis of C_{60} buckminsterfullerenes [3], the ablated carbon atoms produced in the plume plasma were entrained in a gas pulse confined to a narrow channel. Multiple collisions of C and He atoms led to the effective cooling, condensation, and nucleation of carbon species to produce carbon (most notably C_{60}) clusters emerging from the channel exit in a supersonic jet. This rapid cooling triggered a strongly non-equilibrium kinetic process which resulted in nucleation of C_{60}, which is less stable than graphite in thermodynamic sense.

During the BU production phase through the interactions of the laser beam with the target surface, the degree of thermal non-equilibrium between the plasma species strongly depends on the duration of the laser pulse. Let us note that the characteristic time of energy transfer from the electrons heated by the laser to the ions, τ_{ei} is typically within the 1–10 ps range. Interestingly, depending on the relation between the laser pulse duration τ_p and τ_{ei}, the plasma can be either non-equilibrium ($T_e \gg T_i$) or thermal ($T_e \sim T_i$). This condition is quite similar to the thermalization and non-equilibrium conditions for atmospheric-pressure plasmas (See Figure 17 and the associated discussion) [11]. More importantly, these different conditions lead to the very different outcomes in terms of BU production, and eventually the nanoscale synthesis process.

For long pulses $\tau_p \gg \tau_{ei}$, the energy transfer from the electrons to the ions is effective and thermal equilibrium ($T_e \sim T_i$) is established. In this case, the material is heated through the heat conduction mechanism. This heating affects the surface layer of thickness

$$l_h \sim \sqrt{\kappa_h \tau_p}, \tag{73}$$

where κ_h is the solid material-specific heat conduction coefficient.

In this case, the bulk heating, melting, and evaporation of the solid target material take place in the *near-equilibrium* regime. Since the melts usually contain both atoms and atomic clusters, the produced cocktail of BUs in the evaporated plume contains atoms, clusters, and even large droplets. A large abundance of droplets is in many cases undesirable for the synthesis of delicate NSs. On the other hand, the ablated material preserves its stoichiometric elemental composition, which is retained by the deposited nanomaterials.

In the opposite case of very short pulses ($\tau_p \ll \tau_{ei}$), the transfer of energy from the hot electrons to the lattice ions is ineffective and the electrons and ions find themselves out of thermal equilibrium, $T_e \gg T_i$. This happens during the femtosecond (fs) laser ablation when the laser pulse duration is in ∼100 s fs range. In this case, the energy delivery stops well before the material

can be heated through heat conductance. The electrons within the laser penetration depth gain energy, which may exceed the threshold for the electron emission from the surface. As the electrons leave this layer, they pull the oppositely charged ions out of the target. Moreover, the ions also experience strong repulsion due to the loss of the electron screening, which also facilitates their exit from the material. This also leads to very high ionization degrees in fs laser ablation plasmas.

This strongly non-equilibrium ablation leads to several interesting features for the nanoscale synthesis. Most importantly, purely ionic/atomic fluxes are achieved. The degree of ionization and energy (and also clustering) of these BUs can be controlled by the electric fields, distance between the target and the substrate, as well as the pressure and composition of the background gas. This process is also energy efficient since the strong non-equilibrium conditions reduce the energy loss due to the material bulk heating. These very interesting non-equilibrium processes have made fs laser ablation a common nanotool [354,355], as was predicted earlier [352].

Plasma-specific non-equilibrium and process kinetics-related effects are ubiquitous and critical in other cases involving ionized physical vapor of solids, e.g. HED plasmas, physical sputtering, ion beam-assisted evaporation, and a variety of hybrid techniques [62,356,357].

5.2. *Nano-plasmas meet plasmons*

In the previous section, we did not specify the sizes of the solid targets from which atoms of ablated solid-state materials evaporate to form plasma plumes from the physical vapor phase. Importantly, the power density delivered by the laser beam should be sufficient for the rapid transformation from the solid phase to the plasma phase. In other words, the laser intensity is expected to be high to produce the plasmas with possible sub-micrometer dimensions (nano-plasmas) near the solid target.

Let us now pose the not so obvious but important questions:

(1) is it possible to generate nano-plasmas near solids using much lower energy than in Section 5.1?
(2) can reducing the size of solids to the nanoscales help achieving these goals?

In other words, we will continue discussing the interplay of the plasma and size effects at the nanoscale.

The answer to the first question is a yes if the energy delivered to the solid can be concentrated to a very small volume, for example, NPs. The amount of the energy needed to generate plasmas near solids may be further reduced if some resonant phenomena within these NPs are used to quickly 'expel' the energy out of the NP (e.g. to prevent melting and evaporation of the NP itself) and further concentrate the energy to even smaller volumes. As will be shown in the example below, this can be achieved using plasmonic excitations in gold NPs generated by low-intensity ultra-fast fs lasers. This also gives a positive answer to the second question.

The plasmonic effects originate due to the collective responses of the free-electron gas within the ordered lattice of metal ions to external electromagnetic fields. The eigenfrequency of collective electron oscillations (plasmons) with respect to the lattice ions is determined by the free electron density and is described by the same equation as the plasma frequency ω_{pe} in (1). This similarity in mathematical descriptions (within the framework of classical physics) of electron resonant phenomena has led to many parallels between the plasma-like effects in gaseous plasmas and solids with free electrons [358–363]. When plasmons are excited (e.g. by a laser with the frequency in the optical range matching the plasmon frequency) within metal NPs, the energy of resonant plasmon oscillations (LSPs) is mostly concentrated within the NP.

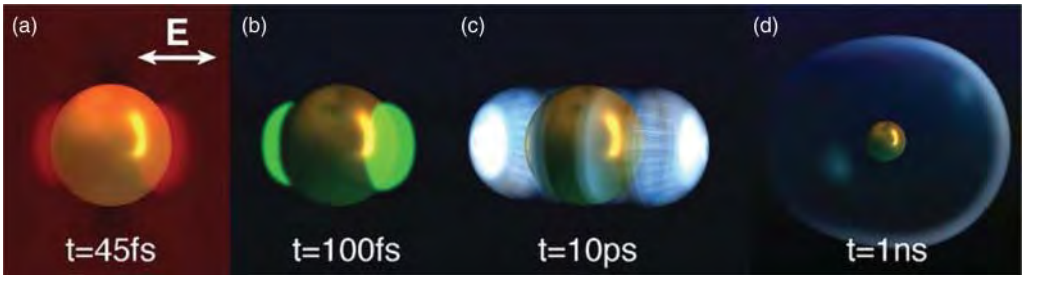

Figure 35. Sequence of physical processes leading to the formation of a nano-plasma and then a vapor nano-bubble around a plasmonic NP exposed to an ultra-fast IR laser [374]: (a) near-field is enhanced during the laser pulse; (b) enhanced near-field ionizes the surrounding water, creating a nano-plasma near the poles of the particle; (c) water heating due to the plasma fast relaxation and collisions with the plasma ions; a strong pressure wave is then released in the water; (d) a nanoscale bubble is formed around the particle. Time count starts from the onset of the laser irradiation [Reprinted with permission from [374], Copyright © 2012 American Chemical Society].

In other words, the plasmon oscillations are localized within the nanometer scale. However, it is very important to emphasize that these plasma-like oscillations originate without the nano-plasma generation through the common sequence of phase transitions. Indeed, the matter within the metal NP remains in the solid state despite significant electron delocalization. Thus, nano-plasma-like oscillations and the associated nanoscale electromagnetic energy localization may arise without nano-plasma generation within solids. This is why care should be taken not to over-simplify terminology to, e.g. to 'nano-plasma oscillations' without a clear explanation on what is actually meant.

When the external electromagnetic field is off-resonance with the plasmon excitations, the field is scattered, focused, and strongly enhanced outside of the NP. This effect is used to generate nano-plasmas in a liquid near the NP in the example discussed below. Further details of the effects of nanoscale energy localization which arise due to the plasma-like and size effects in nano-solids can be found elsewhere [364–372].

Let us now consider how nano-plasmas may be generated in a medium surrounding the plasmonic NP. In liquid media, these nano-plasmas in turn may generate nano-bubbles, the physical phenomenon that is usually referred to as nano-cavitation. These nano-bubbles are quite different from common vapor bubbles and are actively pursued in medical imaging and cancer research. The nano-bubbles may be generated by heating the NPs and the surrounding media in two different ways.

The first way relies on the resonant heating of plasmonic NPs and the excitation laser wavelength is chosen relatively close to the plasmon resonance where optical absorption dominates the scattering [373]. The nano-cavitation mechanism is then determined by the heat transfer from the hot NP to the surrounding water. The nano-plasma oscillations are thus selectively excited to generate the heat to produce the nano-bubbles.

The other way sketched in Figure 35 relies on fs (45 fs) laser excitation in the IR wavelength (800 nm) where the scattering cross-section is much larger compared with the absorption [374]. The 600–1100 nm wavelength excitations are particularly important to medical imaging and therapy because of good transparency of living tissues in this range.

As can be seen from Figure 35(a), the near-field is strongly enhanced near the opposite poles of the gold NP, which is not heated because of the low, off-plasmon-resonance optical absorption. Consequently, the strong near-field ionizes the surrounding water as shown in Figure 35(b).

It is quite possible that the gaseous molecules dissolved in the water are ionized first similar to the plasma discharges in liquids mentioned in Section 4.1.2.3. However, because of the very small size of the NP ($\sim$100 nm), it is not clear whether any small gaseous nano-bubbles surround the NP before the laser excitation. Therefore, the exact mechanisms of this ionization are currently unclear and represent an interesting opportunity for the future research.

Importantly, the plasma is confined to the near-field localization area, thus clearly becoming a nano-plasma. This plasma may reach its peak density $\sim 4 \times 10^{22}$ cm^{-3} which rapidly reduces by at least one order of magnitude within a few picoseconds [374]. The energy absorbed in the nano-plasma is one order of magnitude higher compared with the energy absorbed by the NP. Localized energy transfer from the nano-plasma is then responsible for the generation of the pressure wave (Figure 35(c)) and eventually, cavitation nano-bubbles around the plasmonic NP (Figure 35(d)).

Therefore, by tuning the resonant and non-resonant plasmon excitations within a nano-solid, one can selectively enable very different nanoscale heating mechanisms of the surrounding nano-bubbles in water. The more recently demonstrated mechanism which involves the nano-plasma generation in the liquid medium around the poles of the plasmonic NP [374] is particularly interesting. Indeed, it shows that nano-plasmas may be generated at the nanometer-sized solid interface through plasma-like effects of nanoscale energy localization and opens many new opportunities for future research.

6. Conclusion and outlook

We hope that the examples presented in this review have convinced the reader that both dimensions of plasma nanoscience – the plasma-for-nano and nano-plasma not only represent very interesting research areas on their own, but also in many cases interact at the interdisciplinary interface. This makes the field particularly fertile and sets it for the future expansion, both in breadth and depth.

In the *plasma-for-nano* aspect, non-equilibrium and kinetic properties of the plasma offer many effective controls in nanoscale synthesis and processing thereby opening many interesting opportunities for non-equilibrium nanoscale synthesis and processing. In this way, the nano-architectures can be tailored to feature unusual properties that originate from the exotic, non-equilibrium, kinetic-driven approach to nano-assembly.

The many plasma-specific effects also offer a plethora of opportunities to process nano-solids with different structural complexity. These solid materials range from simple 0D atomic clusters to complex and hierarchical hybrid structures. We have focused on the plasma–surface interactions with microscopic spatial localizations and followed the unique features of these interactions that arise because of the ionized state, reactivity, non-equilibrium, and other attributes of the plasmas. These attributes lead to the unique synthesis and processing of a broad range of materials systems and nanoscale objects with all possible dimensionalities.

In the *nano-plasma* aspect, microscopic spatial localization of the plasma enables many exotic physical effects. Micro-plasmas of gas discharges or even smaller plasmas of dense ionized physical vapors of solids feature extremely non-equilibrium properties and ultra-fast dynamics. These features make these plasmas very effective for the production of metastable nano-solids under far-from equilibrium conditions. Non-equilibrium nano-plasmas around nanometer-sized solid objects in liquids is a very interesting yet unexplored area, which is relevant to applications where nanoscale energy localization is required. Size-dependent plasma-like (plasmonic) effects in nano-solids help generating the above nano-plasmas and are thus also of interest to plasma nanoscience research.

An open question remains if it is possible to generate nano-plasmas within solids? Exotic states of matter, such as warm dense matter generated in nanometer-thin metal films by ultra-fast HED

lasers, have attributes of both superheated nano-solids and strongly coupled nano-plasmas [375–378]. Future research may clarify if it is possible to control the relative importance of these two phases.

The plasma nanoscience approaches should be tailored to lead to new materials with properties that are difficult to achieve otherwise. The functional properties should be targeted for applications in several important fields such as energy conversion and storage, biomedical, environmental, nanoelectronic, and other devices.

It is important that the new materials, devices, and processing technologies being developed using the plasma nanoscience approaches need to be energy-efficient as well as environment- and human-health friendly. For example, very high energy efficiency in nanoscale synthesis can be approached using control of energy and matter with nanometer and nanosecond precision in strongly non-equilibrium plasmas [379]. Plasma-based approaches are also capable to produce nanostructured materials directly from natural resources rather than commonly used expensive purified precursors [263,380]. The physics-based, deterministic approaches, similar to the ideas advocated in this review are quite likely to lead to positive outcomes.

The number of relevant reports is increasing very rapidly, and a substantially larger body of new knowledge on the plasma-specific effects and their utility in nanoscale applications may be expected in the near future. Numerical modeling of the plasma-specific effects involved is, therefore, highly warranted to improve the level of our understanding of the many promising experimental results.

The many examples in this review suggest that the interplay of the nanometer spatial localization and plasma-specific effects generates a plethora of interesting and rich physics, which offer many exciting opportunities for future interdisciplinary research and the development of relevant applications. Finally, *nano-size matters – so does the fourth state of matter!*

Note added in proof

Since the manuscript has been submitted for production, we became aware of the following most recent relevant publications. Nanoscale plasma-surface interactions are very effective for the precise surface engineering of Si nanocrystals to enable specific quantum confinement effects [381] and carbon nanotube growth without metal catalysts [382]. By controlling the plasma process parameters, it is possible to tailor the volume fraction of Si nanocrystals embedded in amorphous Si matrix (nc-Si films), which dramatically improves the efficiency of recombination-free charge transfer (and also the open circuit voltage and photo-conversion efficiency) in nc-Si:H-based solar cells [383]. Microwave plasma CVD was used to produce the previously unknown SiC tetrapod structures which show photoluminescence at wavelengths spanning the visible to near-infrared spectral range; other methods have previously failed to synthesise these nanostructures [384]. Relevant effects have been discussed in Sections 4.1 and 4.2.1. Self-organization of nanoparticles on plasma-exposed surfaces can now be monitored in real time through the very recent advent of *in situ* transmission electron microscopy-based platform for real-time characterization of nanoscale plasma-surface interactions [385]. See Sections 3.6 and 4.1.3 for relevant physics. Plasma-assisted electrochemistry improves control of the properties and size distributions of plasmonic Au nanoparticles through the unique plasma-specific mechanisms [386]. Interactions of light with similar surface-supported nanoparticles lead to interesting plasma-like effects on the tunnel current in nanoislanded gold films [387]. Relevant discussions can be found in Sections 4.1.2 and 5.2. Surface functionalization and morphology control in networks of vertical graphene-like structures can be used to control their wettability and magnetotransport properties [388,389]. These 2D structures have been extensively discussed in Section 4.3.2. Plasma nanoscience approaches help achieving the goals of green and sustainable nanoscience [390] briefly mentioned in Section

6. Plasmas enable reforming of diverse precursors ranging from fatty substances (e.g., butter) [391] to petroleum asphalt [392] to generate graphene nanosheets (see Section 4.3.2). These and similar graphene-like structures have shown superior performance in supercapacitor [391] and fuel cell [393] applications. Synergistic effects of atmospheric-pressure plasmas and nanometer-sized catalysts prove instrumental in the solution of environmental problems such as ozone destruction [394]; plasma-catalysis is presently developing at a very rapid pace and represents a topical area of research. These randomly selected examples suggest that the number of relevant publications is increasing very rapidly and the reader is encouraged to use the basic information and references presented in this review to continuously monitor the progress in the fertile and rapidly developing plasma nanoscience research field.

Acknowledgements

We sincerely thank many our colleagues for fruitful collaborations, discussions, and critical comments with apologies of not being able to mention by name due to limited space. We also thank all authors of original figures for the permissions to reproduce. This work was partially supported by the Australian Research Council and CSIRO's Science Leadership Program. K. O. is grateful to the University of Sydney (Australia) and Nanyang Technological University (Singapore) as Host Organizations for his ARC Future Fellowship as well as Huazhong University of Science and Technology (China), the University of Technology Sydney (Australia), and the University of Wollongong (Australia) for the visiting, adjunct, and honorary professor support. We are particularly thankful to the anonymous referee for the insightful discussion of states of matter and phase transitions at nanoscales. We also thank every person who has ever contributed to the relevant areas and apologize for not being able to include all these results, although would certainly do that if that were physically possible.

References

[1] S.D. Bader, Rev. Mod. Phys. 78 (2006), pp. 1–15.
[2] K. Ostrikov, *Plasma Nanoscience: Basic Concepts and Applications of Deterministic Nanofabrication*, Wiley-VCH, Weinheim, Germany, 2008.
[3] H.W. Kroto, J.R. Heath, S.C. O'Brien, R.F. Curl, and R.E. Smalley, Nature 318 (1985), pp. 162–163.
[4] S. Iijima, Nature 354 (1991), pp. 56–58.
[5] M. Meyyappan, L. Delzeit, A. Cassel, and D. Hash, Plasma Sources Sci. Technol. 12 (2003), pp. 205–216.
[6] K. Ostrikov, Rev. Mod. Phys. 77 (2005), pp. 489–511.
[7] F.J. Gordillo-Vazquez, V.J. Herrero, and I. Tanarro, Chem. Vapor. Depos. 13 (2007), pp. 267–279.
[8] M. Hori and T. Goto, Appl. Surf. Sci. 253 (2007), pp. 6657–6671.
[9] U. Kortshagen, J. Phys. D 42 (2009), art. 113001.
[10] M. Meyyappan, J. Phys. D 42 (2009), art. 213001.
[11] D. Mariotti and R.M. Sankaran, J. Phys. D 43 (2010), art. 323001.
[12] J. Zheng, R. Yang, L. Xie, J. Qu, Y. Liu, and X. Li, Adv. Mater. 22 (2010), pp. 1451–1473.
[13] R. Hatakeyama, T. Kaneko, T. Kato, and Y.F. Li, J. Phys. D 44 (2011), art. 174004.
[14] Y. Lan, Y. Wang, and Z.F. Ren, Adv. Phys. 60 (2011), pp. 553–678.
[15] K. Ostrikov, U. Cvelbar, and A.B. Murphy, J. Phys. D 44 (2011), art. 174001.
[16] R.M. Sankaran (ed.), *Plasma Processing of Nanomaterials*, CRC Press, Boca Raton, FL, 2012.
[17] E.C. Neyts, J. Vac. Sci. Technol. B 30 (2012), art. 030803.
[18] K. Ostrikov and S. Xu, *Plasma-Aided Nanofabrication: From Plasma Sources to Nanoassembly*, Wiley-VCH, Weinheim, Germany, 2007.
[19] D. Das, J. Phys. D 36 (2003), pp. 2335–2346.
[20] T. Kato and R. Hatakeyama, Chem. Vapor. Depos. 12 (2006), pp. 345–352.

[21] K.S. Novoselov, D. Jiang, F. Schedin, T.J. Booth, V.V. Khotkevich, S.V. Morozov, and A.K. Geim, Proc. Natl. Acad. Sci. USA 102 (2005), pp. 10451–10453.
[22] R. Murali, Y. Yang, K. Brenner, T. Beck, and J.D. Meindl, Appl. Phys. Lett. 94 (2009), art. 243114.
[23] M. Zhu, J. Wang, B.C. Holloway, R.A. Outlaw, X. Zhao, K. Hou, V. Shutthanandan, and D.M. Manos, Carbon 45 (2007), pp. 2229–2234.
[24] S.Q. Xiao and S. Xu, J. Phys. D 44 (2011), art. 174033.
[25] D. Borah, M.T. Shaw, S. Rasappa, R.A. Farrell, C. O'Mahony, C.M. Faulkner, M. Bosea, P. Gleeson, J.D. Holmes, and M.A. Morris, J. Phys. D 44 (2011), art. 174012.
[26] I. Mann, Annu. Rev. Astron. Astrophys. 48 (2010), pp. 173–203.
[27] J.V. Barth, G. Costantini, and K. Kern, Nature 437 (2005), pp. 671–679.
[28] M.R. Anklam and A. Firoozabadi, J. Chem. Phys. 121 (2004), pp. 11867–11875.
[29] A. Colli, A. Fasoli, S. Hofmann, C. Ducati, J. Robertson, M.P. Siegal, and A.C. Ferrari, Nanotechnology 17 (2006), pp. 1046–1051.
[30] M.R. Diehl, S.N. Yaliraki, R.A. Beckman, M. Barahona, and J.R. Heath, Angew. Chem. Int. Ed. 41 (2002), pp. 353–356.
[31] S. Mitragotri and J. Lahann, Nature Mater. 8 (2009), pp. 15–23.
[32] S.M. Woodley and R. Catlow, Nature Mater. 7 (2008), pp. 937–946.
[33] O.M. Yaghi, M. O'Keeffe, N.W. Ockwig, H.K. Chae, M. Eddaoudi, and J. Kim, Nature 423 (2003), pp. 705–714.
[34] L. Qu, L. Dai, M. Stone, Z. Xia, and Z.L. Wang, Science 322 (2008), pp. 238–242.
[35] E. Munch, M.E. Launey, D.H. Alsem, E. Saiz, A.P. Tomsia, and R.O. Ritchie, Science 322 (2008), pp. 1516–1520.
[36] S. Park, D.H. Lee, J. Xu, B. Kim, S.W. Hong, U. Jeong, T. Xu, and T.P. Russell, Science 323 (2009), pp. 1030–1033.
[37] G. Conibeer, Thin Solid Films 511–512 (2006), pp. 654–662.
[38] A. Javey and H. Dai, J. Am. Chem. Soc. 127 (2005), pp. 11942–11943.
[39] C. Forestiere, G. Miano, S.V. Boriskina, and L. Dal Negro, Opt. Express 17 (2009), pp. 9648–9661.
[40] Z.-P. Yang, L. Ci, J.A. Bur, S.-Y. Lin, and P.M. Ajayan, Nano Lett. 8 (2008), pp. 446–451.
[41] Y.F. Huang, S. Chattopadhyay, Y.J. Jen, C.Y. Peng, T.A. Liu, Y.K. Hsu, C.L. Pan, H.C. Lo, C.H. Hsu, Y.H. Chang, C.S. Lee, K.H. Chen, and L.C. Chen, Nature Nanotechnol. 2 (2007), pp. 770–774.
[42] S. Chattopadhyay, Y. Huang, Y. Jen, A. Ganguly, K.H. Chen, and L.C. Chen, Mater. Sci. Eng. Rev. 69 (2010), pp. 1–35.
[43] I. Levchenko and K. Ostrikov, Appl. Phys. Lett. 92 (2008), art. 063108.
[44] C. Hsu, H. Lo, C. Chen, C. Wu, J. Hwang, D. Das, J. Tsai, L. Chen, and K. Chen, Nano Lett. 4 (2004), pp. 471–475.
[45] F. Ding, K. Bolton, and A. Rosen, J. Phys. Chem. B 108 (2004), pp. 17369–17377.
[46] E.C. Neyts, Y. Shibuta, A.C.T. van Duin, and A. Bogaerts, ACS Nano 4 (2010), pp. 6665–6672.
[47] E.C. Neyts, A.C.T. van Duin, and A. Bogaerts, J. Am. Chem. Soc. 133 (2011), pp. 17225–17231.
[48] E.C. Neyts, A.C.T. van Duin, and A. Bogaerts, J. Am. Chem. Soc. 134 (2012), pp. 1256–1260.
[49] I. Levchenko and K. Ostrikov, J. Phys. D 40 (2007), pp. 2308–2319.
[50] B.J. Kim, J. Tersoff, S. Kodambaka, M.C. Reuter, E.A. Stach, and F.M. Ross, Science 322 (2008), pp. 1070–1073.
[51] M.C. Tringides, M. Hupalo, and M. Yakes, Physica A 357 (2005), pp. 216–249.
[52] A. La Magna, Surf. Sci. 601 (2007), pp. 308–314.
[53] K. Ostrikov, I. Levchenko, and S. Xu, Pure Appl. Chem. 80 (2009), pp. 1909–1918.
[54] A.S. Barnard and P. Zapol, J. Chem. Phys. 121 (2004), pp. 4276–4283.
[55] J. Park and W. Lu, Appl. Phys. Lett. 95 (2009), art. 073110.
[56] V. Tomar, M.R. Gungor, and D. Maroudas, Phys. Rev. Lett. 100 (2008), art. 036106.
[57] A.I. Persson, L.E. Froeberg, S. Jepessen, M.T. Bjoerk, and L. Samuelsson, J. Appl. Phys. 101 (2007), art. 034313.
[58] P. Sigmund, Phys. Rev. 184 (1969), pp. 383–416.
[59] M.A. Makeev and A.-L. Barabasi, Appl. Phys. Lett. 71 (1997), pp. 2800–2802.
[60] D. Marton, J. Fine, and G.P. Chambers, Phys. Rev. Lett. 61 (1988), pp. 2697–2700.

[61] F. Frost, B. Ziberi, A. Schindler, and B. Rauschenbach, Appl. Phys. A 91 (2008), pp. 551–559.
[62] A. Anders, J. Phys. D 40 (2007), pp. 2272–2284.
[63] Z.J. Han, B.K. Tay, M. Shakerzadeh, and K. Ostrikov, Appl. Phys. Lett. 94 (2009), art. 223106.
[64] P. Jensen, Rev. Mod. Phys. 71 (1999), pp. 1695–1735.
[65] P. Jensen and N. Combe, Comput. Mater. Sci. 24 (2002), pp. 78–87.
[66] E.I. Meletis and J.C. Jiang, J. Nanosci. Nanotechnol. 6 (2006), pp. 1807–1810.
[67] F.L. Wang, J.C. Jiang, and E.I. Meletis, J. Appl. Phys. 95 (2004), pp. 5069–5074.
[68] N. Combe, P. Jensen, and A. Pimpinelli, Phys. Rev. Lett. 85 (2000), pp. 110–113.
[69] M. Degawa and E.D. Williams, Surface Sci. 595 (2005), pp. 87–96.
[70] H.G. Yang, C.H. Sun, S.Z. Qiao, J. Zou, G. Liu, S.C. Smith, H.M. Cheng, and G.Q. Lu, Nature 453 (2008), pp. 638–641.
[71] G.S. Rohrer, C.L. Rohrer, and W.W. Mullins, J. Am. Ceram. Soc. 84 (2001), pp. 2099–2104.
[72] K. Ostrikov, Phys. Plasmas 18 (2011), art. 057101.
[73] B.N. Khare, M. Meyyappan, A.M. Cassell, C.V. Nguyen, and J. Han, Nano Lett. 2 (2002), pp. 73–77.
[74] K. Ostrikov, J. Phys. D 44 (2011), art. 174003.
[75] K. Ostrikov, Vacuum 83 (2008), pp. 4–10.
[76] A. Bogaerts and R. Gijbels, Phys. Rev. A 52 (1995), pp. 3743–3751.
[77] A. Bogaerts, M. Eckert, M. Mao, and E. Neyts, J. Phys. D 44 (2011), art. 174030.
[78] M.J. Kushner, J. Appl. Phys. 63 (1988), pp. 2532–2551.
[79] S.V. Vladimirov and K. Ostrikov, Phys. Rep. 393 (2004), pp. 175–380.
[80] G. Morfill and A. Ivlev, Rev. Mod. Phys. 81 (2009), pp. 1353–1404.
[81] S. Tinck, W. Boullart, and A. Bogaerts, J. Phys. D 41 (2008), art. 065207.
[82] H. Sugai, I. Ghanashev, M. Hosokawa, K. Mizuno, K. Nakamura, H. Toyoda, and K. Yamauchi, Plasma Sources Sci. Technol. 10 (2001), pp. 378–385.
[83] E.C. Zipf, Can. J. Chem. 47 (1969), pp. 1863–1870.
[84] C.E. Johnson, Phys. Rev. A 5 (1972), pp. 2688–2689.
[85] C.F. Fischer and H.P. Saha, Phys. Rev. A 28 (1983), pp. 3169–3178.
[86] M. Mozetic, J. Phys. D 44 (2011), art. 174028.
[87] U. Cvelbar, Z. Chen, M.K. Sunkara, and M. Mozetic, Small 4 (2008), pp. 1610–1614.
[88] I. Denysenko, S. Xu, P. Rutkevych, J. Long, N. Azarenkov, and K. Ostrikov, J. Appl. Phys. 95 (2004), pp. 2713–2724.
[89] E. Gogolides, D. Mary, A. Rhallabi, and G. Turban, Jpn. J. Appl. Phys., Part 1 34 (1995), pp. 261–270.
[90] C. Hopf, K. Letourneur, W. Jacob, T. Schwarz-Selinger, and A. Von Keudell, Appl. Phys. Lett. 74 (1999), pp. 3800–3802.
[91] A. Von Keudell, T. Schwarz-Selinger, M. Meier, and W. Jacob, Appl. Phys. Lett. 76 (2000), pp. 676–678.
[92] N. Mutsukura, S. Inoue, and Y. Machi, J. Appl. Phys. 72 (1992), pp. 43–53.
[93] C. Hopf, T. Schwarz-Selinger, W. Jacob, and A. Von Keudell, J. Appl. Phys. 87 (2000), pp. 2719–2725.
[94] D. Hash, M. Bell, K. Teo, B. Cruden, W. Milne, and M. Meyyappan, Nanotechnology 16 (2005), pp. 925–930.
[95] I. Levchenko, K. Ostrikov, D. Mariotti, and A.B. Murphy, J. Appl. Phys. 104 (2008), art. 073308.
[96] I. Levchenko, K. Ostrikov, and S. Xu, IEEE Trans. Plasma Sci. 36 (2008), pp. 864–865.
[97] K. Ostrikov, H.J. Yoon, A. Rider, and S.V. Vladimirov, Plasma Proc. Polym. 4 (2007), pp. 27–40.
[98] S. Morsch, P.S. Brown, and J.P.S. Badyal, J. Mater. Chem. 22 (2012), pp. 3922–3929.
[99] J.-C. Charlier, X. Blase, and S. Roche, Rev. Mod. Phys. 79 (2007), pp. 677–732.
[100] K. Ostrikov and H. Mehdipour, ACS Nano 5 (2011), pp. 8372–8382.
[101] K. Ostrikov, IEEE Trans. Plasma Sci. 39 (2011), pp. 963–970.
[102] S. Hofmann, C. Ducati, J. Robertson, and B. Kleinsorge, Appl. Phys. Lett. 83 (2003), pp. 135–137 .
[103] S. Hofmann, G. Csanyi, A.C. Ferrari, M.C. Payne, and J. Robertson, Phys. Rev. Lett. 95 (2005), art. 036101.
[104] C. Ducati, I. Alexandrou, M. Chhowalla, G.A.J. Amaratunga, and J. Robertson, J. Appl. Phys. 92 (2002), pp. 3299–3303.
[105] A. Gohier, T.M. Minea, A.M. Djouadi, A. Granier, and M. Dubosc, Chem. Phys. Lett. 421 (2006), pp. 242–245.

[106] V.G. Dubrovskii, N.V. Sibirev, J.C. Harmand, and F. Glas, Phys. Rev. B 78 (2008), art. 235301.
[107] T. Kato and R. Hatakeyama, ACS Nano 4 (2010), pp. 7395–7400.
[108] L. Qu, F. Du, and L. Dai, Nano Lett. 8 (2008), pp. 2682–2687.
[109] Z. Ghorannevis, T. Kato, T. Kaneko, and R. Hatakeyama, J. Amer. Chem. Soc. 132 (2010), pp. 9570–9572.
[110] O. Volotskova, J.A. Fagan, J.Y. Huh, F.R. Phelan, A. Shashurin, and M. Keidar, ACS Nano 4 (2010), pp. 5187–5192.
[111] K. Ostrikov and H. Mehdipour, J. Amer. Chem. Soc. 134 (2012), pp. 4303–4312.
[112] Z.F. Ren, Z.P. Huang, J.W. Xu, J.H. Wang, P. Bush, M.P. Siegal, and P.N. Provencio, Science 282 (1998), pp. 1105–1107.
[113] E.C. Neyts, K. Ostrikov, Z.J. Han, S. Kumar, A.C.T. van Duin, and A. Bogaerts, Phys. Rev. Lett. 110 (2013), art. 065501.
[114] O. Lehtinen, J. Kotakoski, A.V. Krasheninnikov, A. Tolvanen, K. Nordlund, and J. Keinonen, Phys. Rev. B 81 (2010), art. 153401.
[115] C. Bower, W. Zhu, S. Jin, and O. Zhou, Appl. Phys. Lett. 77 (2000), pp. 830–832.
[116] V.I. Merkulov, A.V. Melechko, M.A. Guillorn, D.H. Lowndes, and M.L. Simpson, Appl. Phys. Lett. 79 (2001), pp. 2970–2972.
[117] J.F. AuBuchon, L.-H. Chen, A.I. Gapin, D.-W. Kim, C. Daraio, and S. Jin, Nano Lett. 4 (2004), pp. 1781–1784.
[118] H. Wang and Z.F. Ren, Nanotechnology 22 (2011), art. 405601.
[119] J. Robertson, G. Zhong, H. Telg, C. Thomsen, J.H. Warmer, G.A.D. Briggs, U. Detlaf-Weglikowska, and S. Roth, Appl. Phys. Lett. 93 (2008), art. 163111.
[120] E. Tam and K. Ostrikov, Appl. Phys. Lett. 93 (2008), art. 261504.
[121] G. Arnoult, T. Belmonte, and G. Henrion, Appl. Phys. Lett. 96 (2010), art. 101505.
[122] Z.L. Tsakadze, I. Levchenko, K. Ostrikov, and S. Xu, Carbon 45 (2007), pp. 2022–2030.
[123] I. Levchenko, K. Ostrikov, and D. Mariotti, Carbon 47 (2009), pp. 344–347.
[124] I. Levchenko, K. Ostrikov, D. Mariotti, and V. Svrcek, Carbon 47 (2009), pp. 2379–2390.
[125] G.L. Kellogg, Phys. Rev. Lett. 70 (1993), pp. 1631–1634.
[126] G.S. Khoo, C.K. Ong, N. Itoh, and J. Kanasaki, J. Appl. Phys. 75 (1994), pp. 255–258.
[127] Z. Zhang, F. Wu, and M.G. Lagally, Surf. Rev. Lett. 3 (1996), pp. 1449–1462.
[128] A. Kobayashi, F. Grey, E. Snyder, and M. Aono, Phys. Rev. B 49 (1994), pp. 8067–8070.
[129] D. Kandel and E. Kaxiras, Phys. Rev. Lett. 76 (1996), pp. 1114–1117.
[130] B. Golding, C. Bednarski-Meinke, and Z. Dai, Diam. Relat. Mater. 13 (2004), pp. 545–551.
[131] K. Makihara, K. Shimanoe, M. Ikeda, S. Higashi, and S. Miyazaki, Jpn. J. Appl. Phys. 47 (2008), pp. 3099–3102.
[132] J.C. Ho, I. Levchenko, and K. Ostrikov, J. Appl. Phys. 101 (2007), art. 094309.
[133] I. Levchenko, U. Cvelbar, M. Modic, G. Filipic, X.X. Zhong, M. Mozetic, and K. Ostrikov, J. Phys. Chem. Lett. 4 (2013), pp. 681–686.
[134] N.-M. Park, C.-J. Choi, T.-Y. Seong, and S.-J. Park, Phys. Rev. Lett. 86 (2001), pp. 1355–1357.
[135] D.J. Lockwood, Z.H. Lu, and J.-M. Baribeau, Phys. Rev. Lett. 76 (1996), pp. 539–541.
[136] Q.J. Cheng, S. Xu, S.Y. Huang, and K. Ostrikov, Cryst. Growth Design 9 (2009), pp. 2863–2867.
[137] P. Roca i Cabarrocas, Phys. Stat. Sol. (c) 1 (2004), pp. 1115–1130.
[138] H. Vach and Q. Brulin, Phys. Rev. Lett. 95 (2005), art. 165502.
[139] H. Vach, Q. Brulin, N. Chaâbane, T. Novikova, P. Roca i Cabarrocas, B. Kalache, K. Hassouni, S. Botti, and L. Reining, Comput. Mater. Sci. 35 (2006), pp. 216–222.
[140] N. Ning and H. Vach, J. Phys. Chem. A 114 (2010), pp. 3297–3305.
[141] M.O. Watanabe, T. Miyazaki, and T. Kanayama, Phys. Rev. Lett. 81 (1998), pp. 5362–5365.
[142] G.F. Grom, D.J. Lockwood, J.P. McCaffrey, H.J. Labbé, P.M. Fauchet, B. White Jr., J. Diener, D. Kovalev, F. Koch, and L. Tsybeskov, Nature 407 (2000), pp. 358–361.
[143] S.N. Baker and G.A. Baker, Angew. Chem. Int. Ed. 49 (2010), pp. 6726–6744.
[144] J. Wang, C.-F. Wang, and S. Chen, Angew. Chem. Int. Ed. 51 (2012), pp. 9297–9301.
[145] P. Bruggeman and C. Leys, J. Phys. D. 42 (2009), art. 053001.
[146] A. Jaiswal, S.S. Ghosh, and A. Chattopadhyay, Chem. Commun. 48 (2012), pp. 407–409.

[147] M. Shigeta and A.B. Murphy, J. Phys. D 44 (2011), art. 174025.
[148] U.V. Bhandarkar, M.T. Swihart, S.L. Girshik, and U. Kortshagen, J. Phys. D 33 (2000), pp. 2731–2746.
[149] K. De Bleecker, A. Bogaerts, and W. Goedheer, Phys. Rev. E 69 (2004), art. 056409.
[150] G. Viera, M. Mikikian, E. Bertran, P. Roca i Cabarrocas, and L. Boufendi, J. Appl. Phys. 92 (2002), pp. 4684–4694.
[151] P. Roca i Cabarrocas, Th. Nguyen-Tran, A. Abramov, E. Johnson, and G. Patriarche, J. Phys. D 40 (2007), pp. 2258–2266.
[152] Z. Holman and U. Kortshagen, J. Phys. D 44 (2011), art. 174009.
[153] R.J. Anthony, K.Y. Cheng, Z.C. Holman, R.J. Holmes, and U.R. Kortshagen, Nano Lett. 12 (2012), pp. 2822–2825.
[154] H.R. Maurer and H. Kersten, J. Phys. D 44 (2011), art. 174029.
[155] T. Hawa and M.R. Zachariah, J. Phys. Chem. C 112 (2008), pp. 14796–14800.
[156] A.S. Barnard, J. Phys. Chem. B 110 (2006), pp. 24498–24504.
[157] S. Sriraman, S. Agarwal, E.S. Aydil, and D. Maroudas, Nature 418 (2002), pp. 62–65.
[158] W. Chiang and R.M. Sankaran, Nature Mater. 8 (2009), pp. 882–886.
[159] D. Mariotti, V. Svrcek, and D.G. Kim, Appl. Phys. Lett. 91 (2007), art. 183111.
[160] D. Mariotti and K. Ostrikov, J. Phys. D 42 (2009), art. 092002.
[161] T. Nozaki, K. Sasaki, T. Ogino, D. Asahi, and K. Okazaki, Nanotechnology 18 (2007), art. 235603.
[162] T. Nozaki, K. Ohnishi, K. Okazaki, and U. Kortshagen, Carbon 45 (2007), pp. 364–374.
[163] D. Bera, S.C. Kuiry, M. McCutchen, A. Kruize, H. Heinrich, M. Meyyappan, and S. Seal, Chem. Phys. Lett. 386 (2004), pp. 364–368.
[164] W.G. Graham and K.R. Stalder, J. Phys. D. 44 (2011), art. 174037.
[165] S.W. Lee, D. Liang, X.P.A. Gao, and R.M. Sankaran, Adv. Funct. Mater. 21 (2011), pp. 2155–2161.
[166] S.A. Meiss, M. Rohnke, L. Kienle, C.Z. El Abedin, F. Endres, and J. Janek, Chem. Phys. Chem. 8 (2007), pp. 50–53.
[167] X.Z. Huang, X.X. Zhong, Y. Lu, Y.S. Li, A.E. Rider, S.A. Furman, and K. Ostrikov, Nanotechnology 24 (2013), art. 095604.
[168] D. Mariotti, V. Svrcek, J.W.J. Hamilton, M. Schmidt, and M. Kondo, Adv. Funct. Mater. 22 (2012), pp. 954–964.
[169] D. Riabinina, M. Chaker, and F. Rosei, Appl. Phys. Lett. 89 (2006), art. 131501.
[170] A.V. Whitney, B.D. Myers, and R.P. van Duyne, Nano Lett. 4 (2004), pp. 1507–1511.
[171] L. Yuan, X.X. Zhong, and K. Ostrikov, Nanotechnology 19 (2008), art. 155304.
[172] X. Wu, X.X. Zhong, and K. Ostrikov, Appl. Phys. Lett. 92 (2008), art. 223104.
[173] I. Levchenko, K. Ostrikov, K. Winkler, K. Diwan, and D. Mariotti, Appl. Phys. Lett. 93 (2008), art. 183102.
[174] M. Delanty, I. Levchenko, K. Ostrikov, S. Rebic, and S. Xu, Appl. Surf. Sci. 255 (2009), pp. 7477–7482.
[175] V. Ligatchev, J. Phys. D 44 (2011), art. 174013.
[176] M. Shiratani, K. Koga, S. Ando, T. Inoue, Y. Watanabe, S. Nunomura, and M. Kondo, Surf. Coat. Technol. 201 (2007), pp. 5468–5471.
[177] A.J. Nozik, Nano Lett. 10 (2010), pp. 2735–2741.
[178] J. Shieh, T.S. Ko, H.L. Chen, B.T. Dai, and T.C. Chu, Chem. Vapor Depos. 10 (2004), pp. 265–269 .
[179] Q.J. Cheng, S. Xu, J.D. Long, and K. Ostrikov, Appl. Phys. Lett. 90 (2007), art. 173112.
[180] H. Cui, X. Yang, M.L. Simpson, D.H. Lowndes, and M. Varela, Appl. Phys. Lett. 84 (2004), pp. 4077–4079.
[181] T. Kato, G.-H. Jeong, T. Hirata, and R. Hatakeyama, Chem. Phys. Lett. 381 (2003), pp. 422–426.
[182] J. Robertson, Mater. Today 10 (2007), pp. 44–53.
[183] S. Helveg, C. Lopez-Cartes, J. Sehested, P.L. Hansen, B.S. Clausen, J.R. Rostrup-Nielsen, F. Abild-Pedersen, and J.K. Norskov, Nature 427 (2004), pp. 426–429.
[184] I. Denysenko and K. Ostrikov, J. Phys. D. 42 (2009), art. 015208.
[185] G.Y. Chen, B. Jensen, V. Stolojan, and S.R.P. Silva, Carbon 49 (2011), pp. 280–285.
[186] I. Denysenko and K. Ostrikov, Appl. Phys. Lett. 90 (2007), art. 251501.
[187] Q. Cao and J.A. Rogers, Adv. Mater. 21 (2009), pp. 29–53.
[188] R.H. Fowler and L. Nordheim, Proc. R. Soc. London, Ser. A 119 (1928). pp. 173–181.

[189] M. Chhowalla, K.B.K. Teo, C. Ducati, N.L. Rupesinghe, G.A.J. Amaratunga, A.C. Ferrari, D. Roy, J. Robertson, and W.I. Milne, J. Appl. Phys. 90 (2001), pp. 5308–5317.
[190] A.V. Melechko, V.I. Merkulov, T.E. McKnight, M.A. Guillorn, K.L. Klein, D.H. Lowndes, and M.L. Simpson, J. Appl. Phys. 97 (2005), art. 041301.
[191] S. Kumar, I. Levchenko, K. Ostrikov, and J.A. McLaughlin, Carbon 50 (2012), pp. 325–329.
[192] S. Kumar, H. Mehdipour, and K. Ostrikov, Adv. Mater. 25 (2013), pp. 69–74.
[193] M. Meyyappan and M.K. Sunkara, *Inorganic Nanowires: Applications, Properties, and Characterization*, CRC Press, Boca Raton, FL, 2010.
[194] U. Khalilov, G. Pourtois, A.C.T. van Duin, and E.C. Neyts, Chem. Mater. 24 (2012), pp. 2141–2147.
[195] S. Hofmann, C. Ducati, R.J. Neill, S. Piscanec, and A.C. Ferrari, J. Geng, R.E. Dunin-Borkowski, and J. Robertson, J. Appl. Phys. 94 (2003), pp. 6005–6012.
[196] P.-J. Alet, L. Yu, G. Patriarche, S. Palacin, and P. Roca i Cabarrocas, J. Mater. Chem. 18 (2008), pp. 5187–5189.
[197] P. Aella, S. Ingole, W.T. Petuskey, and S.T. Picraux, Adv. Mater. 19 (2007), pp. 2603–2607.
[198] F. Iacopi, P.M. Vereecken, M. Schaekers, M. Caymax, N. Moelans, B. Blanpain, O. Richard, C. Detavernier, and H. Griffiths, Nanotechnology 18 (2007), art. 505307.
[199] K. Ostrikov and H. Mehdipour, Appl. Phys. Lett. 98 (2011), art. 033104.
[200] H. Mehdipour and K. Ostrikov, J. Am. Chem. Soc. 135 (2013), pp. 1912–1918.
[201] D.D.D. Ma, C.S. Lee, F.C.K. Au, S.Y. Tong, and S.T. Lee, Science 21 (2003), pp. 1874–1877.
[202] V. Schmidt, S. Senz, and U. Gosele, Nano Lett. 5 (2005), pp. 931–935.
[203] V. Schmidt, J.V. Wittemann, and U. Gosele, Chem. Rev. 110 (2010), pp. 361–388.
[204] U. Cvelbar, K. Ostrikov, I. Levchenko, M. Mozetic, and M.K. Sunkara, Appl. Phys. Lett. 94 (2009), art. 211502.
[205] M. Mozetic, U. Cvelbar, M.K. Sunkara, and S. Vaddiraju, Adv. Mater. 17 (2005), pp. 2138–2142.
[206] Z.Q. Chen, U. Cvelbar, M. Mozetic, J.Q. He, and M.K. Sunkara, Chem. Mater. 20 (2008), pp. 3224–3228.
[207] K. Ostrikov, I. Levchenko, U. Cvelbar, M.K. Sunkara, and M. Mozetic, Nanoscale 2 (2010), pp. 2012–2027.
[208] G. Schierning, R. Theissmann, H. Wiggers, D. Sudfeld, A. Ebbers, D. Franke, V.T. Witusiewicz, and M. Apel, J. Appl. Phys. 103 (2008), art. 084305.
[209] S. Sharma and M. K. Sunkara, J. Amer. Chem. Soc. 124 (2002), pp. 12288–12293.
[210] U. Cvelbar, K. Ostrikov, A. Drenik, and M. Mozetic, Appl. Phys. Lett. 92 (2008), art. 133505.
[211] U. Cvelbar, J. Phys. D 44 (2011), art. 174014.
[212] S. Vaddiraju, A. Mohite, A. Chin, M. Meyyappan, G. Sumanasekera, B.W. Alphenaar, and M.K. Sunkara, Nano Lett. 5 (2005), pp. 1625–1631.
[213] V. Kumar, J.H. Kim, C. Pendyala, B. Chernomordik, and M.K. Sunkara, J. Phys. Chem. C 112 (2008), pp. 17750–17754.
[214] V. Kumar, J.H. Kim, J.B. Jasinski, E.L. Clark, and M.K. Sunkara, Cryst. Growth Des. 11 (2011), pp. 2913–2919.
[215] H. Chandrasekaran, G. Sumanasekera, and M.K. Sunkara, J. Phys. Chem. B 110 (2006), pp. 18351–18357.
[216] X. Xu, F. Liu, K. Yu, W. Huang, B. Peng, and W. Wei, Chem. Phys. Chem. 8 (2007), pp. 703–711.
[217] K.S. Novoselov, A.K. Geim, S.V. Morozov, D. Jiang, Y. Zhang, S.V. Dubonos, I.V. Grigorieva, and A.A. Firsov, Science 306 (2004), pp. 666–669.
[218] H. Ago, Y. Ogawa, M. Tsuji, S. Mizuno, and H. Hibino, Phys. Chem. Lett. 3 (2012), pp. 2228–2236.
[219] H. Mehdipour and K. Ostrikov, ACS Nano 6 (2012), pp. 10276–10286.
[220] S.M. Wang, Y.H. Pei, X. Wang, H. Wang, Q.N. Meng, H.W. Tian, X.L. Zheng, W.T. Zheng, and Y. C. Liu, J. Phys. D 43 (2010), art. 455402.
[221] G. Nandamuri, S. Roumimov, and R. Solanki, Appl. Phys. Lett. 96 (2010), art. 154101.
[222] L. Xie, L. Jiao, and H. Dai, J. Amer. Chem. Soc. 132 (2010), pp. 14751–14753.
[223] D.C. Elias, R.R. Nair, T.M.G. Mohiuddin, S.V. Morozov, P. Blake, M.P. Halsall, A.C. Ferrari, D.W. Boukhvalov, M.I. Katsnelson, A.K. Geim, and K.S. Novoselov, Science 323 (2009), pp. 610–613.
[224] A. Savchenko, Science 323 (2009), pp. 589–590.

[225] A. Nourbakhsh, M. Cantoro, T. Vosch, G. Pourtois, F. Clemente, M.H. van der Veen, J. Hofkens, M.M. Heyns, S. De Gendt, and B.F. Sels, Nanotechnology 21 (2010), art. 435203.
[226] Y.-D. Lim, D.-Y. Lee, T.-Z. Shen, C.-H. Ra, J.-Y. Choi, and W.J. Yoo, ACS Nano 6 (2012), pp. 4410–4417.
[227] T. Gokus, R.R. Nair, A. Bonetti, M. Boehmler, A. Lombardo, K.S. Novoselov, A.K. Geim, A.C. Ferrari, and A. Hartschuh, ACS Nano 3 (2009), pp. 3963–3968.
[228] Y. Wang, X.F. Xu, J. Lu, M. Lin, Q.L. Bao, B. Ozyilmaz, and K.P. Loh, ACS Nano 4 (2010), pp. 6146–6152.
[229] Y.-C. Lin, C.-Y. Lin, and P.-W. Chiu, Appl. Phys. Lett. 96 (2010), art. 133110.
[230] H. Terrones, R. Lv, M. Terrones, and M.S. Dresselhaus, Rep. Prog. Phys. 75 (2012), art. 062501.
[231] A. Eckmann, A. Felten, A. Mishchenko, L. Britnell, R. Krupke, K.S. Novoselov, and C. Casiraghi, Nano Lett. 12 (2012), pp. 3925–3930.
[232] G. Diankov, M. Neumann, and D. Goldhaber-Gordon, ACS Nano 7 (2013), pp. 1324–1332.
[233] Z. Luo, T. Yu, K.-J. Kim, Z. Ni, Y. You, S. Lim, Z. Shen, S. Wang, and J. Lin, ACS Nano 3 (2009), pp. 1781–1788.
[234] R. Yang, L. Zhang, Y. Wang, Z. Shi, D. Shi, H. Gao, E. Wang, and G. Zhang, Adv. Mater. 22 (2010), pp. 4014–4019.
[235] Z. Shi, R. Yang, L. Zhang, Y. Wang, D. Liu, D. Shi, E. Wang, and G. Zhang, Adv. Mater. 23 (2011), pp. 3061–3065.
[236] J. Roth and C. Garcia-Vazquez, Nucl. Fusion 36 (1996), pp. 1647–1659.
[237] B.V. Mech, A.A. Haasz, and J.W. Davis, J. Appl. Phys. 84 (1998), pp. 1655–1669.
[238] S. Liu, J. Sun, S. Dai, T. Stirner, and D.A. Wang, J. Appl. Phys. 108 (2010), art. 073302.
[239] G. Kalita, K. Wakita, and M. Umeno, RSC Adv. 2 (2012), pp. 2815–2820.
[240] L. Liu, Y. Zhang, W. Wang, C. Gu, X. Bai, and E. Wang, Adv. Mater. 23 (2011), pp. 1246–1251.
[241] J. Bai, X. Duan, and Y. Huang, Nano Lett. 9 (2009), pp. 2083–2087.
[242] L. Jiao, L. Zhang, X. Wang, G. Diankov, and H. Dai, Nature 458 (2009), pp. 877–880.
[243] L. Jiao, L. Zhang, L. Ding, J.E. Liu, and H.J. Dai, Nano Res. 3 (2010), pp. 387–394.
[244] L. Xie, H. Wang, C. Jin, X. Wang, L. Jiao, K. Suenaga, and H. Dai, J. Amer. Chem. Soc. 133 (2011), pp. 10394–10397.
[245] T. Kato and R. Hatakeyama, Nature Nanotechnol. 7 (2012), pp. 651–656.
[246] Y.M. Han, J.C. Brant, and P. Kim, Phys. Rev. Lett. 104 (2010), art. 056801.
[247] T. Kato and R. Hatakeyama, ACS Nano 4 (2010), pp. 7395–7400.
[248] Y.-W. Son, M.L. Cohen, and S.G. Louie, Nature 444 (2006), pp. 347–349.
[249] M. Cheng, R. Yang, L. Zhang, Z. Shi, W. Yang, D. Wang, G. Xie, D. Shi, and G. Zhang, Carbon 50 (2012), pp. 2581–2587.
[250] S.W. Lee, C. Mattevi, M. Chhowalla, and R.M. Sankaran, J. Phys. Chem. Lett. 3 (2012), pp. 772–777.
[251] A.H. Castro Neto, F. Guinea, N.M.R. Peres, K.S. Novoselov, and A.K. Geim, Rev. Mod. Phys. 81 (2009), pp. 109–162.
[252] D.S.L. Abergel, V. Apalkov, J. Berashevich, K. Ziegler, and T. Chakraborty, Adv. Phys. 59 (2010), pp. 261–482.
[253] N.O. Weiss, H. Zhou, L. Liao, Y. Liu, S. Jiang, Y. Huang, and X. Duan, Adv. Mat. 24 (2012), pp. 5782–5825.
[254] M. Hiramatsu, K. Shiji, H. Amano, and M. Hori, Appl. Phys. Lett. 84 (2004), pp. 4708–4711.
[255] A. Dato, V. Radmilovic, Z. Lee, J. Phillips, and M. Frenklach, Nano Lett. 8 (2008), pp. 2012–2016.
[256] J.D. Long, S. Xu, S.Y. Huang, P.P. Rutkevych, M. Xu, and C.H. Diong, IEEE Trans. Plasma Sci. 33 (2005), pp. 240–241.
[257] A.T.H. Chuanga, J. Robertson, B.O. Boskovic, and K.K.K. Koziol, Appl. Phys. Lett. 90 (2007), art. 123107.
[258] D.H. Seo, S. Kumar, and K. Ostrikov, Carbon 49 (2011), pp. 4331–4339.
[259] M. Cai, R.A. Outlaw, S.M. Butler, and J.R. Miller, Carbon 50 (2012), pp. 5481–5488.
[260] D.H. Seo, S. Kumar, and K. Ostrikov, J. Mater. Chem. 21 (2011), pp. 16339–16343.
[261] S. Kumar and K. Ostrikov, Nanoscale 3 (2011), pp. 4296–4300.
[262] A.E. Rider, S. Kumar, S.A. Furman, and K. Ostrikov, Chem. Comm. 48 (2012), pp. 2659–2661.

[263] D.H. Seo, A.E. Rider, S. Kumar, L.K. Randeniya, and K. Ostrikov, Carbon 60 (2013), pp. 221–228.
[264] S. Karmakar, N.V. Kulkarni, A.B. Nawale, N.P. Lalla, R. Mishra, V.G. Sathe, S.V. Bhoraskar, and A.K. Das, J. Phys. D 42 (2009), art. 115201.
[265] O. Volotskova, I. Levchenko, A. Shashurin, Y. Raitses, K. Ostrikov, and M. Keidar, Nanoscale 2 (2010), pp. 2281–2285.
[266] I. Levchenko, O. Volotskova, A. Shashurin, Y. Raitses, K. Ostrikov, and M. Keidar, Carbon 48 (2010), pp. 4570–4574.
[267] A.B. Murphy, Phys. Rev. Lett. 89 (2002), art. 025002.
[268] A.H. Castro Neto and K. Novoselov, Mater. Express 1 (2011), pp. 10–17.
[269] J. Osaka, M.S. Kumar, H. Toyoda, T. Ishijima, H. Sugai, and T. Mizutani, Appl. Phys. Lett. 90 (2007), art. 172114.
[270] S. Tawil, D. Krishnamurthy, R. Kakimi, S. Emura, S. Hasegawa, and H. Asahi, J. Cryst. Growth 323 (2011), pp. 351–354.
[271] D. K. Seo, S. Shin, H.H. Cho, B.H. Kong, D.M. Whang, and H.K. Cho, Acta Mater. 59 (2011), pp. 6743–6750.
[272] H. Watanabe and S. Shikata, Diam. Relat. Mater. 20 (2011), pp. 980–982.
[273] F.J. Aparicio, M. Holgado, A. Borras, I. Blaszczyk-Lezak, A. Griol, C.A. Barrios, R. Casquel, F.J. Sanza, H. Sohlström, M. Antelius, A.R. González-Elipe, and A. Barranco, Adv. Mater. 23 (2011), pp. 761–765.
[274] D. Mariotti, A.C. Bose, K. Ostrikov, and T. Sasaki, Nanotechnology 19 (2008), art. 495302.
[275] B. Varghese, M.V. Reddy, Z. Yanwu, C.S. Lit, T.C. Hoong, G.V. Subba Rao, B.V.R. Chowdari, A.T.S. Wee, C.T. Lim, and C.H. Sow, Chem. Mater. 20 (2008), pp. 3360–3367.
[276] X.L. Wang, Phys. Rev. Lett. 100 (2008), art. 156404.
[277] L. Fu, C.L. Kane, and E.J. Mele, Phys. Rev. Lett. 98 (2007), art. 106803.
[278] F. Banhart, Nanoscale 1 (2009), pp. 201–213.
[279] A. Gohier, B. Laik, K.-H. Kim, J.-L. Maurice, J.-P. Pereira-Ramos, C.S. Cojocary, and P.T. Van, Adv. Mater. 24 (2012), pp. 2592–2597.
[280] A.L.M. Reddy, S.R. Gowda, M.M. Shaijumon, and P.M. Ajayan, Adv. Mater. 24 (2012), pp. 5045–5064.
[281] S. Yick, Z.J. Han, and K. Ostrikov, Chem. Comm. 49 (2013), pp. 2861–2863.
[282] T. Kaneko, Y. Li, S. Nishigaki, and R. Hatakeyama, J. Amer. Chem. Soc. 130 (2008), pp. 2714–2715.
[283] E.C. Neyts and A. Bogaerts, Carbon 47 (2009), pp. 1028–1033.
[284] E.C. Neyts, A. Maeyens, G. Pourtois, and A. Bogaerts, Carbon 49 (2011), pp. 1013–1017.
[285] A. Borras, A. Barranco, J.P. Espinos, J. Cotrino, J.P. Holgado, and A.R. Gonzalez-Elipe, Plasma Proc. Polym. 4 (2007), pp. 515–527.
[286] J.W. Coburn and H. Winters, J. Vac. Sci. Technol. 16 (1979), pp. 391–403.
[287] T. Lill and O. Joubert, Science 319 (2008), pp. 1050–1051.
[288] N. Marchack and J. Chang, J. Phys. D 44 (2011), art. 174011.
[289] C. Petit-Etienne, M. Darnon, L. Vallier, E. Pargon, G. Cunge, F. Boulard, O. Joubert, S. Banna, and T. Lill, J. Vac. Sci. Technol. B 28 (2010), pp. 926–935.
[290] S. Samukawa, Jpn. J. Appl. Phys. 45 (2006), pp. 2395–2407.
[291] M. Igarashi, M.F. Budiman, W. Pan, W. Hu, Y. Tamara, M.E. Syazwan, N. Usami, and S. Samukawa, Nanotechnology 24 (2013), art. 015301.
[292] C.Q. Sun, Prog. Mater. Sci. 54 (2009), pp. 179–307.
[293] W.S. Lim, S.D. Park, B.J. Park, and G.Y. Yeom, Surf. Coat. Technol. 202 (2008), pp. 5701–5704.
[294] A. Agarwal and M.J. Kushner, J. Vac. Sci. Technol. A 27 (2009), pp. 37–50.
[295] J. Shieh, C.H. Lin, and M.C. Yang, J. Phys. D 40 (2007), pp. 2242–2246.
[296] S. Xu, I. Levchenko, S.Y. Huang, and K. Ostrikov, Appl. Phys. Lett. 95 (2009), art. 111505.
[297] I. Levchenko, S.Y. Huang, K. Ostrikov, and S. Xu, Nanotechnology 21 (2010), art. 025605.
[298] D.A.G. Bruggeman, Ann. Phys. 416 (1935), pp. 636–664.
[299] S. Xu, S.Y. Huang, I. Levchenko, H.P. Zhou, D.Y. Wei, S.Q. Xiao, L.X. Xu, W.S. Yan, and K. Ostrikov, Adv. Energy Mater. 1 (2011), pp. 373–376.
[300] M.Y. Chen, K.Y. Wu, J. Hwang, M.T. Chang, L.J. Chou, and C.S. Kou, Nanotechnology 18 (2007), art. 455706.

[301] I. Levchenko, K. Ostrikov, J.D. Long, and S. Xu, Appl. Phys. Lett. 91 (2007), art. 113115.
[302] B.B. Wang and B. Zhang, Carbon 44 (2006), pp. 1949–1953.
[303] K.H. Muller, J. Appl. Phys. 59 (1986), pp. 2803–2807.
[304] B.B. Wang, Q.J. Cheng, L.H. Wang, K. Zheng, and K. Ostrikov, Carbon 50 (2012), pp. 3561–3571.
[305] J. Robertson, Phys. Rev. B 53 (1996), pp. 16302–16305.
[306] M. Fuele, J. Budai, S. Toth, M. Veres, and M. Koos, J. Non-Cryst. Solids 352 (2006), pp. 1340–1343.
[307] S. Bhattacharyya, O. Auciello, J. Birrell, J.A. Carlisle, L.A. Curtiss, A.N. Goyette, D.M. Gruen, A.R. Krauss, J. Schlueter, A. Sumant, and P. Zapol, Appl. Phys. Lett. 79 (2001), pp. 1441–1443.
[308] D.M. Gruen, MRS Bull. 26 (2001), pp. 771–776.
[309] M. Eckert, E.C. Neyts, and A. Bogaerts, Chem. Vapor Depos. 14 (2008), pp. 213–223.
[310] M. Eckert, E.C. Neyts, and A. Bogaerts, Cryst. Growth Design 10 (2010), pp. 4123–4134.
[311] H.-J. Lee, H. Jeon, and W.-S. Lee, J. Appl. Phys. 110 (2011), art. 084305.
[312] A.S. Barnard and M. Sternberg, J. Mater. Chem. 17 (2007), pp. 4811–4819.
[313] Y. Lifshitz, T. Koehler, T. Frauenheim, I. Guzmann, A. Hoffman, R.Q. Zhang, X.T. Zhou, and S.T. Lee, Science 297 (2002), pp. 1531–1533.
[314] M. Eckert, V. Mortet, L. Zhang, E. Neyts, J. Verbeeck, K. Haenen, and A. Bogaerts, Chem. Mater. 23 (2011), pp. 1414–1423.
[315] A. Krueger and D. Lang, Adv. Funct. Mater. 22 (2012), pp. 890–906.
[316] J.-C. Arnault, T. Petit, H. Girard, A. Chavanne, C. Gesset, M. Sennour, and M. Chaigneau, Phys. Chem. Chem. Phys. 13 (2011), pp. 11481–11487.
[317] N.A. Marks, M. Lattemann, and D.R. McKenzie, Phys. Rev. Lett. 108 (2012), art. 075503.
[318] A. Taylor, F. Fendrych, L. Fekete, J. Vlcek, V. Rezacova, V. Petrak, J. Krucky, M. Nesladek, and M. Lier, Diam. Relat. Mater. 20 (2011), pp. 613–615.
[319] Y.P. Ren, S. Xu, A.E. Rider, and K. Ostrikov, Nanoscale 3 (2011), pp. 731–740.
[320] H.K. Yasuda, *Plasma Polymerization*, Academic Press, London, 1985.
[321] R. Di Mundo, R. Gristina, E. Sardella, F. Intranuovo, M. Nardulli, A. Milella, F. Palumbo, R. d'Agostino, and P. Favia, Plasma. Process. Polym. 7 (2010), pp. 212–223.
[322] F. Bretagnol, A. Valsesia, T. Sasaki, G. Ceccone, P. Colpo, and F. Rossi, Adv. Mater. 19 (2007), pp. 1947–1950.
[323] A. Valsesia, T. Meziani, F. Bretagnol, P. Colpo, G. Ceccone, and F. Rossi, J. Phys. D 40 (2007), pp. 2341–2347.
[324] S. Simovic, D. Losic, and K. Vasilev, Chem. Commun. 46 (2010), pp. 1317–1319.
[325] A. Michelmore, P.M. Bryant, D.A. Steele, K. Vasilev, J.W. Bradley, and R.D. Short, Langmuir 27 (2011), pp. 11943–11950.
[326] K. De Bleecker, A. Bogaerts, and W. Goedheer, Phys. Rev. E 73 (2006), art. 026405.
[327] M. Alcaire, J.R. Sanchez-Valencia, F.J. Aparicio, Z. Saghi, J.C. Gonzales-Gonzales, A. Barranco, Y.O. Zian, A.R. Gonzales-Elipe, P. Midgley, J.P. Espinos, P. Groening, and A. Borras, Nanoscale 3 (2011), pp. 4554–4559.
[328] E. Gogolides, A. Tserepi, V. Constantoudis, G. Kokkoris, D. Kontziampasis, K. Tsougeni, G. Boulousis, and M.E. Vlachopoulou, J. Phys. D 44 (2011), art. 174021.
[329] S. Facsko, T. Dekorsy, C. Koerdt, C. Trappe, H. Kurz, A. Vogt, and H.L. Hartnagel, Science 285 (1999), pp. 1551–1553.
[330] P. Cordier, F. Tournilhac, C. Soulie-Ziakovic, and L. Leibler, Nature 451 (2008), pp. 977–980.
[331] M.G. Kong, G. Kroesen, G. Morfill, T. Nosenko, T. Shimizu, J. van Dijk, and J.L. Zimmermann, New J. Phys. 11 (2009), art. 115012.
[332] M. Laroussi, IEEE Trans. Plasma Sci. 37 (2009), pp. 714–725.
[333] G. Lloyd, G. Friedman, S. Jafri, G. Schultz, A. Fridman, and K. Harding, Plasma Process. Polym. 7 (2010), pp. 194–211.
[334] K.W. Ng, S.P. Khoo, B.C. Heng, M.I. Setyawati, E.C. Tan, X. Zhao, S. Xiong, W. Fang, D.T. Leong, and J.S. Loo, Biomaterials 32 (2011), pp. 8218–8227.
[335] M. Keidar, R. Walk, A. Shashurin, P. Srinivasan, A. Sandler, S. Dasgupta, R. Ravi, R. Guerrero-Preston, and B. Trink, Br. J. Cancer 105 (2011), pp. 1295–1301.
[336] N.Y. Babaeva and M.J. Kushner, J. Phys. D 43 (2010), art. 185206.

[337] H.W. Lee, G.Y. Park, Y.S. Seo, Y.H. Im, S.B. Shim, and H.J. Lee, J. Phys. D 44 (2011), art. 053001.
[338] X. Yan, Z. Xiong, F. Zou, S. Zhao, X. Lu, G. Yang, G. He, and K. Ostrikov, Plasma Proc. Polym. 9 (2012), pp. 59–66.
[339] X. Pei, X. Lu, J. Liu, D. Liu, Y. Yang, K. Ostrikov, P.K. Chu, and Y. Pan, J. Phys. D 45 (2012), art. 165205.
[340] D. Dobrynin, G. Fridman, G. Friedman, and A. Fridman, New J. Phys. 11 (2009), art. 115020.
[341] G.C. Kim, G.J. Kim, S.R. Park, S.M. Jeon, H.J. Seo, F. Iza, and J.K. Lee, J. Phys. D 42 (2009), art. 032005.
[342] M.G. Kong, M. Keidar, and K. Ostrikov, J. Phys. D 44 (2011), art. 174018.
[343] E. Karakas, A. Munyanyi, L. Greene, and M. Laroussi, Appl. Phys. Lett. 97 (2010), art. 143702.
[344] Z. Xiong, X. Lu, Y. Cao, Q. Ning, K. Ostrikov, Y. Lu, X. Zhou, and J. Liu, Appl. Phys. Lett. 99 (2011), art. 253703.
[345] J.Y. Kim, Y. Wei, J. Li, P. Foy, T. Hawkins, J. Ballato, and S.-O. Kim, Small 7 (2011), pp. 2291–2295.
[346] M. Yusupov, E.C. Neyts, U. Khalilov, R. Snoeckx, A.C.T. van Duin, and A. Bogaerts, New J. Phys. 14 (2012), art. 093043.
[347] M. Yusupov, E.C. Neyts, A.C.T. van Duin, and A. Bogaerts, J. Phys. Chem. C 117 (2013), pp. 5993–5998.
[348] H. Kroto, Rev. Mod. Phys. 69 (1997), pp. 703–722.
[349] S. Komatsu, J. Phys. D 40 (2007), pp. 2320–2340.
[350] Y. Malhotra, S. Roy, M.P. Srivastava, C.R. Kant, and K. Ostrikov, J. Phys. D 42 (2009), art. 155202.
[351] V. Surla and D.N. Ruzic, J. Phys. D 44 (2011), art. 174026.
[352] P. Willmott and J. Huber, Rev. Mod. Phys. 72 (2000), pp. 315–328.
[353] N. Bulgakova, A.V. Bulgakov, and O.F. Bobrenok, Phys. Rev. E 62 (2000), pp. 5624–5635.
[354] S. Juodkazis, H. Misawa, O.A. Louchev, and K. Kitamura, Nanotechnology 17 (2006), pp. 4802–4805.
[355] A.V. Kabashin, Ph. Delaporte, A. Pereira, D. Grojo, R. Torres, Th. Sarnet, and M. Sentis, Nanoscale Res. Lett. 5 (2010), pp. 454–463.
[356] U. Helmersson, M. Lattemann, J. Bohlmark, A. Ehiasarian, and J. Gudmundsson, Thin Solid Films 513 (2006), pp. 1–24.
[357] R.S. Rawat, Nanosci. Nanotechnol. Lett. 4 (2012), pp. 251–274.
[358] D. Pines, Rev. Mod. Phys. 28 (1956), pp. 184–199.
[359] M.F. Hoyaux, Contemp. Phys. 9 (1968), pp. 165–196.
[360] S. Raimes, Rep. Prog. Phys. 20 (1957), pp. 1–37.
[361] A.K. Jonscher, Brit. J. Appl. Phys. 15 (1964), pp. 365–377.
[362] Y. Wang, E.W. Plummer, and K. Kempa, Adv. Phys. 60 (2011), pp. 799–898.
[363] A.E. Rider, K. Ostrikov, and S.A. Furman, Eur. J. Phys. D 66 (2012), art. 226.
[364] M.I. Stockman, Phys. Today 64 (2011), pp. 39–44.
[365] S. Maier and H. Atwater, J. Appl. Phys. 98 (2005), art. 011101.
[366] A.V. Zayats, I. Smolyaninov, and A.A. Maradudin, Phys. Rep. 408 (2005), pp. 131–314.
[367] K.M. Mayer and J.H. Hafner, Chem. Rev. 111 (2011), pp. 3828–3857.
[368] M.A. Green and S. Pillai, Nature Photon. 6 (2012), pp. 130–132.
[369] Y. Akimov, W. Koh, and K. Ostrikov, Opt. Express 17 (2009), pp. 10195–10205.
[370] Y.A. Akimov, K. Ostrikov, and E.P. Li, Plasmonics 4 (2009), pp. 107–113.
[371] M.G. Silverinha, Phys. Rev. B 79 (2009), art. 035118.
[372] E. Hao and G.C. Schatz, J. Chem. Phys. 120 (2004), pp. 357–366.
[373] E. Lukianova-Hleb, Y. Hu, L. Latterini, L. Tarpani, S. Lee, R.A. Drezek, J.H. Hafner, and D.M. Lapotko, ACS Nano 4 (2010), pp. 2109–2123.
[374] E. Boulais, R. Lachaine, and M. Meunier, Nano Lett. 12 (2012), pp. 4763–4769.
[375] A. Ng, Int. J. Quantum Chem. 112 (2012), pp. 150–160.
[376] B.I. Cho, K. Engelhorn, A.A. Correa, T. Ogitsu, C.P. Weber, H.J. Lee, J. Feng, Y. Ping, A.J. Nelson, D. Prendergast, R.W. Lee, R.W. Falcone, and P.A. Heimann, Phys. Rev. Lett. 106 (2011), art. 167601.
[377] M. Koenig, A. Benuzzi-Mounaix, A. Ravasio, T. Vinci, N. Ozaki, S. Lepape, D. Batani, G. Huser, T. Hall, D. Hicks, A. MacKinnon, P. Patel, H.S. Park, T. Boehly, M. Borghesi, S. Kar, and L. Romagnani, Plasma Phys. Control. Fusion 47 (2005), pp. B441–B449.

[378] V. Recoules, J. Clerouin, G. Zerah, P.M. Anglade, and S. Mazevet, Phys. Rev. Lett. 96 (2006), art. 055003.
[379] D.Z. Pai, K. Ostrikov, S. Kumar, D.A. Lacoste, I. Levchenko, and C.O. Laoux, Sci. Rep. 3 (2013), art. 1221.
[380] K. Moothi, S.E. Iyuke, M. Meyyappan, and R. Falcon, Carbon 50 (2012), pp. 2679–2690.
[381] D. Mariotti, S. Mitra, and V. Svrcek, Nanoscale 5 (2013), pp. 1385–1398.
[382] D. Mariotti, V. Svrcek, A. Mathur, C. Dickinson, K. Matsubara, and M. Kondo, J. Phys. D. 46 (2013), art. 122001.
[383] K.G. Kiriluk, J.D. Fields, B.J. Simonds, Y.P. Pai, P.L. Miller, T. Su, B. Yan, J. Yang, S. Guha, A. Madan, S.E. Shaheen, P.C. Taylor, and R.T. Collins, Appl. Phys. Lett. 102 (2013), art. 133101.
[384] A.P. Magyar, I. Aharonovich, M. Baram, and E.L. Hu, Nano Lett. 13 (2013), pp. 1210–1215.
[385] K. Tai, T.J. Houlahan, J.G. Eden, and S.J. Dillon, Sci. Repts. 3 (2013), art. 1325.
[386] J. Patel, L. Nemcova, P. Maguire, W.G. Graham, and D. Mariotti, Nanotechnology 24 (2013), art. 245604.
[387] M.M.A. Yajadda and K. Ostrikov, Appl. Phys. Lett. 102 (2013), art. 111115.
[388] H. Watanabe, H. Kondo, M. Hiramatsu, M. Sekine, S. Kumar, K. Ostrikov, and M. Hori, Plasma Proc. Polym. (2013). doi: 10.1002/ppap.201200141
[389] Z. Yue, I. Levchenko, S. Kumar, D.H. Seo, X.L. Wang, S.X. Dou, and K. Ostrikov, Nanoscale (2013). doi: 10.1039/C3NR00550J
[390] K. Ostrikov, IEEE Trans. Plasma Sci. 41 (2013), art. 6403566.
[391] D.H. Seo, Z.J. Han, S. Kumar, and K. Ostrikov, Adv. Energy Mater. (2013). doi: 10.1002/aenm.201300431
[392] Y.F. Li, Q. Chen, K. Xu, T. Kaneko, and R. Hatakeyama, Chem. Eng. J. 215 (2013), pp. 45–49.
[393] M. Hiramatsu, S. Mitsuguchi, T. Horibe, H. Kondo, M. Hori, and H. Kano, Jpn. J. Appl. Phys. 52 (2013), art. 01AK03.
[394] I. Jogi, K. Erme, A. Haljaste, and M. Laan, Eur. Phys. J. Appl. Phys. 61 (2013), art. 24305.

Appendix 1. Alphabetic list of acronyms used in the review

0D–zero-dimensional
1D–one-dimensional
2D – two-dimensional
3D – three-dimensional
a-Si – amorphous silicon
AD – adsorption
AFM – atomic force microscopy
ALE – atomic layer etching
BD – bulk diffusion
BU – building unit
C-dot – carbon (quantum) dot
CNF – carbon nanofiber
CNP – catalyst nanoparticle
CNT – carbon nanotube
CNTP – carbon nanotip
CNW – carbon nanowall
CVD – chemical vapor deposition
DBD – dielectric barrier discharge
DC – direct current
DNA – deoxyribonucleic acid
EEDF – electron energy distribution function
EFE – electron field emission
fs – femtosecond
GML – graphene monolayer
GNR – graphene nanoribbon
GNS – graphene nanosheet

GO – graphene oxide
GT – Gibbs–Thomson (effect)
HED – high energy density (plasma)
HRTEM – high-resolution transmission electron microscopy
LOM – local-order measure
LSP – localized surface plasmon
i-PVD – ionized physical vapor deposition
MD – molecular dynamics
MW – microwave
MWCNT – multi-walled carbon nanotube
nc-Si – nanocrystalline silicon
NCD – nanocrystalline diamond
NND – nearest neighbor distance
NP – nanoparticle
NS – nanostructure
NW – nanowire
PECVD – plasma-enhanced chemical vapor deposition
PG – peptidoglycan
PL – photoluminescence
PLD – pulsed laser deposition
PLE – photoluminescence excitation
PSS – plasma-solid system
QD – quantum dot
RF – radiofrequency
RIE – reactive ion etching
RNS – reactive nitrogen species
ROS – reactive oxygen species
SD – surface diffusion
SWCNT – single-walled carbon nanotube
TEM – transmission electron microscopy
UNCD – ultra-nanocrystalline diamond
USGs – unsupported graphenes
UV – ultra-violet
Vis – visible
VLS – vapor–liquid–solid
VSGs – vertically standing graphenes